Advancements in Polymer Electrolyte Fuel Cell Architecture and Performance using Electrochemical Modelling and Advanced Characterisation

Nivedita Narendra Kulkarni

Supervisors:

Prof D. J. L. Brett and Prof P.R. Shearing

Submitted in partial fulfilment of the requirements for the degree of Doctor of Philosophy, 2020

Electrochemical Innovation Lab

Department of Chemical Engineering

University College London

I WOULD LIKE TO DEDICATE THIS THESIS

TO THE MAN OF MY LIFE, SHRI,

TO MY LOVING PARENTS,

&

TO OUR MOST BEAUTIFUL DOG, LAIKA …

Declaration

I, Nivedita Narendra Kulkarni, confirm that the work presented in this thesis is my own. Where information has been derived from other sources, I confirm that this has been indicated in the thesis.

Nivedita Narendra Kulkarni

Date

Acknowledgements

First and foremost, I would like to profoundly thank my supervisor, Dan Brett, for his trust, vision and unbeatable enthusiasm during this project. Without his support, this PhD thesis would not have been possible. His continuous guidance, ideas and suggestions throughout the project have been insightful and made me the researcher that I am today. His exceptional leadership skills have helped to keep my enthusiasm and motivation intact throughout the project. I also would like to thank my secondary PhD supervisor, Paul Shearing, for his advice and insightful discussions during the meetings, and his continuous support throughout the PhD. Dan and Paul together have offered me the best research experience at EIL. Thank you both.

This PhD started while I was working with Intelligent Energy, Loughborough. I am thankful to my then manager, Simon Nicholas, Senior Engineering Manager, for his trust in me from day one of joining Intelligent Energy as an Analysis engineer and his support. I am also thankful and grateful to Dr Paul Adcock, then *Director of Research and Technology* at Intelligent Energy for trusting me and getting me in contact with EIL, arranging in-kind support from Intelligent Energy and support during my time at the company that continued even after joining full-time PhD. I would like to thank Chris Gurney for being my industrial supervisor and a friend. I am grateful to the scientific discussions I had with Chris, Rama Pratap, and Samuel Cruiz, for their excellent suggestions, and furthermore for the sharp arguments about the results, which significantly helped me to streamline the project at the beginning of the PhD. Not to forget, I thank my ex-colleagues Ricardo Pimenta, Andrew Paxton, Chris James, for cheering me up while I was managing a full-time job and a PhD and bearing me during the much-needed coffee breaks.

More than anything I am massively thankful to Quentin Meyer and Francesco Iacoviello for their support throughout this journey. Quentin, who indeed introduced

me to the EIL life, helped me to form the PhD outline, to settle down at EIL during his time in the UK and to keep an eye on the progress even after moving to Australia. Francesco whose happy and positive outlook always helped me in my great, good, bad, worst days, and of course I cherished our everlasting discussions about the coffee, culture and travel with him. Without this duo as friends and guides, this PhD wouldn't have been possible. Not to forget, but I am hugely thankful to Rhod Jervis for the discussions about work and helping me to setup Deben experiments at random hours and never giving up on my poor writing.

No PhD would be complete without many sharp interactions with fellow PhD students and PDRAs. I am hugely thankful to Fabiola, Daniella Ledwoch, Jason Cho, James Doddwel, Josh Bailey, Jon Morgado, Tanveerkhan Pathan, Jude, Donal, Aliya, Amal, Mayowa. Without their presence, the time during this PhD would not have been the same, ranging from the technical discussions, politics, culture, travel, food etc. etc. etc. For their attention to details, for their advice, for their support, for never giving up on me even when I didn't deserve it, for the pub times, for being such amazing friends. Not to forget, the new PhDs and PDRAs, Jen, Lara, Rhod Owen, Drasti, Zahra, Ana, Martin. You all bought so much more strength to the group and made EIL a fun place to work at. Thank you so much. Again, cannot thank enough to Fabiola, for being such a fantastic friend who was always available for technical, non-technical talks and for forcing me every now and then to take a break and relax. To Jason Cho, for all his help ever since my early days at EIL, who was always there to help in the project, then it could be experimental, could be modelling or on the system level. Thank you, Jason. This duo indeed ensured that I would laugh a lot while in the office and never stressed.

I am fortunate and grateful for the time I spend in the lab, learning from lab wizards, lab manager Toby Neville, Jason Cho, Lara Rasha, Yunsong Wu, Jennifer Hack and Rhod Owen. Thank you each of you for exposing me to the entirely different world of lab work, helping to design and set-up the experiments and all sort of discussions I had with you. All of this gave me a much broader experience of a PhD in the Chemical

Engineering department. All of you, for making the EIL feel like a family, I would always look forward to work with.

Every PhD takes expected, and unexpected twists and turns and one such turn introduced me to the world of X-ray computed tomography. When Quentin, Rhodri J, Francesco helped to understand how to set-up the experiment, my go-to person for every single AVIZO doubt was Xuekun Lu, a mastermind of segmentation and Avizo. Big thanks to him. Not to forget, always thankful to Matt Kok, for sharing his knowledge in COMSOL, for helping me to streamline the papers and thoroughly reviewing them. No computation PhD can ever be complete with the help from IT services. I am thankful for all the support Dave and Martyn (IT manager) offered throughout my tenure at EIL.

Never the less, I am thankful to the researchers I met at various conferences, and they became good friends. For their continual support, motivation, drive and passion for the hydrogen era, for exposing me to different cultures and for making the conference experience very unique. Thank you each one of you.

While all the friends and colleagues at EIL were a treasure, my personal friends formed a great support system throughout the PhD phase. Ishrat for most random chats at random hours of the day, Ruth, Remy and their beautiful daughter Annabel for allowing me to crash at their home whenever required and for the warm, delicious food, Tanmayee and Rohan for their overall support. I am thankful to Ankita and Shubham for all their help in the last and most busy year. Not to forget I am grateful to all my friends and guides at the Derbyshire and Lancashire Gliding Club and fellow climbing friends for teaching me not to stop but keep pursuing.

My thanks are not enough for the continuous support and motivation I received from my family (and second family!) for being sympathetic, for understanding me and cheering me up with the thousands of different ways. I always cherished the discussions with them ranging from politics to poetry, to art, to science, to philosophy, which helped me to keep motivated and look at the world from different perspectives. I especially thank Nachiket (and indeed Ujjwal) for being the most annoying brother

and a friend who knows how to make me laugh. And last, but certainly not the least, I must make a vain attempt at expressing the full extent of my gratitude to Shri, the man of my life, for all his sacrifices, for his love and compassion, for understanding me and bearing with me and for the best gift he offered me during last year of PhD, Laika, our gorgeous and lovely Labrador. This duo ensured I am always happy and fresh in these final months of the PhD. I will indeed continue to thank them for many years to come!!

Abstract

With the ever depleting traditional energy sources and increasing the carbon footprints, the new landscape of the renewable energy sources has evolved. With the versatility of required environmental conditions, topological locations, operating temperature, polymer electrolyte fuel cells (PEFCs) operating on hydrogen has been recognised as a prominent renewable energy technology. PEFCs offers the possibility of zero-emission and high power density electricity generation for a wide range of transport, portable, and stationary power applications. While technology continues to improve, there are still some challenges concerning durability, cost and performance. An improved understanding of the processes occurring within operational fuel cells and optimisation of the cell architecture will accelerate large-scale commercialization of PEFCs. The most powerful ways to understand and resolve these challenges is to understand the complex interplay of the internal workings of fuel cells and cell design and architecture and operating conditions. Hence, the current research aims to analyse the advancements in the fuel cell design and architecture using a thermo-structural multiphase electrochemical modelling and the advanced characterisation techniques

Firstly, the intricate relationship between cell compression and the flow-field architecture is established by determining the morphological factors using X-ray computed tomography (CT) techniques. The results provide insight into the complex interplay of the morphological factors deciding fuel cell performance and durability. Also, this study provides insight into the extent at which the morphological factors decide water and thermal management of the fuel cell, which are key issues to tackle to broad-scale commercialisation of the technology. Further, the multiphase non-isothermal two-dimensional numerical model was developed. The two-dimensional current, temperature and liquid water saturation profiles reveal the *in-situ* gradients and their correlations with the voltage decay with respect to an increase in cell compression. Finally, the effects of cell compression on the PEFC water dynamics were analysed using in-plane and through-plane in-operando neutron radiography. Neutron radiography provides a detailed understanding of what constitutes the thickness of liquid water present in the operating fuel cell. The Neutron radiography results were also used to validate the numerical models developed. Finally, this work also investigates the effect of secondary flow-field on the dead-ended anode performance and highlights the importance of the manufacturing and assembly tolerances on fuel cell efficiency.

Collectively; this project delineates the comprehensive suite of characterisation techniques and numerical modelling to resolve the PEFC challenges and achieve the cell optimisation and durability required for wide-scale commercialisation of the technology.

Impact Statement

Low-temperature polymer electrolyte fuel cells are one of the most promising devices for low-carbon energy conversion technologies. This thesis presents original research concepts, methodologies and analysis techniques which have been disseminated in the form of international conference talks, journal publications, and public engagement activities.

The main academic impact of the work is the combined use of the novel characterisation techniques and electrochemical modelling for the improved understandings of the critical mechanisms that impact fuel cell performance and potentially inhibit the durability of the fuel cells in the commercial market. The particular methodologies and techniques developed by the author are presented in details in this thesis allowing their application to future research of various fuel cells designs and architecture both for academic and commercial use. The study also presents an existence of the secondary flow-field in the fuel cell, which has a potential impact on commercial fuel cell performance and degradation and proposes the advancements in fuel cell architecture. Thus the adoption of proposed improvements in fuel cell design and architecture should aid enhancement in fuel cell efficiency, thereby facilitating wide-scale commercialisation of fuel cell technology.

Beyond the academic research, parts of the PhD project have also attracted considerable interest during public events and by the industry, especially electrochemical modelling and characterisation techniques for the improved understandings of the fuel cell operations. The present research has bridged many fields of discipline from fundamental science to engineering and has impacted many areas of the public from the school children to the industry specialists.

Publications

Primary Publications

1. ***N. Kulkarni***, Q. Meyer, J. Hack, R. Jervis, F. Iacoviello, K. Ronaszegi, P. Adcock, P.R. Shearing, D.J.L. Brett, Examining the effect of the secondary flow-field on polymer electrolyte fuel cells using X-ray computed radiography and computational modelling, Int. J. Hydrogen Energy. 44 (2019) 1139–1150. doi:10.1016/j.ijhydene.2018.11.038.

2. ***N. Kulkarni***, M.D.R. Kok, R. Jervis, F. Iacoviello, Q. Meyer, P.R. Shearing, D.J.L. Brett, The effect of non-uniform compression and flow-field arrangements on membrane electrode assemblies - X-ray computed tomography characterisation and effective parameter determination, J. Power Sources. 426 (2019) 97–110. doi:10.1016/j.jpowsour.2019.04.018.

3. ***N. Kulkarni***, J.I.S. Cho, L. Rasha, R.E. Owen, Y. Wu, R. Ziesche, J. Hack, T. Neville, M. Whiteley, N. Kardjilov, H. Markötter, I. Manke, P.R. Shearing, D.J.L. Brett, Effect of cell compression on the water dynamics of a polymer electrolyte fuel cell using in-plane and through-plane in-operando neutron radiography, J. Power Sources. 439 (2019) 227074. doi:10.1016/j.jpowsour.2019.227074.

Secondary Publications

1. Y. Wu, J.I.S. Cho, M. Whiteley, L. Rasha, T.P. Neville, R. Ziesche, R. Xu, R. Owen, ***N. Kulkarni***, J. Hack, M. Maier, N. Kardjilov, H. Markötter, I. Manke, F.R. Wang, P.R. Shearing, D.J.L. Brett, “Characterization of water management in metal foam flow-field based polymer electrolyte fuel cells using in-operando

neutron radiography”, Int. J. Hydrogen Energy. (2019). doi:10.1016/j.ijhydene.2019.11.069

Conferences

Oral presentation

1. X-ray tomography investigation and modelling the effect of non-uniform cell compression of polymer electrolyte membrane fuel cell membrane electrode assemblies: channel blocking and effective parameters generation", Gordon Research Seminar for fuel cells – July 2018, Smithfield, USA.

2. "X-ray tomography investigation of the effect of non-uniform cell compression of polymer electrolyte membrane fuel cell membrane electrode assemblies" WHEC-June 2018, Rio De Janeiro, Brazil.

3. "Examining the effect of the secondary ('forgotten') flow-field during dead-ended PEMFC operation", European Fuel Cell Forum, July 2017, Lucerne, Switzerland.

4. "A model-based investigation of the effect of nitrogen blanketing in dead-ended anode PEMFC", H2FC Supergen, December 2016, Belfast, UK.

Poster presentations

1. “Structural characterisation and modelling of the effect of non-uniform compression on reactant transport and performance of polymer electrolyte membrane fuel cells” Gordon Research Conference for fuel cells – 2018, Smithfield, USA.

2. “X-ray tomography investigation and modelling the effect of non-uniform cell compression of polymer electrolyte membrane fuel cell membrane electrode assemblies”, MODVAL, April 2018, Aarau, Switzerland.

3. “X-ray CT investigation of the effect of cell compression on potential blocking of the flow-field”, H2FC Supergen, December 2017, St. Andrews, UK.

4. “1-D modelling of open-cathode air proton exchange membrane fuel cells and its extension to 3-D modelling”, H2FC Supergen, December 2015, Bath, UK.

5. “Computational modelling of open-cathode air-breathing proton exchange membrane fuel cells”, Electrochem, September 2015, Durham, UK

Table of Contents

List of Figures

List of Tables

Nomenclature

Abbreviations

1D	One-dimensional
2D	Two-dimensional
3D	Three-dimensional
ACL	Anode Catalyst Layer
AFC	Alkaline Fuel Cell
ASR	Area specific resistance
BP	Bi-polar plates
BV	Butler-Volmer
CCL	Cathode Catalyst Layer
CL	Catalyst Layer
CFD	Computational Fluid Dynamics
CT	Computed Tomography
DEA	Dead-Ended Anode

ECSA	Electrochemically Active Surface Area
EIS	Electrochemical Impedance Spectroscopy
EOD	Electro-Osmotic Drag
EPA	Environmental Protection Agency
EV	Electric Vehicle
FBP	Filtered Back Projection
FCV	Fuel Cell Vehicle
FEA	Finite Element Analysis
FIB	Focused Ion Beam
FOV	Field-of-View
GDL	Gas Diffusion Layer
GHG	Greenhouse Gas Emissions
HEV	Hybrid Electric Vehicle
HOR	Hydrogen Oxidation Reaction
IC	Internal Combustion
IPCC	Intergovernmental Panel on Climate Change
LBM	Lattice-Boltzmann Method

MCFC	Molten Carbonate Fuel Cell
MEA	Membrane Electrode Assembly
MPL	Microporous Layer
OCV	Open Circuit Voltage
OECD	Organisation for Economic Co-operation and Development
ORR	Oxygen Reduction Reaction
PAFC	Phosphoric Acid Fuel Cell
PDE	Partial Differential Equation
PEFC	Polymer Electrolyte Fuel Cell
PEM	Proton Exchange Membrane
PTFE	Polytetrafluoroethylene
PV	Photovoltaics
REV	Representative Elementary Volume
RH	Relative humidity
SDG	Sustainable Development Goals
SEM	Scanning Electron Microscopy
SOFC	Solid Oxide Fuel Cell

TPB	Triple-Phase Boundary
VOF	Volume of Fluid

Symbols

A	Cross-sectional area, [m^2]
C	Dimensionless concentration
c	Concentration [mol m^{-3}]
$c_{p,i}$	Specific heat capacity of the species i, [J mol^{-1} K^{-1}]
D	Diffusivity, [m^2 s^{-1}]
D_c	Capillary diffusion coefficient, [m^2 s^{-1}]
D_{ij}	Stefan-Maxwell diffusion coefficient matrix, [m^2 s^{-1}]
E	Electric voltage, [V]
E_r	Effectiveness factor
E^0	Open circuit voltage, [V]
EW	Equivalent weight of Nafion® membrane, [g mol^{-1}]
F	Faraday's constant, [C mol^{-1}]
f	Platinum mass ratio to Pt/C
ΔG	Gibbs free energy

H_i	Henry's constant for species *i*, [Pa m^3 mol^{-1}]
h	Height, [m]
J_0	Exchange current density, [A cm^{-2}]
j	Current densit, [A cm^{-2}]
$J(s)$	Leverett function
k	Rate coefficient, [s^{-1}]
k_i	Thermal conductivity of species *i*, [W m^{-1} K^{-1}]
K	Absolute permeability, [m^2]
K_r	Relative permeability, [m^2]
K_p	Hydraulic permeability, [m^2]
M_j	Molecular weight for specie *i*, [kg mol^{-1}]
M_n	Mean molecular weight, [kg mol^{-1}]
m_{pt}	Platinum loading, [mg cm^{-2}]
m_c	Carbon loading, [mg cm^{-2}]
n_e	Number of electrons participating in the reaction
P	Pressure, [Pa]
R	Universal gas constant, [J kg^{-1} mol^{-1}]

r	Radius, [m]
S	Source term
s	Liquid water saturation
T	Temperature, [K]
$\boldsymbol{u}$	Velocity vector
V	Mole volume, [m^3]
V_{phase}	Volume fraction of the phase
w	Width, [m]
x	Mole fraction

Greek letters

α	Charge transfer coefficient
α_w	Water activity
δ	Thickness of ionomer/liquid water film,[m]
ε	Porosity
η	Overpotential, [V]
θ	Contact angle, [°]
λ	Water content

v	Poisson's ratio
ξ	Reactant stoichiometry
ρ	Density, [kg m^3]
σ	Surface tension, [N m^{-1}]
σ_s	Electronic conductivity, [S m^{-1}]
σ_l	Ionic conductivity, [S m^{-1}]
φ	Potential, [V]

Superscripts

d	dissolved
eff	effective
eq	equilibrium
g	Gas-phase
l	Liquid-phase
ref	reference
v	Vapour-phase

Subscripts

a	Anode

act	Activation
ads	Adsorption
agg	Agglomerate
C	Carbon
c	Cathode
con	Condensation
conc	Concentration
CL	Catalyst layer
des	desorption
eva	Evaporation
i	Species i
j	Species j
mem	membrane
ohm	Ohmic
Sat	Saturation
v	Vapour-phase
vl	Vapour to liquid

vd	Vapour to dissolved
dl	Dissolved to liquid

Chapter 1
Introduction and motivation

Abstract

This chapter presents the aims and objectives of the PhD project, placing it in a broader context. Firstly, the environmental context is discussed. With increasing global warming and the current target to deeply decarbonise the environment by 2050, investment in research and development activities combined with the need for renewable energy sources as a replacement to fossil fuels is higher than ever. Hydrogen fuelled fuel cells, which are practically free from any CO_2 emission at point of use, are presented as one of the most suitable technology advancements towards the sustainable development goals (SDGs).

After a brief history of fuel cells from their discovery in the 1800s' to today's developments, followed by a review of fuel cell technologies, the polymer electrolyte fuel cell (PEFC) is presented. The present chapter discusses the PEFC architecture and internal operations to form the foundation of the technology. Furthermore, this chapter also provides an overview of the techno-commercial challenges to the wide-scale commercialisation of the technology, leading towards the aim and objective of the current project. Finally, the structure of the thesis is presented.

"Limiting global warming to 1.5 °C above pre-industrial levels would require transformative systemic change, integrated with sustainable development. Such change would require the upscaling and acceleration of the implementation of far-reaching, multilevel and cross-sectoral climate mitigation and addressing barriers. Such systemic change would need to be linked to complementary adaptation actions, including transformational adaptation, especially for pathways that temporarily overshoot 1.5°C."

The Intergovernmental Panel on Climate Change
October 2018
The Republic of Korea

1.1 Motivation

As modern society relies on energy being available for transportation, industrial and residential use, and other day-to-day activities, the social-economic growth of society has resulted in the depletion of fossil fuel resources with ever-increasing consumption. The demand for energy, especially petroleum, and the accompanying greenhouse gas emissions (GHG) have been increasing almost steadily over the past century [1–4]. This would be likely to cause further warming, exacerbating global warming challenges, and increasing the irreversible impact on the entire ecosystem. In order to maintain future economic standards and minimize the environmental impact caused by energy production, the investigation and the investment in sustainable energy systems is mandatory. The recent report by the Intergovernmental Panel on Climate Change (IPCC) agrees on 'warming of the climate system is unequivocal' [4–6]; however, the report states with high confidence that limiting the global warming below 1.5 °C is possible, and would need substantial social and technological transformations, dependent, in turn, on global and regional sustainable development pathways. IPCC further states that hydrogen is one of the means that lead to profound emission reductions, required in energy-intensive industries to limit temperature rise to the defined goal.

Figure 1.1 provides an overview of the sources of GHG emission and global warming. Combined transportation and power sectors are responsible for almost 57% of GHG emissions, followed by the industry sector, with 22% share in GHG emission [7]. The power and the transportation sector have observed more than a 2-fold increase in the CO_2 emission over the last century [3,4,6]. Hence, to mitigate the energy crisis and the carbon footprint, the sustainable development and the use of renewable energy sources for power generation and transportation, is crucial. The net requirement of the power sector can be mitigated by renewable energy sources, such as solar energy, wind power, hydro-power or the ocean energy. The share of wind energy and solar

photovoltaics (PV) in the renewable power generation sector has been ever increasing in the last three decades (1991-2016), recently reached 37.3% and 26.6%, respectively [8]. This represents a positive shift towards lowering the GHG emission and use of low-carbon energy generation techniques. However, it is essential to note that the majority of the renewable power generation techniques are dependent on environmental factors such as time of the day, local weather, season and the availability of resources. Hence, the requirement of renewable sources, free from the external/environmental factors is essential, especially for the power sector.

Likewise, with the depletion in petroleum resources, alternative energy sources are required for the transportation industry, such as battery electric vehicles (BEVs), hybrid plug-ins and the fuel cell electric vehicles (FCEVs). However, there are currently various barriers to the widespread adoption of these technologies. For BEVs, the significant challenge is the relatively low energy density of the batteries and the consequent limited range. Therefore, BEVs are mainly suitable for personal vehicles and short-distance commuter vehicles [9]. With an increase in travel distance and vehicle size, FCEVs are more suitable [9–11] and claims to be the most significant stakeholder in the automobile sector.

Hence, high efficiency and the higher power density have made fuel cell technology the dominant alternative to traditional power sources [12]. While technology continues to improve, there are still some challenges with respect to durability, cost and performance. An improved understanding of how fuel cell devices work, the processes occurring within operational fuel cells and optimisation of the cell architecture will accelerate large-scale commercialization of PEFC technology.

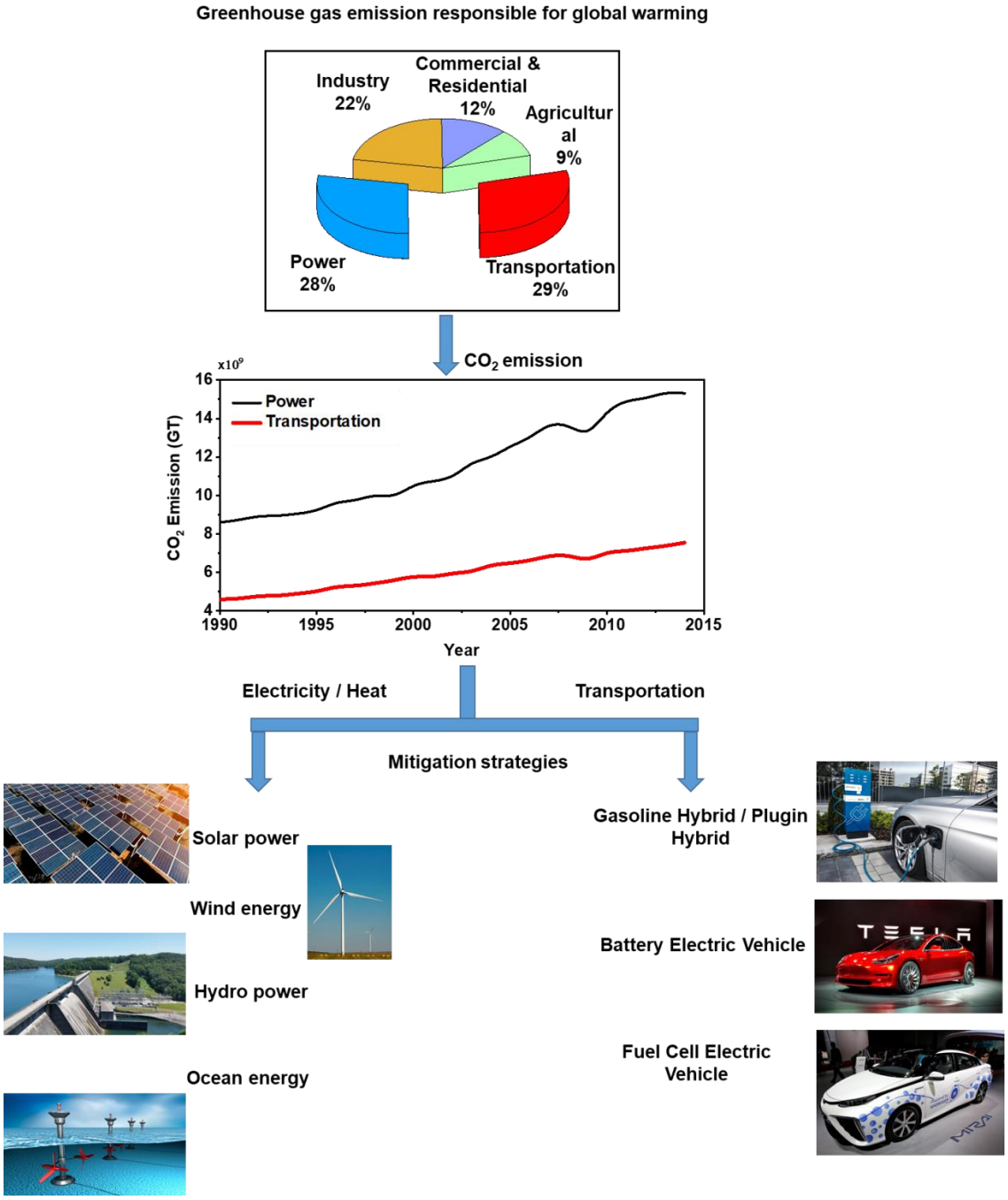

Figure 1.1– Global energy crisis and the mitigation strategies [3,8]

1.2 What is a fuel cell?

Fuel cells are electrochemical energy conversion devices that convert the chemical energy of the fuel to DC electricity [13] with the common by-product of heat and water. Unlike other electrochemical cells, such as batteries that reduce and oxidises the electrode material, a fuel cell needs a constant flow of reactants to operate, as shown in Figure 1.2. Though H_2 combustion is limited by Carnot efficiency, the electrochemical conversion in fuel cells is not limited by the 'Carnot cycle'; hence, fuel cells operate at a higher efficiency than conventional internal combustion engines when operated at low temperature [13].

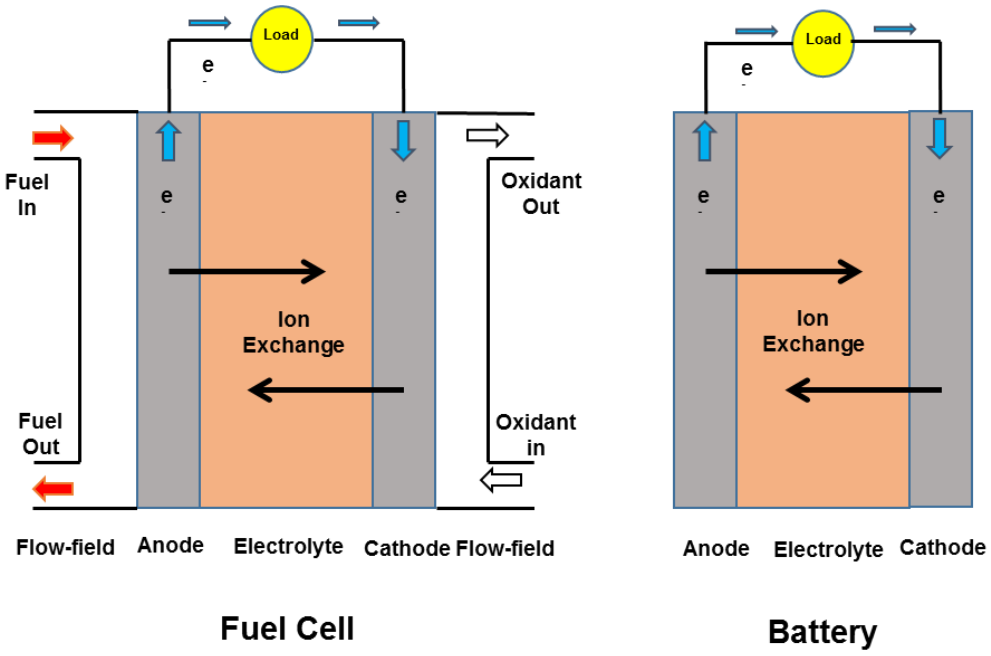

Figure 1.2– Operating principle of (a) a fuel cell and (b) a battery

1.2.1 A brief history of fuel cell development

Since the first recorded invention of fuel cell technology by Sir W. Grove as a gas battery, dating back to 1839, the technology has gone through scientific developments for almost two centuries. The development of fuel cell technology can be broadly divided into three phases, namely, the phase of scientific curiosity when the environmental challenges were not in the foresight, reinvention of the technology that was tailored during the industrial era, and thirdly the beginning of a new industry where the technology is presented as potential candidate to achieve SDGs with large scale commercialisation. Figure 1.3 gives a brief overview of the fuel cell development timeline.

During the invention/experiments of a gaseous voltaic battery by Sir Grove (1839), while the platinum electrodes and sulfuric acid were used as an electrolyte, hydrogen and oxygen were used as reactants. The fundamental principle behind this discovery was the use of reverse electrolysis to obtain electricity and water. During the scientific curiosity phase, in 1893, Friedrich Wilhelm Ostwald, experimentally determined the interconnection of various components of a fuel cell: electrodes, electrolyte, oxidizing and reducing agents, anions and cations, and provided the ‘working principal ‘ of the fuel cell. Over the era of industrial curiosity, the first operating fuel cell stack was developed. During World War II, Thomas Francis Beacon developed a fuel cell to be used in the Royal Navy submarines. With acquiring patent of Beacons' work, despite the high cost, the interest in fuel cells kept growing from a scientific curiosity to its use in the Apollo Space Program in 1960-1970.

Around the same time, a material called Teflon (polytetrafluoroethylene or PTFE) was introduced. With the involvement of General Electric in the research, the era of low temperature ‘Proton Exchange Membrane (PEM)’ fuel cell started. General Electric (GE) developed the first PEM fuel cells with platinum electrodes and acid electrolyte, and/or with carbon electrodes and an alkaline electrolyte. Ever since then, the

technology has seen the tremendous growth in terms of working devices, types of membranes, operating temperatures, reactants and reformates, and materials for fuel cell internals.

The birth of a new industry was witnessed in the 1990s, particularly in the shadow of the energy crisis, and with the target of reduction of CO_2 emission. Although still considered by some, the energy for the future, fuel cells have seen sustainable growth over the last two decades, and attempts of market drilling in automobile, marine, aerospace and back-up power sectors.

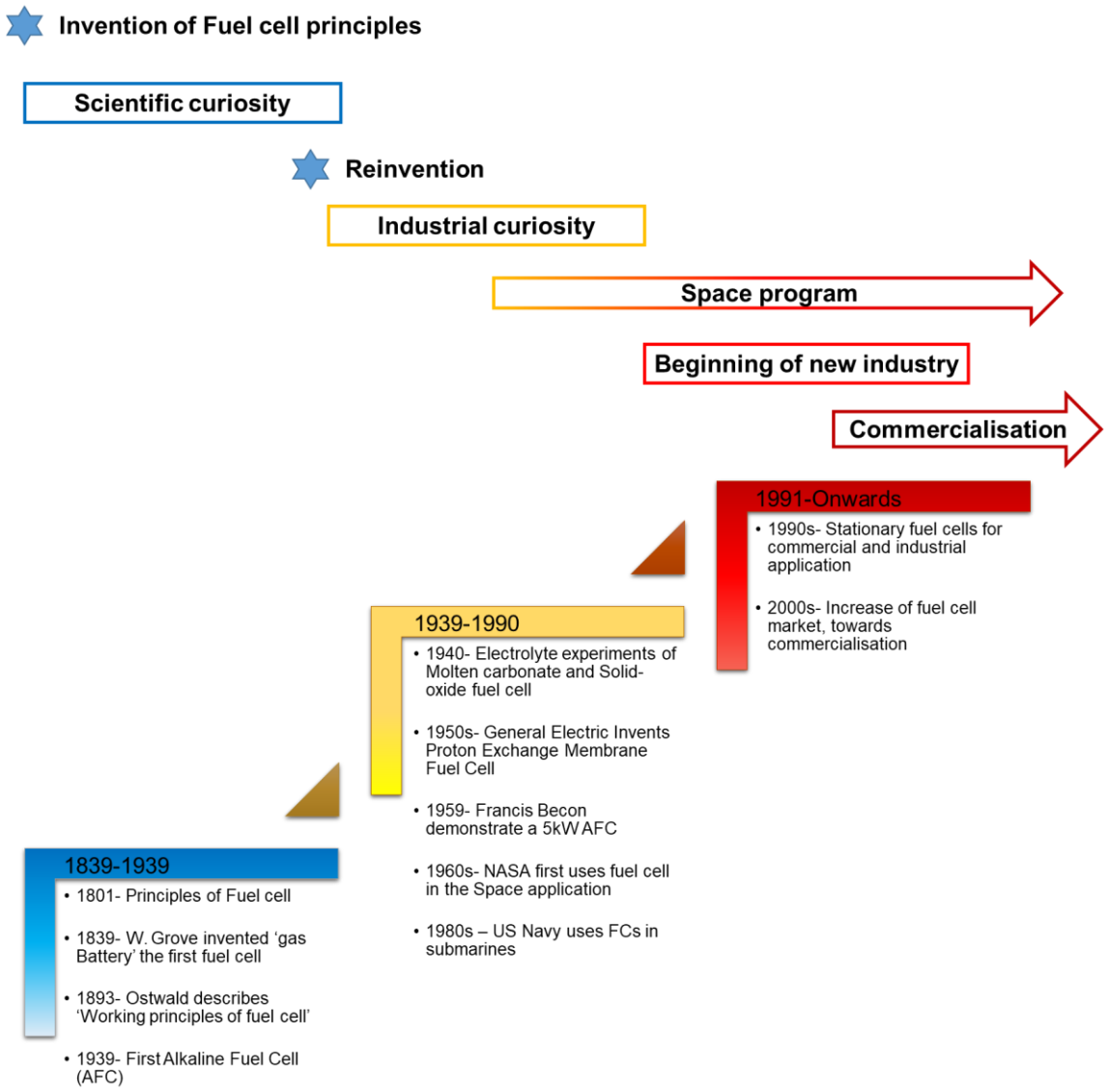

Figure 1.3– Timeline of fuel cell development [13]

Despite technology being older than the era of 'thermodynamic engines' presenting an internal combustion engine, the inherent engineering challenges resulted in the slow development curve for fuel cell technology. Also, the complexity of electrochemical fuel cells, cost of the electrode, the engineering challenges, durability, cost of the systems and mainly the infrastructure required for the deep penetration of the technology have hindered large scale commercialisation and development.

1.2.2 Types of fuel cell

Various types of fuel cell technologies are being developed. Commonly known fuel cell types include, the solid oxide fuel cell [SOFC], the molten carbonate fuel cell [MCFC], the alkaline fuel cell [AFC], the phosphoric acid fuel cell [PAFC], and the polymer electrolyte fuel cells [PEFC]. Table 1.1 and Figure 1.4 provides a summary of the various types of fuel cells, their applications, advantages and disadvantages.

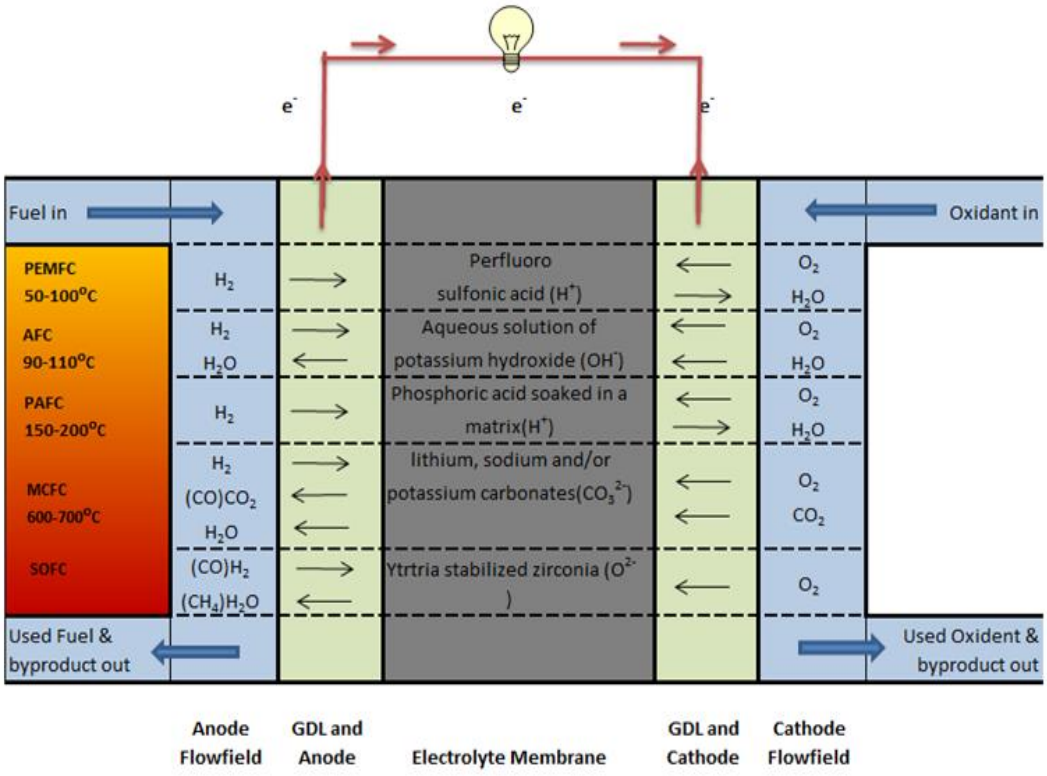

Figure 1.4–Types of fuel cells and their operating temperature

The noteworthy features of PEFCs include low operating temperature, high power density, ease of scale-up, and can be readily integrated into systems. Collectively, this makes PEFC technology a promising candidate for the next generation of power sources for transportation, stationary, and portable applications.

Table 1-1 – Fuel cell technologies and their applications [14]

Type of fuel cell	Electrolyte	Power output (W)	Operating temperature (°C)	Efficiency (%)	Application
Polymer electrolyte (PEFC)	Perfluoro sulfonic acid	<1 kW – 100 kW	50-100	Motive 60% Stationary 35%	Backup power, Distributed generation, Motive, Consumer Electronics
Alkaline (AFC)	An aqueous solution of potassium hydroxide, soaked in a matrix.	10 - 100 kW	90-110	60%	Military,Space
Phosphoric acid (PAFC)	Phosphoric acid, soaked in a matrix	400 kW 100 kW module	150-200	40%	Distributed generation

Molten Carbon (MCFC)	The solution of lithium, sodium and/or potassium carbonates, soaked in a matrix	300 kW - 3MW 300 kW module	600-700	45-50%	Electric utility, Distributed generation
Solid oxide (SOFC)	Ytrtria stabilized zirconia	1kW – 2 MW	700-1000	60%	Auxiliary power, Electric utility, Distributed generation

1.3 Polymer electrolyte fuel cells

1.3.1 System-level

The PEFC technology has the potential to achieve higher efficiency than IC engines at lower operating temperature. Various PEFC designs available in the market can be categorised based on their operations. This section explains a broad classification of PEFC systems, based on the operating and cooling strategies.

Heat is generated during the fuel cell operation, and in order to maintain the stack performance, generated heat should be removed with appropriate cooling mechanisms, such as a liquid or air cooling. Hence, the fuel cells are further classified based on an open-cathode or a closed-cathode design in which the cathode is either

open to the environment, and air diffuses to the system, or adequate air is fed by an external compressor.

1.3.1.1 Liquid-cooled closed-cathode

Liquid-cooled fuel cells use an external coolant loop to regulate the heat generation and maintain the stack temperature (Figure 1.5) [15]. These fuel cells are suitable for high power density systems preliminary used in stationary and/or automobile applications.

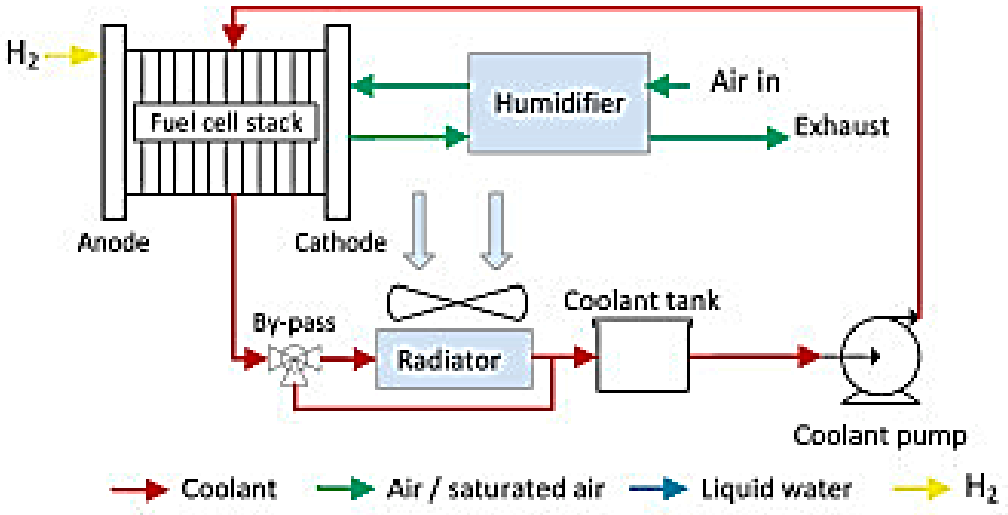

Figure 1.5– Principles of the liquid-cooled closed-cathode fuel cell [16]

1.3.1.2 Air-cooled closed-cathode

Air-cooled fuel cells are usually smaller in size and suitable for portable applications with lower power requirement (Figure 1.6).

In this system, two separate air loops are used. In the first air loop, pressurised air supplied by the compressor is used for the electrochemical operation to generate usable power. The second air loop requires air to maintain the stack temperature, and

prevent it from overheating. In this loop, the cooling air is supplied by a fan mounted on the system [17]. Despite being suitable for small portable applications, the system experiences higher parasitic losses. This leads to alternative simpler designs of air-cooled PEFCs where cooling channels are used as the cathode flow-field.

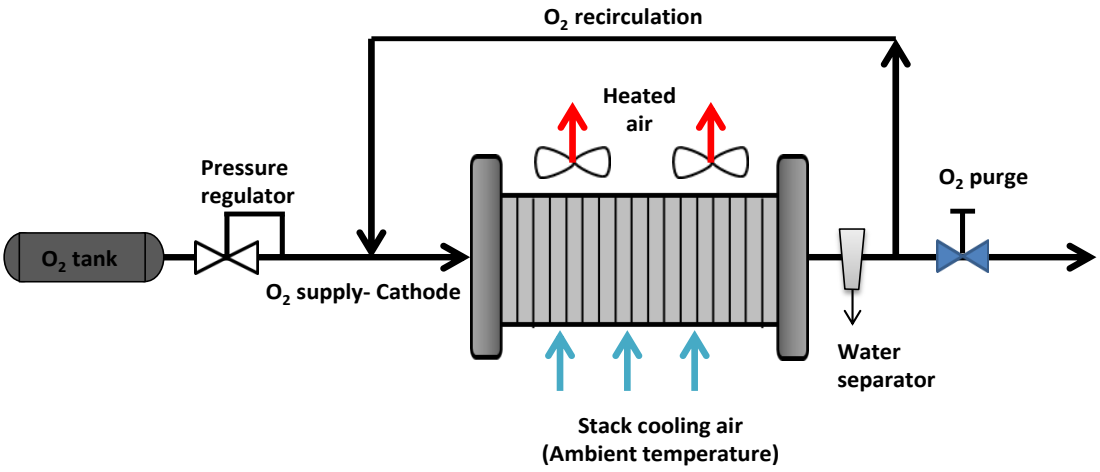

Figure 1.6– Schematic diagram of an air-cooled closed-cathode technique

1.3.1.3 Air-breathing open-cathode fuel cells

Being a prominent technology, air-breathing open-cathode PEFCs have received significant interest (Figure 1.7) [18–21]. This is comparatively simple technology to operate, giving high power density and lower parasitic losses compared to the closed-cathode PEFCs.

In open-cathode fuel cells, the stack temperature and the stack performance is sensitive, not only to the heat generated from within the stack but also to the ambient air temperature entering through cooling channels and the relative humidity (RH). Hence, though simplistic to design and operate, it demands a detailed trade-off study for the fuel cell output along with thermal and water management of the stack.

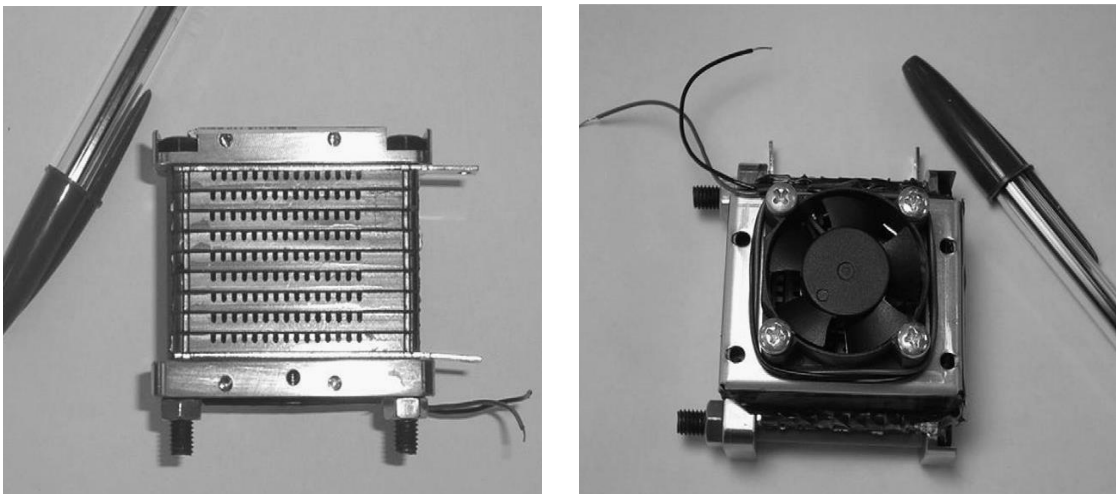

(a) (b)

Figure 1.7– Open-cathode stack, with the fan installed on top: (a) front-side and (b) back-side [13]

1.3.2 Cell-level architecture

The modular architecture of the fuel cell facilitates PEFCs to scale up to the size tailored to the power requirement. The internal architecture of PEFC is as shown in the exploded view of Figure 1.8. The cell architecture comprises of multiple layers which are sandwiched together in a particular order. A membrane electrode assembly (MEA) typically consists of a polymer electrolyte membrane (typically Nafion) sandwiched between two thin electrodes known as catalyst layers (CL). Adjacent to the MEA is a microporous layer (MPL) and a gas diffusion layer (GDL) on either side of the MEA. The entire assembly is sandwiched between bipolar plates, in which flow-field channels are machined for transportation of the reactant and product water.

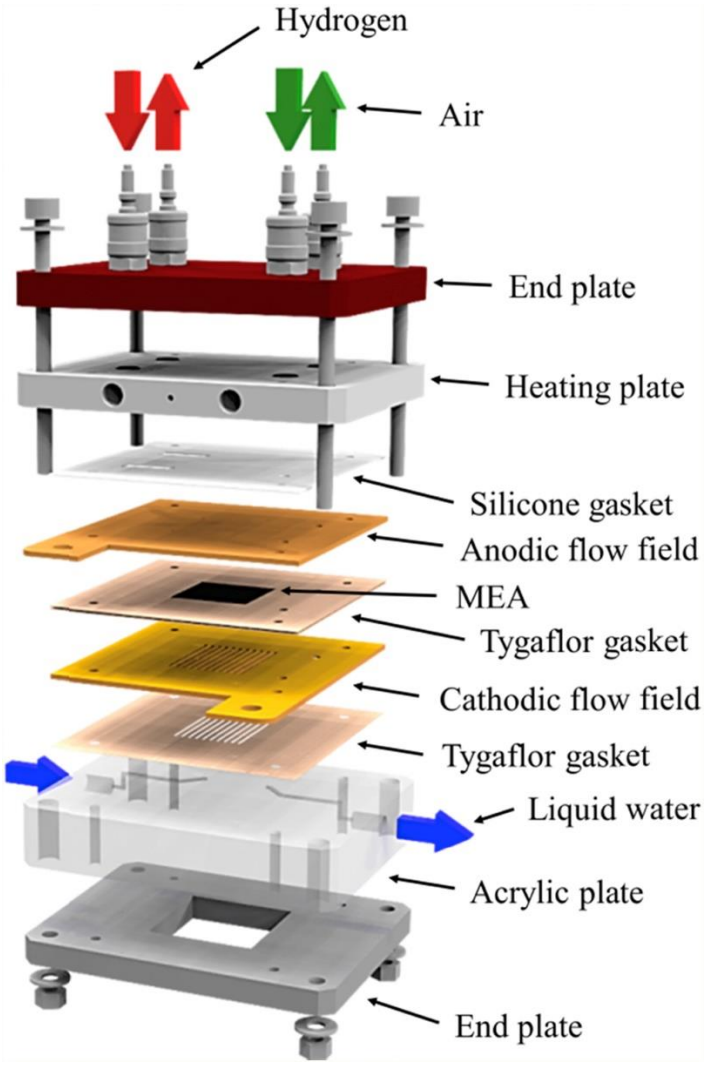

Figure 1.8– Exploded view of individual PEFC components used in the generic single-cell fuel cell, The green, red, and blue arrows represent the direction of air, hydrogen, and liquid water, respectively [22]

This section discusses the fuel cell architecture in details, as shown in Figure 1.9.

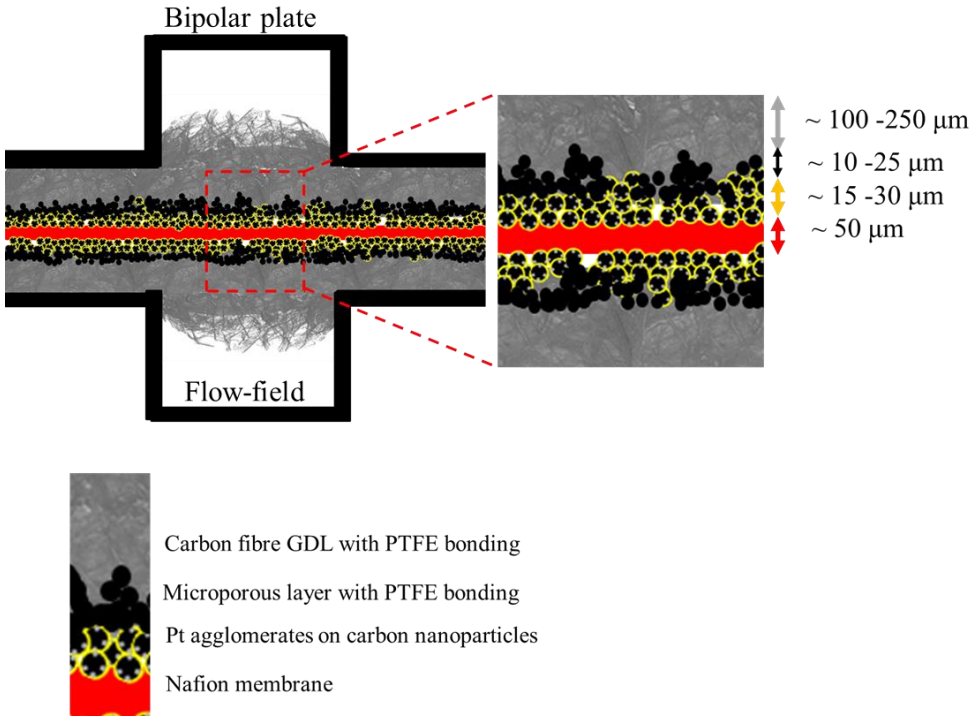

Figure 1.9 – Schematic of the PEFC architecture (Not to scale)

1.3.2.1 Polymer Electrolyte Membrane

Polymer electrolyte membranes are widely divided into proton-conducting based membranes and anion-conducting based membranes. However, in this work, polymer electrolyte membrane refers to the proton-conducting membrane (PEM). A proton-conducting polymer electrolyte membrane is the heart of a fuel cell. Typically, Nafion ionomer membrane developed by Dupont is used. It uses perfluoro-sulfonyl fluoride ethyl-propyl-vinyl ether (PSEPVE) [13]. This has excellent thermal and chemical stability [23,24]. The Nafion membrane thickness varies from 20-175 µm. The desired properties for a membrane include good chemical, mechanical, electrical, thermal and hydrolytic stability, higher proton conductivity to support high current, minimal resistive losses and no electronic conductivity, minimum permeability to reactant and gas species to maximise performance and efficiency and high durability and low-cost.

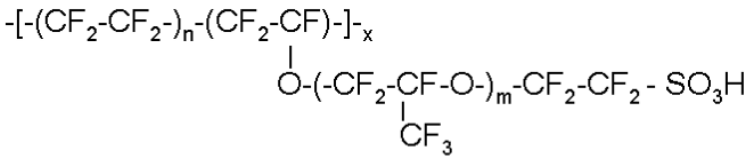

Figure 1.10– Representative chemical structure of Nafion® of 1,100 equivalent weight (EW), [24]

The Nafion morphology has been rigorously researched [25–28]. The general form of the Nafion phase comprises of discrete hydrophilic and hydrophobic regions. The hydrophobic region is a continuous semi-crystalline Teflon region known as the 'backbone' of the membrane, as shown in Figure 1.10 [24]. The hydrophilic regions are sulfonate groups which interact with water and protons. The ingress of water causes the membrane to expand during operation known as a 'membrane swelling'. Membrane swelling is the function of water content that forms the continuous network required for proton conduction. Thus, two transport mechanisms are observed in the membrane, namely proton transport and water transport.

Protonic-conduction is described by two phenomena, proton diffusion or 'vehicular' mechanism and proton hopping or the Grotthus mechanism [10,29].

In the vehicular diffusion mechanism, hydrated protons, i.e. hydronium ions (H_3O^+) diffuse through an aqueous medium from high to low proton concentration regions. Hence, this mechanism mainly depends on the diffusivity of water in the membrane.

Proton hopping mechanism takes place when sufficient water content is present, and the side chains of the Nafion backbone are connected. Protons produced at the anode CL get attached to the water molecules and form a hydronium ion, and one proton from the same hydronium ion hops on another water molecule, i.e. from one hydrolysed ionic site ($SO_3^- H_3O^+$) to another, across the membrane (Figure 1.11). This is the most commonly used proton conductivity modelling approach, based on the empirical co-relation developed by Springer et al. (for Nafion 117 membrane) [30].

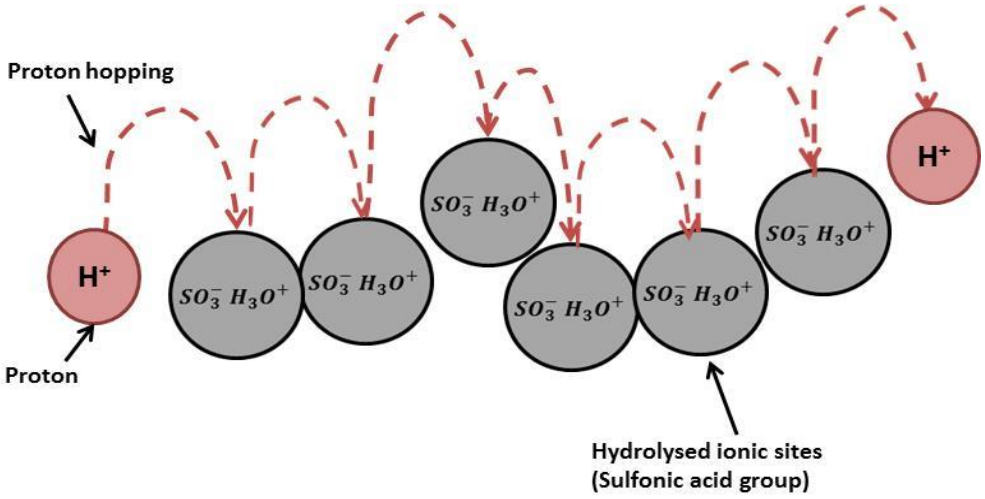

Figure 1.11–Schematic of a proton hopping mechanism

$$\sigma_{mem} = \exp\left[1268\left(\frac{1}{303} - \frac{1}{T_{cell}}\right)\right](0.5139\lambda - 0.326) \quad (1.1)$$

where σ_{mem} [S m^{-1}] is the protonic conductivity of the membrane and λ is water content, usually defined as the number of moles of water per mole of acid sites attached to the membrane, i.e. SO_3H^+, and related to a water activity of the surrounding fluid [30–32]. This is derived by weighing membranes equilibrated above aqueous solutions of lithium chloride concentration at constant temperature 30˚C and constant pressure conditions.

The experiment suggested that the inherent discontinuity in the membrane water content exist between the membrane with liquid water and with saturated water vapour when measured at equilibrium. Unity water activity exhibits in both cases. This phenomenon is commonly referred to as ‘‘Schröeder’s paradox” (Figure 1.12) and observed in a wide variety of polymer materials and solvents [30–32].

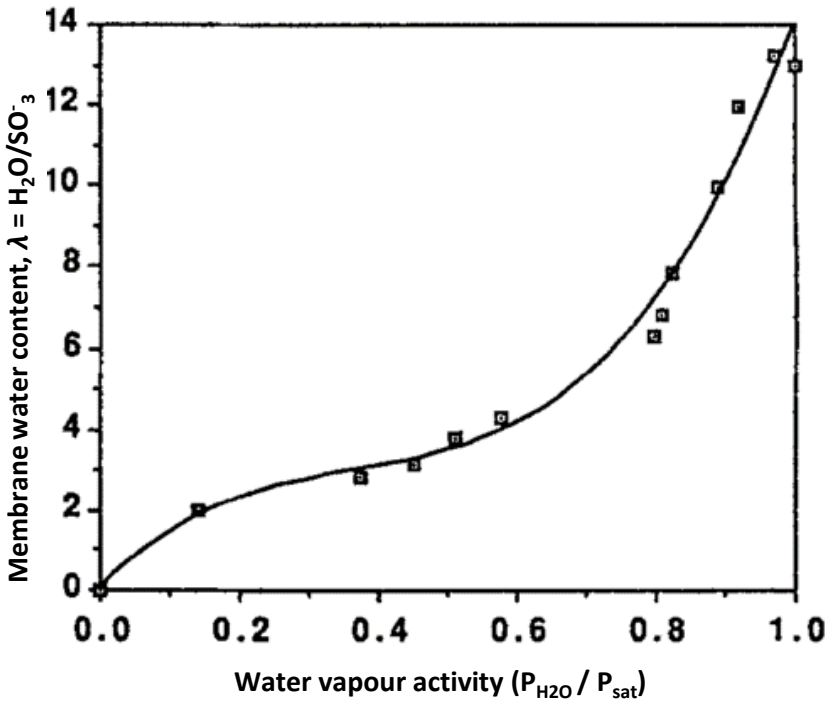

Figure 1.12– Water sorption isotherm as a function of water content and water vapour activity [30]

The water molecules adhered protons result in an electro-osmotic drag (EOD). In the case of Nafion, it is also strongly dependent upon its water content [30,33]. The diffusion coefficient of water in Nafion and its dependence on water content are the critical inputs required for PEFC modelling. In addition to EOD water transport, “back-diffusion” of water from the cathode to the anode is another crucial factor, defining water balance in a membrane. This is linked to the water diffusion coefficients as a function of membrane water content [34]. Proton and water transport in membranes play a vital role in articulating PEFC performance.

1.3.2.2 Catalyst layer

The catalyst layers (CL) are located between the membrane and the gas diffusion layers (GDL). CLs are fabricated either by ink printing on a membrane or deposited on the GDL and then hot-pressed on the Nafion membrane [35]. CLs are typically

composed of Pt/C particles (in case of PGM alloy CLs). During CL fabrication, Pt nanoparticles are formed on comparatively larger carbon particles. The carbon ensures a high electronic conductivity and surface area support for catalyst nanoparticles; whereas the platinum is an adequate catalyst material for electrochemical reactions. Nafion is used as a binding agent that increases the extent of the triple-phase boundary (TPB). TPBs are the confined sites where electrolyte, reactant species and electrically connected catalyst regions connect. Electrochemical reactions occur at the TPB [36,37]. Therefore, four material phases are present in CLs, namely carbon, platinum, membrane phase and the void phase [38]. Figure 1.13 provides the schematic of the electrode/electrolyte interface in a fuel cell, illustrating the TPB reaction site.

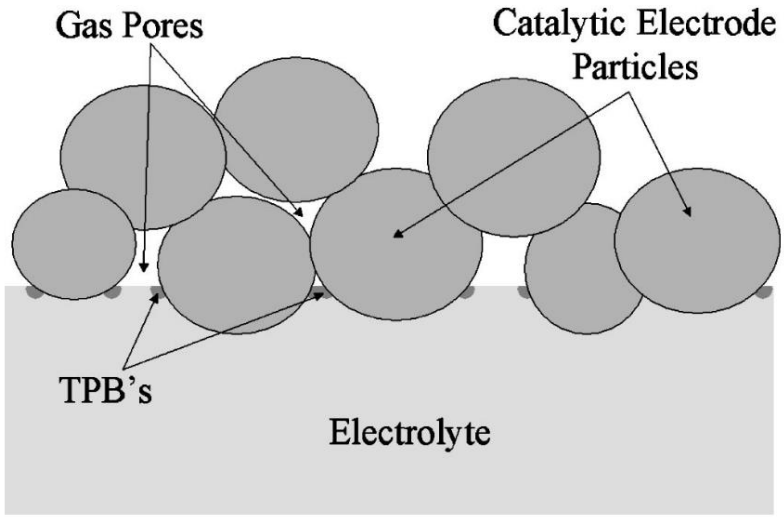

Figure 1.13– Water sorption isotherm as a function of water content and water vapour activity [30]

As an output of the focused research efforts, the cost of the CLs is no longer the primary barrier towards the commercialisation of PEFCs. However, CL properties such as reactant diffusivity, ionic and electrical conductivity have to be investigated carefully to achieve higher output and minimum CL degradation.

1.3.2.3 Gas diffusion layer

The GDL is a carbon fibre porous layer, sandwiched between the CL and flow-field channels. GDL thickness varies from 50-300 μm; density ranges between 0.21 to 0.73 g cm^{-3} and porosity varies between 40% to 80% [39]. GDL does not directly participate in electrochemical reactions; however, it serves essential functions such as ensuring effective reactant diffusion to CLs [40,41], aiding in water management, ensuring the required humidity is maintained inside fuel cells, effectively removing the heat generated by electrochemical reactions, and effectively conducting electric current. GDLs protect CLs from corrosion/erosion caused by reactant flow and provides mechanical support to the MEA. Parameters that affect GDL performance are PTFE loading, porosity, electrical conductivity, compressibility and permeability.

The transport phenomena inside the GDL depends on the local microstructural characteristics of the carbon fibre network. The microscopic structure of the GDL can be obtained from micro/nano-X-ray computed tomography (CT), as shown in Figure 1.14, and discussed in details in Chapter 3 and Chapter 4.

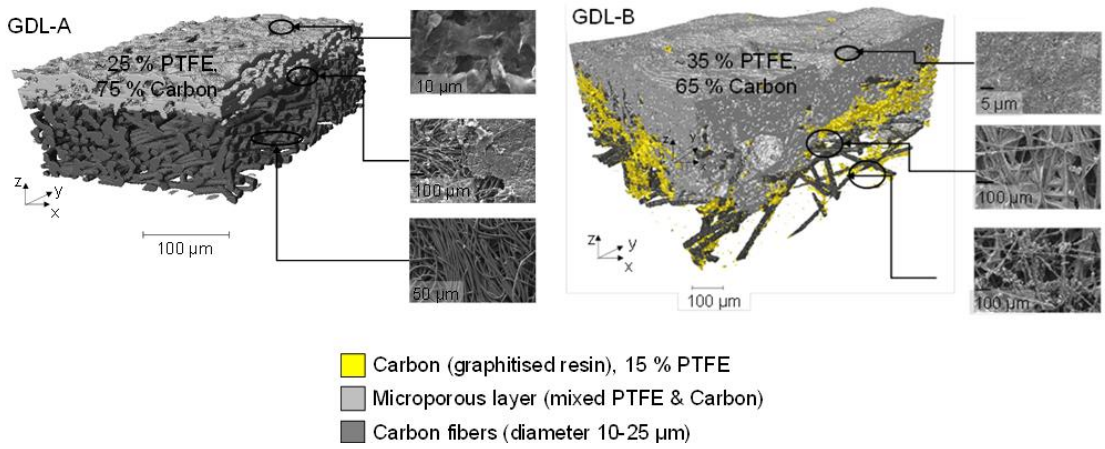

Figure 1.14– X-ray computed tomography (CT) images of two GDLs with PTFE and MPL [42]

GDLs can either be PTFE treated or untreated. Untreated GDLs are prone to flooding the cell and affecting cell performance. Therefore, GDLs are typically coated with hydrophobic PTFE .This is a crucial requirement for water management that improves stack performance at higher current densities [43]. Figure 1.15 shows the effect of PEFE treatment on fuel cell performance [44].

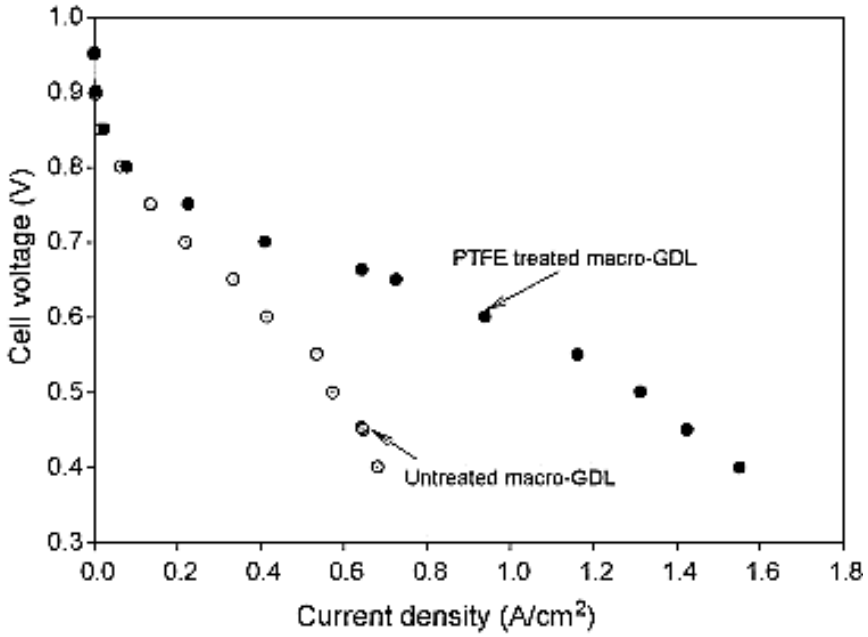

Figure 1.15– Experimental data of PTFE treated and untreated GDLs under 65°C, H_2 stoichiometry = 1.2, O_2 stoichiometry = 2.5, 0 psig [44]

The effects of stack compression on GDL characteristics and stack performance has been an area of interest for various research groups [45–47]. The details of the effect of stack compression on fuel cell performance are discussed in section 2.4.1.

Multiphase mass transport in the GDL is governed by capillary force, shear force, and evaporation/condensation. The relative magnitudes of these forces control two-phase distribution and mass transport [48]. Experimental studies [19,20] showed that water

management in diffusion layers could be improved significantly by adding a microporous layer (MPL). MPL increases water retention in the membrane; hence, improving the membrane conductivity. The MPL is highly hydrophobic in nature, and its thickness varies between 10 - 30 µm. The computational studies by Shimpalee et al. showed that fuel cell performance could be significantly improved by using MPL layers [51]. The results shown in Figure 1.16 highlights the substantial improvement in the performance at higher current density operation.

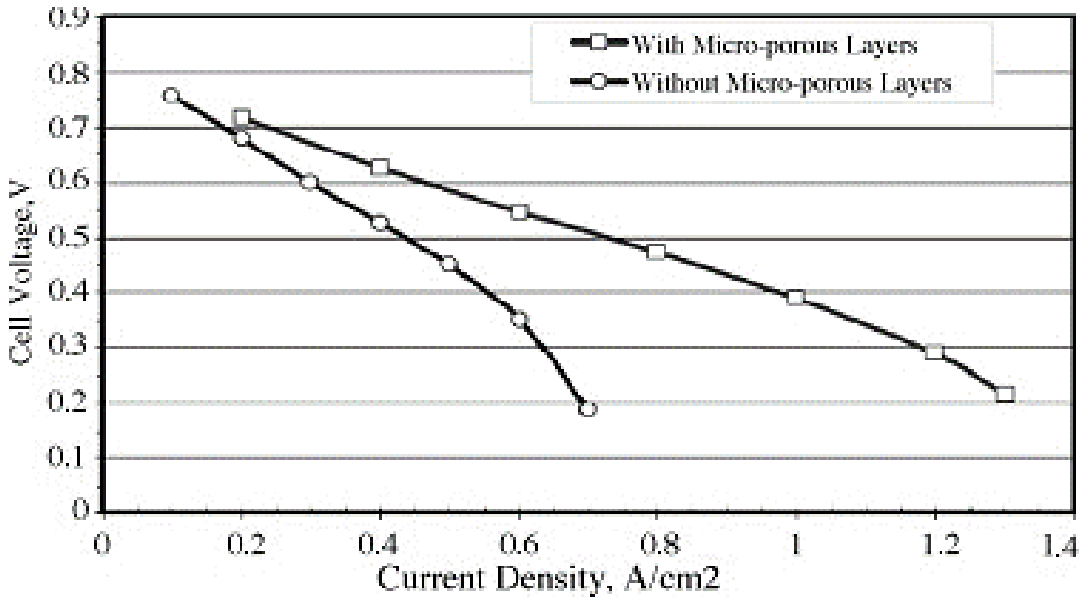

Figure 1.16– Cell performance with and without MPL at T_{cell} = 60 °C; $T_{anode\ humidifier}$= 80 °C; $T_{cathode\ humidifier}$ = 30 °C; H_2 stoichiometry = 2.5, O_2 stoichiometry = 2.5 [48]

Various studies [51–53] showed the lower diffusivity of MPL aids in even distribution of reactants to the CLs. This improves contact between CL and GDL, reducing the CL damage caused by the clamping force applied during the fuel cell assembly process.

However, the MPL has some unfavourable impacts; it is less permeable to oxygen as compared to GDLs, and increased water pressure at CL could block the pathways of

gaseous oxygen [52]. These factors should be considered when designing the cell architecture [54].

1.3.2.4 Bipolar plates and current collectors

In PEFC stacks, bipolar plates (BP) are multifunctional components that complete the electrical path between two adjacent cells by electrically connecting the anode of one cell to the cathode of the neighbouring cell. The component provides structural support to the stack, which composes 80% of the stack weight and is responsible for ~45 % of fuel cell cost [55,56].

BPs material properties for effective performance include [57]

- Plate resistance should be less than 0.01 Ω cm^{-2},
- Gas permeability should be less than 10^{-4} cm^3 $S^{-1}cm^{-2}$,
- Rate of corrosion should be less than 0.016 mA cm^{-2},
- High compressive strength is required to take care of stack compression load and stack operation load. As a thumb rule, it should be higher than 0.15 MPa.

BPs are broadly classified based on the material used, such as [55–58]

- Non-metals, non-porous graphite.
- Coated or non-coated metal plates are made up of an aluminium or austenitic or ferritic stainless steel. Titanium could be used to lower the stack weight.
- Carbon or metal-based composites are used for higher strength.

Flow-fields are imprinted on the back-side of the bipolar plates which ensure the delivery of the feed of reactants from an inlet to the active area of the cell, adequate cooling of the cell, and removal of water from the system, ensuring adequate humidity [59]. The flow-field designs and arrangements form the fuel-cell architecture. The impact of flow-field architecture on the performance is discussed in Chapter 2 and Chapter 4 .

1.4 Principle of operation

PEFC operation is multi-physics in nature, highly coupled, and nonlinear in terms of species transport and electrochemical processes.

1.4.1 Thermodynamic operating principle

The basic principle of PEFC operation involves oxidation and reduction reaction (Figure 1.17).

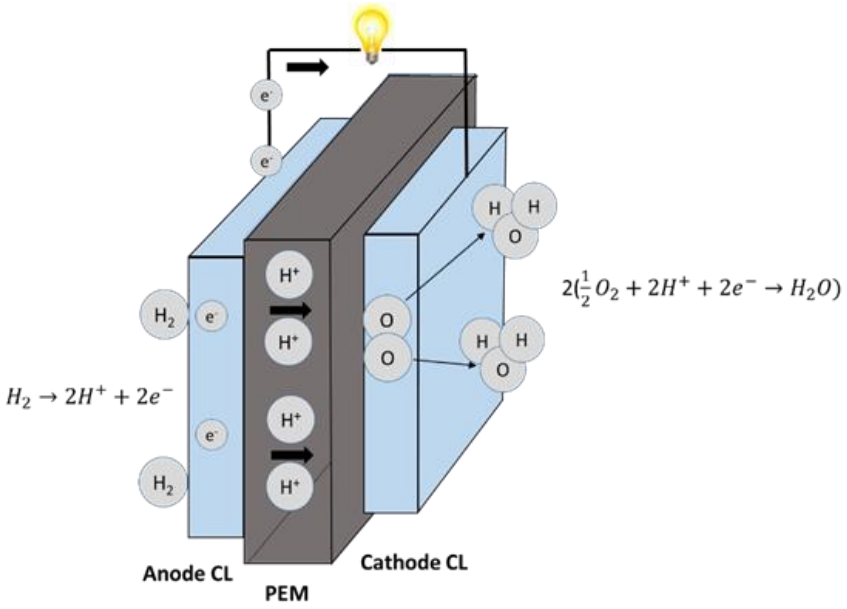

Figure 1.17– Schematic of oxidation-reduction reaction at proton-exchange PEFCs

Hydrogen (H_2) and air are supplied to the anode and cathode domains, respectively. H_2 flows through the porous GDLs/MPLs and diffuses into the anode CL where it oxidises forming protons and electrons. This is known as the hydrogen oxidation reaction (HOR) or anode half-cell reaction.

$$H_2 \rightarrow 2H^+ + 2e^- \quad (1.2)$$

Protons migrate through a membrane towards cathode CL along with water molecules under electro osmotic drag (EOD). Electrons generated by HOR, conduct via GDL carbon fibres to the anode current collector. An external electrical circuit that connects two electrodes acts as a conducting path for electrons.

Oxygen (O_2) is supplied simultaneously to the cathode, either in the form of air or pure O_2, where it is reduced to water by combining with the electrons and protons. The oxygen reduction reaction (ORR) or cathode half-cell reaction is

$$2H^+ + 2e^- + \frac{1}{2}O_2 \rightarrow H_2O \quad (1.3)$$

Generated water is transported through the cathode GDL/MPL and taken out through the cathode outlet. This process is dominated by diffusion in the GDL/MPL and intensively studied under PEFC water management.

Heat is generated mainly in the cathode CL due to the sluggish ORR, and it is conducted out of the cell through bipolar plates [29]. The complete PEFC reaction is,

$$2H_2 + O_2 \rightarrow 2H_2O \quad (1.4)$$

The ORR can be simplified as a 'general reversible reaction' that takes place under mechanical, thermal, and chemical equilibrium

$$aA + bB \leftrightarrow mM + nN \quad (1.5)$$

A and *B* represent reactants, *M* and *N* are products. *a, b, m* and *n* represent the number of moles of *A, B, M* and *N* respectively. The change in Gibb's free energy of the forward reaction is

$$\Delta G = -RTlnK + RTln\frac{[M]^m[N]^n}{[A]^a[B]^b} \quad (1.6)$$

where *R* is the universal gas constant [J Kg^{-1} mol^{-1}], *K* is an equilibrium constant for the reaction at temperature, *T* [K] and $[X]^X$ is the activity of species, *X*. This equation is known as Van't Hoff's isotherm and explains the change in Gibb's free energy *(ΔG)* of the system is a function of a species activities [60].

The maximum electrical work ($W_{el,max}$) can be obtained from the change in Gibb's free energy at a constant temperature, *T* and constant pressure, *P*.

$$\Delta G = W_{el,max} = -nFE \quad (1.7)$$

where *n* is a number of electrons participating in the reaction, *F* is Faraday's constant [C mol^{-1}] and *E* is electrical voltage [V]. Hence, the reversible cell voltage varies as a function of chemical activities.

$$E = \frac{RT}{\mathrm{n}F}lnK + \frac{RT}{nF}ln\frac{[A]^a[B]^b}{[M]^m[N]^n} \quad (1.8)$$

The change in Gibb's free energy at standard state (ΔG^o) can be defined in terms of the electromotive force at standard-state, also known as the standard-state potential (E^o). Thus

$$E = E^o + \frac{RT}{nF}ln\frac{[A]^a[B]^b}{[M]^m[N]^n} \quad (1.9)$$

It is known as the 'Nernst Equation'. This equation relates to the concentration gradient of a reactant and a product to the electrical gradient obtaining reaction equilibrium.

1.4.2 Irreversible voltage losses

The usable electrical energy can only be obtained from PEFC when a reasonably large current is drawn. Under such conditions, the cell potential decreases from its thermodynamic equilibrium potential due to various forms of irreversible losses. This voltage loss mechanism can be characterised by plotting the change in voltage as a function of an increase in current density, often referred to as a 'polarisation curve' or *J-V* curve. The cause of the irreversible losses includes electrode kinetics (Activation losses, η_{act}), Ohmic resistance offered by the electrode and electrolytes (Ohmic losses, η_{ohmic}) and mass transport limitations (concentration losses, η_{conc}).

1.4.2.1 Activation potential

At low current densities (0.001 – 0.1 A cm^{-2}) the activation losses are mainly because of the irreversible voltage loss in a fuel cell. Activation losses explain the slowness of the reactions occurring at the fuel cell electrodes, i.e. anode and cathode CLs. The sluggish cathode kinetics is the prime cause of the overall activation losses [61]. Activation losses can be reduced by increasing the cell temperature, T_{cell}, increasing the electrochemical activity of the electrode with suitable catalysts and by increasing the electrochemically active surface area (ECSA) and surface roughness of the electrode. Assuming that the anode overvoltage is small compared to that of the cathode, the activation loss can be described as follows using the general form of the Tafel equation [13].

$$\eta_{act} = \frac{RT}{\alpha nF}(ln(j) - ln(j_o)) \tag{1.10}$$

Here, *R, F* and *T* are universal gas constant [J kg^{-1} mol^{-1}], Faradays constant [C mol^{-1}] and temperature [K], respectively, α is charge transfer coefficient, and *n* is a number of atoms participating in the reaction. *j* is the net current density and j_0 is the exchange

current density corresponds to the rate at which hydrogen is oxidised and oxygen is reduced according to the reversible reaction given by Equation (1.5).

1.4.2.2 Ohmic losses (η_{ohmic})

At intermediate current densities,the irreversible losses are mainly due to Ohmic losses in the cell. These losses are caused by an ionic resistance to the flow of ions in the electrolyte and electronic conduction process in CLs and BPs. The Ohmic losses are present throughout the polarisation curve and follow Ohm's law relationship. The Ohmic resistance is also related to the hydration of a membrane, as a well-hydrated membrane will enable the smoother flow of protons, reducing Ohmic losses.

$$\eta_{ohmic} = j \times ASR_{ohm} \tag{1.11}$$

ASR is the area-specific resistance.

Increase in the proton water content in the electrolyte membrane results in an improvement in the ionic conductivity of the membrane [30,33]. Maintaining good electrical contact between electron-conducting components of the PEFC and selecting the adequate cell compression is a key to reduce Ohmic losses.

1.4.2.3 Mass transport losses (η_{conc})

At higher current densities, the resistance offered to the reactant transport to the active sites (TPBs), dominates the irreversible losses. With an increase in the rate of reaction, the amount of reactant available on the catalyst surface starts to deplete. At specific current density, called the limiting current density (j_L), the reactant is consumed faster than it can reach the surface. An indirect side effect of increasing current density is an increase in water production. The water, if not adequately managed, ends up blocking the electrode surface, causing flooding; therefore, even further reducing the amount of reactant reaching the electrode surface. Hence, these

irreversible losses are also known as the concentration losses and can be calculated as follows,

$$\eta_{conc} = \frac{RT}{\alpha nF}\left((ln(j_L) - ln(j_L - j)\right) \quad (1.12)$$

1.4.3 Polarisation curve

The overall cell performance is given by subtracting reversible losses discussed in the preceding section from the open circuit potential of the cell. Therefore,

$$V(j) = E_{thermo} - \eta_{act}(j) - \eta_{Ohmic}(j) - \eta_{conc}(j) \quad (1.13)$$

where E_{thermo} is the thermodynamic voltage (or open-circuit voltage, when $i_{anode} = i_{cathode}$), for the pressure, temperature, the stoichiometry of reactants.

$$E_{P,T}^{OCV} = E_o + \frac{RT}{\mathrm{n}F} ln(\frac{P_{H_2}(P_{O_2})^{0.5}}{P_{H_20}}) \quad (1.14)$$

where E_o [V] is a standard state reversible potential of the fuel cell. At standard temperature and pressure, the highest voltage attainable for PEFC (H_2-O_2 fuel) is 1.23 V. The classical polarisation curve model can be derived using the equations stated in this section.

Table 1-2 – Typical parameter values for Equation (1.13)

Properties	Values
Cell potential at STP, E_{thermo} [V]	1.23
Area Specific resistance, ASR [Ω cm^{-2}]	0.01
Exchange current density, j_0 [A cm^{-2}]	0.0001
Transfer coefficient, α	0.5
Limiting current density, j_L [A cm^{-2}]	2
Temperature, T [K]	355
No of atoms, n	2
Universal gas constant, R [J mol^{-1} K^{-1}]	8.314
Faradays constant, F [C mol^{-1}]	96485

Figure 1.18(a) shows the contribution of each type of losses on the cell potential. This suggests activation losses are higher at low current density; whereas mass transport losses are higher at higher current density. The Ohmic losses increase with increases in current density. Details of individual losses are explained in Chapter 2. The polarisation curve and the power density curve obtained from the above empirical model is shown in Figure 1.18(b).

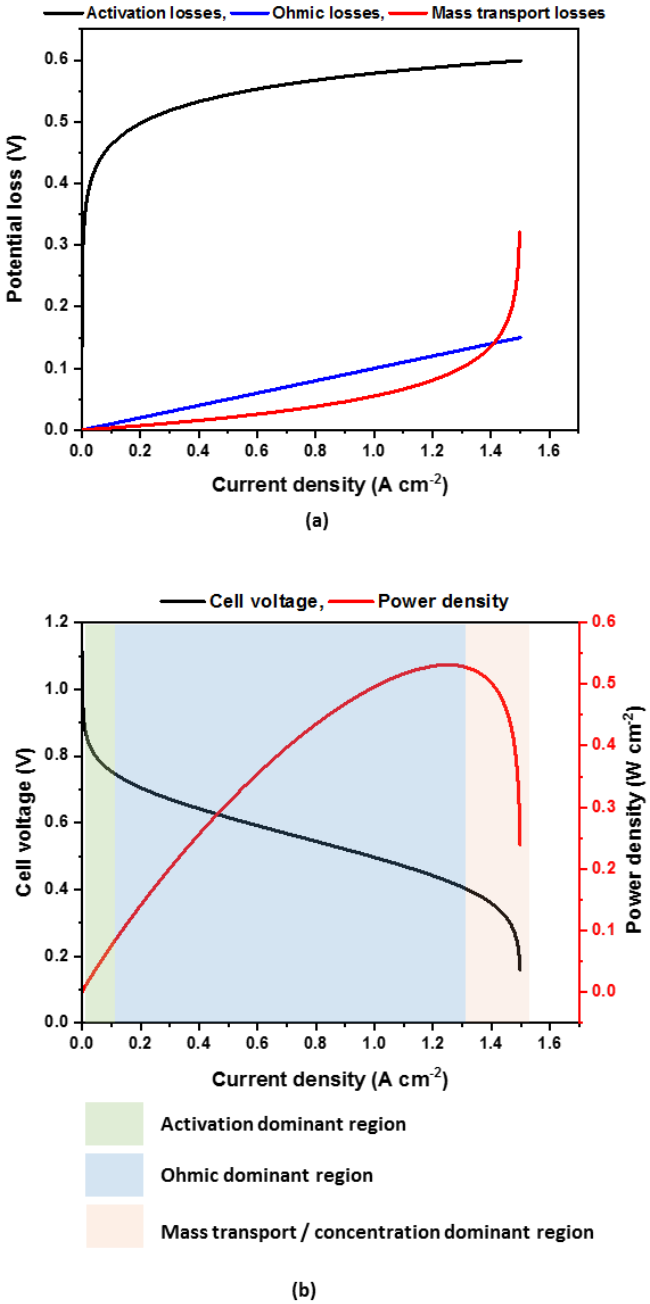

Figure 1.18– (a) Contribution of potential losses, (b) basic polarisation and power density curve showing the regions dominated by the irreversible losses

1.5 Project objective and thesis structure

The main objective of this project is to develop a better understanding of the effect of fuel cell architecture on PEFC performance. This dissertation presents a systematic approach to analyse the architectural and electrochemical factors affecting the fuel cell performance and develop a suite of experimentally validated robust computational models capable of analysing and predicting PEFC behaviour.

The key objectives of this project are listed below,

- Provide insight into the electrochemical kinetics and reactant transport phenomenon.
- Study the impact of cell compression using X-ray CT technique and develop the set of the input parameters for computational modelling.
- Identify the strengths and weaknesses of the previous modelling approaches and develop a 2D non-isothermal multiphase mathematical model predicting PEFC performance.
- Develop the coupled structural – electrochemical continuum model predicting the effect of fuel cell mechanical compression on the performance.
- Experimentally validate the models using novel techniques such as neutron imaging to map internal water distribution.
- Emphasise the presence of the ‘secondary flow-field’ architecture in the cell and examine its effect under various cell compression conditions.

These objectives were achieved by developing a suite of a comprehensive 2D PEFC models accounting for seven main domains, namely, bipolar plates, gas diffusion layer and catalyst layer on anode and cathode side and the membrane. This dissertation is divided into nine chapters, as follows

Chapter 1

This chapter of the thesis discusses the fundamental motivation behind this research project, and briefly introduces PEFC technology. This chapter further discusses the aims and objectives of the research and provides an outline of the thesis.

Chapter 2

This chapter presents an in-depth review of the practical factors governing PEFC performance. It forms the foundation of the thesis presenting the way architectural and mechanical factors govern the performance.

Chapter 3

This chapter presents the experimental techniques used throughout this project. This includes the experiments developed/used to characterise PEFC to generate input parameters for the model and the experiments used for the model validation.

Chapter 4

This chapter provides X-ray CT characterisation of MEA subjected to various degrees of compression and provides the morphological properties of the MEA, which can be used as an input parameter in high-fidelity computational models. Part of this chapter has been published as a peer-reviewed journal article [62].

Chapter 5

This chapter presents a literature review of different fuel cell modelling approaches and description of the fundamentals, principles and governing equations. It also provides the modelling framework used in this research.

Chapter 6

The effect of non-uniform compression on the performance of PEFCs is presented through the development of a comprehensive, multi-phase, non-isothermal two-dimensional model. Part of this chapter has been submitted to a peer-reviewed journal.

Chapter 7

This chapter presents the effect of non-uniform compression on water dynamics in the PEFC using in-plane and through-plane in-operando neutron radiography. The experimental results are used to validate the computational models developed in the previous chapter. Part of this chapter has been published as a peer-reviewed journal article [63].

Chapter 8

The presence of the ‘secondary flow-field’ architecture, how it is affected under various cell compression levels, how it affects the dead-ended anode operation is presented in this chapter via combined X-ray radiography and 3D modelling. Part of this chapter has been published in a peer-reviewed journal article [64].

Chapter 9

The final chapter outlines the achievements and conclusions of this thesis and provides suggestions for further work.

Chapter 2
Practical factors governing PEFC performance

Abstract

This chapter presents a comprehensive review that aims to provide a structured understanding of the practical factors that governs the performance and durability of PEFCs. The chapter is divided into three key underlying factors that can alter the PEFC efficiency. The first section of the chapter provides the details of the electrochemical kinetics with particular focus on the factor that constitutes individual losses, i.e. activation, Ohmic and mass transport losses. The second section of this chapter provides a detailed literature review on the operating parameters that govern the performance. Finally, the last section of the chapter provides a detailed review of the effect of mechanical and architectural parameters on the performance. This section also highlights the existence of secondary flow-field in the fuel cells. Overall, this chapter forms the foundation of the current research project.

2.1 Introduction

PEFC technology has been thoroughly researched with the prime focus on developing commercially viable systems suitable for automotive and stationary power applications [65]. The main difference between fuel cells used for both of these applications is the load cycling that defines the durability requirements. The US DoE previously set a 2020 target of 5,000 h and a long-term target of 8,000 h of operation for the passenger car application, while public transport application has a durability target of 25,000 h with 65% peak efficiency [66]. The target for stationary power application is specified at 45% electrical efficiency and 60,000 - 80,000 h durability of the equipment while maintaining tolerance to fuel impurities in the gas feed. While the differences in the ultimate commercialisation goals, the practical factors governing the performance and the durability of the PEFC are identical. The current review discusses the factors defining the performance and the architecture of PEFC independent of the application [67]. The performance of the PEFC is governed by a complex interaction of the electrochemical, structural/architectural and operating parameters and modes. Figure 2.1 gives an overview of the factors that affect the life cycle of the fuel cell system.

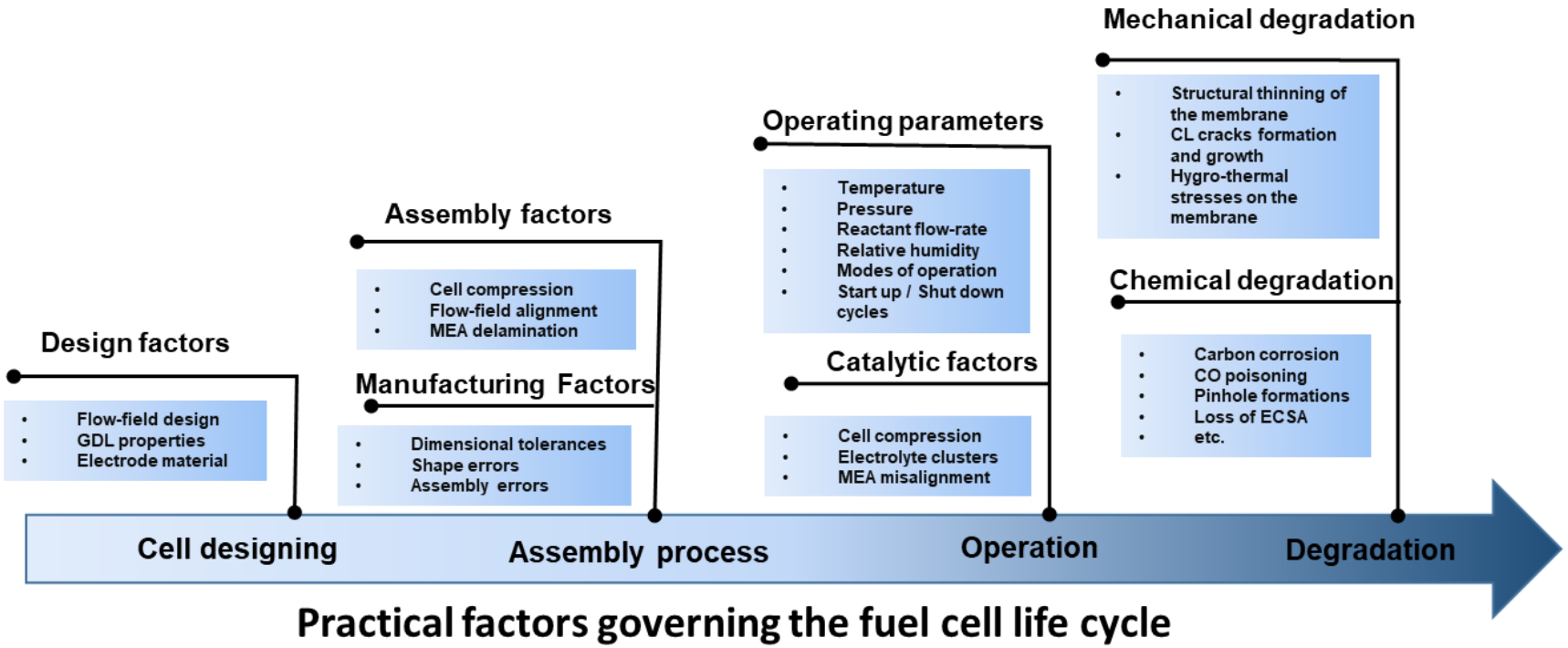

Figure 2.1– Schematic of practical factors governing the fuel cell life cycle

2.2 Electrochemical kinetics

The catalyst layer (CL) where HOR and ORR take place is strongly linked with the cost, performance, and the durability of PEFCs. This section discusses the catalytic factors that preliminary defines activation kinetics and cell performance.

Electrochemical performance of the fuel cell is dominated by the exchange current density (j_0), which can be calculated as [13],

$$j_0 = j_0^{ref} a_{pt} m_{pt} \left(\frac{C_r}{C_r^{ref}}\right)^{\Upsilon} e^{-\left(\frac{E_0}{RT}\left(1-\frac{T}{T_{ref}}\right)\right)} \quad (2.1)$$

where j_0^{ref}[A cm^{-2} Pt] is the reference exchange current density measured at the reference temperature and pressure per unit catalyst surface area, a_{pt} [cm^2 mg^{-1}] is catalyst surface area, m_{pt} [mg cm^{-2}] is the Pt loading on the catalyst layer, C_r [mol m^{-3}] is the reactant concentration, C_r^{ref} [mol m^{-3}] is reference concentration, Υ is reaction coefficient, which varies between 0.5 and 1, E_0 [kJ mol^{-1}] is an activation energy barrier. Hence, the factors governing activation losses are,

- Activation barrier (E_0)
- Surface roughness ($a_{pt}m_{pt}$)
- Reactant concentration (C_r)
- Operating temperature (*T*)

The effect of catalytic factors on the PEFC performance are discussed in details in Appendix A

2.3 Operating parameters

The performance of PEFC is influenced by the operating parameters such as temperature, pressure or concentration, reactant stoichiometry, relative humidity (RH) ratio, and modes of operation. All these parameters have a substantial impact on PEFC performance, and they are related to each other nonlinearly, making the effect of the operating parameters and the mode of operation on the fuel cell performance a complex phenomenon. This section presents and discusses the findings from the previous studies showing the impact of these parameters on the polarisation performance.

2.3.1 Temperature

Both the operating temperature and the inlet temperature of the reactant feed influence the PEFC performance. An increased inlet temperature impacts the membrane hydration and enhances the electrode kinetics, improving the performance of the fuel cell. Section 2.3.4 discusses the effect of relative humidity on the performance in more details

The performance of the fuel cell is strongly dependent on the operating temperature irrespective of the electrode and the membrane material. Operating temperature affects both irreversible cell voltage and kinetic losses associated with the fuel cell operation. Reversible cell voltage, E_{rev} [V], at constant pressure can be calculated as,

$$E_{rev} = E_0 + \frac{\Delta \hat{s}}{nF} T \tag{2.2}$$

where E_0 [V] is a standard state reversible potential of the fuel cell, equivalent to 1.23 V. $\Delta \hat{s}$ [J mol^{-1} K^{-1}] is the change in entropy during the rection For H_2-O_2 operated fuel

cells with $H_2O_{(g)}$ as a product, PEFC, $\Delta\hat{s}$ is -44.34 J mol^{-1} K^{-1}. Hence when cell operating temperature increase from 25 °C to 100 °C, the reversible cell potential decreases, as shown in Figure 2.2.

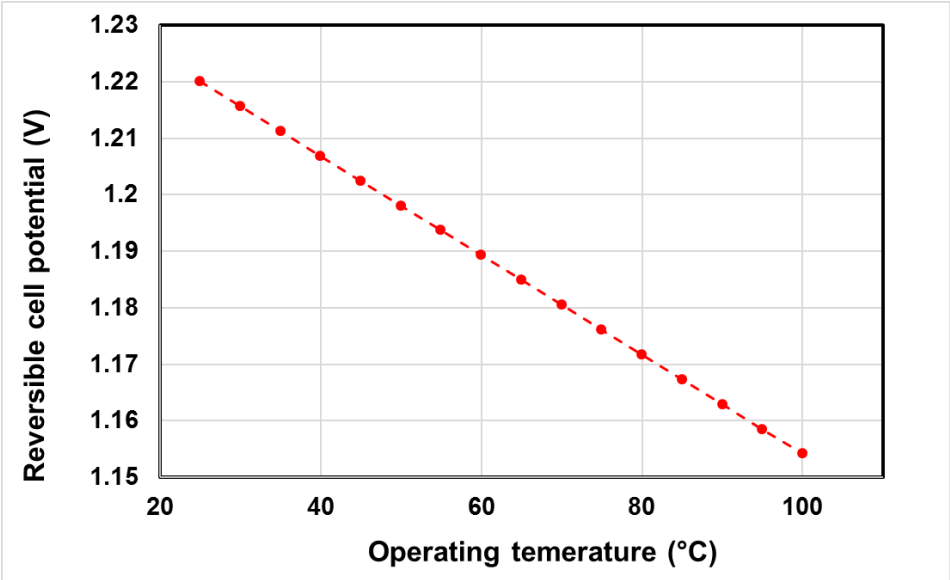

Figure 2.2– The effect of operating temperature on the reversible cell potential

Therefore, reversible cell potential decreases with an increase in operating temperature. However, low-temperature PEFCs generally operates between 50 °C to 80 °C. The change in operating temperature between 50- 80°C lowers reversible cell potential by approximately 30 mV. Operating temperature also affects the kinetic losses associated with the fuel cell. Operating temperature defines the membrane hydration, which decreases with an increase in the temperature, decreasing the proton conductivity of the membrane [68,69]. An experimental study by Williams et al. [70] highlighted an influence of operating temperature (T_{cell}) on the fuel cell performance when T_{cell} varied between 60 °C to 80 °C, independent of humidification factor at fixed anode and cathode stoichiometric flow rates, (1.3 and 1.5, respectively). The study suggests the relationship between T_{cell} and the performance varies nonlinearly under

a dry condition with performance increased steadily up to 75 °C, with further increase in the temperature resulted in a sharp increase in the membrane resistance (from 0.079 to 0.133 Ω cm^{-2}, at 0.4 A cm^{-2} and hence lowered the cell performance. Nevertheless, this study suggested that the effect of T_{cell} can be mitigated by balancing the cathode and anode stoichiometry and relative humidity; for example, the membrane drying phenomenon at high operating temperature can be reversed by humidifying only the anode stream while cathode feed remains dry. A similar conclusion has been derived by 2D multiphase modelling study by Natarajan et al. [71] and the experimental analysis by Yan et al. [72].

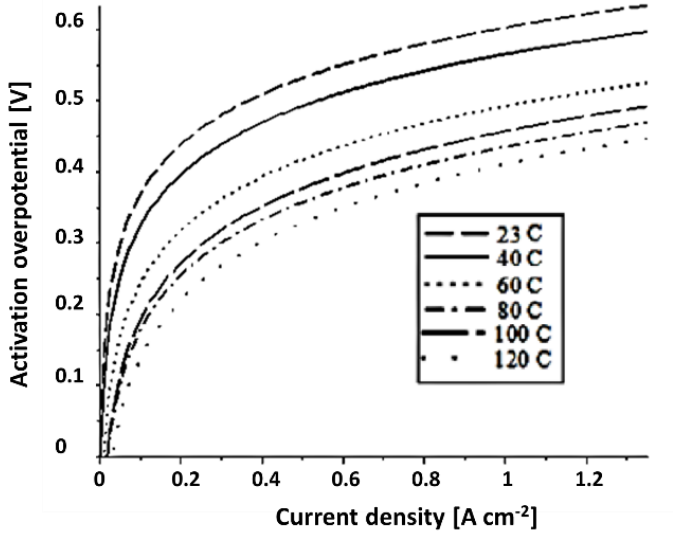

Figure 2.3– The effect of operating temperature on the mass transfer/concentration over-potential and activation overpotential [73]

The parametric modelling study by Esfeh et al. showed the effect of operating temperature on the activation and mass transport losses when T_{cell} varied from 23 °C to 120 °C [73], as shown in Figure 2.3. The effect of operating temperature on the

activation losses was observed to be nonlinear. Higher activation over-potential was observed at the lowest temperature of 23 °C. The activation over-potential lowered with an increase in the cell temperature up to 80 °C; however, it increased again at 100 °C before reducing at 120 °C. This nonlinearity in the activation over-potential could be due to the effect of temperature on the localised over-potential on both the electrodes (Figure 2.3.(a)). The concentration over-potential, i.e. mass transport losses decrease with an increase in temperature; however, an increase in current density increase mass transport losses exponentially, highlighting the significance of it at the higher current density (Figure 2.3(b)). This study also highlights that operating temperature influences the exchange current density (j_0) and ECSA. Increase in T_{cell} result in an increase in j_0, both for anode and cathode electrodes. However, an increase in T_{cell} above 60 °C resulted in a loss of ECSA, which could be due to the combined effect of membrane drying at higher temperatures and carbon corrosion (Figure 2.4). These results agree with the modelling study presented by Shimpalee et al. [74].

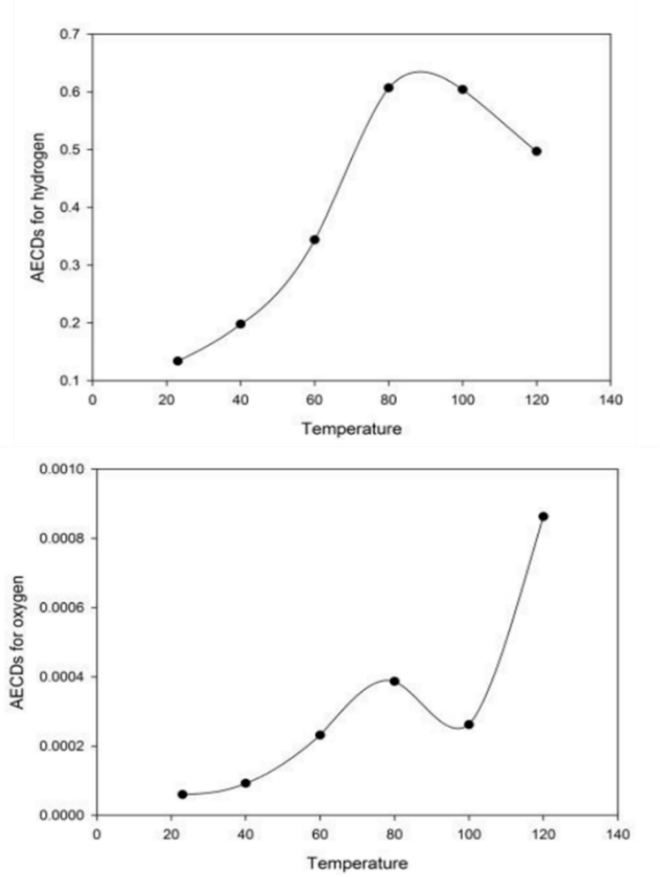

Figure 2.4– The effect of operating anode and cathode apparent exchange current density (AECD) (Adapted from [73])

Direct water visualisation study by Ous et al. suggested increasing the operating temperature is the effective means to water management in the cell where $T_{cell} > 60$ °C was sufficient to evaporate all the water in the flow-fields while enhancing the cell performance and maintaining membrane humidification [75]. A modelling study by Hottinen et al. suggested the effect of operating temperature is linked with the cell architecture, such as flow-field arrangements and cell compression, and the non-uniform cell compression results in the non-uniform distribution of cell temperature affecting the cell performance [76]. These studies suggest that the operating temperature affects the fuel cell performance by altering activation, Ohmic and mass

transport losses; however, these effects are closely linked with other operating parameters and cell architecture.

2.3.2 Reactant pressure

The pressurised reactant entering in the system defines the performance of the fuel cell, and the range of the pressure varies from the atmospheric pressure for air-breathing fuel cell way up to 6 – 7 bars [13]. Effect of pressure on reversible cell voltage can be obtained from the Gibbs Free energy (Equation (1.7)). However, pressure, like temperature, have the minimal effect of reversible cell voltage [60]. According to the Nernst equation, as shown in Equation (2.3), increases in the partial pressure of the reactant, i.e. the cell operating pressure results in increasing the activation overpotential of the cell and hence improves the overall performance of the system.

$$E = E_0 + \frac{RT}{nF}\ln\left(\frac{P_{H_2}P_{O_2}^{0.5}}{P_{H_2O}}\right) \tag{2.3}$$

Similarly, the surface concentration of the reactants is directly proportional to the operating pressure. Hence, according to Equation (2.1) and (2.4), an increase in operating pressure results in an improvement in the exchange current density [j_0].

$$j_0 = j_0^{ref}\left(\frac{P}{P_{O_2}}\right)^{\gamma} \tag{2.4}$$

Thus, the cell potential elevates at the increased operating pressure. The theoretical treatment defining the effect of pressure is given by Equation (2.5)

$$\Delta V = \frac{RT}{nF}\ln\left[\left(\frac{P_{H_2}}{P_0}\right)\left(\frac{P_{O_2}}{P_0}\right)^{0.5}\right] + \frac{RT}{nF}\ln\left(\frac{P}{P_0}\right) \tag{2.5}$$

The experimental study by Yan et al. investigates the effects of operating parameters on the fuel cell performance [72]. An increase in operating pressure from 1 atm to 4 atm, improved the fuel cell performance, highlighting the significant effect operating pressure has on the performance. Secondly, the increased operating pressure results in an increased bulk concentration of the reactant; hence, increasing the limiting current density (j_{lim}). Therfore, the operating pressure affects all three losses defining the fuel cell performance. The similar results have been observed with both experimental and the numerical studies by various researchers [77–80].

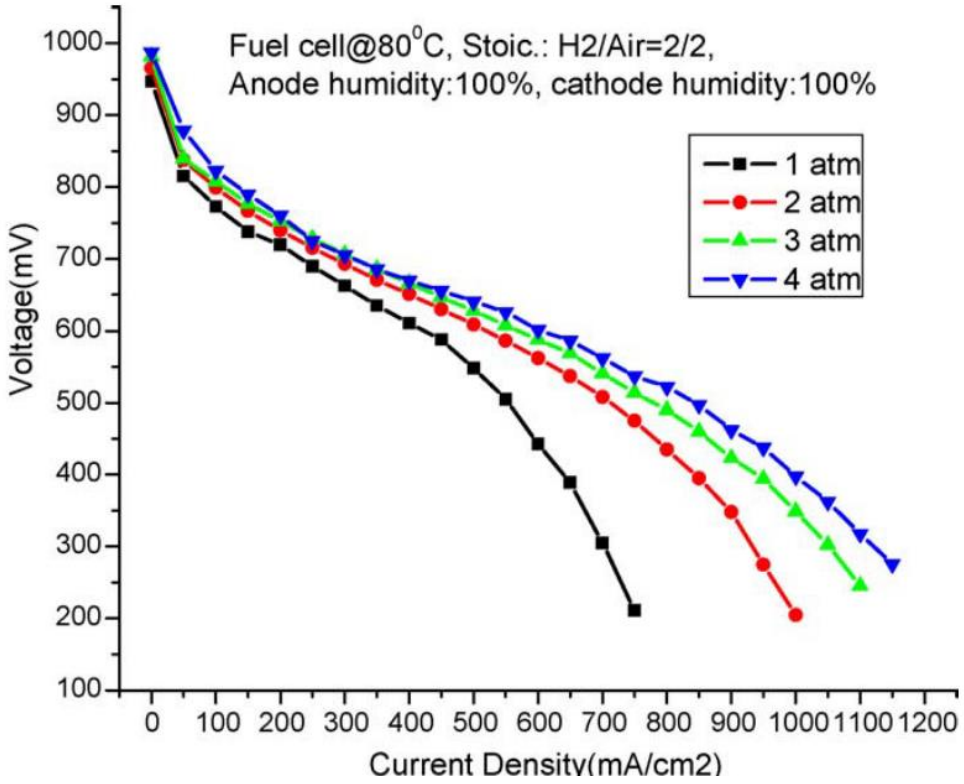

Figure 2.5–The effects of air pressure on fuel cell performance (25 cm^2 fuel cell with triple-serpentine flow pattern, hydrogen stoichiometry = 1.2, air stoichiometry = 2) [72]

2.3.3 Reactant flow rate

The reactant flow-rates at the inlet of a fuel cell must be equal or higher than the rate of reactant consumption in the cell. Fuel cells are generally operated either on the constant flow rate of the constant reactant stoichiometry. At constant flow rate mode, the same amount of reactant is supplied to the cell, regardless of the current drawn, while at constant stoichiometry mode the rate at which the reactant is supplied to the system depends upon the current drawn. The reactant stoichiometry (ξ) is a ratio of the amount of reactant available in the flow stream to the amount of reactant used in the electrochemical reaction of interest, as shown in Equation (2.6).

$$\xi = \frac{\dot{N}_{feed}}{\dot{N}_{reactant}} \tag{2.6}$$

$$\dot{N}_{reactant} = \frac{i}{nF} \tag{2.7}$$

where, $\dot{N}_{feed}$ (mol s^{-1}) represents the rate at which reactant enters in the system and $\dot{N}_{reactant}$ (mol s^{-1}) represent the rate of reactant consumption to generate the required output. Hence, at constant flow rate mode, the system efficiency varies with the current drawn as the amount of excess reactant available at the mass transport region is much lowered compared to the activation region. This results in affecting mass transport losses. On the other hand, in constant stoichiometry mode, the system is always provided with the fixed excess rate irrespective of the operating load.

Kim et al. performed the experimental study to investigate the effect of fixed reactant stoichiometries (anode/cathode) on the polarisation performance of the fuel cell [81]. The polarisation curves were obtained at three stoichiometric conditions, (a) baseline case corresponding to anode/cathode stoichiometries to 1.2/2.0, (b) anode-rich condition (2.4/2.0), and (c) cathode-rich condition (1.2/3.0). As water is generated at

the cathode catalyst layers, high stoichiometric cathode flow facilitates an efficient water removal from the cathode domain, allowing O_2 to reach active sites and improving the fuel cell performance. The polarisation curves shown in Figure 2.6 confirm that the cathode flow stoichiometry governs the cell performance at variable reactant flow-rates.

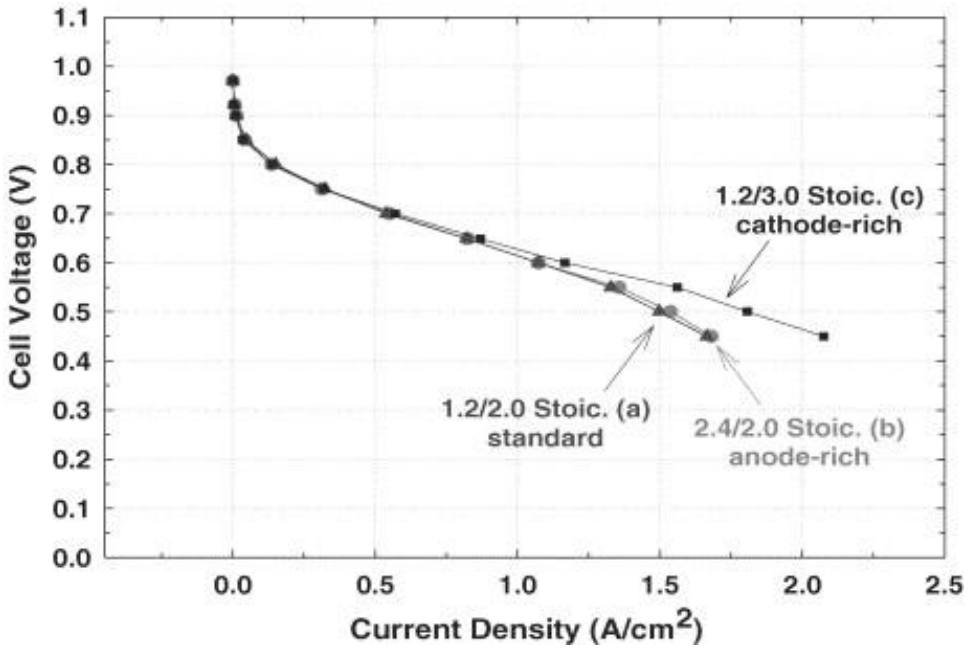

Figure 2.6– Polarisation curves for various stoichiometric flows of the anode/cathode.(▲) 1.2/2.0, (●)2.4/2.0, and (■)1.2/3.0 [81]

Turhan et al. analysed the effect of reactant stoichiometries on the water accumulation in the cell using neutron imaging technique [82]. The experiments conditions on parallel channel PEFCs and images were obtained at j= 0.35 A cm^{-2}. Fully humidified reactants were supplied to the cell at two stoichiometries, 2 and 5. At the low stoichiometry condition, a significant amount of liquid water accumulation in the channel was observed, as shown in Figure 2.7. On the contrary, at higher stoichiometry condition, the liquid water accumulation in the channel almost entirely diminished. Consequently, the total water mass in the cell decreased significantly

(30%) on increasing stoichiometric ratio from 2 to 5, suggesting an improvement in the rate of removal of product water by increasing the stoichiometric ratio. Hence, water management in the fuel cell that defines the fuel cell performance and durability is also governed by the reactant flow rates.

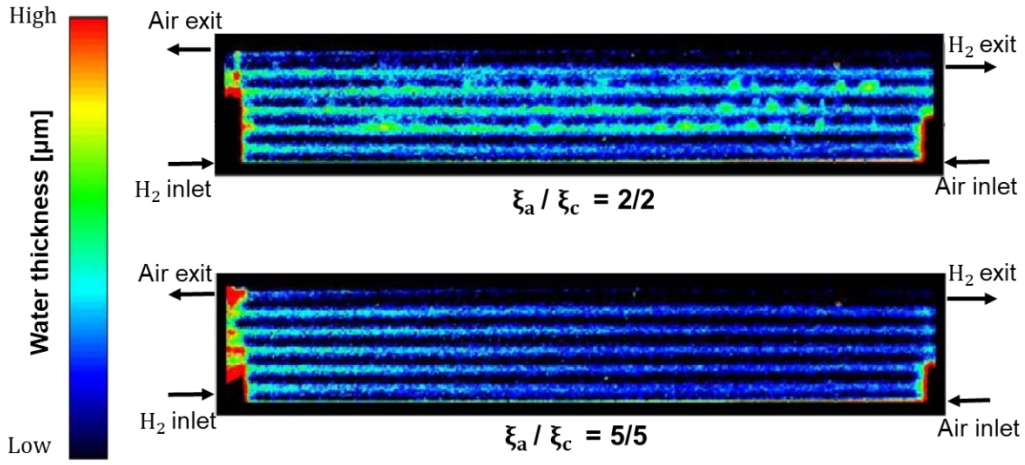

Figure 2.7– The effect of reactant stoichiometry on the water content in the cell obtained at j = 0.35 A cm^{-2}, using the neutron radiography technique. [82]

2.3.4 Relative humidity

The high inlet humidity conditions are generally observed for the stationary application while lower humidity inlet condition is more common for the automotive applications [66,83] Humidified feed gases allow maintaining PFSA membrane humidification that defines the proton conductivity. Both experimental and numerical studies have been done in various research evaluating the effect of relative humidity on fuel cell performance [69,70,84–90]. Jeon et al. studied the effect of low and high humidification conditions on various flow-field designs [91]. At low humidity conditions, irrespective of flow-field arrangements, the contribution of cathode overpotential was dominant in the activation region; however, a prominent increase in the Ohmic losses

was observed with an increase in current density, due to low membrane water content (λ). At high humidity conditions, the effect of cell flooding and mass transport losses was more prominent along with the flow-field design that governs the water removal efficiency. A neutron radiography study was performed on a 50 cm^2 active area cell by Iranzo et al. to evaluate the effect of a varying anode and cathode humidification on the voltage, Ohmic losses and GDL/MEA water content [92]. The galvanostatic study showed that the cathode humidification has a more significant influence on cell performance compared to the anode RH. However, an increase in anode humidification raised the water content in the GDL/MEA while the Ohmic losses lowered, suggesting improved membrane humidification. It is widely recognised both by the experimental and the numerical analysis that maintaining relatively high RH of reactant streams throughout the active area of the cell is vital to have stable performance and long durability. As PEFCs operate in a narrow water management region between cell flooding caused by too much water and membrane dehydration/cell drying due to too little water, it is crucial to develop the cell architecture that maintains the balance between water entering through the feed gases, i.e. RH, water generated by an electrochemical reaction and water removal efficiency. The dynamic response of air humidity on the PEFC performance was shown by Yan et al. [72]. The experiments were performed at the cathode humidity level varying from 0%, i.e. dry gas to 100% RH, i.e. fully saturated air at 80 °C. An improvement in the instantaneous performance was observed at high humidity conditions, as shown in Figure 2.8. The galvanostatic operation observed a higher rate of voltage drop at lower humidity conditions, highlighting the significance of the humidity conditions on the PEFC performance.

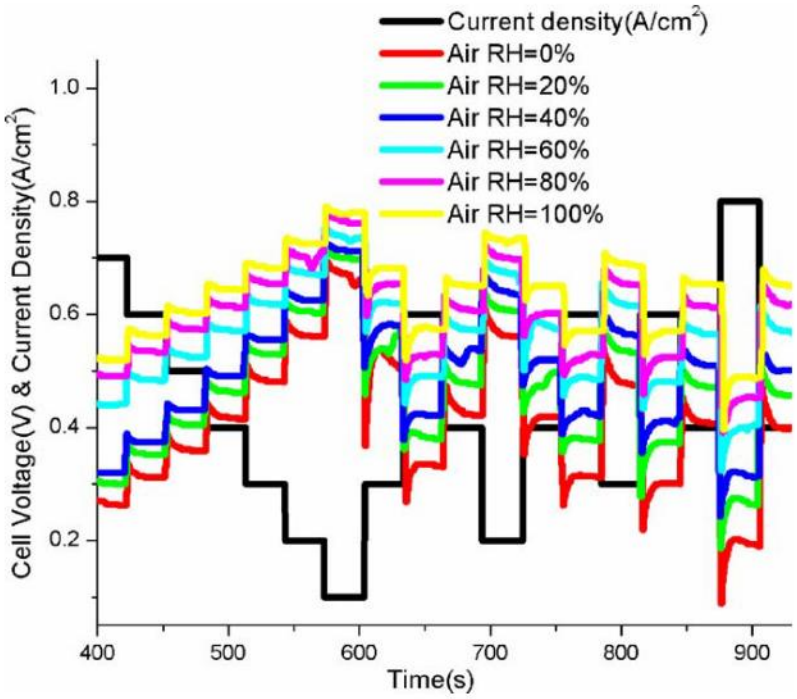

Figure 2.8– Dynamic responses of the fuel cell voltage operating with different air humidity to the step changes of current density (25 cm^2 fuel cell with triple- serpentine flow pattern, hydrogen stoichiometry = 1.2, air stoichiometry = 2)[72]

2.3.5 Mode of operation

The hydrogen required at the PEFC anodes is produced externally in the form of the reformate and needs to be stored inside the system. The system operating at higher hydrogen stoichiometry i.e. ξ_{H_2}>1 results in increased the operating cost of the system due to frequent refilling of the reformat. Hence, for the system optimisation, the hydrogen losses should be minimal throughout the operation. This leads to two commonly used modes of operation: the through-flow mode and the dead-ended anode (DEA) mode of operation [93].

In the through-flow mode, the downstream anode valve is ON, and the flow through the system is controlled by a mass-flow controller (MFC) . Such a system often needs extra external equipment to maintain cell humidification such as humidifiers and heaters. In through-flow mode, the hydrogen is often supplied at the stoichiometric ratio higher than unity [94–97]. The extra reactant is either circulated in the system and reused as fuel, as shown in Figure 2.9(a), or rarely vented in the atmosphere, reducing fuel efficiency. For example, if the anode stoichiometry is 4, only 25% of fuel will be utilised to generate the desired output and remaining 75% of the fuel will either be vented in the open atmosphere, increasing the operating cost of the system or it's recirculated in the system.

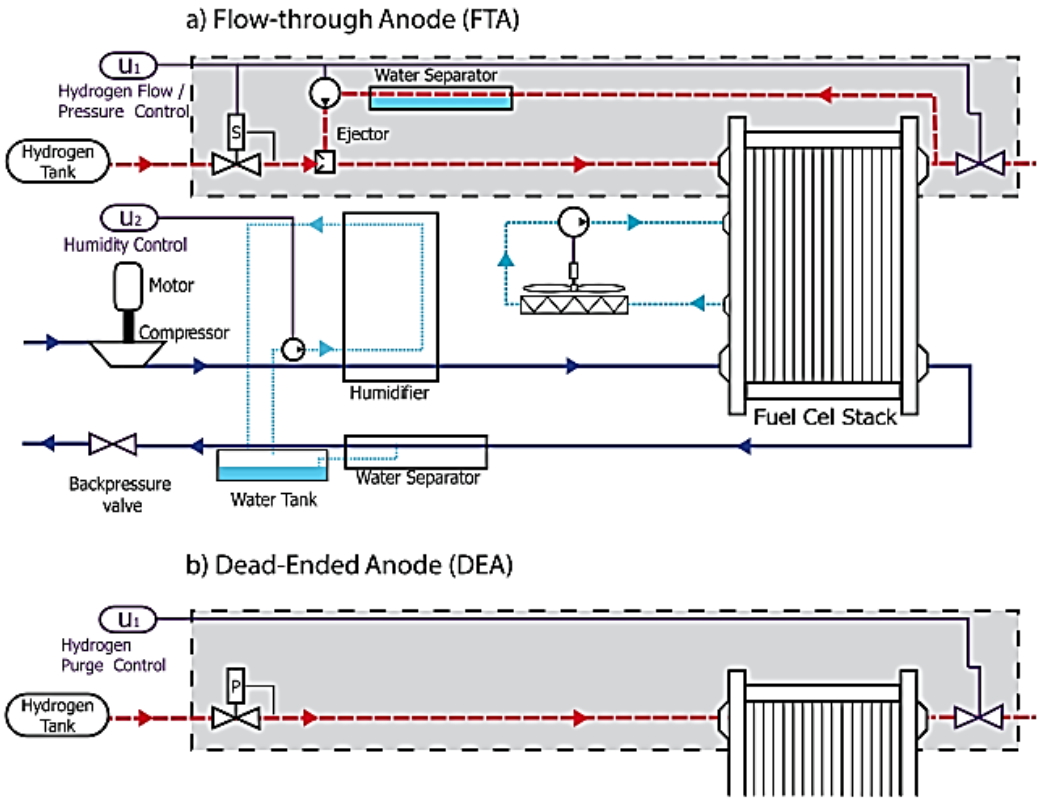

Figure 2.9– Schematic of a fuel cell system with (a) flow-through anode mode and (b) dead-ended anode mode of operation [93]

In order to improve the system efficiency / fuel utilisation, the dead-ended anode mode is used where the pressurised hydrogen is supplied at the anode inlet, and the downstream valve is closed, i.e. in the OFF position. This allows the system to operate at unit hydrogen stoichiometry, improving fuel utilisation to almost 100% [98]. DEA mode simplifies the system, increases fuel efficiency, reduces operating cost, and significantly lowers the parasitic power consumption. However, numerous researchers have observed a gradual voltage loss during the DEA operation [93,99–103]. The system efficiency can be regained by the intermittent opening of the purge valve, the result of which is shown in Figure 2.10. The voltage loss is influenced by several factors such as accumulation of back-diffused water in the anode compartment, and non-uniform membrane hydration; however, nitrogen crossover from the cathode to anode has been reported as the prominent cause of voltage loss (Figure 2.10). The performance of the fuel cell can be regained by intermittently opening the purge / through-flow vale, yet lowering the fuel efficiency. Meyer et al. [104] performed dead-ended/ purge cycling experiments on the commercial open cathode self-humidifying fuel cell, to investigate the effect on the voltage drop when examined at constant current. This work observed the nitrogen accumulation increases from 0.25% to 0.5% during dead-ended operation mode. Similar results were observed by Strahl et al. [21] showing that the nitrogen accumulation increases with membrane dryness, causing an increase in nitrogen crossover rate.

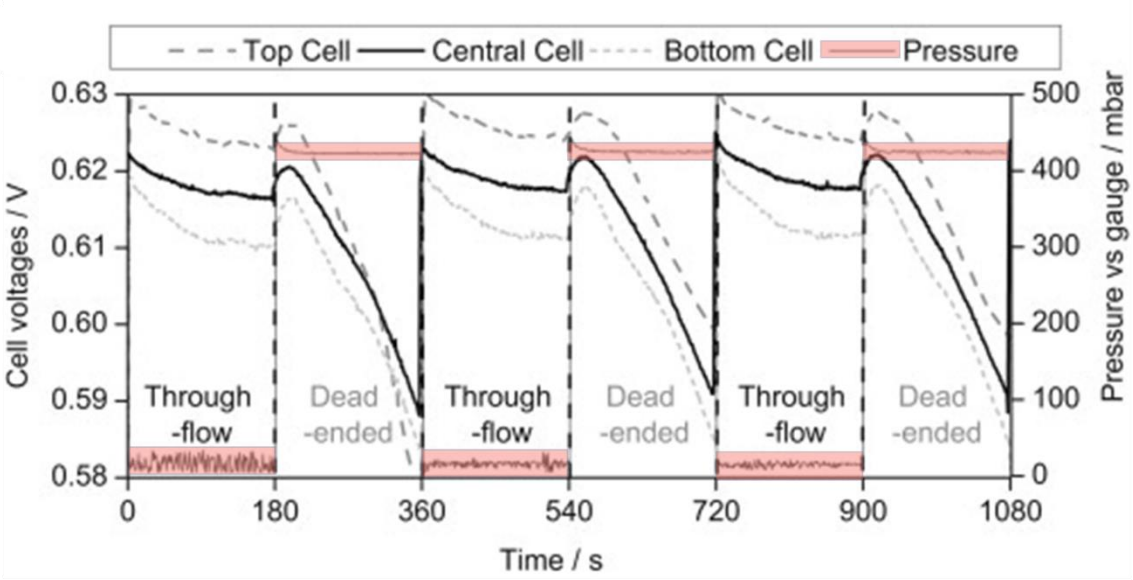

Figure 2.10–The effect of dead-ended/purge cycling on voltage loss at current density (j) =0.75A cm^{-2} [104]

2.4 Mechanical and architectural factors

The effects of mechanical factors such as cell compression, flow-field designs and arrangements have been found to play a vital part in influencing the fuel cell performance [62]. Each of these factors is associated with the fuel cell performance losses. In this section, such mechanical factors governing the performance are introduced.

2.4.1 Fuel cell compression

The individual components of the fuel cell stack, such as MEA, GDL and bipolar plates, should be held together with sufficient mechanical pressure to prevent leaking of the reactants and improve electrical contacts between the layers. Typically, the cell or multiple cells are stacked together and sandwiched between the endplates with the

help of tie rods. Various compression methods have been utilised in the past, such as hydraulic and pneumatic presses [105], compression springs [106], clamping plates or compression torque [107]. However, these methods are designed for pressure-based compressions, and the extent of dimensional change of the MEA cannot be directly measured or controlled. The degree of cell compression can also be controlled by varying the thickness of 'incompressible' sealing gaskets [108]. This method ensures the cell is evenly compressed and leak-free, as shown in Figure 2.11(a). Practically, the way in which the cell/stack is brought into mechanical compression also has an effect on performance as it has an effect on the structure of components (how much they are compressed/deformed). The fuel cell is compressed between 10% and 40% of its initial thickness for adequate electrical contact and adequate sealing [109,110], with the MEA components taking the majority of the compressive dimension change. However, it's important to note that the over-compression has typically argued as a most common occurrence in the commercial fuel cells, leading to detrimental results such as loss of performance, loss of cell durability, flooding, etc.

Corrugations on the bipolar plate (the alternating lands and channels) result in non-uniform compression of the GDL leading to constriction of the GDL under the land regions and the protrusion of carbon fibres onto the gas channels ('tenting'), creating distinct 'under the land' and 'under the channel' zones, as shown in Figure 2.11(b). Such non-uniform and excess compression can lead to irreversible morphological changes which can significantly influence the mass transport across the porous medium [45,76,111–113]. The effect cell compression on the GDL morphology have been extensively investigated using scanning electron microscopy (SEM) [114–116], and X-ray CT techniques [47,117–119]. Mason et al. performed a study on the effect of compression on Ohmic resistance and investigated the compression reversibility of non-PTFE carbon fibre GDLs [109].

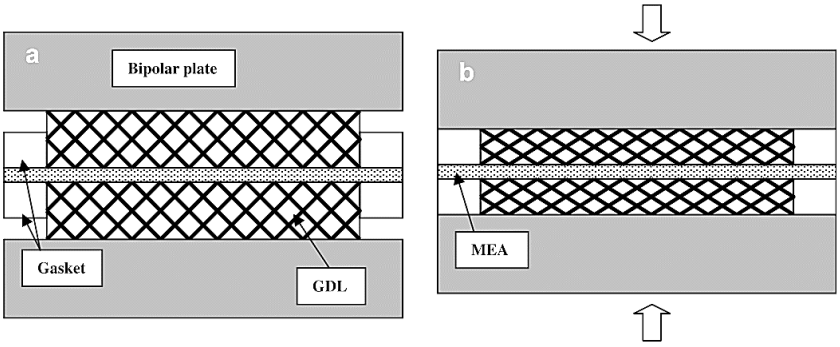

(a)

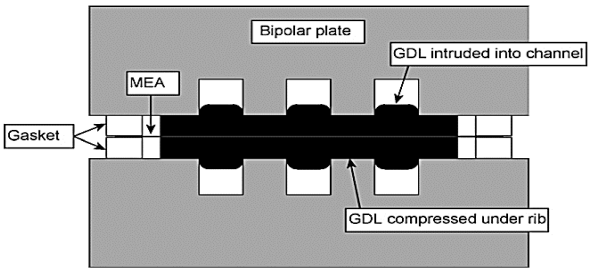

(b)

Figure 2.11 (a) Schematic of the cell compression that ensures proper sealing is achieved, Adapted from [120], (b) schematic of non-uniform compression resulting in under-the-channel and under-the-land (rib) zones [121]

The SEM images of the GDL subjected to 2.5 MPa compressive load resulted in the distinguishable compressed (under the land) and uncompressed (under the channel) GDL (Figure 2.12(a)). The close-up study visually revealed that the carbon fibres under the land are broken and compacted, increasing the fibre-to-fibre contact and reducing the porosity. This resulted in an improved electrical contact under the land region. However, the region under the channel has remained at its initial morphology. (Figure 2.12(b)).

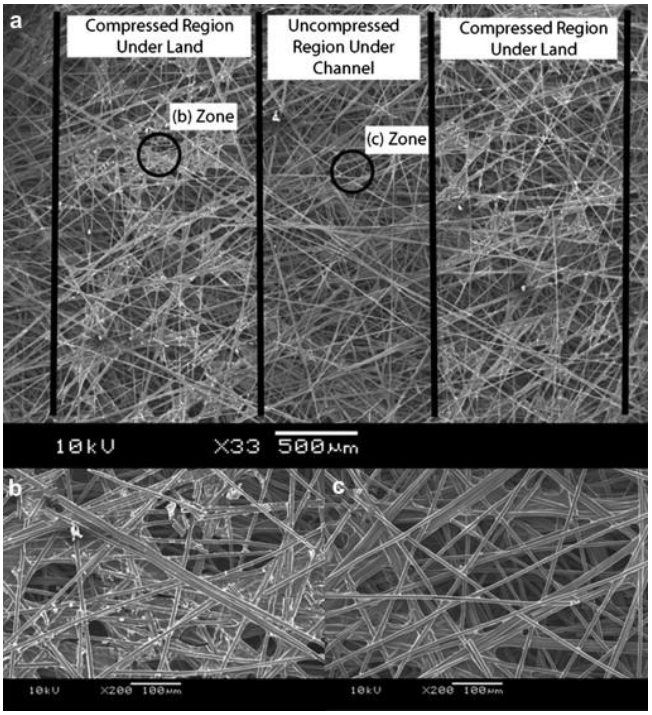

Figure 2.12 SEM images of non-PTFE Toray paper showing: (a) the impression of the flow-field land made upon compression to 2.5 MPa with the black vertical lines as a visual aid, (b) a close up of the compressed zone under the land area showing broken fibres and (c) showing the uncompressed region from under the flow channel [109]

The X-ray CT study provides better insight into the morphology evolution under compression. The X-ray CT study by James et al. revealed that the compression leads to the effective properties of the porous medium such as porosity, electronic conductivity, permeability, being different under the land and the channel region [47]. The GDL porosity under the channel was 20% higher than under the land region when measured at 40% compression. This change in porosity affects the permeability and gas diffusivity. While increased compression reduces porosity, permeability and gas diffusivity under the land, GDL 'tenting' typically increases these properties under the channel, inducing an uneven distribution of effective properties that affect the cell performance. X-ray CT compression study by Atkinson et al. showed that an increase in compression to 41% resulted in a reduction in the average pore size radius by 24

μm and lowered the GDL porosity, for SGL 29BC commercial carbon paper GDE [122]. The X-ray CT study by James et al. showed that an increase in cell compression improves the electrical and thermal conductivities of GDLs; however, it adversely results in a loss of pore volume, primarily in the region under the land [47]. This results in a loss of GDL porosity and permeability, and an increase in mass transport resistance [45,76].

The effect of compression on fuel cell performance was studied experimentally by Mason et al. using electrochemical impedance spectroscopy (EIS) [121]. The study was performed at three different compressive loads ranging from 0.5 MPa to 2.5 MPa. It was seen that the increase in compression lowered the fuel cell performance, preliminary at the higher current densities (Figure 2.13).

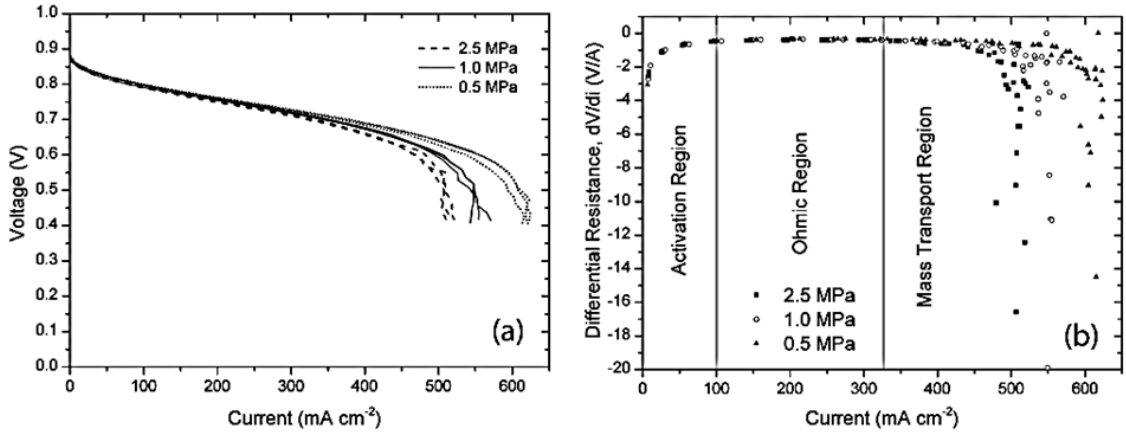

Figure 2.13 The effect of cell compression on fuel cell performance (a) polarisation performance obtained by repeated tests for various compressions. (T_{cell} 80 °C, anode and cathode flow rate 100 ml min^{-1} at 100% RH, (b) Representation of the performance regions in the form of differential resistance showing the different loss dominated regions and highlighting the limiting currents under different compressions, Adapted from [121]

An increase in cell compression results in lowering the limiting current that promotes early mass transport, as shown in Figure 2.14. The effect of compression on the increase in mass transport losses have been supported by various experimental and modelling studies [80–83].

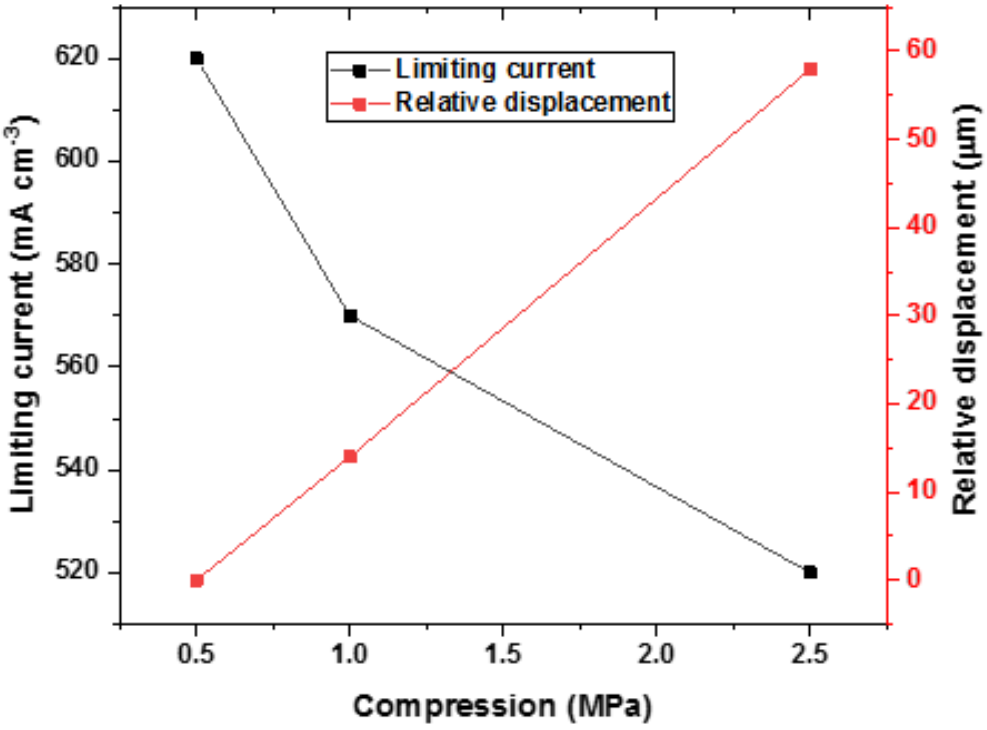

Figure 2.14 Effect of cell compression on limiting current, Adapted from [121]

Effect of compression on water management was studied by Wu et al. using neutron radiography in *xz* plane (i.e. plane parallel to the active area of the fuel cell) [125], the findings from which supports the trade-off situation between electrical contact resistance and mass transport limitation due to flooding. While increasing the cell compression improves the electrical and thermal conductivities of GDLs, it adversely results in a loss of pore volume, primarily in the region under the land. A careful balance has to be struck in achieving effective water management and performance

improvement in a fuel cell. The cumulative effect of the cell compression on fuel cell performance is graphically presented in Figure 2.15.

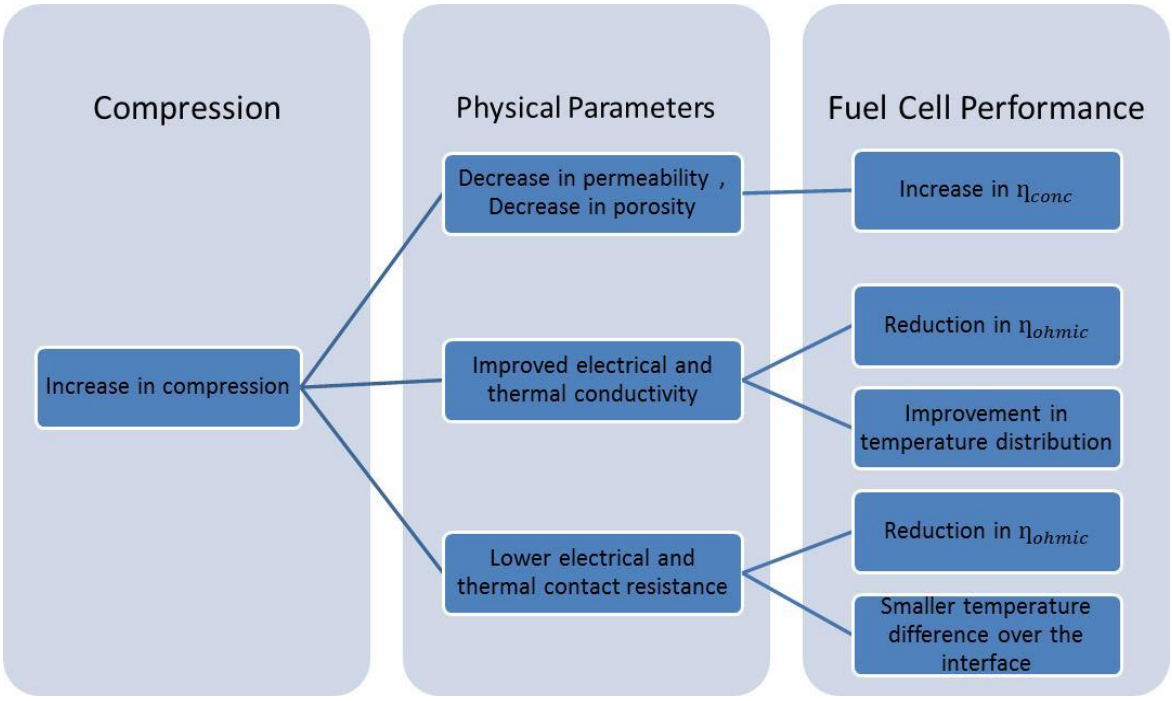

Figure 2.15 Schematic of the effect of GDL compression on the performance

2.4.2 Flow-field configurations and pattern design

The key functions of the flow-field are to deliver an even distribution of reactant species over the active area of the electrode and removal of the by-products, water and temperature management, and providing mechanical support to the MEA while ensuring good current collection [59,127–129]. The flow-field channel configurations and arrangement has a significant impact on PEFC performance. Numerous research has claimed to improve as much as 50% in the PEFC performance by altering the flow-field designs or arrangements [130–132]. The majority of PEFCs depend on the conventional flow-field for reactant distribution; although some fuel cell designs dispense with a conventional flow-field and rely on the lateral flow of reactant through

the GDL or around it edges [103,133–137]. Thus, broadly, the flow-field configurations can be divided into two groups, namely primary flow-fields and the secondary flow-fields.

2.4.2.1 Primary flow-field

Primary flow-fields are conventional and intentionally designed flow-fields that may vary in shape, dimensions, orientation and configuration [13,132]. The flow-fields are typically rectangular or square in cross-section, which is ideal for the laboratory or low-temperature PEFC applications; however, rarely other configurations such as trapezoidal (moulded carbon composite plate), semi-circular or triangular, sinusoidal (stamped metal plates) are observed [132,138–140]. Zhu et al. and Lorenzini-Gutierrez et al. numerically studied the effect of channel cross-section on the water transport highlighting the significance channel cross-section on the dynamic water transport behaviour and overall pressure drop in the system [140,141]. Figure 2.16 shows the typical cross-section of the fuel cell, irrespective of the flow-field designs.

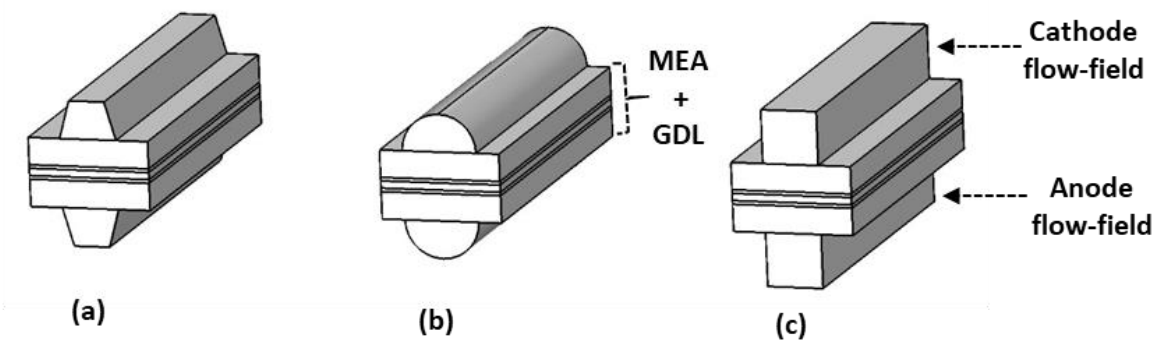

Figure 2.16 Schematics of (a) trapezoidal, (b) semi-circular, and (c) square channel cross-section for flow-field plates.

The three most conventional primary flow-field designs reported in the literature are parallel, serpentine and interdigitated [Figure 2.17]. A number of studies investigated the effects of primary flow-fields designs on fuel cell performance, highlighting the

change in flow-field patterns affect the pressure drop and water management in the fuel cell [142–148].

Various experimental and numerical studies suggested the flow-field channel geometries such as channel length, width, height and the coatings affect the rate of water removal in the fuel cell altering the performance [82,131,140,145,149]. An analytical model by Kornyshev et al. showed that the dependence of channel length on the reaction rate parameters and defined by the smallest flow-field length either at the cathode or at the anode domain [147]. The analytical modelling study by Dohle et al. confirmed the dependence of the performance of flow-field length [150]. The characteristic length defines the length of availability of the fuel or reactant in the flow-fields. The current density can be maximised using an adaptive width approach. In lower humidity operating conditions, bigger channel width at the inlet, and comparatively narrower channel width at the region away from the inlet should result in maximising current density [151].

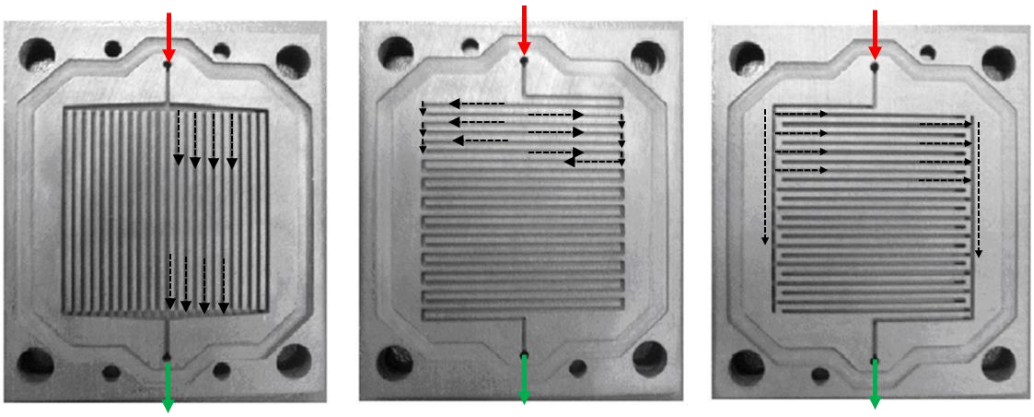

Figure 2.17 Schematics of parallel (left), serpentine (middle), and interdigitated (right) channel architectures for flow-field plates. Red and green arrows represent inlet and outlet channels, respectively, and black arrows represent the direction of flow, adapted from [148]

2.4.2.2 Secondary flow-field

Accurate and reproducible cell/stack assembly is the key to ensuring good performance and durability. Depending on the tolerance of the manufacturing processes and the components used, integration of a membrane electrode assembly (MEA) into a cell can lead to a narrow gap between the GDL and the gasket/sealing or the edge of the bipolar plate. This gap can act as a 'secondary flow-field' (SFF) with unexpected results, which can be potentially advantageous or damaging to PEFC performance [103,152]. This feature has been widely neglected in the literature. Figure 2.18 shows the narrow gap between gasket and GDL in a generic fuel cell design.

In the case of bipolar plate designs without a macroscopic (conventional) flow-field, the SFF offers a path of low resistance to reactant transport through the GDL [103]. In such designs, the reactant diffuses laterally through the GDL, and the SFF may act as a primary flow-field [103]. The presence and extent of the SFF depend on the cell design, fabrication and assembly, GDL material, component positioning accuracy and the compression process.

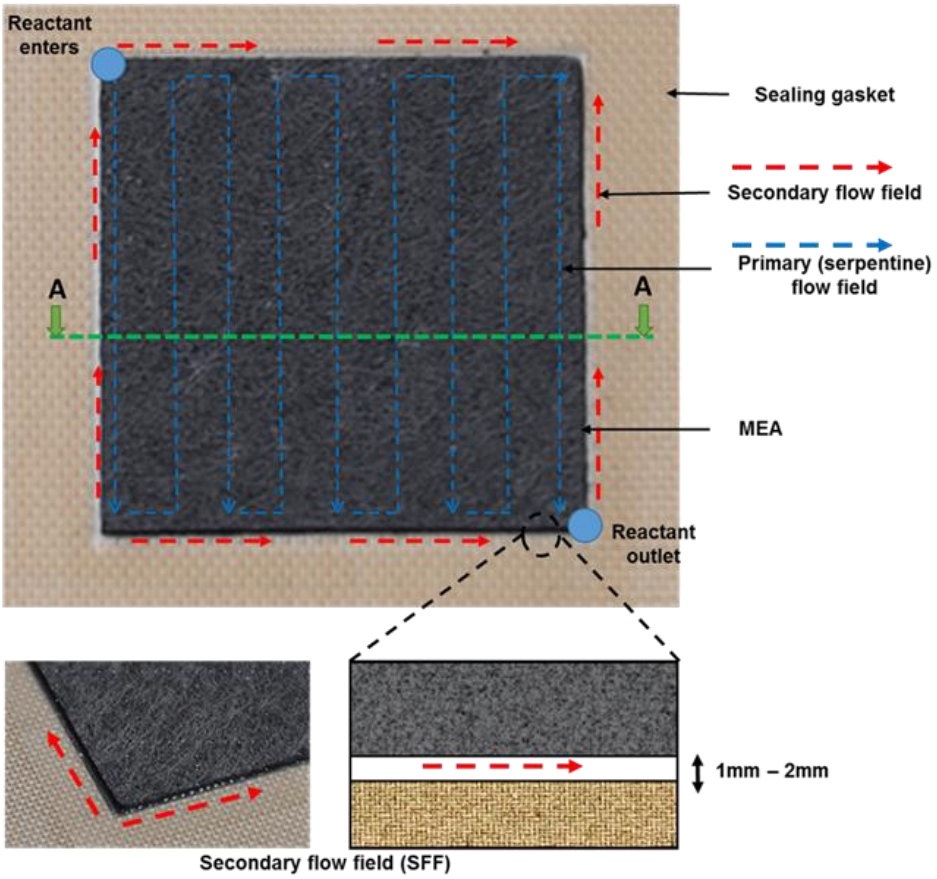

Figure 2.18 The cell assembly process resulting in a thin gap between the MEA and a sealing gasket, referred as the 'secondary flow-field' (SFF), observed in the generic fuel cell design with serpentine flow-field arrangement

Flow-field arrangements discussed in the literature can be broadly classified in the two groups, namely symmetrical and asymmetrical arrangement of the flow channels. At the symmetrical arrangement, the primary flow-fields on either side of the membrane, and land and channels are in perfect alignment, as shown in Figure 2.16. However, few designs adopt the asymmetrical approach where a flow-field channel is only present on one side, as is the case in many commercial fuel cell designs. In these designs, hydrogen supply to the anode occurs laterally through the GDL, without a

macroscopic flow-field and may rely on a secondary (peripheral) flow-field [98,103,104].

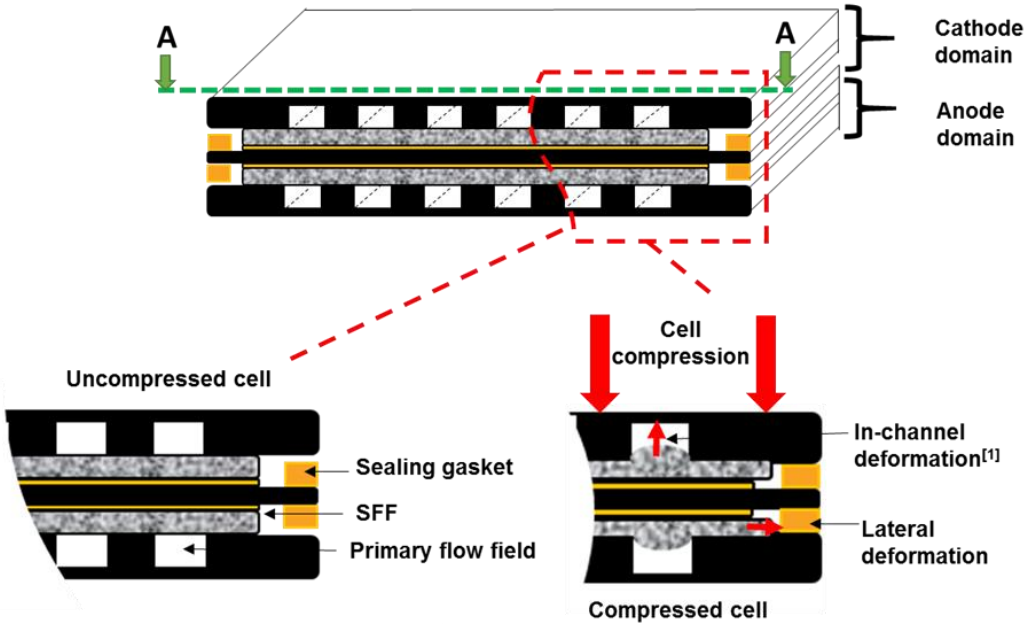

Figure 2.19 Schematic of the effect of cell compression during cell assembly process that results in the lateral and in-channel deformation of GDL, partially blocking the primary and the secondary flow-field

2.5 Conclusion

The review presented in this chapter provides a background of the practical factors governing PEFC performance. The purpose of this review is to establish an understanding of the role that design, operating and manufacturing processes have on PEFCs performance. The conclusions from this chapter are as graphically illustrated in Figure 2.20

- Catalytic factors - Catalytic factors form the backbone of the electro-kinetic properties of the fuel cell defining the activation performance which further

contributes to the performance loss or system failure that occurs as a consequence of structural and electrochemical degradation of the cell.

- Operating parameters – Operating parameters such as temperature, pressure, reactant flow-rates, humidity defines the activation and transport losses in the fuel cell altering the cell performance.
- Operating cycles and modes of operation – start-stop cycles, sub-zero operating conditions, and modes of operation collectively contribute to the degradation of catalytic factors, defining the fuel cell durability and performance.
- Mechanical and architectural factors: factors such as fuel cell compression, flow-field designing and arrangements and assembly process collectively forms more than 40% of the fuel cell designing and operation cost. These factors define the Ohmic and mass transport losses, affects water and temperature management, the localised performance of the cell, and the system durability.

The fundamentally important phenomenon of electrochemical transport and water management has been identified as the key factor deciding the performance and life span of the fuel cell. However, these factors can be altered by optimising the balance between the complex interplay of mechanical and architectural factors. Thus, the focus of the following chapters is on the advancement in the understanding the influence of mechanical and architectural factors on PEFC performance, through advanced characterisation and numerical modelling methods.

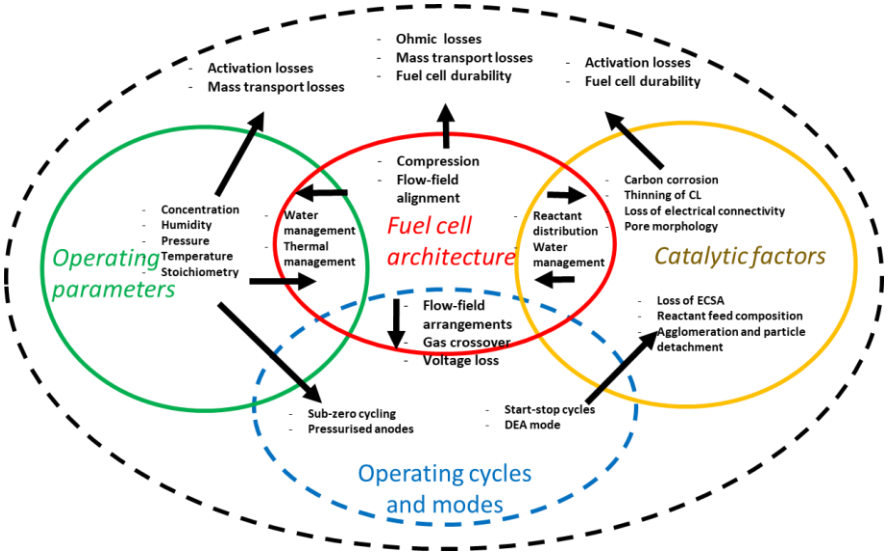

Figure 2.20 Factors governing the fuel cell performance - the graphical conclusion

Chapter 3
Experimental methodology and characterisation techniques

Abstract

This chapter provides the details of various performance evaluation and characterisation techniques used in this research and the methodologies used to evaluate the generated data. The first section of the chapter provides the details of the sample preparation and an overview of the experimental methodologies used in the research to characterise the fabricated MEAs and evaluate the performance of fuel cells developed in-house. This section also discusses the novel non-destructive diagnostic methodology implemented in this research to investigate and optimise the effect of fuel cell compression and the architecture on the liquid water accumulation.

The second section of the chapter provides theoretical and experimental details of the software used and to evaluate the results, and subsequently, a detailed summary of the metrological approaches or ‘metrics’ used to evaluate and generate the useful data from that can be used to develop the computational models.

3.1 Experimental methodologies

PEFC performance can be evaluated by the most established electrochemical technique for fuel cell characterisation, i.e. a polarisation curve which can be combined with the advanced characterisation techniques such as current / temperature mapping, liquid water visualisation, electrochemical impedance spectroscopy (EIS), etc.

3.1.1 MEA fabrication

MEA fabrication process comprises of three steps, selection and/or printing the suitable GDL and membrane material, hot pressing and conditioning, as outlined in Figure 3.1. In the present study, a 6.3 cm^2 MEA was fabricated in-house by hot pressing commercial GDLs with a platinum catalyst loading of 0.4 mg cm^{-2} (HyPlat, South Africa) and a 50 µm thick ionomer membrane (GORE, USA) using a 12-ton thermal press (Carver, 4122CE, US). The membrane was used without any pre-treatment, and the assembly was pressed at 130 °C for 3 minutes with an applied pressure of 450 psi. The hot pressing conditions were chosen based on previous work [153]. The fabricated MEA samples were further conditioned with the parameters detailed in Table 3-1.

For the X-ray CT microstructural evaluation, the cylindrical MEA samples were cut to the dimension using a suitable biopsy punch. These were fresh samples cut-to-dimension before conditioning.

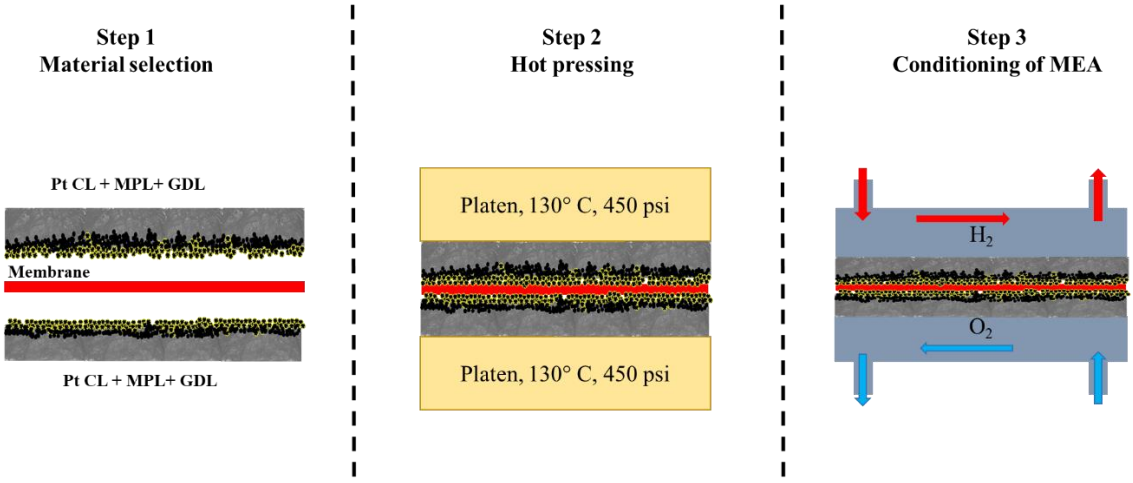

Figure 3.1–Schematic of the MEA fabrication process

Table 3-1 – Cell conditioning parameters

Operation	Conditions
Polarisation range	OCV to 0.3 V
Cell conditioning	10 min (fast polarisation)
Hold time per current increment (0.1 A cm^{-2})	1 min
Flushing time	10 min

3.1.2 Fuel cell components

Figure 3.2 shows an exploded view of a closed-cathode PEFC with an active area of 6.3 cm^2 used in the study. The cell comprised of aluminium end-plates, current collectors and flow-fields. The end-plates, current collectors and flow-fields were gold-coated to increase corrosion resistance and decrease electrical resistance. PTFE gasket sheets were used to seal the perimeter of the MEA on either side of the

membrane. Tygaflor gasket sheet (70 μm thickness) was used for electrical insulation between the current collector and the end-plate. VITON rubber O-rings were used to provide a gas/liquid seal at the interface between current collectors and flow-fields.

Incompressible PTFE sheets of 50 μm and 75 μm thickness were laser-cut to the cell's dimension. Multiple sheets stacked together were used to achieve the required degree of compression. The particular compression levels were chosen to evaluate the typical range of cell compression that assures adequate sealing and the performance of the fuel cell. The initial torque of 1.5 Nm was used to tighten the bolts. A micrometre (RS Pro, accuracy ±5 μm) was used to reassure the changes in GDL thickness with compression.

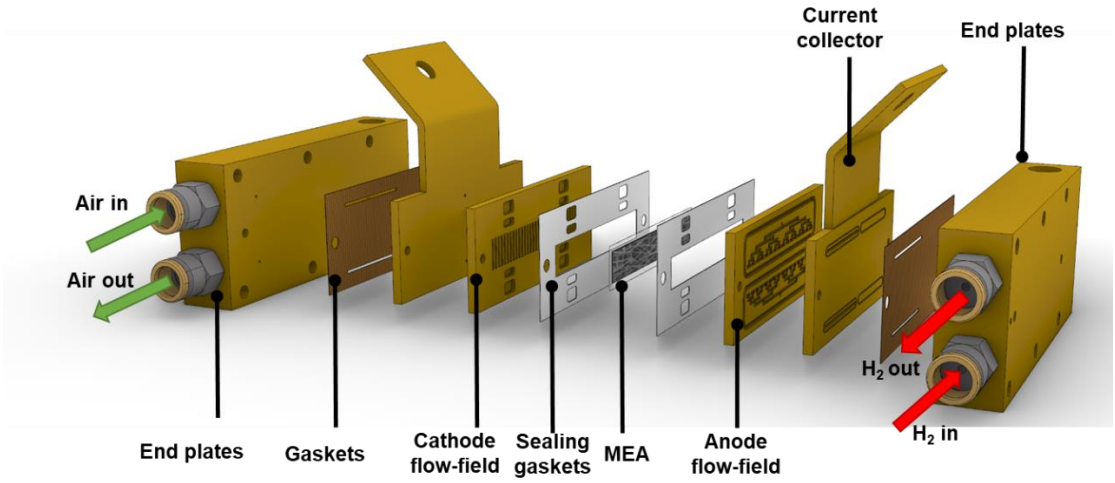

Figure 3.2– Exploded view of a closed-cathode PEFC with an active area of 10 cm^2, red and green arrows represent hydrogen and air respectively

A parallel flow-field arrangement was used to give a clear visualisation of water emerging into the channel. This is not possible with a serpentine configuration where meanders overlap in the in-plane direction. The bifurcating reactant delivery channels were designed on the back of the flow-field to ensure uniform gas distribution across individual parallel gas channels, as shown in Figure 3.3 [131,148,154].

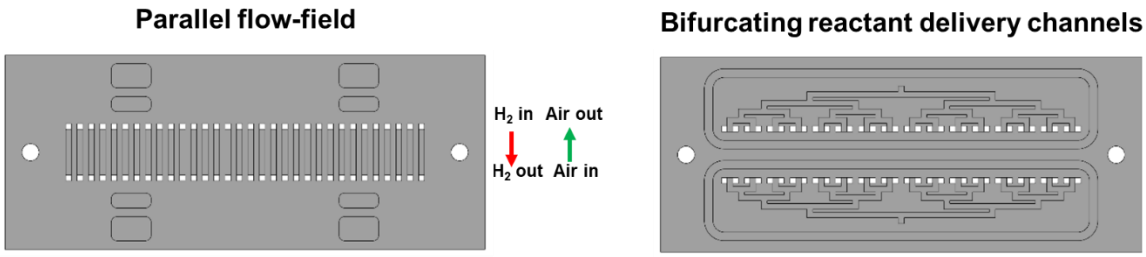

Figure 3.3– The parallel flow-field design for the reactant delivery to the active area and the bifurcating reactant delivery channels on the backside of the flow-field to ensure uniform reactant delivery to individual parallel gas channels

3.1.3 Fuel cell diagnostics – polarisation curve

A polarisation curve captures the evolution of the voltage from the cell activation current density to a high current density (or vice-versa), allowing the various voltage losses (overpotential) as discussed in the previous chapters. It can either be performed in potentiostatic (constant voltage) or galvanostatic (constant current) mode. As one of the easiest and widely used diagnostics used to measure and compare the fuel cell performance, the effect of the current density of the voltage losses has been extensively measured [15,155–159].

The initial fuel cell conditioning and testing were carried out using a commercial fuel cell test station (850e, Scribner Associates, USA). A schematic of the experimental setup is outlined in Figure 3.4. Fuel cell temperature, inlet gas flow rate, relative humidity, and electronic load were regulated using a commercial setup. The anode (ξ_{H_2}) and the cathode (ξ_{O_2}) stoichiometric ratio were maintained at 1.2 and 3, respectively, by controlling the gas flow rate. The fuel cell temperature and relative humidity (RH) of the inlet gas were set to 70 ºC and 100%, respectively. During operation, the gas line temperature was kept higher than the humidifier temperature to prevent any condensation prior to entering the fuel cell.

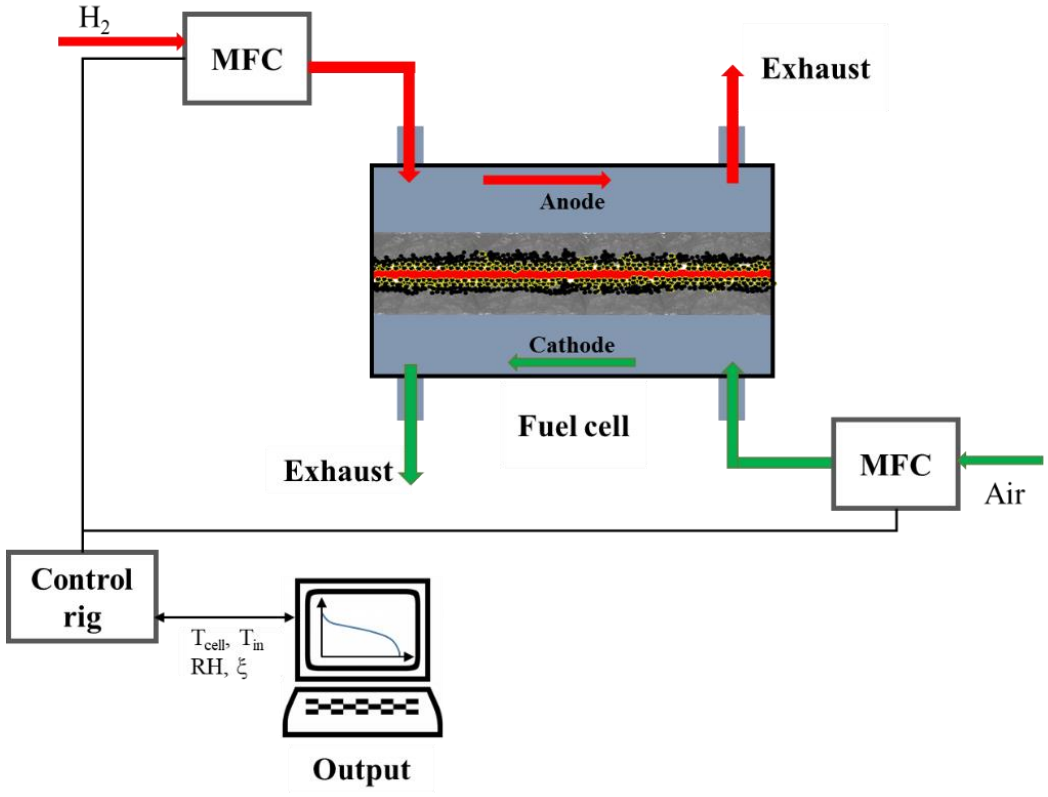

Figure 3.4– Simplified schematic of the experimental setup used in this study to evaluate the fuel cell performance. MFC stands for digital mass flow-controller.

3.1.4 Liquid water visualisation

As discussed in the previous chapter, effective water management is the key to attain efficient fuel cell technology. Liquid water visualisation in the PEFCs allow understanding of the water formation, transport, and removal mechanisms, and gain insight into the effect of fuel cell architecture on the performance and possible modifications in the architecture. Various experimental techniques have been developed in the past decades that allow *in situ* visualisation of the water content in both the MEA and flow-field channels such as fluorescence microscopy [160,161], X-ray tomography and radiography [162–165] and neutron radiography [88,92,103,166–

168]. Though all the techniques allow visualisation water in the fuel cell, the suitability of a visualisation technique should be determined by the required spatial and temporal resolution.

3.1.4.1 Neutron radiography

Neutron imaging is a versatile non-destructive liquid water visualisation technique and has been used to analyse challenges regarding in-situ and in-operando water management in the fuel cell. Neutrons can penetrate deeply through standard fuel cell structural materials and have a high sensitivity to light elements such as hydrogen, hydrogenous substances, or lithium [168–172]. The higher attenuation by light elements is due to the fact that neutrons interact predominately with the nucleus, rather than the electron density, as in the case of X-rays. These qualities allow investigating different aspects of water management such as the effect of different flow-field geometries [131,149,173], materials [166,174,175], operating conditions [176,177], architecture [63,103], degradation [24,25].

3.1.4.2 Experimental methodology - Helmholtz-Zentrum Berlin (HZB)

In the current project, neutron radiographs were generated at the V7-low energetic (cold) neutron radiography (CONRAD-2) beamline facility at Helmholtz-Zentrum Berlin (HZB). The neutron radiography setup is shown in Figure 3.5. The cold neutron facility provides high attenuation contrast for thin hydrogenous based (hydrogen-containing) layers of the fuel cell, making it the best option to generate in-operando radiographs of the fuel cell [180–183]. The beam formed by a pinhole of 3 cm at a distance of 5 m is transmitted through the PEFC. The detector consisted of a digital camera with sCMOS chip (Andor Neo 2560 × 2160 pixel) facing a 200 µm scintillator screen. The cell mounted on a fixture was placed on a rotating table, allowing radiographs in both the in-plane and through-plane orientation.

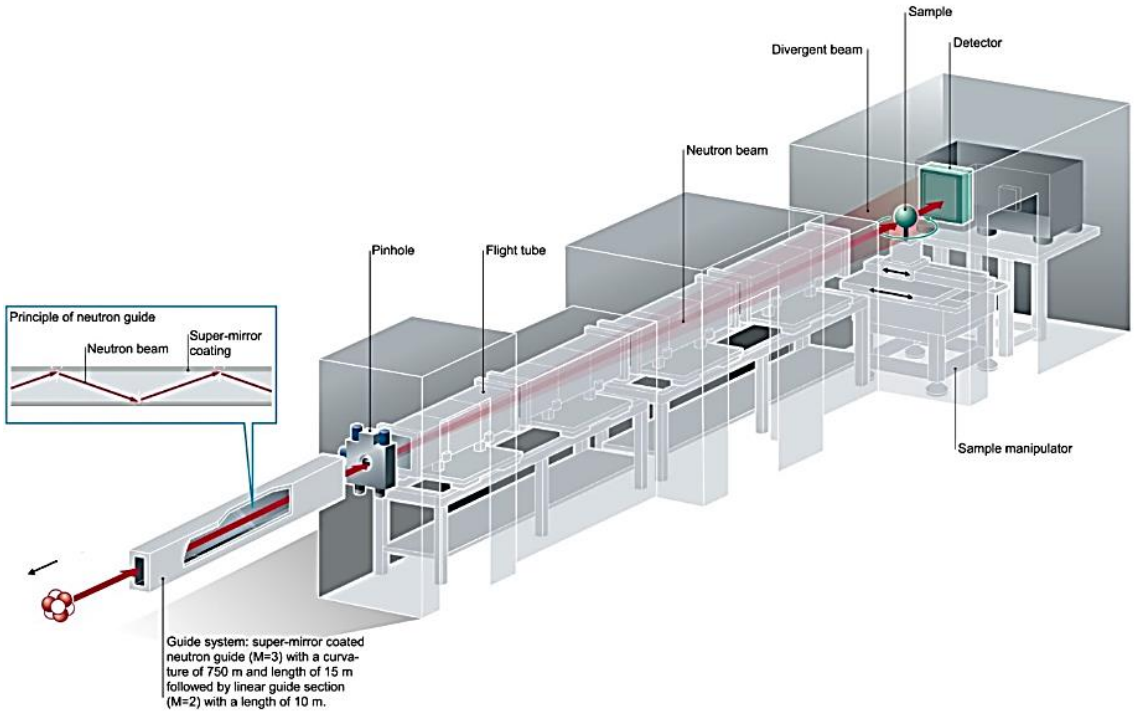

Figure 3.5– Schematic view of V7 CONRAD beam facilities at HZB [180]

An imaging field-of-view of 40×34 mm^2 with 15.2 μm $pixel^{-1}$ resolution was achieved using the imaging set-up previously developed by Kardjilov et al. [180]. In-plane imaging at a resolution of 15.2 μm $pixel^{-1}$ cannot unequivocally separate the GORE membrane from the catalyst layers and are thus grouped and referred to as the 'membrane electrode assembly (MEA). Each image was taken with an exposure time of 5 s. The liquid water image was generated by normalising the wet image to the dry fuel cell image taken at the beginning of each experiment and any non-uniformity in the beam-intensity was corrected with an open-beam image. The quantification of the water thickness from neutron images was performed using the Beer-Lambert law:

$$\delta_{water} = \frac{-ln\left(\frac{I}{I_o}\right)}{\epsilon_{water}} \tag{3.1}$$

where δ_{water} refers to the liquid water thickness in cm, ϵ_{water} is the attenuation coefficient of the neutron in liquid water, measured in the given setup as 5.3 cm^{-1}, I_0 is the intensity of the dry image taken before the cell operation starts, and I is the intensity of the wet image taken during the cell operation. The radiographs presented have initially been grey-scale images which were masked with a yellow-to-blue 'parula' colour-map, blue representing the presence of higher levels of water, discussed in chapter 7.

3.1.5 Microstructural evaluation- X-ray computed tomography

Since the first publication on the pivotal work by W.C. Roentgen in 1896 [184], X-ray radiography has seen ever-increasing growth in the research interests, instrumentations and the applications. Initially, it started with the fundamental role in the field of medicine; however, in past few decades, it's been widely used in the research of material science, earth sciences, archaeology, etc.

Nevertheless, 2D projections provide the *in situ* information of the sample; X-ray radiographs are limited in order to provide the information in the third dimension, which is crucial to generate understanding of the sample. This led to the development of X-ray computed tomography (CT). Ever since the first successful use of X-ray CT was recorded the 1970s, the substantial improvement has been observed in CT instruments, ranging from lab-based to the synchrotron-based CT sources, reconstruction algorithms and the analysis techniques. This section briefly discusses the details of lab-based X-ray CT technique used in this research to generate the images of fuel cell internals and the data analysis techniques implemented.

3.1.5.1 Lab-based resources

Synchrotron-based CT instruments provide parallel X-ray beams and therefore result in higher resolution and better image contrasts [185,186], while lab-based X-ray CT

sources are not able to generate parallel beams. Instead, they use a point source which produces a small angle cone X-ray beam in the object area, as seen in Figure 3.6. In this work, lab-based X-ray CT instrument Zeiss xRadia Versa 520D (Carl Zeiss, USA) is used.

The lab-based X-ray CT imaging technique consists of three steps: (i) image acquisition; (ii) back projection and 2D slice reconstruction and; (iii) 3D reconstruction and volume rendering.

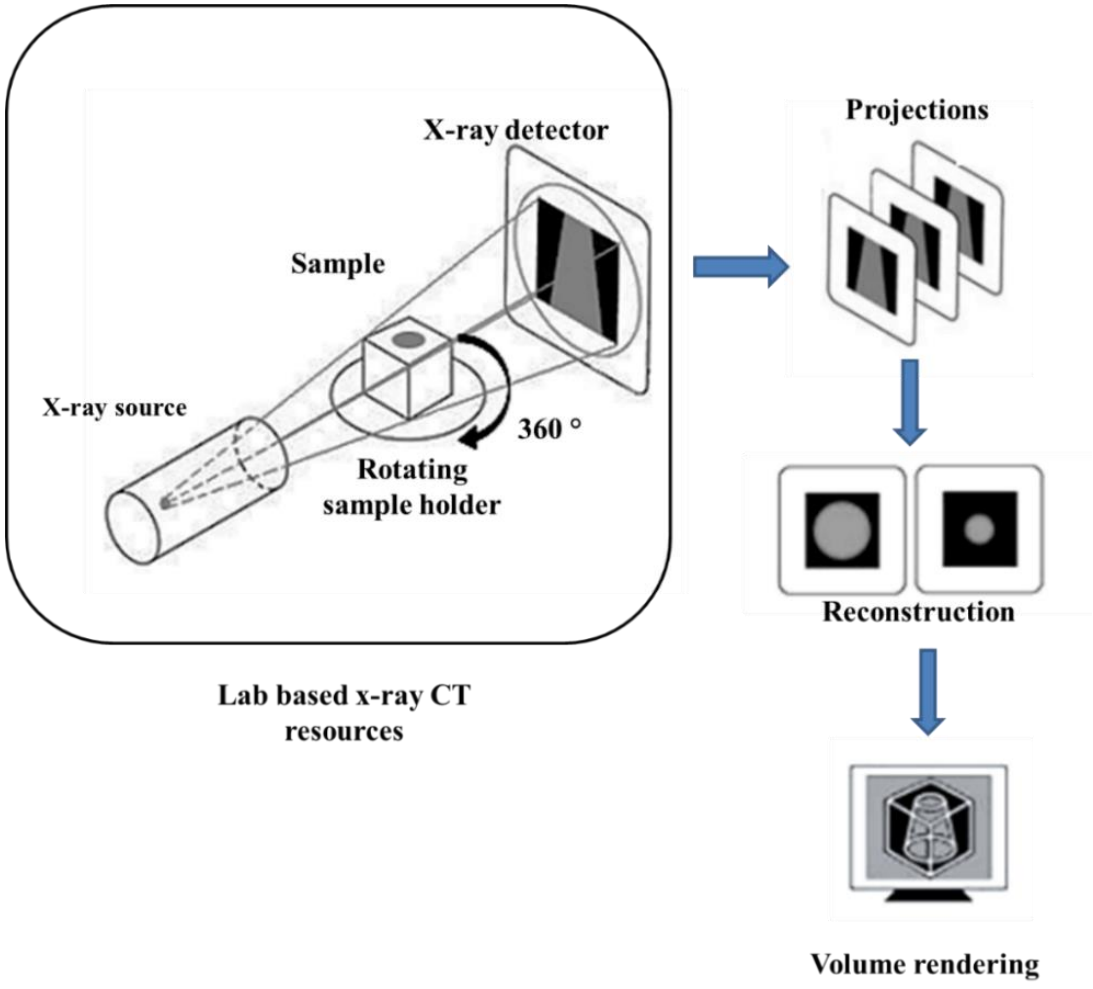

Figure 3.6–Schematic of X-ray CT image generation process.

During the image acquisition, the sample object placed on the revolving disk in front of an X-ray source and rotated step-by-step (Figure 3.6). Increasing the number of projection by rotation steps, the localization becomes more defined, as illustrated in Figure 3.7. Therefore, an increasing number of projections increases the accuracy of the X-ray CT image; however, increases the computational time and cost proportionally.

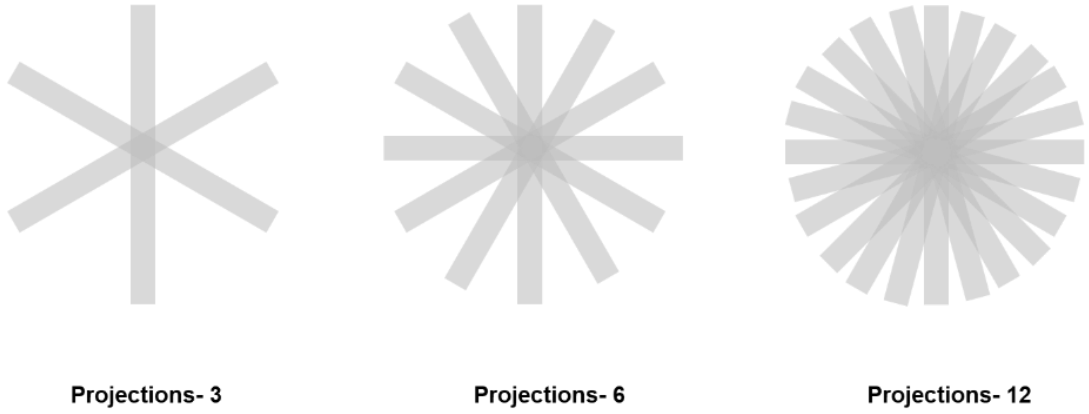

Figure 3.7– Effect of the number of projections on the image quality.

Better contrast and image quality can be achieved by optimising the transmission voltage and current. However, increasing the X-ray voltage results in X-ray over transmission, meaning that projections become over-bright, especially when the X-ray passes through soft materials, affecting the phase contrast, and hence the quality of the image. Therefore, the image acquisition parameters has to be chosen effectively in order to generate the good quality images that captures morphological details of the component, The image acquisition parameters used in the current research are detailed in Table 3-2. Greyscale projections are then generated using an X-ray detector array which is based on the level of X-ray attenuation and reflects the localised density of the sample. The generated radiographs are further assembled to reconstruct the 3D volume.

Table 3-2 – X-ray CT image acquisition parameters

Operation	Conditions
Source voltage	80 kV
No of projections	1801
Field-of-view	3 mm × 3 mm
Magnification	4X
Resolution	1.6 μm

Further, the 2D slices have to be reconstructed using a tailored algorithm. The CT techniques involve reconstructing 2D projections of an object viewed from different projection angles derived from Radon function. Radon function computes the line integrals from multiple sources along parallel beams or paths in a specific direction, assuming that projection of a 2D image (function) is a set of lines (line integrals) [18,187,188]. Therefore, with a sufficient number of projections, an inverse Radon transforms the detailed 3D digital image of the sample object can be generated. However, use of Randon function is computationally expensive; hence, in practice, computationally less expensive methods such as back projection methods are used. Backprojection methods project each recorded image back into the object space at the angle at which the original image was recorded. Thus, to generate the detailed high-resolution digital image of the sample object the balance between a number of projections and scanning time has to be achieved. Thus, in current research, reconstruction of the radiographs into a 3D volume was achieved using a cone-beam

filtered back-projection algorithm (Xradia XMReconstructor) resulting in a voxel size of 1.63 µm.

3.1.5.2 Image analysis

In order to generate useful information from the 3D volume rendering data, the images have to be phase segmented according to the greyscale values. The image analysis process is detailed in Figure 3.8.

One of the crucial steps in the X-ray CT-based digital reconstruction is adequate noise reduction and the thresholding, in which structures are evaluated in voxels with greyscale values and segmented to distinguish solids phases from empty pores using threshold values. The generic method for image segmentation, i.e. global thresholding, has been documented in previous studies [52,153,188,189]. This approach is useful for the initial segmentation of the phases; however, it is not always very accurate where greyscale values of the component overlap. This can be due to either the phases with similar absorption or the artefacts or noise during the scanning. Hence, a conservative bulk threshold was used to segment the majority of the materials and the 'magic wand' tool was used to fine-tune the phases where grey values were similar [18,190]. A systematic approach with a slice-by-slice segmentation was used to ensure the validity of the phase separation throughout the volume. Although a robust segmentation approach was implemented, it is essential to note that the segmentations are sensitive to chosen threshold values, and these sensitivities can affect the valid bulk parameters [112,188].

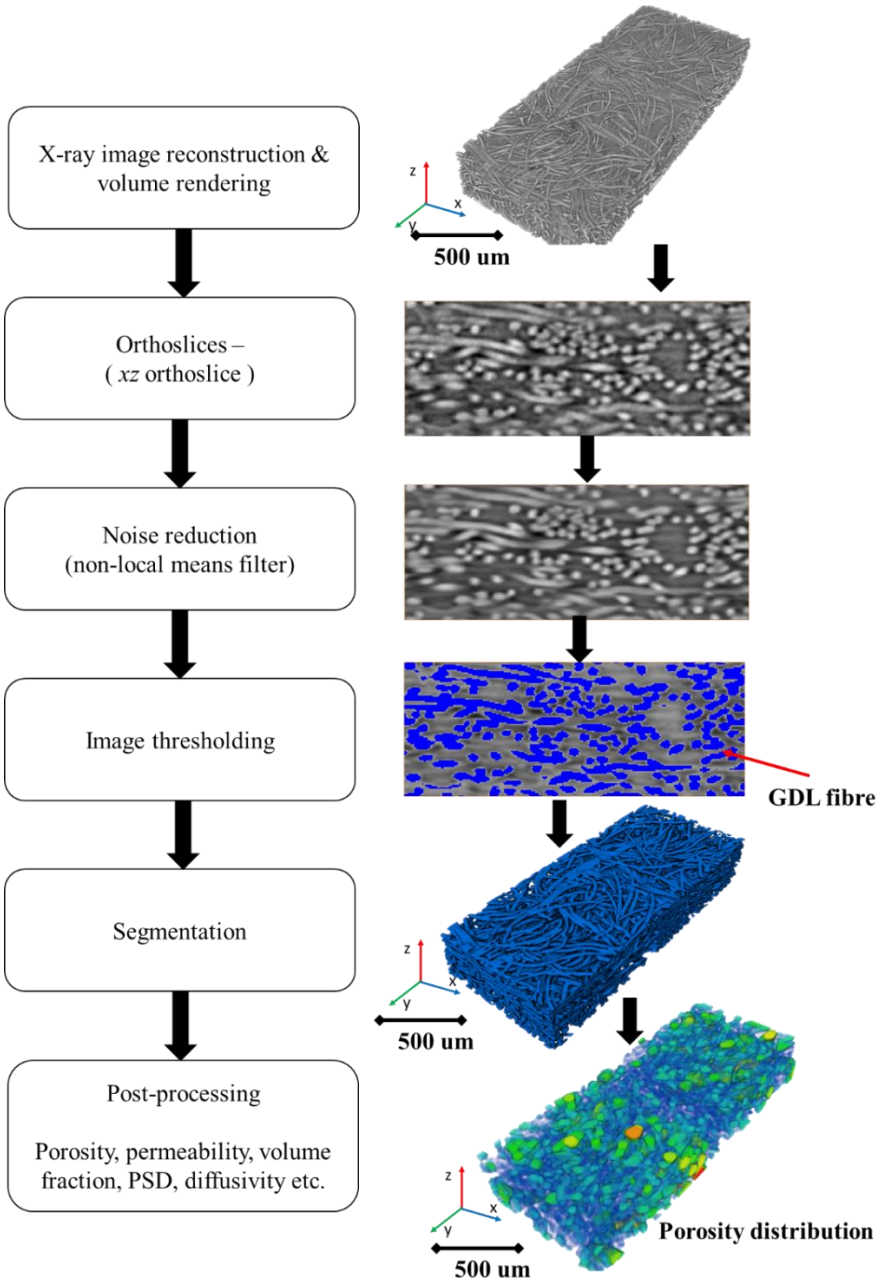

Figure 3.8–Image-based quantification of the effective properties was performed using Avizo Fire. Non-local means (NLM) filter was used in this study to mitigate the effect of image artefacts. Greyscale image thresholding was used for phase separation and segmentation. The segmented images were further used for image-based quantification.

The post-processing of the volume rendering data was performed using Avizo Fire (Thermo Fisher Scientific) and the geometrical calculations were calculated using Fiji/ImageJ open-source code, discussed in details in section 3.2.

3.2 Image processing and image-based quantification

3.2.1 Image processing software

The two-dimensional and three-dimensional images generated through neutron imaging and X-ray CT were post-processed using three software packages, namely Fiji (ImageJ), Avizo and MATLAB. This section provides brief information to these software packages.

3.2.1.1 Fiji (ImageJ)

ImageJ is a freeware developed by the National Institutes of Health, Fiji, (NIH, Maryland, USA). This is a standard open-source image-processing software tool based on Java with a long history of scientific image analysis [191]. This cross-platform compatible tool enables implementing issue-tailored plugins. In conclusion, an extensive collection of macros and plugins are already available, which can be used for the bespoke applications. Using ImageJ is, therefore valuable for the here-proposed open-source approach for visualising, pre/post-processing, aligning, and preparing the images from data acquired via various characterisation techniques used in this project [192].

3.2.1.2 Avizo

The visualisation, processing, filtering, registration, and 3D rendering of the generated X-ray CT data was carried out using Avizo 9.4/9.5 (ThermoFisher Scientific, Oregon, USA). This software allows the import of proprietary filetypes such as ‘.txm’ from the

lab-based X-ray CT instrument used in this research, as well as standard image formats such as .tif stacks. The bespoke filters such as “non-local means” and “unsharp masking” were used to denoise the images and improve the image segmentation ability [193,194]. The built-in registration module “Register Images” is also extensively used, which was applied after manually aligning 3D datasets close to their optimum alignment. More details can be found in the Avizo user guide [195]. Secondly, the algorithms such as local thickness mapping, volume fraction, image-to-stack density function, i.e. z-projection algorithms, were comprehensively used in to generate the result datasets.

3.2.2 Matrices

Various standard length, areal, and volumetric matrices can be obtained / extracted from 3D X-ray CT reconstructions. One of the most common matrices extracted from the 3D reconstruction is the volume data or phase fraction (V_{phase}). Phase faction can be calculated as the summation of all the assigned segmented voxels divided by the total number of voxels in the entire volume, given by:

$$V_{phase} = \frac{N_{phase}}{N_{total}} \tag{3.2}$$

where N_{phase} is the number of voxels assigned to the particular phase, and N_{total} is the total number of voxels. The volume fraction on the empty phase or air phase is termed as the porosity (ε) of the domain that determines the effective transport properties in the fuel cell, as discussed in Chapter 2. The volume fractions of the solid phases give the idea of % composition of the heterogeneous material and could be useful deriving the advanced matrices from the reconstructed data such as triple point boundary.

Similar to the volume matrix, spatial surface information can also be derived from the 3D reconstructed volumes. In this work, the information derived from the surface data is used to investigate the distribution of the material fraction and the porosity along the

width of the fuel cell. This gives the detailed map of the porosity and volume fraction distribution of the porous material, under the influence of fuel cell architecture and the assembly process.

3.2.3 Representative elementary volume (REV)

The porous materials in the fuel cells are inherently heterogeneous; hence, it is essential to assess the validity of sub-sectional datasets to determine whether the dataset adequately represents the macroscopic properties of the entire domain. Various techniques have been adopted in the literature to perform REV, that includes a growing cuboid approach [196,197]; multiple sampling regions [118,198], or statistical correlation methods.

In this research, the MATLAB-based The open-source software ‘Taufactor’ was used to determine the REV using tortuosity factor and porosity [197,199]. Here, to determine the REV, the thickness of the top GDL was kept constant while changing the volume, which is the z-constant algorithm (Figure 3.9). This method was chosen due to its ease-of-use and to retain consistency in approach.

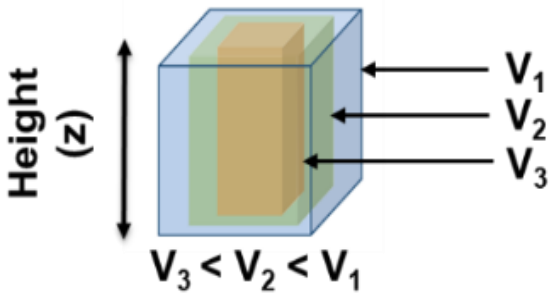

Figure 3.9–Height (z) constant REV algorithm

3.3 Conclusion

In this chapter, three main experimental characterisation and diagnostic techniques used in present research was explored, namely, polarisation curve, Neutron radiography and X-ray computed tomography. The chapter also provides the details of MEA fabrication methodology adapted during this project. Additionally, the basic theory behind X-ray imaging, microstructural characterisation using computed tomography and in-situ visualisation techniques such as neutron imaging was explored in this chapter. Finally, image processing and image-based quantification techniques were described. The following chapter is the first of the results chapters and describes experiments carried out in a lab-based CT system, where numerous image-based quantification techniques described here were applied.

Chapter 4
Microstructural study of the non-uniform compression of MEAs

Abstract

The performance of PEFCs is governed by a complex interaction of the structure of the membrane electrode assembly (MEA), cell compression, and operating parameters. Adequate cell compression for improved current collection and gas sealing can structurally deform MEA with adverse consequences. Non-uniform MEA compression exerted by the flow-field design and arrangement induces heterogeneous transport properties. Hence, understanding morphological evolution and effective transport properties as an effect of MEA compression is an important factor for improving fuel cell performance and durability. In this paper, an X-ray computed tomography study of the entire MEA compression is presented, comprising of gas diffusion and microporous layers, catalyst layers, and the electrolyte membrane, subjected to non-uniform compression under two distinct flow-field arrangements. This study presents a comprehensive dataset of the non-uniform effective properties required for robust computational modelling; including porosity, permeability, tortuosity, and diffusivity, along with the extent of blocking of the flow channel due to cell compression and effect of compression on the structural properties of the membrane.

4.1 Introduction

Chapter 3 discussed the importance of effective parameters on defining PEFC performance. These effective parameters are affected by the way in which the flow-fields are designed, and the cell is mechanically compressed [57,200,201]. Significant research has focused on flow-field designs to ensure even reactant distribution over the active area of the cell, adequate removal of product water, and effective current collection [13,56,135,202]. The majority of systems are dependent on the primary flow-fields that vary in shape, dimension, orientation, and configuration, some systems rely on the reactant flowing laterally through the gas diffusion layer (GDL), taking advantage of the 'secondary' flow-field, specifically the narrow gap between the GDL and the sealing gasket [103,152,203,204]. The effect of non-uniform compression on the fuel cell performance and the GDL morphology has been discussed in details in Section 2.4.1. As discussed previously, multiple researchers have used the non-destructive X-ray CT approach to evaluate the effect of compression on the GDL. Atkinson et al. showed a nonlinear relationship between GDL compression and PEFC performance [122]. Nitta et al. highlighted the nonlinear effect of compression on the electrical contact resistance [126], while, similarly, Ge et al. showed that compression has a significant effect on performance at higher current density, where mass transport becomes critical [46]. Mass transport in the fuel cell, specifically reactant diffusion and liquid water transport through the capillaries, is governed by the materials used in the critical components of the MEA and their morphology (e.g., porosity, tortuosity, pore size, and level of deformation). In order to fully understand and optimise the assembly of these components, specifically under compression, it is essential to effectively determine these parameters and quantify their effect on cell performance. Zenyuk et al. used X-ray computed tomography (CT) to evaluate multiple commercial GDLs under uniform compression, showing decreasing porosity and pore sizes [205]. Tötzke et al. expanded the study by examining the differences between uniformly and non-uniformly compressed GDLs [206]. Non-uniform compressions come from the design

of the flow-fields, often composed of discrete channel and land zones. Compression by these corrugations leads to constriction of the GDL under the lands and potential protrusion of the carbon fibres into the active channels. This phenomenon, referred to as ‘tenting’, can result in partial blocking of the primary flow-fields [109]. Lu et al. highlighted that the flow-field arrangements could affect the structural stresses in the MEA, potentially leading to anisotropic deformation of the membrane [139]. This deformation may induce cracks in the catalyst and microporous layer, which will affect the performance and durability of the fuel cell [207,208].

X-ray CT, used in conjunction with computational modelling, has expanded the understanding of crucial processes taking place inside fuel cells [111,189,209–214]. The technique has been useful particularly for examining the effect of compression on PEFCs, but the majority of the studies have focused on the GDL under even compression [47,119,205,215,216], and ignored the effect of compression on other layers of the MEA that play a critical role in the fuel cell performance. Therefore, in this chapter, the entire MEA under non-uniform compression exerted by multiple flow-field arrangements is considered. This work aims to provide a comprehensive data-set of structural and morphological properties of the entire MEA and derive effective parameter values that can be used as inputs to computational models of PEFC performance. Importantly, the study examines not only ‘symmetrical’ compression, where the land and channel on both sides of the MEA are correctly aligned, but also ‘asymmetrical’ compression where a flow-field channel is only present on one side, as in the SFF dominated designs [103,104,217].

4.2 Experimental

In this work, two commonly used flow-field arrangements were compared, namely symmetrical and asymmetrical flow-fields (Figure 4.1(a and b)). The symmetrical flow-field is comprised of parallel flow channels on either side of the MEA [127,218,219];

whereas asymmetrical flow-field arrangements have a flow channel on one side of the MEA with a flat plate on the other side [104,220].

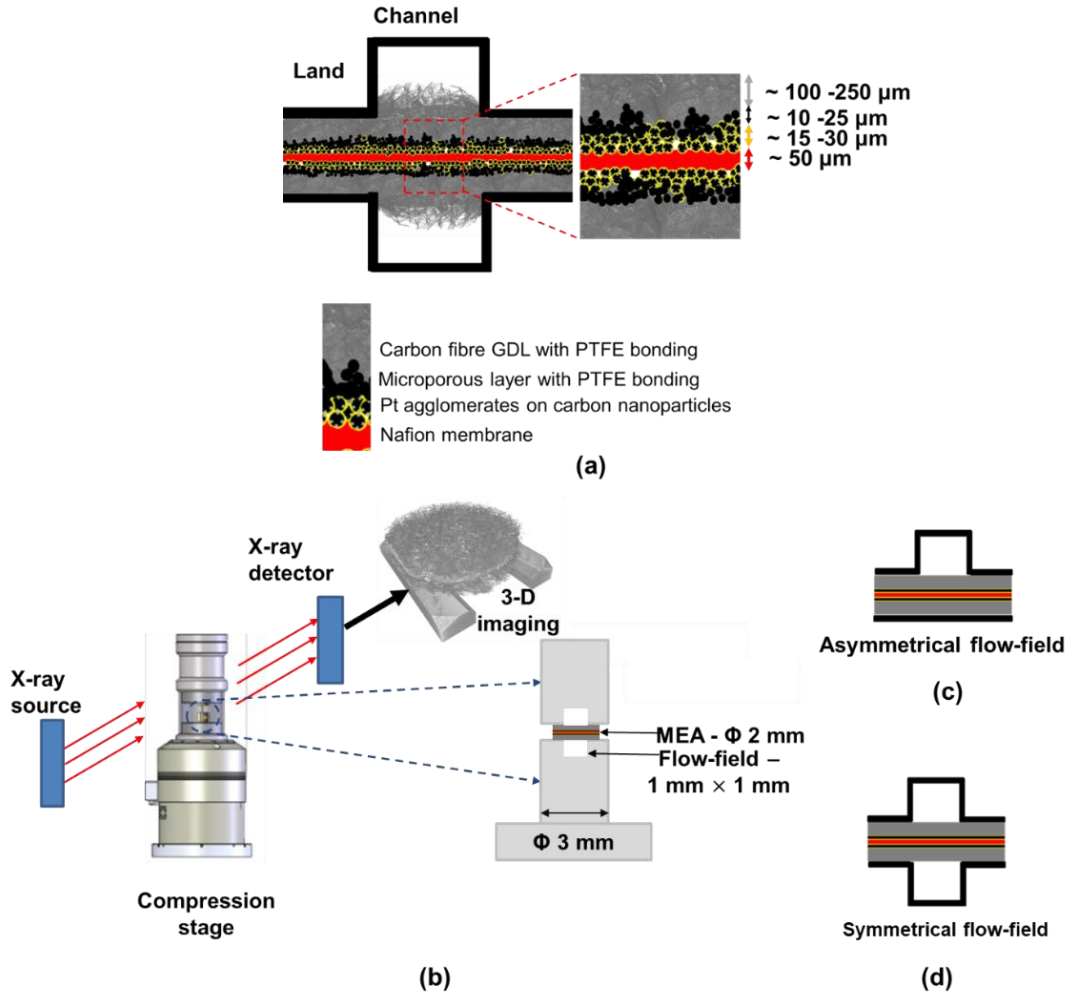

Figure 4.1– (a) Schematic of the MEA compression with partial blocking of the flow-field channel by the GDL, the interface between individual components and their typical thicknesses (not to scale); (b) imaging set-up with the compression stage; (c) asymmetrical flow-field, and (d) symmetrical flow-field arrangement.

The MEA was prepared as per the method discussed in section 3.1.1. The in-situ compression rig (MICROTEST 5 kN, Deben, UK) (Figure 4.1(b)) offers compression by displacement through the movement of the bottom piston towards the fixed upper

plate. In this study, four different compressions were imposed on the entire MEA ranging from 0% (no compression) to 60% compression, in steps of 20%. Separate experiments were carried out for each flow-field arrangement, using freshly prepared MEA samples.

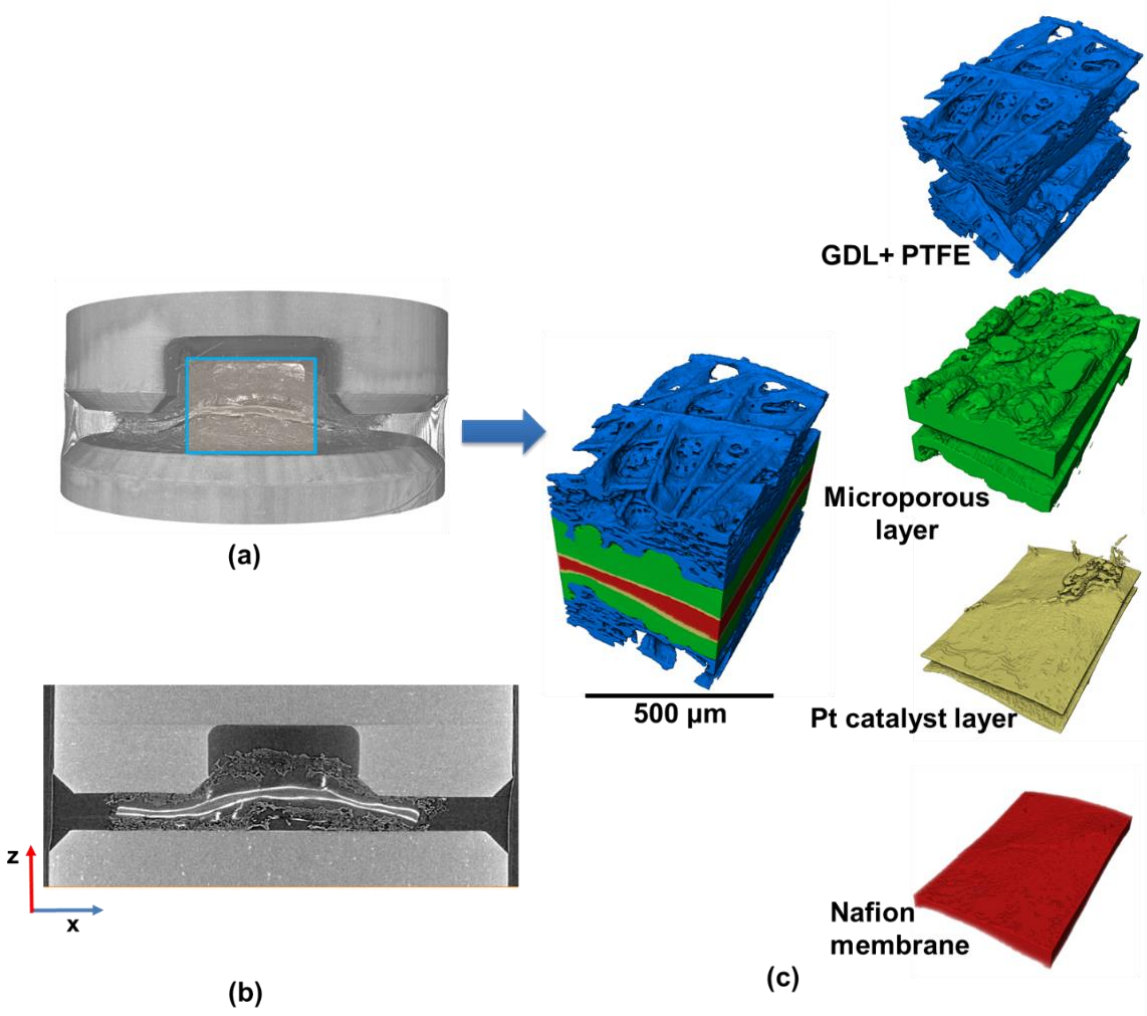

Figure 4.2– Image visualisation and segmentation (a) 3D rendering of the reconstructed greyscale data for 60% compression in the asymmetrical arrangement; (b) greyscale ortho-slice showing an *xz*-plane; and (c) volume rendering of the segmented data with an exploded view of each separate layer in the MEA. The colour legend used for the segmented images is common throughout the thesis.

X-ray tomographs of the sample were obtained using a laboratory-based X-ray CT system, ZEISS Xradia 520 Versa (Carl Zeiss). The details of the instrument, the experimental methodology and image post-processing techniques are presented in Chapter 3. Figure 4.2 shows the volume rendering image of the entire MEA with individual phase segmentation. Each sample image was segmented into five distinct phases; specifically the carbon fibre GDL and PTFE binder phase (blue), the microporous layer (green), the catalyst layer (yellow), and the Nafion membrane (red). The void space forms the fifth phase but is not shown in the 3D rendering for clarity. (Figure 4.2(c))The *z*-direction passes through the thickness of the MEA and is the direction in which the compression was applied.

4.3 Results and discussions

In this section, the X-ray CT analysis of the compressed MEA is presented. The influence of non-uniform compression exerted by flow-field arrangements on the morphology of the MEA is evaluated. The qualitative and quantitative analysis generates a database of the effective parameters required for the numerical modelling of PEFCs.

4.3.1 Representative elementary volume (REV)

The characteristic properties of the compressed MEA are non-homogenous and differ between the channel and the land areas. To better understand the smallest volume at which the effective properties are representing that of the sub-domain, a discrete representative elementary volume (REV) analysis has been applied to the GDL under the sub-domains as shown in Figure 4.3. The smallest volume above which the standard deviation of the properties is lower than 5% is defined as the REV. The REV is above 70% of the entire sub-domain, i.e. under the land and the channel.

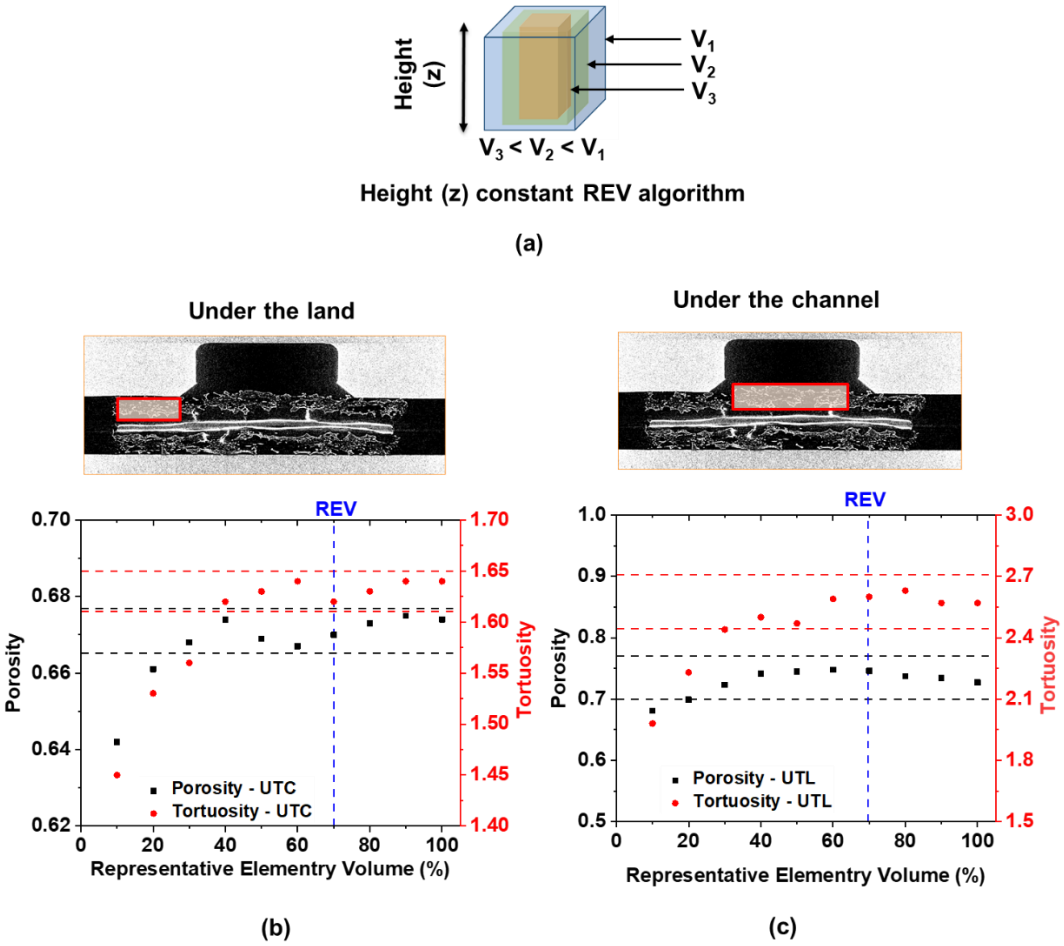

Figure 4.3– Determination of the representative elementary volume (REV) for uncompressed (0% compression) carbon-fibre commercial GDL (HyPlat, South Africa) under the land and the channel, based on tortuosity factor and porosity (a) height (z) constant algorithm that changes volume keeping height of sample constant; (b) REV analysis for the sub-domain under the land; (c) REV analysis for the sub-domain under the channel. (Black and red dash lines highlight the region of acceptable standard deviation for a material fraction and tortuosity factor, respectively and the blue vertical dashed line represents acceptable REV, i.e. above 70% of the maximum volume available.)

4.3.2 Material fraction

The solid phase fraction describes the distribution of an individual phase across the normalised thickness (Figure 4.4). A thickness of zero represents the bottom of the subdomain, while one represents the top. Depending on the location of the subdomain, this could be the interface between the GDL phase and air in the channel or the GDL phase and the piston.

The catalyst layer and the membrane were relatively unaffected by arrangement and sampling location. A number of phases experience significant overlap. During the manufacturing of the gas-diffusion medium, the catalyst ink is deposited on the microporous layer. The ink penetrates into the microporous layer, leading to the phase overlap. This overlap remains relatively unaffected by the compression and arrangements.

Secondary overlap exists between the microporous layer and carbon fibre GDL. At 40% compression, irrespective of the arrangement, the entire microporous layer invades 65% of the GDL phase under the land (Figure 4.4(c and d)), and approximately 52% under the channel (Figure 4.4 (e and f)). The extent of MPL intrusion into GDL carbon fibres is mostly dependent on the material recipe, fabrication process, and the method of MPL deposition onto the carbon fibres. These complex interactions between the GDL and the micro-porous layer have been previously reported by Odaya et al., Atkinson et al. and García-Salaberri et al. for carbon fibre GDLs [118,122,210].

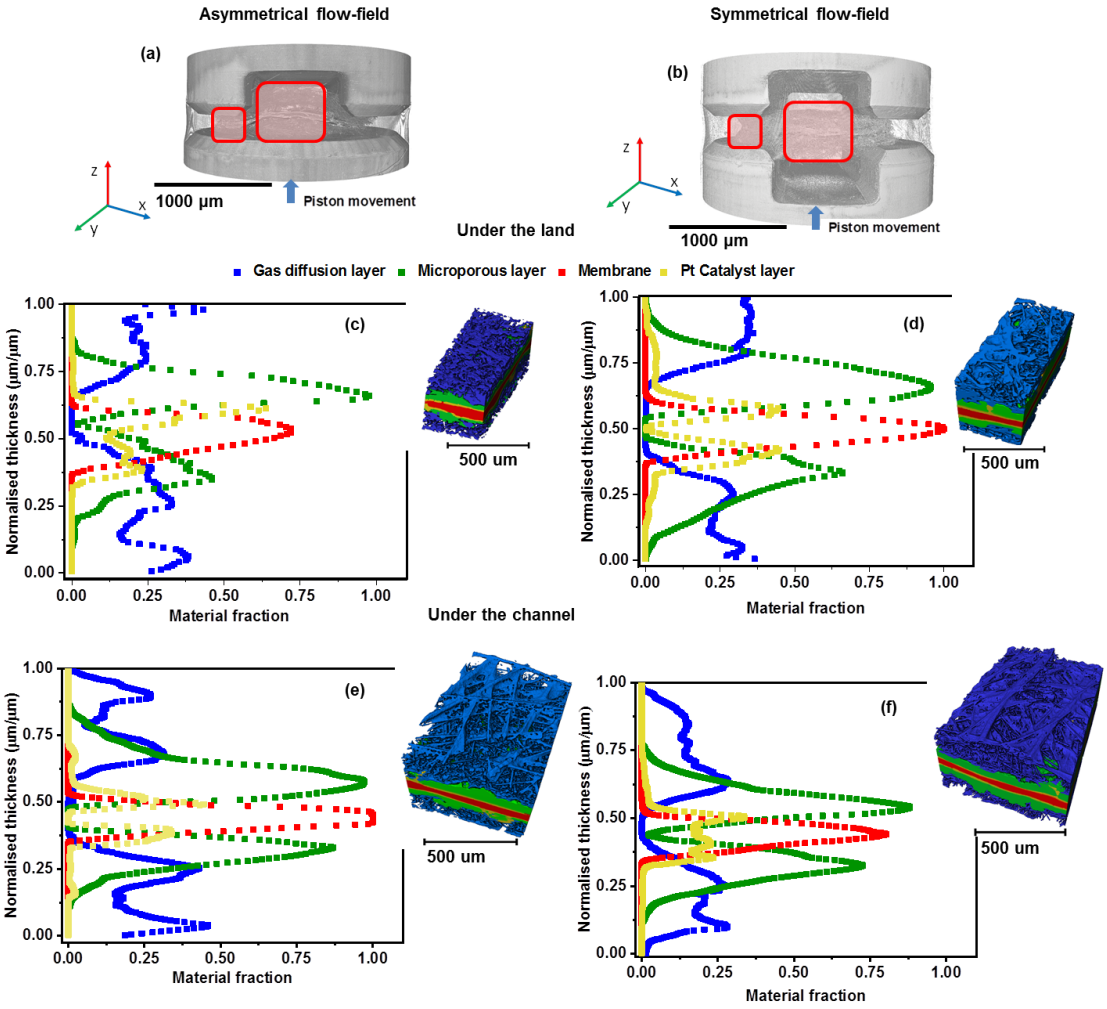

Figure 4.4– X-ray CT of 40% compression revels solid-phase material fraction of the individual phases along the normalised thickness (z-direction) (a,b) volume rendering image of asymmetrical and symmetrical arrangement; (b,c) solid-phase material fraction under the land at 40% compression; (e,f) solid-phase material fraction under the channel; and (g,h) change in the solid fraction of the GDL along the thickness under the channel with an increase in the compression from 20% to 60% at the asymmetrical and the symmetrical flow-field arrangement, respectively.

Depending on the arrangement, the overlap behaved differently on either side of the membrane. Relatively uniform overlap was observed in the symmetrical arrangement, while in the asymmetrical arrangement, the overlap was 25% higher in the bottom region of the subdomain. This was due to the restricted space offered by the

asymmetric arrangement, which prevented the expansion of the GDL on the bottom side of the sample.

The GDL thickness distribution forms a characteristic 'W' shape due to inherent heterogeneities incurred during the fabrication process. Previous 'GDL only' studies on Toray carbon fibre paper, as well as fibre-based, felt type Freudenberg GDL had seen similar results [112,113,210]. Fishman et al. attributed this behaviour to the 'ply moulding process' commonly used in GDL fabrication [53], where others have suggested this could be due to the typical agglomeration of the binder and PTFE in the gas diffusion layer [210]. This characteristic is less pronounced under the land, possibly due to the preferential realignment of the GDL fibres under compression.

Figure 4.5(a and b) shows the change in GDL material fraction with compression for the subdomain under the channel. At lower compression (20%), the fibres spread relatively evenly on either side of the membrane, independent of arrangements. With the asymmetrical arrangement, the previously explained restricted expansion results in distinct fibre density distributions on either side of the membrane. For the symmetrical arrangement, the GDL expands into the channels with compression in both directions, lowering the solid phase volume on either side of the membrane. The manufacturing heterogeneities in the gas diffusion medium, such as large pores and PTFE loading, may affect the microstructural behaviour of the sample at higher compression by the augmentation of the space between the GDL's fibres near large pores (Figure 4.5(b)) [47,122,205,221–223]. The *xz*-ortho-slices in the detailed view give a pictorial representation of the compressed sub-domain under the channel.

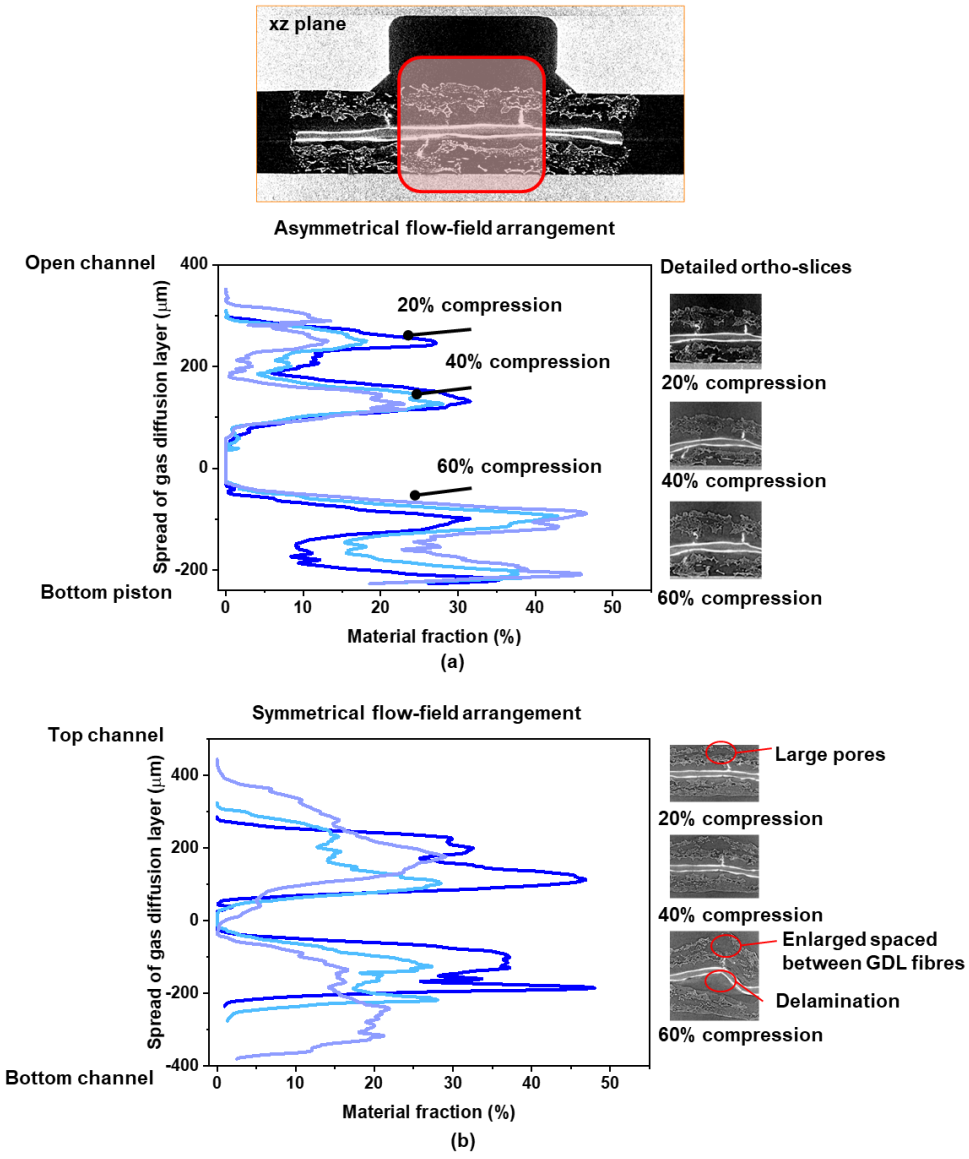

Figure 4.5– Change in the solid fraction of the GDL along the thickness under the channel with an increase in the compression from 20% to 60% at the asymmetrical and the symmetrical flow-field arrangement respectively.

4.3.3 Partial blocking of the flow-field and membrane deflection

X-ray CT ortho-slices, shown in Figure 4.6(a and b), illustrate the effect of compression on the vertical and lateral deformation of the GDL. The vertical deformation clearly shows the GDL protruding into the flow channel, potentially blocking the primary flow-field. The lateral deformation of the GDL leads to partial blocking of the secondary flow-field. The extent of the blocking was calculated as the reduction in void volume in the flow-field.

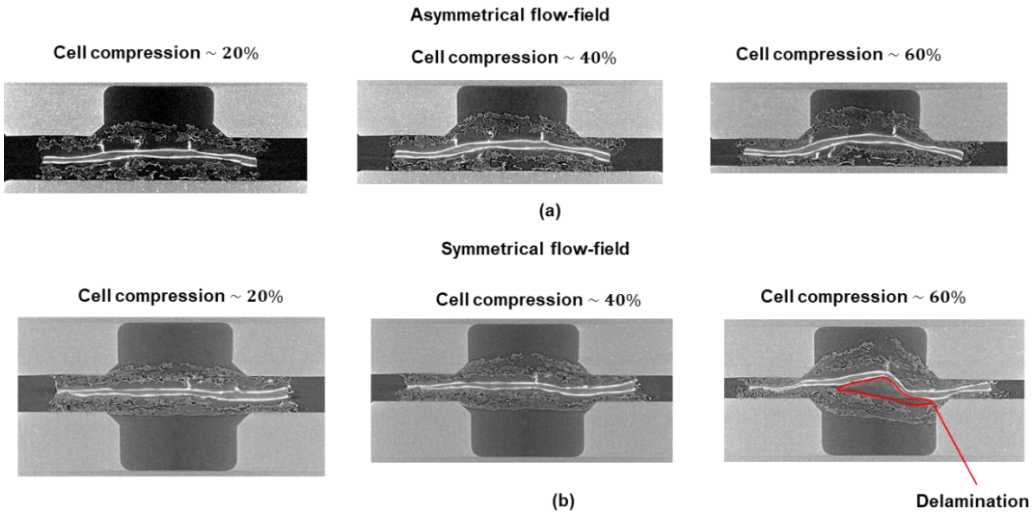

Figure 4.6– Partial blocking of the active flow channels, ortho-slices showing partial blocking of the flow-field with compression at (a) the asymmetrical flow-field and (b) symmetrical flow-field, measured at 20%, 40% and 60% cell compression. Note: At 60% compression in symmetrical flow-field, the top piston laterally slipped by 60 µm inside the compression stage.

The degree of blocking of the primary flow-field was affected by both the arrangement as well as the degree of compression (Figure 4.6 (a)). In the asymmetrical case, 45% of the primary flow-field was blocked; versus 25% of the total channel space in the symmetrical arrangement (15% top and 10% bottom) was blocked. These measurements were made at the typical case of 40% compression. GDL deformation in the secondary flow-field was primarily caused by compression, while the flow-field

arrangement did not play a key role (Figure 4.7(b)). The deformation increased with increasing compression.

Figure 4.6(a and b) also shows the effect of the compression and the different arrangements on the membrane deformation. To the authors' knowledge, this is the first time that the X-ray CT has been used to quantify the effect of the arrangement on the structural deformation of the membrane under compressive load, in isolation from chemical / hygro-thermal stresses [139,224,225].

Here, membrane deflection refers to non-uniform deformation of the membrane. This phenomenon can be seen clearly on the far right of Figure 4.6(b), 60% compression. The deflection was quantified as the vertical distance between the initial and final mid-plane position of the membrane, correcting the bottom piston's movement. Membrane deflection was significant under the asymmetrical arrangement, mainly due to restricted compression of the GDL on the opposite surface. Conversely, in the symmetric arrangement, the GDL is able to expand in both directions, leaving minimal membrane deflection until extreme compressions (Figure 4.7(a)).

Under 60% compression, the symmetric arrangement experienced misalignment, shifting by 60 µm. This resulted in the membrane deflection increasing by 30% as well as the sample delamination, as shown in the highlighted view of Figure 4.6(b). Therefore, the membrane deflection is not only subject to the flow-field arrangement and compression, but also to the accuracy of the cell assembly process (Figure 4.7(c)).

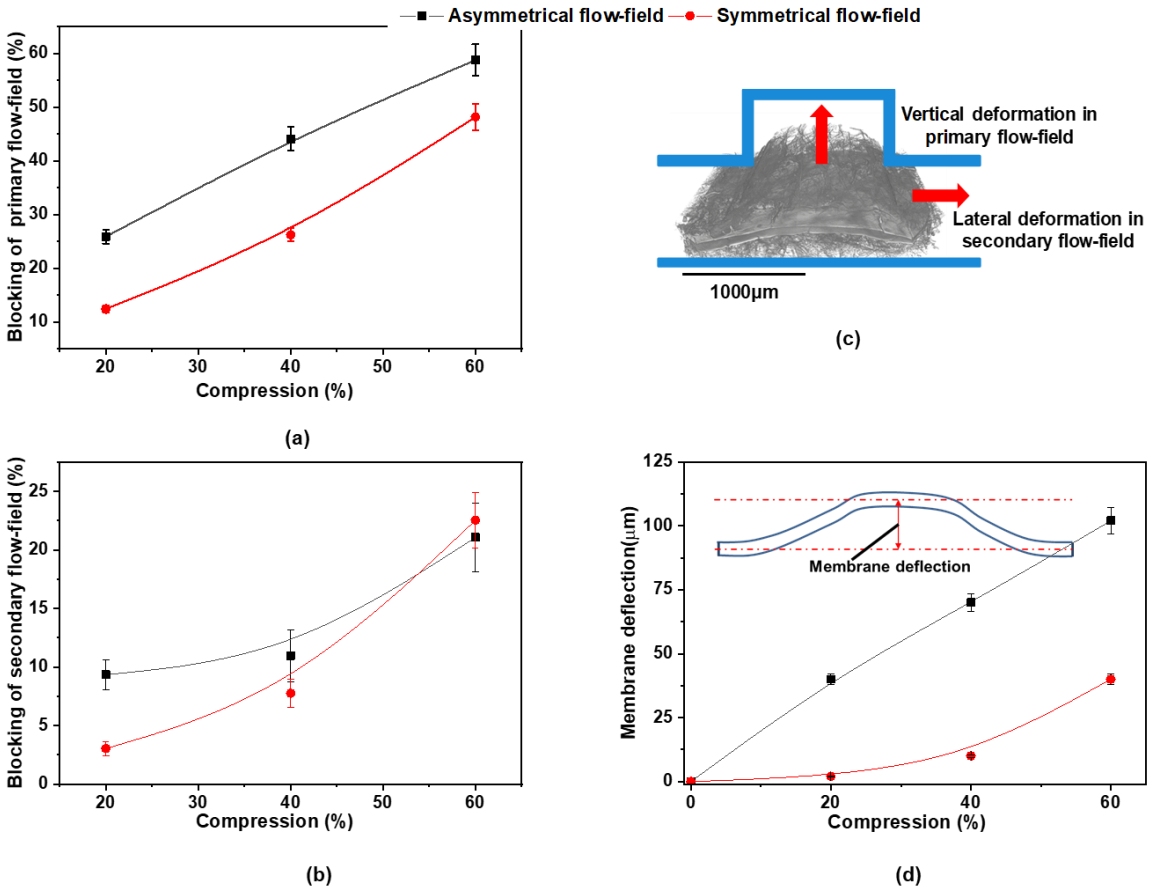

Figure 4.7– Extent of blocking of the active flow-fields (a) partial blocking of the primary flow-field, (c) partial blocking of the secondary flow-field, (d) schematic of MEA deformation in vertical and lateral direction, (d) quantification of membrane deflection in +z direction. Membrane deflection schematic shows the location where membrane deflection was measured. B-spline passing through the data points is included as a guide to the eye. Note: At 60% compression in symmetrical flow-field, the top piston laterally slipped by 60 µm inside the compression stage.

4.3.4 Structural thinning of the membrane

The localised membrane thickness was calculated based on the local thickness method derived from the binary image; defined by the diameter of the largest sphere, that entirely fits in the domain (Figure 4.8(a)). A region where a distinct membrane

phase could not be segmented, i.e. the thickness was below the material resolution, was not considered and appeared white Figure 4.8(a).

Non-uniform compression exerted by the flow-fields results in localised membrane thinning. There was an inherent initial membrane thickness distribution (at zero compression) with a standard deviation of 25.99 µm and 25.76 µm (average thickness of 45.6 µm and 43.04 µm) for the symmetrical and asymmetrical arrangements, respectively. This is a consequence of the MEA fabrication process, where the hot pressing results in varying levels of impregnation of MPL/GDL into the membrane, as identified in previous studies [115,153].

The change in membrane thickness was quantified by using a chord length function [226]. Chords refer to the straight lines drawn at each membrane voxel element, and their length represents the membrane thickness at particular coordinates. The resulting probability density function distribution can be seen in Figure 4.8(b) for the asymmetrical and Figure 4.8(c) for the symmetrical arrangements. The peak of every distribution represents the expected thickness of the membrane at any given location. Two distinct peaks in the thickness distribution could the collective consequence hot-pressing conditions and inherent variation in the membrane thickness [115].

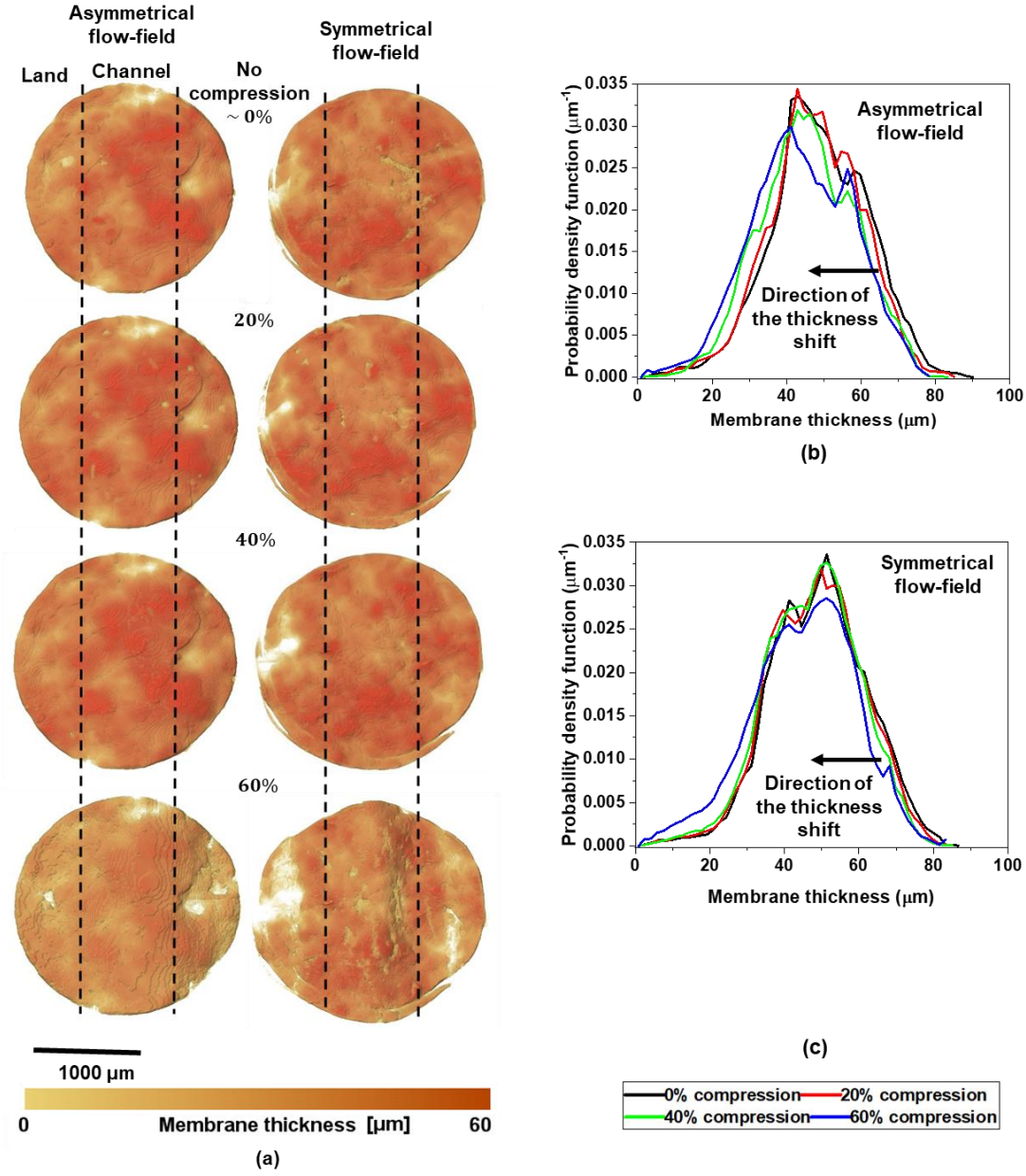

Figure 4.8– Thinning of the membrane; (a) thickness map of the membrane as a function of compressive load comparing the two different flow-field arrangements, the perforated black line represents the division between the land and the channel regions; (b) thickness distribution in the membrane subjected to asymmetrical cell compression; (c) thickness distribution in the membrane subjected to symmetrical cell compression

Comparative illustrations of the change in membrane thickness measured under the channel and land region are shown in Figure 4.9. No noticeable change in the membrane thickness was observed under the channel, irrespective of the arrangements but significant membrane thinning was detected under the land. At the typical case of 40% compression, the membrane thinning measured under the land was 6%, regardless of the arrangements. This increased to 7.5%, again, regardless of the arrangement, at 60% compression; suggesting that the overall thickness of the membrane under the land reduces with compression. This has not been previously observed in-situ through X-ray CT.

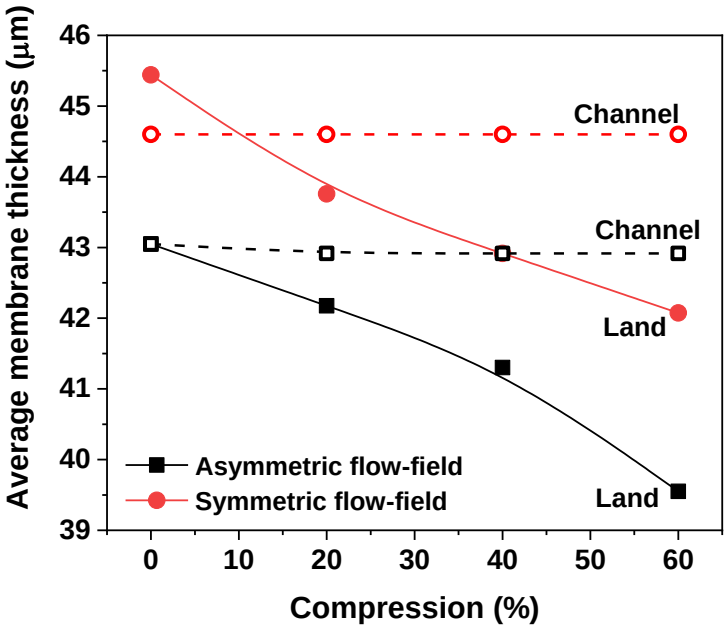

Figure 4.9– Overall reduction in average membrane thickness measured under the land and under the channel. ○ represent symmetrical and □ represent asymmetrical arrangement, the 'solid' points represent under the land and open points represent under the channel subdomain. B-spline passing through the data points is included as a guide to the eye.

The thickness of the membrane can significantly affect cell performance. A thinner membrane exhibits lower Ohmic losses, while also needing lower cell humidification due to a higher rate of water back-diffusion. At the beginning of a cell's life, these properties will improve cell performance; however, a thinner membrane will also be subjected to higher gas crossover and overall inferior mechanical durability. The rate of electrochemical degradation of the membrane is also a function of its thickness. Thinner membranes are subjected to higher in-situ stresses leading to membrane cracking and pinning, further increasing degradation. Similarly, irregularities in the membrane thickness would result in unbalanced behaviour of the aforementioned properties, inducing higher stresses on the mechanical structure of the membrane.

The initial irregular thickness of the membrane and the thinning under compression would affect the transport properties required for the robust modelling of PEFC systems. For example, the gas crossover is inversely proportional to the membrane thickness [100]. Therefore, if the cell is compressed at 40% under the symmetrical arrangement, 6% thinning in the membrane thickness under the land would increase the rate of the gas crossover under the land region. Similar data derived from these results would help to fine-tune the membrane parameters required for continuum modelling.

4.3.5 Contact surface area

The 3D reconstructed volume provides information regarding the effect of the compressive load on the interfacial contact between GDL fibres and the current collector (aluminium piston). The electrical contact resistance was determined by the surface area and the 'quality' of the contact. This is affected by force exerted between the contacting layers that, along with the nature of the materials, influence the surface contact resistivity. The contact resistance is given by [227–229]

$$R = \sum_{surfaces} \left(\sum_{i=1}^{n} \frac{A_i}{\rho_i} \right)^{-1} \tag{4.1}$$

where *R*, *A*, and *ρ* are the contact resistance, accumulative contact area, i.e. quality of contact and the interfacial contact area between fibre and piston, and the resistivity of the contact element, respectively. Increase in compression improves not only the quality of contact between adjacent fibres that improve charge transport capacity but also increase the interfacial contact area between the piston and GDL fibres. The contact resistance is inversely proportional to the accumulative contact area. Therefore, an increase in contact area reduces the contact resistance by the same factor.

The *xy*-ortho slices shown in Figure 4.10(a) illustrate that the GDL phase density increases with compression when measured under the land. Increased fibre packing density increases interfacial contact between GDL fibres and the piston (current collector) as well as between adjacent GDL fibres. In the present study, the contact area was calculated as the interfacial surface area adjacent to the piston. The contact area was quantified at the region highlighted in red in Figure 4.10(b). For a fair comparison between arrangements, the bottom contact area highlighted in green was not considered in the analysis.

For the symmetrical arrangement, the contact area increases by approx. 1.2 mm^2 with compression (Figure 4.10(c)). Similar observations have been reported in the experimental and modelling studies by Ihonen et al. and Zhou et al. [106,230]. For the asymmetrical arrangement, higher GDL tenting results the fibre reordering under the land as well as under the channel. This increases the interfacial contact area between the channel surface and the GDL fibres concluding in exponential (11%) increase in the contact at higher compression.

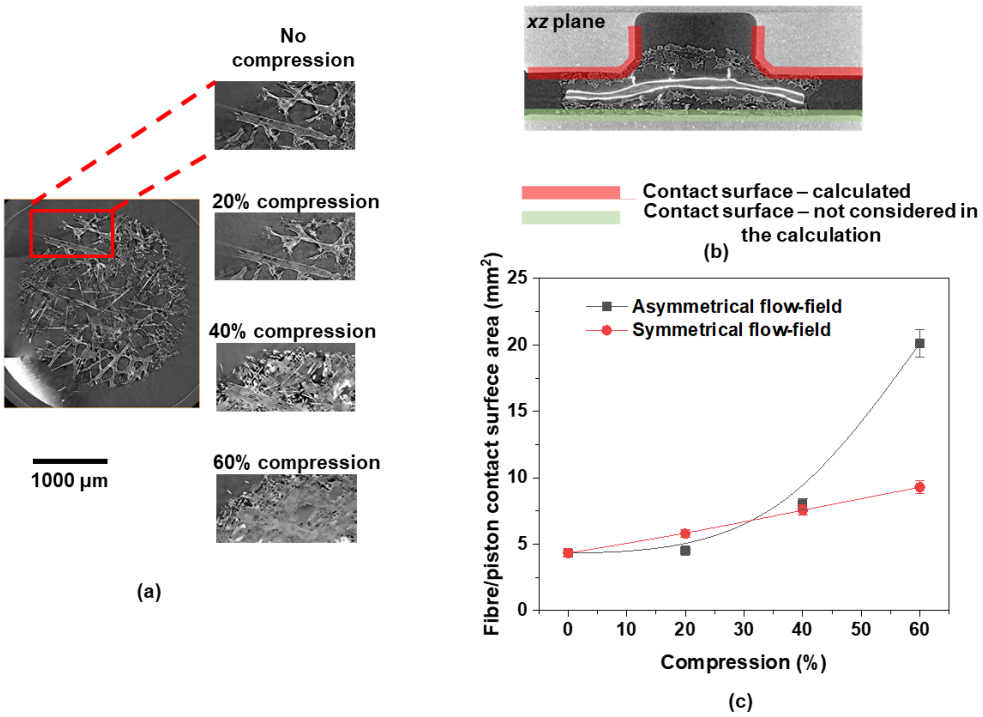

Figure 4.10– Effect of compressive load on the contact surface area between the current collector (piston) and GDL fibres; (a) ortho-slice showing the interfacial surface for the asymmetrical flow-field, the area under the red square shows increase in fibre phase density with compression; (b) the contact sub-domain of GDL fibres and the top piston (red) was considered for the quantification of the contact area, and (c) the change in interfacial contact area between GDL fibres and piston with compression. B-spline passing through the data points is included as a guide to the eye.

Higher contact area results in a subsequent improvement in charge transport and current collection performance at the cost of a reduction in the free-flow area for the reactant. Hence, the combined effect of the compressive load on the change in the interfacial contact area should be considered as a design parameter while designing the flow-field architecture. Moreover, the flow-field arrangements distinctly affects the contact surface area, mainly at higher compression. This emphasises the importance of using adequate flow-field arrangements during contact resistance measurement experiments.

4.3.6 Effective parameters

Most continuum models predicting PEFC performance rely on a single value of the effective parameters to analyse the mass transport properties of the diffusive media. GDL fibre alignment, non-uniform compression and flow arrangements result in spatial variations in effective properties. These values are crucial, mainly in two-phase models, where liquid water generation, accumulation, and super-saturation are predicted. In this section, the spatial effective properties that define the reactant transport in the porous domain are discussed. The datasets presented here can be used as the input parameters for the computational modelling of PEFC performance.

4.3.6.1 Porosity

The porosity distribution affects mass transport in the fuel cell, thus the PEFC performance [45,210,228,231]. Both the bulk and spatial porosity distribution should be considered during GDL selection and computational modelling of PEFCs. Figure 4.11 and Figure 4.12 show the effect of the compression and different arrangements on the bulk and spatial porosities of the sample, respectively. Bulk porosity is calculated as the volume fraction of empty pores in the domain; whereas spatial porosity is the void fraction of the ortho-slices in particular directions.

In under-the-land region, fibre packing density increases with compression. This lowers the bulk porosity by 40% and 50% (at 40% compression) for symmetrical and asymmetrical arrangements, respectively (Figure 4.11 (a)). In contrast, the GDL tenting under the channel results in a linear increase in bulk porosity with compression. The initial porosity of 45% increases to 67% with compression, irrespective of the arrangement (Figure 4.11 (b)).

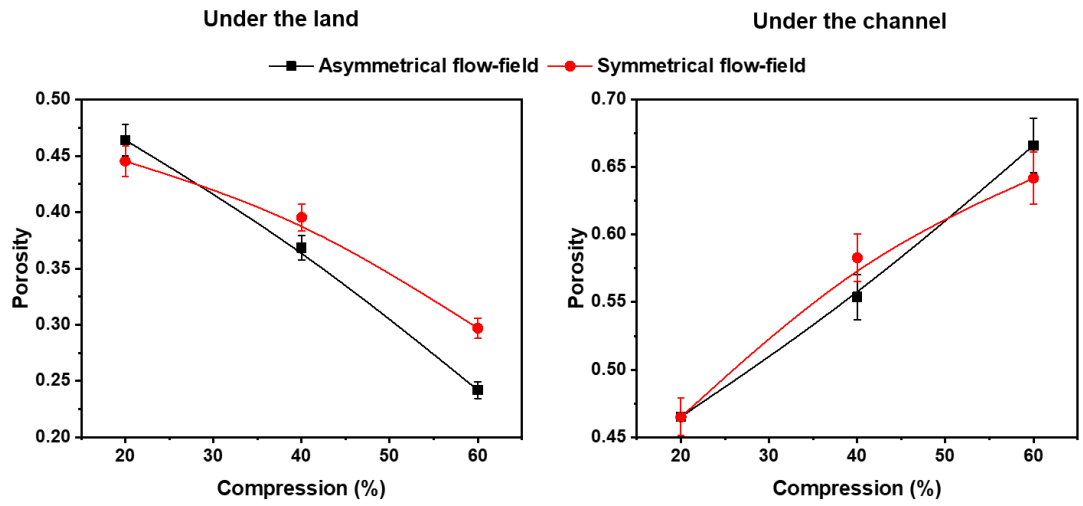

Figure 4.11– The effect flow-field arrangement on the bulk porosity, symmetrical (red) and asymmetrical (black) flow-fields, (a) bulk porosity under the land; (b) bulk porosity under the channel. Bulk porosity is a ratio of void phase voxel to the total number of voxels. The spline passing through the data points is included as a guide to the eye.

Figure 4.12(a and b) illustrate in-plane porosity variation at 40% compression, measured at *yz*-ortho-slices along the width of the sub-domains. This remained almost constant with a standard deviation of 1.2% under the channel and 0.98% under the land, irrespective of the arrangement. The average in-plane porosity matches well with the bulk porosity value.

The through-plane porosity is a function of the material fraction distribution along the normalised cell thickness (Figure 4.12(c and d)). The location of catalyst layers, microporous layers, and the membrane correspond to the lowest through-plane porosity region. Uniform porosity distribution, irrespective of the arrangement, was observed under the land. However, the through-plane porosity distribution under the channel was affected by the arrangement. The uniform distribution was observed in the symmetrical arrangement, contrasting to the distribution at the asymmetrical

arrangement. Comparatively lower through-plane porosity on the bottom side of the membrane at the asymmetrical arrangement was a function of the restricted GDL expansion on the bottom face.

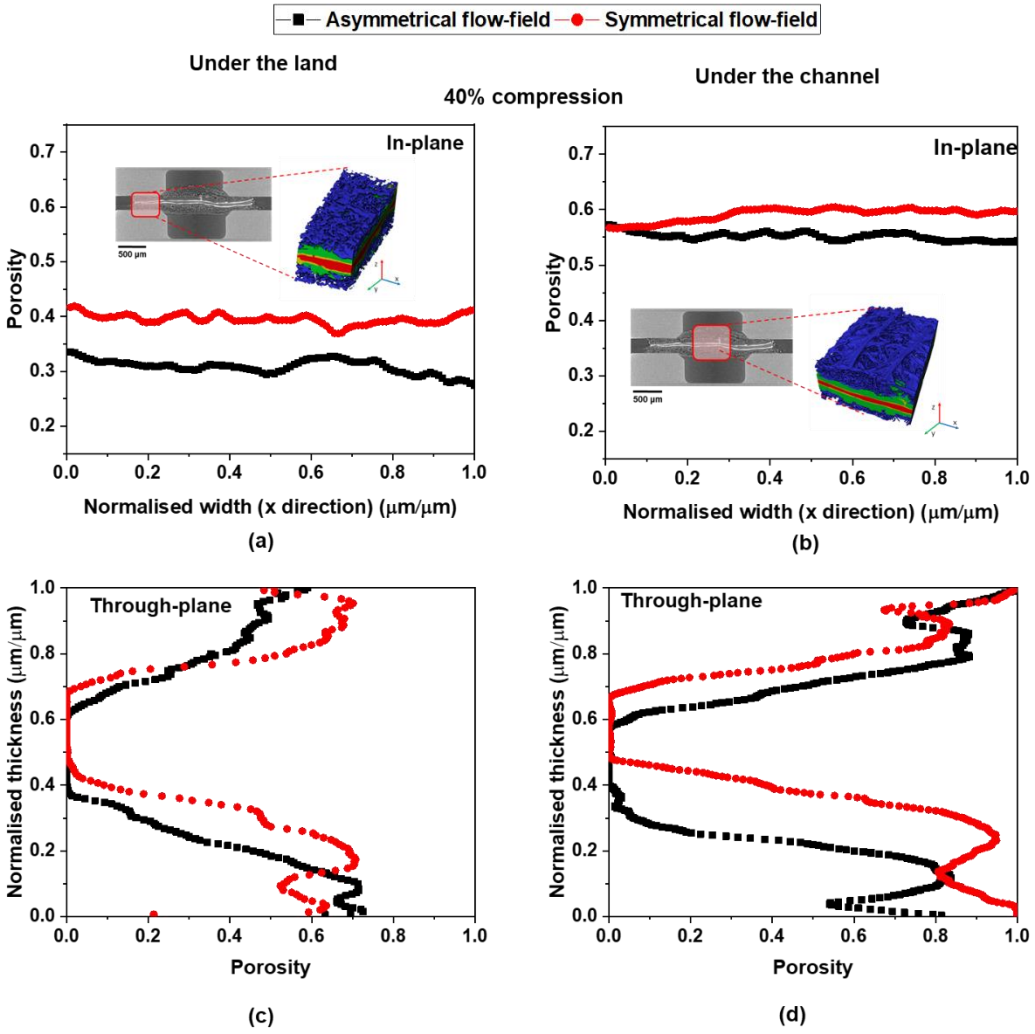

Figure 4.12– The effect flow-field arrangement spatial porosity, symmetrical (red) and asymmetrical (black) flow-field. Spatial porosity distribution at 40% compression; (a) in-plane porosity under the land; (b) in-plane porosity under the channel; (c) through-plane porosity under the land; and (d) through-plane porosity under the channel.

4.3.6.2 Permeability

The permeability is a function of porosity, often calculated using the Carman-Kozeny equation [232–235]. Here permeability was calculated by 'pressure-driven flow simulation' using the Lattice-Boltzmann Method (LBM) [118,233,236–238]. LB simulations were implemented using Sailfish FD [239] open-source Python package. The simulations utilized the standard Bhatnagar-Gross-Krook (BGK) collision operator with a D3Q13 lattice and were solved for each principle direction of the sub-domain, resulting in three velocity fields for each sub-domain at each compression. The fluid was held at rest initially, and the movement was initialized by applying a fixed pressure gradient across the computational volume. The simulation converged when the average proportional deviation, after the iteration, was below 1×10^{-7}.

The spatial permeability decreases with compression under the land and increases under the channel. Arrangements have a marginal effect on the spatial permeability under-the-land (Figure 4.13(a and c)). For the under the land sub-domain, in-plane permeability reduced by approx. 4×10^{-12} m^2 , while through-plane permeability by 3×10^{-12} m^2 over the compression range for the asymmetrical arrangement.

Arrangements affected the spatial permeability under the channel (Figure 4.13(b and d)). The in-plane permeability for the asymmetrical arrangement increased over the compression by 30×10^{-12} and remained almost constant in the through-plane direction. However, at the extreme symmetrical compression, the in-plane permeability increased by 130×10^{-12} m^2 and the through-plane permeability by 16×10^{-12} m^2. The sudden increase in symmetrical permeabilities at extreme compression was due to the augmentation of the space between GDL fibres near large pores and the delamination observed.

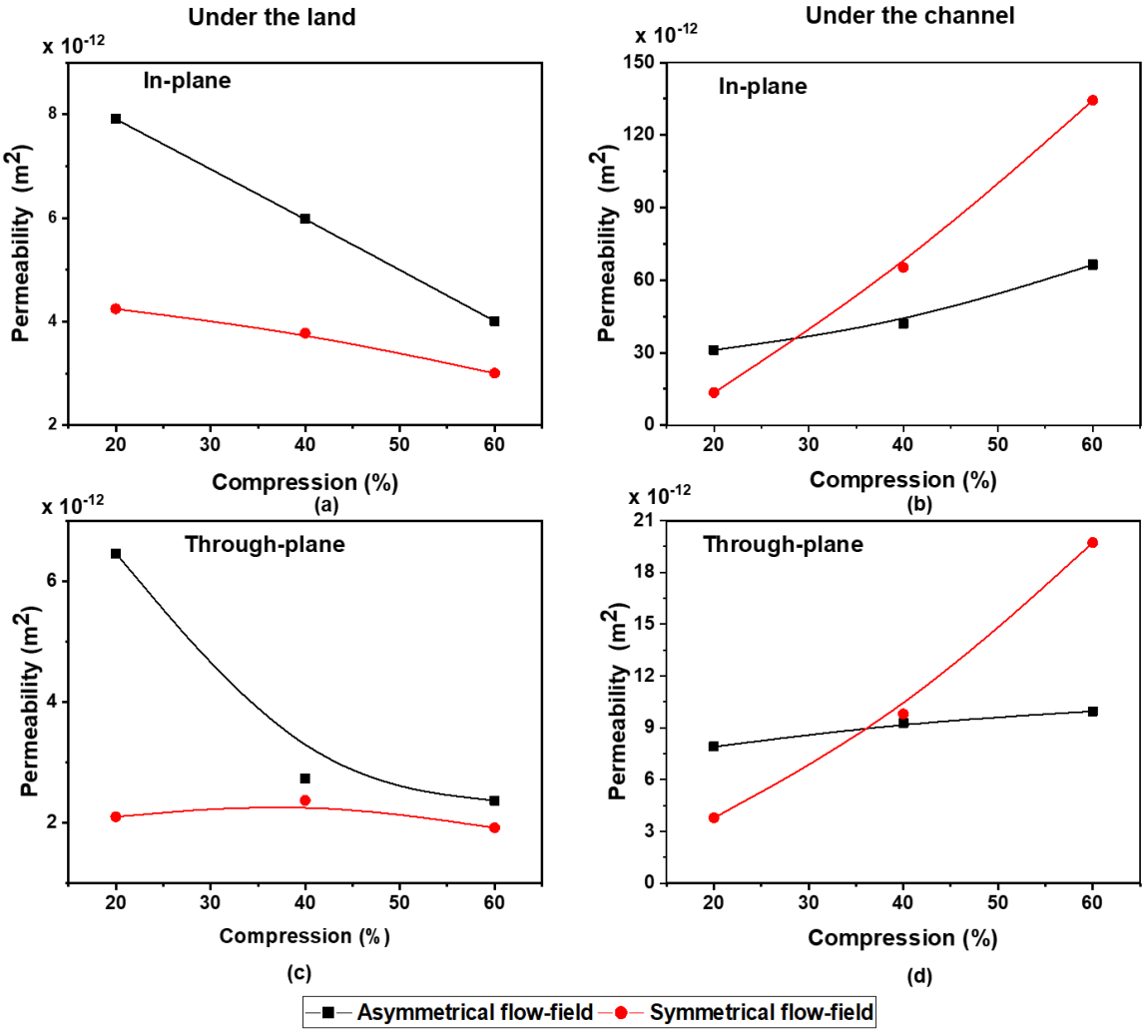

Figure 4.13– Change in directional permeability with compression and flow-fields: (a) in-plane permeability under the land; (b) in-plane permeability under the channel; (c) through-plane permeability under the land; and (d) through-plane permeability under the channel. The B-spline passing through the data points is added as a guide to the eye.

4.3.6.3 Tortuosity factor and diffusivity

Tortuosity and diffusivity of the GDL were calculated on the binarised dataset of individual samples. Generally speaking, tortuosity is inversely proportional to the porosity; hence, the decrease in bulk porosity with compression increases the tortuous

path for the reactant transport and decreases the effective gas diffusivity and vice versa. Therefore, these properties were mainly affected by the location of the sub-domain and were marginally affected by the arrangement. (Figure 4.14)

In this study, the tortuosity factors were calculated using the MATLAB based application 'tauFactor' that uses segmented voxel data for the finite difference simulation. The steady-state scalar diffusion equation was solved with the Dirichlet boundary conditions applied at the opposite faces of the volume (C = 0 and 1 on the bottom and top face, respectively). The approach is described by Cooper et al. [197]. The tortuosity factor (τ) in the specific direction was calculated using the following equation;

$$\tau = \varepsilon \frac{Q_{control\ volume}}{Q_{\ pore\ network}} \tag{4.2}$$

where Q_{pore} is the segmented pore network volume, $Q_{control\ volume}$ is fully dense control volume with the same outer dimension, and ε is the volume fraction of the conductive phase. The intrinsic diffusivity (D) was calculated using Fick's second law on the same segmented voxel data used for calculating the tortuosity factor, where the concentration on opposite faces was prescribed using the Dirichlet boundary conditions. The equation used was

$$\frac{\partial c}{\partial t} = D_0 \nabla^2 C \tag{4.3}$$

Furthermore, the effective diffusivity (D_{eff}) was calculated based on the tortuosity factor using the following expression,

$$D_{eff} = D_0 \frac{\varepsilon}{\tau} \tag{4.4}$$

Irrespective of the arrangements, the in-plane tortuosity factor under the land increased by approximately 27% over the full compression range; whereas under the channel is decreased by approximately 24% (Figure 4.14(a and b)). Similarly, the through-plane tortuosity factor increased by five times under the land and lowered by 2.5 times under the channel over the entire range of compression. (Figure 4.14(c and d)). Again, irrespective of the arrangements, an increase in compressive load decreased the in-plane diffusivity by approx. 34% under the land and increased it by 44% under the channel. Similarly, through-plane diffusivity under the land decreased with compression by 90% and increased under the channel by 44% irrespective of the arrangement.

Compression has a significant effect on the tortuosity and diffusivity in the through-plane direction, due to the random alignment of the gas diffusion fibres in the *xy* plane. Fibres realign themselves under compression, thus affecting these properties. The arrangements have minimal impact on these parameters, emphasizing the nonlinear relationship between spatial property distribution, porosity, and fibre alignment.

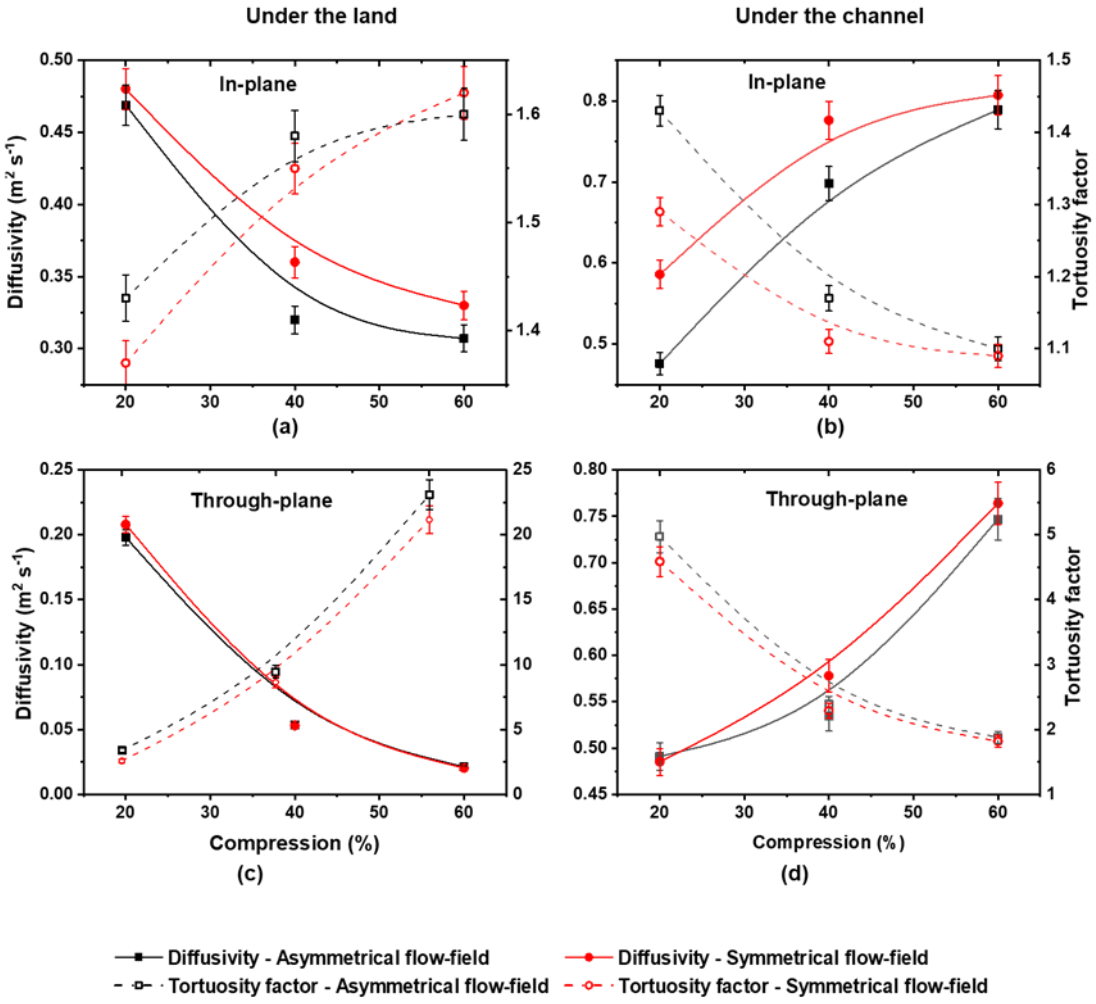

Figure 4.14– Directional tortuosity and diffusivity factors calculated on the binarised image of the GDL as a function of compression and flow-field design; (a) in-plane properties under the land; (b) in-plane properties under the channel; (c) through-plane properties under the land; and (d) through-plane properties under the channel. Left y-axis represents diffusivity (m^2 s^{-1}), and the right y-axis represents the tortuosity factor. B-spline passing through the data points is added as a guide to the eye.

4.4 Conclusion

Lab-based X-ray CT was used to study the geometrical and morphological heterogeneity of the entire MEA under non-uniform compression. Generated datasets can be used as inputs for the continuum modelling of fuel cell operation, incorporating the effect of non-uniform MEA compression. Also, the results can be used to aid system design and optimisation. The key findings from this study are:

- Non-uniform compression results in partial blocking of the active flow-fields. 25 – 40% blocking of the primary flow-field would not only affect the reactant transport capacity of the flow-field but also, it would affect the cell cooling characteristics. This emphasises the importance of considering the compression ratio while designing and modelling flow-fields and their arrangements. The results presented in this study can be used for design guidance.
- The electrolyte membrane undergoes deflection due to non-uniform compression, and the extent of membrane deflection is dependent on the arrangement. The lateral shift of the piston at the extreme symmetrical compression results in delamination of the MEA. This highlights the importance of channel alignment during cell assembly and manufacturing tolerances.
- This study presents the heterogeneity in the membrane that occurs from the MEA fabrication and hot pressing and considers structural thinning of the membrane under the land, due to non-uniform compression. This would affect the membrane durability, gas-crossover rates and subsequent water management.
- Cell compression and arrangements affect the extent of interfacial contact area and quality of the contact, which defines the contact resistance. GDL tenting increases the contact area through carbon fibres touching the flow-channel surface. The increase in contact area with compression would lower the contact

resistance at the cost of flow-field blocking. This emphasises the nonlinear relationship between contact resistance and cell performance.

- The X-ray CT data presented in this study prove that the bulk porosity values used in the modelling is valid only in the in-plane direction and does not represent the through-plane behaviour. Through-plane behaviour is critical in predicting water transport in the porous medium.
- Spatially resolved tortuosity, diffusivity, and permeability follow well-defined trends, such as the reduction in the porosity under the land area resulting in an increase in tortuosity, and a reduction in diffusivity and permeability. The values obtained from the study can be used as the input parameters in continuum modelling.

Thus, the present work provides a comprehensive data-set of the structural and morphological properties of the MEA, as well as effective parameters that can be used as inputs to higher fidelity computational models predicting PEFC performance, and provides detailed insight to the structural behaviour of the membrane under compression.

Chapter 5
Modelling framework

Abstract

The electrochemical performance of the fuel cell is defined by the activation, Ohmic and mass transport losses. Each of these losses is represented by the multiple physical phenomena such as reactant species transport, heat transfer, mass transport coupled with the electrochemical reactions taking place at the electrodes. The fuel cell performance can be mathematically explained by coupling the electrode kinetics with mass, momentum, energy and charge transport. Numerous attempts have been made by researchers to develop detailed fuel cell models depending on various approaches and dimensionality. This chapter outlines PEFC modelling strategies, techniques and challenges, followed by the detailed discussion of the governing processes and equations, and further develop the modelling framework to be used in the rest of the thesis.

5.1 Overview of the modelling efforts

PEFC operation involves the complex interaction of morphological and electrochemical factors, as discussed in the previous chapters. The complicated PEFC physics includes three-dimensional heat transfer, species and charge transport, multiphase flows, electrochemical reactions, and water management. These are in situ phenomenon, and due to complex fuel cell design, the effect of the individual process on PEFC performance is difficult to investigate (deconvolute). Though novel experimental techniques can act as powerful diagnostic tools, multiple experimental techniques should be combined to build a complete picture of fuel cell operation [217]. However, experiments are time-consuming and sometimes expensive to perform for all the design variations and material changes. This highlights the need for comprehensive, robust and experimentally validated fuel cell modelling tools that allows a better understanding of the parameters affecting fuel cell performance. While much progress has been made in recent years in computational modelling of fuel cells, genuinely functional and predictive capabilities remain a challenge due to the very complex nature of fuel cell operation.

5.1.1 Multifaceted transport phenomenon

Computational modelling of the fuel cell is preliminary based on the multiple transport processes (Figure 5.1). These processes are coupled and involve synchronicity of various physical and chemical reactions that defines fuel cell dynamics. The transport phenomenon concerning water and thermal management are particularly intricate, including multi-phase flow coexisting gas and liquid phase, multi-species transport, phase-change of water such as water condensation and evaporation, and water uptake mechanisms by the membrane such as water adsorption and desorption. Coexistence of multiple transport phenomenon has always been recognised as one of

the primary challenges in the development of comprehensive fuel cell models [240–245].

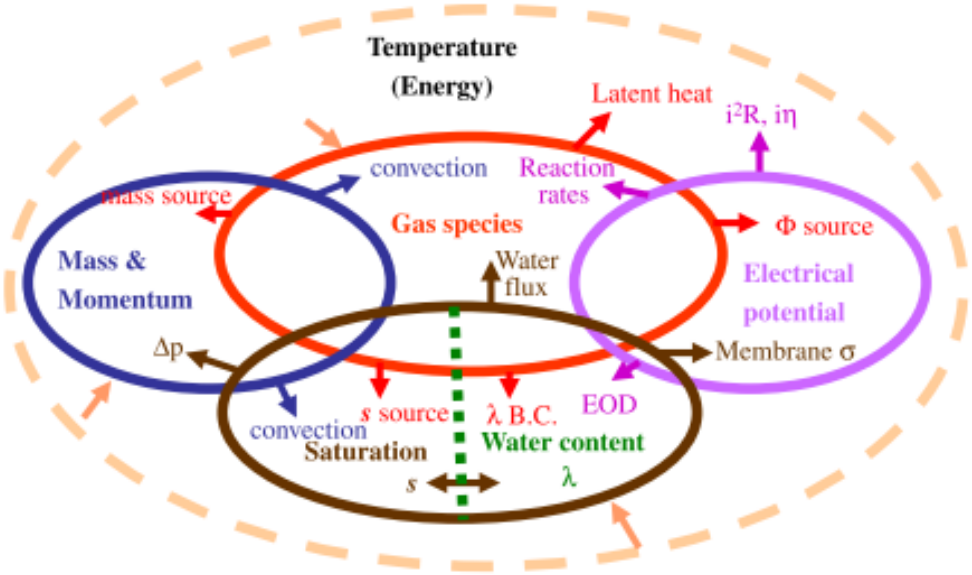

Figure 5.1–Schematic showing the complex coupling of the transport phenomenon in PEFC [240]

5.1.2 Transient nature

The time-dependent polarisation curve is a fundamental diagnostic technique used to understand PEFC performance. Operability of the fuel cell shrinks with time, i.e. fuel cell degradation. Hence, steady-state computational models may give the details of instantaneous reactions but fail to predict the continuous effect of the operation. Hence, co-existence of a wide range of characteristic length and time scales, with electrochemical and thermodynamic reactions, make transient modelling of fuel cells challenging and computationally expensive [240,246–249].

5.1.3 Characteristic time and length scale

The electrochemical processes occurring in the fuel cell can be described by different length scales of the computational domain / control volume, varying from cell level or stack level domains to the material interface and molecular level. To represent the detailed PEFC physics, not only length scales but also time scales should be considered, this is reflected in the computational expense, as shown in Figure 5.2.

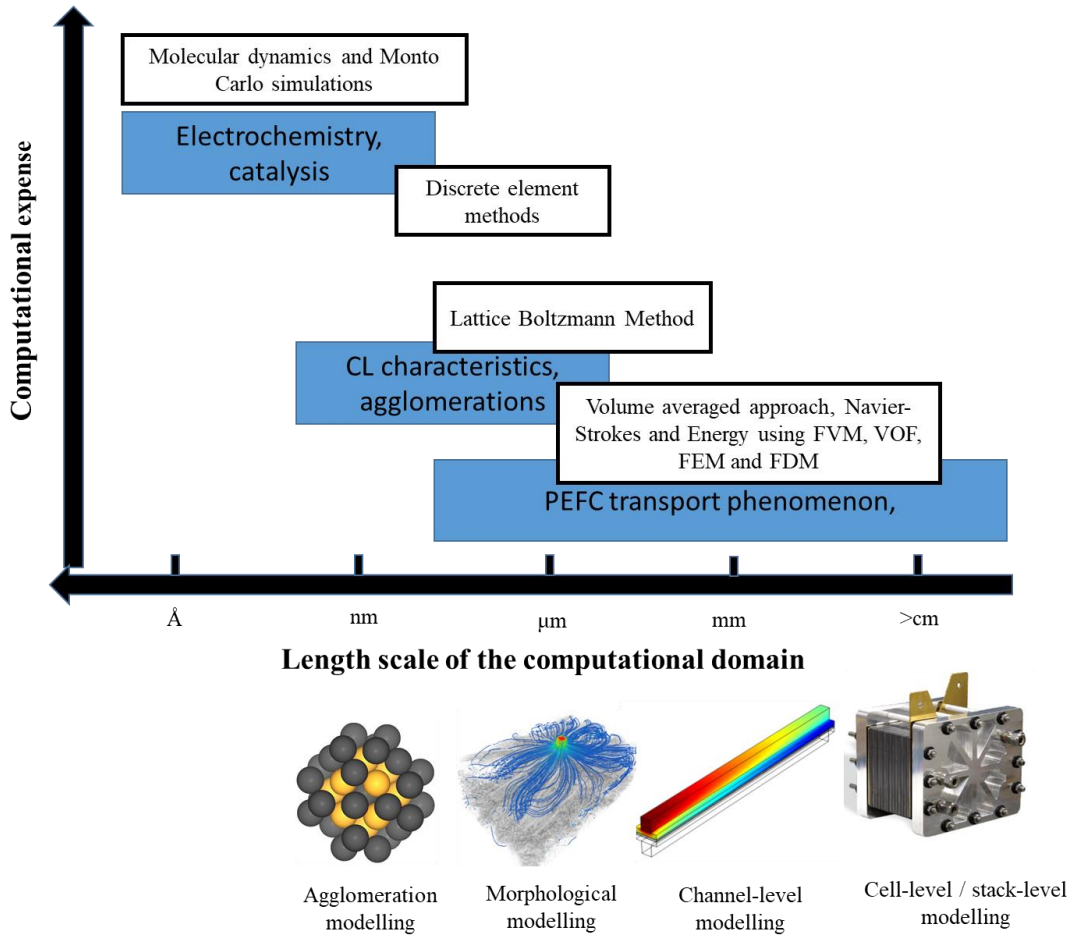

Figure 5.2– An overview of the cost and length scales characteristic of PEFC modelling techniques, white boxes represent the type of modelling and blue boxes represent the physics to be modelled

Modelling and simulation across the entire length and the time scales would provide an exceptional opportunity to understand phenomena and properties, which are inaccessible and difficult to address experimentally; however, it comes with computational expense. Hence, a balance has to be stuck between the scale of the model, complexity of the physics to solve, and modelling techniques.

5.1.4 Model validation

Model validation is a fundamental step in order to develop trust in the model. The majority of models in the literature are based on the stand-alone validation against a simple polarisation curve [127,243,250–252]. Though the polarisation curve is the most commonly used electrochemical method to characterise fuel cells, it provides information on overall performance losses without differentiating the sources of the losses. Fouquet et al. recorded the polarisation curves at nominal, flooded and dried conditions, as shown in Figure 5.3 [253]. The performance at the activation dominant region was not affected by the operating conditions as it is determined by the CL properties. With an increase in operating load to, both flooded fuel cell and dry fuel cell observed loss in the polarisation performance to the similar extent; however, it is challenging to identify the cause of the performance loss between flooding conditions and drying conditions over Ohmic and mass transport dominant regions. Therefore, for the models predicting the water transport behaviour or the processes affecting water transport in the PEFC, the polarisation curve can only be used as a crude indicator of fuel cell operation. Hence, various advanced diagnostic techniques such as EIS [254], neutron radiography [103,168], electro-thermal mapping [217] can be used to validate certain aspects of the performance.

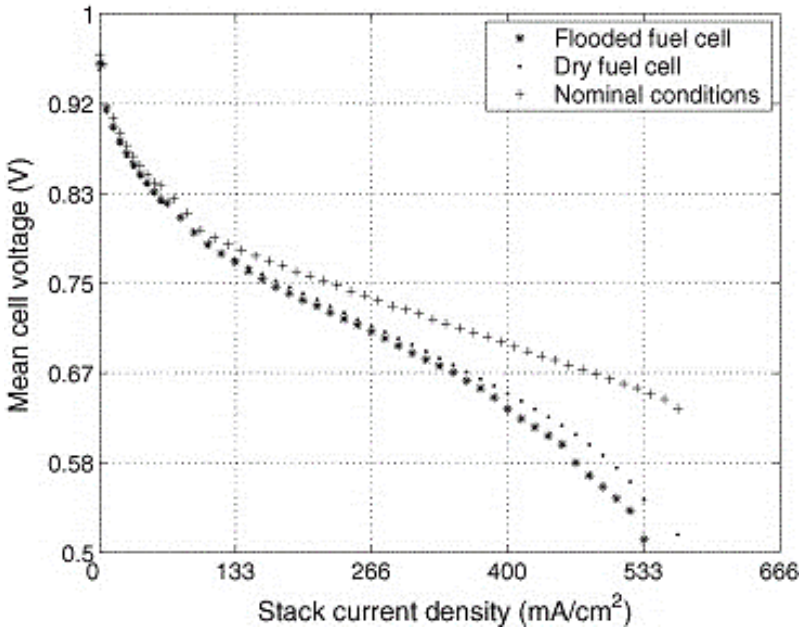

Figure 5.3– Measured polarisation curves for a fuel cell working under flooded, dry and nominal conditions [253]

5.1.5 Spatial dimensions of the model

The computational/numeric models can be characterised as one-dimensional, two-dimensional, and three-dimensional models, based on the spatial dimensions. Figure 5.4 gives an overview of the spatial dimensions of PEFC modelling.

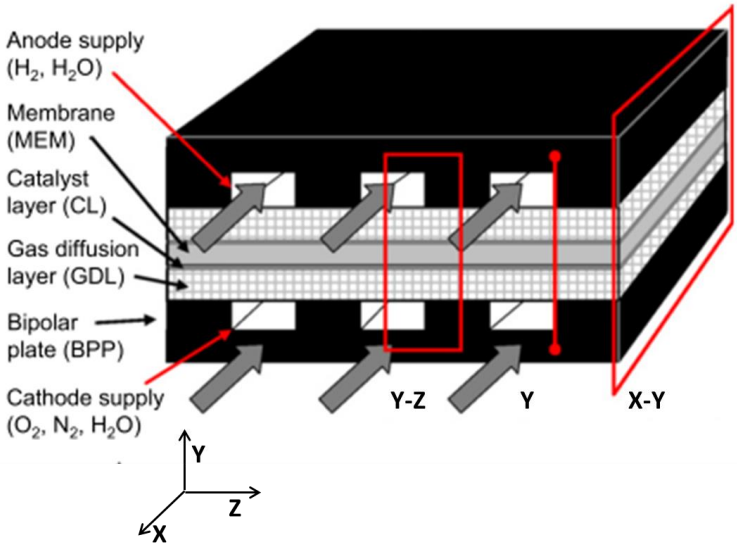

Figure 5.4– Schematic illustration of different computational domains (1D in *Y*-direction, 2D in *X*-*Y* and *Y*-*Z* direction and 3D computational domains [249]

1D models describe the spatial electrochemical phenomenon in a specific direction and can broadly be categorised as 'through-the-MEA' models and 'along-the-channel' models. In the pioneering attempts of model development in the early 1990s, the simplified models developed adapted the through-the-MEA approach. These models typically consider the membrane, catalyst layer and gas diffusion layer as the computational domain. The fundamental assumptions in these models are the homogeneous materials and the use of isotropic effective transport properties. Through-the-MEA models can be used to understand water transport mechanisms, diffusion analysis, degradation prediction, transient operation, and models for control strategy. Models developed by Springer [30], Bernardi and Verbrugge [255], Baschuk and Li [256], represent the pioneering work in this segment. The second type of one-dimensional models is the 'along-the-channel' model, which focuses on transport and depletion of the gases along the channel length and its effect on the current density and voltage profile [147,257,258]. Figure 5.5 explains the difference between through these two approaches.

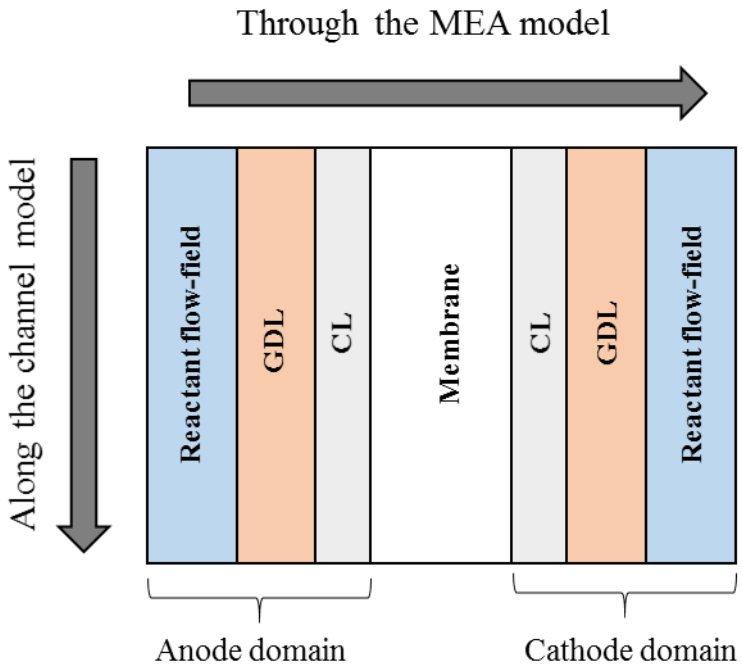

Figure 5.5– 1D modelling approaches, the model can be 'though the MEA' model or 'along the channel' model (Not to scale)

The majority of one-dimensional models focus on the polarisation curve. These models are computationally less expensive, fast, and complicated physics can be incorporated to solve dynamic behaviour [258]. Though these models show functional validation against experimental data, they fail to capture the mass concentration effects that result in the concentration losses when compared to experimental polarisation curves.

Bernardi–Verbrugge [255] developed a steady-state one-dimensional model using an electrode bonded to a membrane approach. The model comprises a solid electrolyte membrane, active CL, GDLs and channels. An active CL was modelled as a one-dimensional macro-homogeneous layer. This is the preliminary model explaining the electro-osmosis process based on the pressure-driven water transport in the fuel cells and uses dilute solution theory (Section 5.2.2) incorporating the Nernst-Plank

approach for ionic transport. The pressure gradient for liquid phase uses a modified form of Schlogl's velocity. Stefan-Maxwell multi-component diffusion solves the gas diffusivity. The critical assumption is the proton concentration inside a membrane is uniform; hence, the model does not account for protonic diffusion, making the membrane uniformly hydrated. The pressure and potential profiles throughout a membrane thickness are linear, making velocity constant.

Springer et al. [30] developed a semi-empirical model using in-house experiments for transport parameters. The model comprises an anode and cathode GDLs and a membrane while CLs were treated as an interface between the GDL and the Nafion membrane. This model also adopts the dilute solution theory. The species conservation equations for anodic and cathodic species are a function of water activity at the membrane and acts as a convergence parameter for numerical solution. The Stefan-Maxwell approach with Bruggeman correction was used to solve multicomponent diffusion in porous GDLs. The model is steady-state, isothermal and isobaric; hence, any pressure-driven migration of the species was not considered, assuming constant pressure on both sides of the membrane. EOD and use of a water sorption isotherm at a membrane resolved the change in water content and proton conductivity along with a membrane thickness.

Baschuk et al. [256,259] presented the literature on mathematical modelling of PEFCs. This model comprises a membrane, cathode CL, GDL and flow channels. This is a one-dimensional steady-state isothermal model, and the membrane is assumed to be fully hydrated. Cathode CL was assumed evenly loaded. Species diffusion was modelled using conservation of species and Fick's law of diffusion. The model evaluated PEFC performance at variable degrees of flooding and showed good agreement with the experimental data available in the literature. With an increase in cell pressure, the water flooding in the electrode increases significantly. The same model was further extended for two-dimensional steady-state isothermal operation.

This model adopts the approach taken by Scattergood and Lightfoot to model the transport of water and ions in the electrolyte [260].

Marr and Li [261] studied the steady-state performance of cathode CL by including both mass transport through CL and an electrochemical reaction at the cathode CL. This study investigates the composition and the performance of CL loading. The model assumes fully hydrated / flooded ionomer layer and the void spaces; a fourth-order shooting method was used to solve the algorithm.

Djilali and Lu [262] developed a one-dimensional steady-state isothermal model to investigate PEFC performance and water-management over the range of the operating-current densities. The model adopted Stefan-Maxwell multicomponent diffusion of the gas species diffusing through the GDLs and considers the effect of non-uniform pressure and temperature distribution on the diffusion process. Effect of Knudsen diffusion was considered for CL modelling. The model studied water in both liquid and vapour form and considers the effects of water transport by back-diffusion and EOD. However, while working at higher current density, the model ignores the possibility of membrane drying, that is the main limitation of the model.

One-dimensional steady-state, single-phase, non-isothermal model was developed by Falcao et al. [263,264]. The model solves water transport through the membrane and comments on thermal management. This model assumes the water transport through a membrane is the combined effect of back diffusion and EOD, similar to the Springer model. The model considers the heat transfer via conduction process through a total of sixteen layers, including aluminium endplates, current collectors, and flow channels, an acetate sheet (to isolate aluminium plate from the current-collector), GDLs, CLs, membrane. Stefan-Maxwell multicomponent diffusion approach was used to solve diffusion-dominant transfer at GDLs and CLs, and water transport through the membrane was solved by the Fick’s law of diffusion. Proton conductivity of a

membrane was modelled using water content (λ), similar to the Springer model. The CL was modelled with a pseudo-homogeneous film approach.

The combination of two one-dimensional models, known as Pseudo 2D or the 1D+1D approach is well discussed in the literature. Instead of solving the coupled conservation equations in a two-dimensional domain, the one-dimensional model is solved at each mesh point along the channel. This reduces the computational expense without the complexity of solving the equations in a two-dimensional domain [265]. The notable pseudo-two-dimensional models were developed by Nguyen and White [266] and Fuller and Newman [267] accounting for the variation in temperature and the membrane hydration conditions along the flow channels. Both the model assumed a well-mixed concentration of the reacting and product species in the flow-channels. Nguyen and White investigated the effectiveness of the reactant humidification on maintaining the membrane hydration, and hence, on cell performance [266]. This model was further modified by Yi and Nguyen [268] by including both liquid and gas phase along the flow channels and the temperature distribution in the solid phase. This model highlights the importance of counter-flow mode to effective heat removal. The model developed by Fuller and Newman adopted concentrated solution theory, itself based on the Stefan-Maxwell diffusion approach for solving the transport mechanism at the membrane [267]. This model highlights the rate of heat removal is the critical parameter deciding the PEFC performance.

With the improvement in the computational facilities, various researchers developed the multidimensional model that solves the multiple coupled PDE using commercial CFD tools such as Ansys-Fluent fuel cell module [264,269,270], COMSOL Battery and Fuel cell module [271,272], AVL Fire fuel cell module [129], etc.

In the aforementioned transport phenomenon in PEFCs, the morphologies of the porous domains (CLs, MPLs, and GDLs) and migration processes in the membrane are extremely complicated and three-dimensional in nature. Hence, three-dimensional

modelling is the obvious choice for the majority of the recent modelling efforts [51,127–129,240,264,269,273–275]. The main advantages of three-dimensional models are illustrative for the distribution of reactant, current density, water generation and the flooding or drying. Models can be validated with experiments such as neutron-imaging [82,133,167] or current and temperature mapping [220], etc. Despite significant advancement in computational capacity and tools, to date, the three-dimensional models are computationally challenging and time-consuming.

Nguyen et al. [137] developed a complete three-dimensional CFD PEFC model with serpentine reactant channels. This model solves the main transport phenomena, such as convective and diffusive heat and mass transfer, electrode kinetics and potential fields. The model implements a ‘voltage to current’ algorithm that solves for the potential fields and computes local activation potential distribution. The coupling of the local activation overpotential distribution and the reactant concentration predicts the local current density distribution accurately. The simulation results reveal current distribution patterns that are significantly different from those obtained, assuming constant surface overpotential. At higher load, the current density is maximum under the channel area, and at lower load, the current density is maximum under the land region.

Shimpalee and Dutta [276] developed a three-dimensional, non-isothermal, straight channel, steady-state model to predict the thermal behaviour of the fuel cell as the result of electrochemical reactions and phase transport of water. The model uses Navier-Stokes equations for bulk transport of the reactant in the flow channels, source terms for mass transport criteria, phase change and heat generation to mimic the electrochemical process. This model predicts that the fuel cell performance depends on the inlet humidity conditions, membrane thickness and fuel cell operating temperature. The model considers five species, including CO_2 and liquid water as a function of phase change. Commercial code Ansys-Fluent is used. Here, evaporation is modelled as the function of partial pressure and a saturated pressure.

Lum et al. [277] made one of the initial efforts to model three-dimensional homogeneous CL PEFC model using in-house code Fuel3D. A multistage validation approach was adapted to build the model using validation data available in the open literature and further locally validated with the experimental data obtained from segmented cell experiments. This model uses Shimpalee's modelling approach discussed previously. A membrane model is adapted from Springer's one-dimensional model, equating water activity at both CL to obtain water profile inside the membrane.

Berning et al. [278] developed a three-dimensional non-isothermal computational model for mass transport in PEFCs using commercial code CFX4.3. The single-phase model accounts for all significant transport mechanisms, except phase change and emphasises on the fundamental understanding of the transport processes with reactant concentration, current distribution, temperature, and water retention areas. This model solves Stefan–Maxwell multi-species diffusion, Nernst-Plank equation for the transport of protons through a membrane, the 'Schlogl approach' for liquid water transport through a membrane and Butler–Volmer equation for electrode kinetics; however, the model neglects the effect of gas crossover, assuming an impermeable membrane. This model assumes two separate pores in GDL for gas diffusion and water diffusion; hence, there is no interaction of gases with liquid water. This model provides a good insight into liquid water saturation and water flooding under various operating conditions; however, it does not account for water content through a membrane.

Al-Baghdadi et al. [279] performed PEFC optimisation study using a detailed three-dimensional, multiphase, non-isothermal PEFC model that incorporates both gas and the liquid phase in the GDL domain, allowing the implementation of phase-change. The realistic local activation losses were predicted by solving the significant species transport phenomenon and electrochemical reactions that allows an improved prediction of the local current density distribution

Baca et al. [127] developed a detailed three-dimensional steady-state non-isothermal model using a single-phase approach. This is a seven domain model with the separate cathode and anode CL modelled as the homogeneous domain. The water content and proton conductivity in a membrane were solved using Springer's approach to calculate current distribution. The unique approach taken in this model is water absorption and desorption on the polymer fraction inside the CL based on the difference between equilibrium water content in the polymer fraction of CL. The model is restricted to 30,000 computational elements and solved using commercial code STAR-CD v3.24.

Iranzo et al. [133,269,275] used commercial fuel cell simulation module developed by ANSYS- Fluent and results were validated against neutron imaging to detect water fraction in the fuel cell. This model uses a fitting parameter of reference exchange current density ($j_{0,a/c}^{ref}$). The study emphasises the need for a mesh independency analysis to model fuel cell operation phenomenon that requires several million elements. Also, the study addresses the computational power as the prime limiting factor in fuel cell modelling.

Fink et al. [129] used AVL-FIRE commercial code to develop three-dimensional model solving for the real-world automotive application. This model uses a thin CL interface approach to model the electrochemical reaction. Similar to the commercial code FLUENT-fuel cell module, the fitting parameters are used to separate activation, ohmic, and mass transport losses in order to achieve the adequate performance of the model.

While three-dimensional models could better represent reality, these models are computationally expensive. Though the one-dimensional model cannot solve the domains with high fidelity, they often allow solving more complex physics. Hence, the trade-off between the complexity of the physics to be modelled and the computational expense can be achieved by the two-dimensional or quasi-2D model framework. Two-dimensional models are preliminary on the cross-section of the fuel cell inclusive of all

the layers either in ‘along-the-channel’ orientation or ‘through-the-MEA’ orientation. Along-the-channel 2D models could better represent the heat-transfer in the fuel cell, the effect of reactant depletion along the channel length. The effect of under the channel and under the land regions are approximated in ‘along-the-channel models. ‘Through-the-MEA’ approach solves for all the layers in the cell including the effect of under the channel, and under the land regions; however, the effect of channel length and orientation is approximated in the model.

The five-layer steady-state, isothermal, and two-dimensional model developed by Kim et al. [81] examines the effect of operating parameters such as humidity and the stoichiometry on the fuel cell performance and membrane/ionomer water content. The study provided insight into how the anode and cathode stoichiometry impacts the back diffusion of water. This model assumes micro-homogeneity of GDLs and CLs, assuming all the components in the porous domains are evenly distributed. The model used a concentration-dependent form of the Butler-Volmer equation for the current modelling as discussed in 5.3.1 and Stefan –Maxwell multicomponent diffusion for the species transport.

A multi-species, two-dimensional non-isothermal and transient model was developed by Dadda et al. to investigate the influence of heat and mass transfer on the potential variation in the PEFC membrane [280]. This model successfully delineated the time and space-dependent temperature and water concentration and showed that the voltage loss is more critical in the regions with less water content. The aim of this model was to evaluate the influence of different cases of boundary conditions on water concentration and heat transfer variation and test the reliability of the proposed computational fluid dynamic (CFD) code. However, the model was a single-phase simplistic model where water transport through the membrane was simply treated as the water molecules instead of the dissolved phase of water; hence, the model could not solve all the coupled physical phenomenon in the cell.

Tiss et al. presented ‘the cathode only’ two-dimensional CFD model to solve electrochemical, mass and heat transfer processes [281]. This model includes the effect of water content in the membrane swelling phenomenon. The study highlighted that the membrane/ionomer water content (λ) is a function of cathode-domain parameters such as humidification temperature and inlet velocity of the reactant. With the increase in the humidification temperature of the reactant, the membrane/ionomer water content increases, increasing the protonic conductivity of the membrane. At higher inlet velocity of the reactant, the convection and diffusion of water from GDL to membrane become more significant than EOD, and the membrane/ionomer water content thus increases. The higher reactant Reynolds number implies the removal of liquid water by convection. Numerically, the PDEs in the model was solved using the ‘Successive over Relaxation’ (SOR) method where two momentum equations corresponding to the axial and the longitudinal velocities are solved first without the pressure solution. This led the numerical conversions at 10^{-4} error.

Chaudhary et al. developed a two-phase, non-isothermal, transient and two-dimensional model solving water uptake mechanisms by the membrane[252]. The model solved two approaches of water-uptake by the membrane, such as one approach considers Schroeder’s paradox and the second approach considers individual contributions of water vapour and liquid water. The model suggested the water uptake mechanism by the membrane affects the current density, membrane/ionomer water content and the in-cell temperature. Transient rate of sorption or desorption of water by membrane responds to the membrane/ionomer water content on the application of voltage change

Xing et al. developed a two-dimensional, isothermal, two-phase flow agglomerate models to explore the effect of dry Nafion ionomer volume fraction and cathode relative humidity on membrane/ionomer water content, the membrane swelling and the cell performance[251,282]. The results showed an increase in dry Nafion ionomer volume fraction, increases membrane/ionomer water content. The model also showed that the

optimum cathode RH should be between 60% and 80% for dry Nafion ionomer volume fraction of 40%. At higher current densities, an increase in the ionomer content in the membrane results in decreasing the cathode RH, initially, that eventually increases with increases in current density. The same model was further enhanced with the non-isothermal energy transport without including the effect of membrane swelling [250]. This model highlights the effect of channel/land arrangement of the water saturation and the in-cell temperature. The model also suggested that at higher anode operating temperature and enlarging the width ratio of the channel/land arrangement could improve the cell performance. However, the model does not account for the effect of change in effective properties with respect to the region under the land and under the channel and the effect of flow-field arrangements on the structural properties of the MEA. As discussed in the previous chapters, the morphology of the fuel cell materials that define the effective properties in the fuel cell is significantly affected by the cell compression, affecting the water and thermal management in the operating fuel cell. Hence, in order to include these effects in the modelling, two-dimensional 'through-the-MEA' approach could be adapted.

5.2 Membrane modelling

Transport processes in the electrolytic solution govern the rate of electrochemical reactions and the overpotential performance of the fuel cell. Membrane modelling comprises mass transport phenomenon that solves ohmic and mass transport losses in PEFCs.

The performance of the PEFC is determined by the constitutive relations governed by the membrane/ionomer water contents. Hence, the water profile established across and along the membrane at steady state is thus a critical step / assumption to develop comprehensive and robust PEFC performance model [267]. The mass transport due to the electrochemical reaction can be modelled with two main approaches, the

concentrated solution theory and the dilute solution theory. The applications of these theories are discussed in this section.

5.2.1 Concentrated solution theory

Concentration solution theory is known as the fundamental approach to solving the transport phenomenon for PEFC modelling. The preliminary assumption in this approach is that the species transport is governed under the electrochemical gradient. The diffusion can be solved by,

$$C_i \nabla \mu_i = \sum_j K_{ij}(v_i - v_j) = RT \sum_{i \neq j}^{n} \frac{c_i c_j}{c_T D_{ij}}(v_j - v_i) \tag{5.1}$$

where C_i is the concentration of species *i*, $\nabla \mu_i$ is an electrochemical gradient of the species *i*, D_{ij} is the binary diffusion coefficient, u_i is the electrochemical potential of species *i*, v_i is the average velocity of the species [m s^{-1}], and K_{ij} is the frictional coefficient of species pair i,j. The frictional coefficient accounts for the local concentrations of pairs of constituent species and the diffusion coefficient of the species pair;

$$K_{ij} = \frac{RT c_i c_j}{c_T D_{ij}} \tag{5.2}$$

The molar flux of a given species can be defined by species concentration and velocity.

$$\dot{N}_i = c_i \, (v_i - v_{ref}) \tag{5.3}$$

where the reference velocity accounts for the bulk fluid motion. Hence, the standard form of the flux equation for concentrated solution theory that forms the basis of a number of PEFC models is given as [267,283–285],

$$\frac{C_i \nabla \mu_i}{RT} = \sum_{i \neq j}^{n} \frac{c_i \dot{N}_j - c_j \dot{N}_i}{c_T D_{ij}} \tag{5.4}$$

The transport across the Nafion membrane can be solved by accounting for the ternary system composed of dissolved water, electrolyte and protons. Thus, the electrochemical potential gradient can be given by,

$$\nabla \mu_i = z_i F \nabla \emptyset + RT \frac{\nabla c_i}{c_i} \tag{5.5}$$

5.2.2 Dilute solution theory

The dilute solution theory can be derived from the concentrated solution theory. The fundamental difference between the two approaches is that the dilute solution theory assumes that the concentration of the solvent is much higher than the concentration of the solutes. Therefore, the transport of each solute species can be assumed negligible. If the solute species is *j* then Equation (5.4) can be expressed as;

$$\dot{N}_i = -\frac{C_i \nabla u_i}{RT} D_{ij} + c_i u_i \tag{5.6}$$

The particular form of the Equation (5.6) is used to represent the transport of dissolved water through the Nafion membrane. Here, the polymer electrolyte is stationary; hence, the velocity of the polymer electrolyte, $u_i = 0$ reducing Equation (5.7),

$$\dot{N}_i = -\frac{C_i \nabla \mu_i}{RT} D_{ij} \tag{5.7}$$

where D_{ij} is the diffusion coefficient of water in the polymer electrolyte and should take into account the fact that it can swell during water uptake. In dilute solution theory, the flux equation is solved using the Nernst-Plank equation. This describes the transport

of the diluted species by three processes: migration due to the electrochemical potential gradient, diffusion due to the concentration gradient, and convection due to the bulk velocity of the solvent.

5.2.2.1 Mass transport through the electrolyte membrane

The mass transfer in the electrolytic solution is the function of ionic species transport, material balance, potential balance and fluid dynamics, known as a species flux transfer. The flux density of each dissolved species in an electrolyte can be obtained by substituting Equation (5.5) into Equation (5.6). This is known as the Nernst-Plank equation.

$$N_i = -z_i u_i F c_i \nabla \emptyset - D_i \nabla c_i + \boldsymbol{u} c_i \tag{5.8}$$

where N_i is a flux density of species *i* [mol cm^{-3}s^{-1}] that defines the direction of species transport, z_i is the number of proton charges carried by the ion, u_i is an average velocity of the species in an electrolyte solution, i.e. mobility of the species, $\boldsymbol{u}$ is the average velocity of the solute [m s^{-1}] and $\nabla\emptyset$ is a potential gradient. This Equation defines three main mechanisms of mass transfer in the electrolyte: migration, diffusion and convection. As the transport of charged particles develops the current,

$$i = F \sum_i z_i N_i \tag{5.9}$$

where current *i* [A] is a function of total charge per mole in the system. The material balance in the individual species can be defined by,

$$\frac{\partial c_i}{\partial t} = -\nabla N_i + R_i \tag{5.10}$$

Accumulation of the species with respect to the time in an electrolyte is the difference between net input of the species flux and rate of production of the species (R_i). In PEFCs, H_2O production is restricted at a cathode CL; hence, R_i in a membrane is 0. This makes the system electrically neutral, except at the boundaries. Mathematically it can be represented as,

$$\sum_i z_i c_i = 0 \tag{5.11}$$

Convection term in Equation (5.8) needs an average velocity of the solute species. This velocity is due to the concentration of the species in an electrolyte. In a concentrated solution approach, as discussed in section 5.2.1, the average velocity of the fluid is considered by the velocity of solvent and solute both; however, if the solution is the dilute solution [section 5.2.2] average velocity equals to the velocity of solvent. Hence, the general form of the Nernst-Plant equation can be represented as,

$$\frac{\partial c_i}{\partial t} = \nabla\left(D_i \nabla c_i - \boldsymbol{u} c_i + \frac{D_i z_i e}{k_B} c_i \nabla \emptyset\right) \tag{5.12}$$

where t is a time [s] that defines the direction of species transport, z_i is the number of proton charges carried by the ion, $\boldsymbol{u_i}$ is an average velocity of the species in an electrolyte solution, i.e. mobility of the species, $\boldsymbol{u}$ is the average velocity of the solute [m s^{-1}] and $\nabla\emptyset$ is a potential gradient.

Mass transport through the membrane is a combination of three processes, electric force generated from the migration of protons from the anode to the cathode, and two water transport mechanisms. Electro-osmotic drag transport due to the potential gradient and a back-diffusion of water caused by the concentration gradient of water across the membrane. The water flux due to the electro-osmotic drag is proportional to the protonic flux, and the back-diffusion of water is a function of the water diffusion

coefficient through the ionomer and the concentration gradient of water between anode and cathode domains, as shown in Figure 5.6.

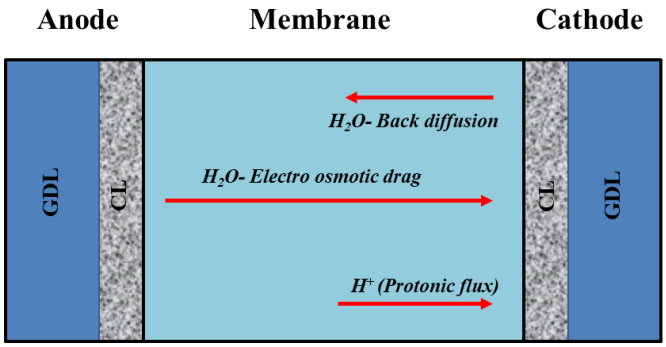

Figure 5.6– Schematic of mass transport phenomenon through the membrane that mainly constitutes of three mechanisms namely back diffusion of water, electro-osmotic drag and transport of protonic flux

An assumption of electroneutrality governs the proton conservation. The proton occupies the fixed SO_3^+ charge sites, distributed homogeneously throughout a membrane. This results in a constant proton concentration throughout a membrane. The protonic flux is indicated as protonic current (i_{cell}/F).

One-dimensional modelling approach assumes a single-phase flow through the membrane. This assumption is driven by the pore size in the membrane being smaller 5 nm; hence, the capillary forces can be neglected neglecting velocity of the mixture in a membrane. The pressure gradient across a membrane is assumed linear, and the membrane does not participate in any electrochemical action. Though this is a reasonable assumption for steady-state modelling, for transient modelling and the gas crossover models such as N_2 blanketing models, this assumption will impact the results considerably.

5.2.2.2 Conservations of protons

Based on the electroneutrality assumption and the homogeneous distribution of charged sites, the mass conservation of protons is expressed as,

$$\frac{\partial c_{H^+}}{\partial z} = 0 \tag{5.13}$$

Hence, whilst the current is withdrawn, the membrane keeps proton concentration constant. This equates to the fixed charged sites available in the solid phase. The diffusive molar flux of proton is,

$$J_{\mathrm{H}^+} = -\frac{F}{RT} D_{\mathrm{H}^+} c_{\mathrm{H}^+} \frac{\partial \emptyset_{\mathrm{m}}}{\partial \mathrm{z}} \tag{5.14}$$

$\emptyset_{\mathrm{m}}$ is a membrane potential and D_{H^+} represents proton diffusivity. Hence, the total molar flux of protons is,

$$N_{\mathrm{H}^+} = i_{\mathrm{H}^+} + c_{H^+} u^m \tag{5.15}$$

Based on the conservation of momentum principle, the generalised Darcy's relation is used as the momentum equation.

$$u^m = -\frac{K k_r^g}{\mu}\left[\frac{\partial p}{\partial z} - \rho g\ (cos\ \theta)\right] \tag{5.16}$$

This equation accounts for the gravitational force on the moment and an angle of species transport with respect to gravitational direction. *K* is the absolute permeability of the porous medium and k_r^g is the relative permeability of the gas phase. ρ is the density of the mixture and μ is the dynamic viscosity of the mixture.

5.3 Electrochemical modelling (e^-, H^+)

An electrochemical reaction takes place within the CLs. Three fundamental approaches have been undertaken in the literature to model the catalyst layers in the PEFC, namely the CL interface model [30], thin-layer model [26,127,262,286], and detailed agglomerate model [218,250,252,287,288]. The CL interface model is simplified and computationally inexpensive; however, it limits the functioning while predicting the influence of operating parameters on the catalyst layer performance. The thin-layer model is the most common approach used for modelling catalyst layers and assumes the catalyst layers have separate pores for both liquid water transport and the gaseous transport. These models also assume uniform properties of the catalyst across the active area. Such models form a good approximation for the performance models but fail to solve the effect of microscale catalyst layer properties on the performance. The third and comparatively new trend used in the present modelling is solving the structure of the catalyst layer in the form of spherical agglomerates. This section discusses the electrochemical model to solve the homogeneous catalyst layer using the Butler-Volmer kinetics and its modification to obtain the agglomerate structure.

5.3.1 Butler-Volmer kinetics

The electrode potential affects the kinetics of the reaction and the activation losses. The fuel cell operation is based on redox reactions that occur at the interface between the ionically conductive membrane and electrically conductive electrodes.

$$i_f = k_f c_{Ox};\ i_b = k_b c_{Rd} \tag{5.17}$$

i_f and i_b are known as the forward and the backwards current, respectively. c_{Ox} and c_{Rd} represents the surface concentrations of the reacting species, and k is the

respective reaction rate constant. Equation (5.17) defines the flux of the forward and the backwards reaction. These reactions either release or consume electrons during the operation. The net current obtained is the difference between electrons released and electrons consumed during the process. Hence, the net current generated is the difference between the forward and the backwards current.

$$i = nF\left(k_f c_{Ox} - k_b c_{Rd}\right) \tag{5.18}$$

At electrode equilibrium conditions, despite the reaction taking place in both forward and reverse direction, the rate of reaction for oxidation is equal to that of reduction and no external current is generated. The current density at this equilibrium condition is known as 'exchange current density'.

The reaction rate coefficient (*k*) is expressed by transition state theory as a function of Gibbs free energy (ΔG), Boltzmann's Constant, k_B (1.38 × 10^{-23} J K^{-1}), and Plank's constant (*h*) is (6.626 × 10^{-34} J s).

$$k = \frac{k_B T}{h} exp\left(\frac{-\Delta G}{RT}\right) \tag{5.19}$$

Gibbs free energy, ΔG represents the change in activation energy for the oxidation and reduction reactions. For reduction reaction,

$$\Delta G_i = \Delta G_{ch} + \alpha_{Rd}\, F\, \emptyset \tag{5.20}$$

and for oxidation reaction,

$$\Delta G_i = \Delta G_{ch} - \alpha_{Ox}\, F\, \emptyset \tag{5.21}$$

where ΔG_{ch} [J mol^{-1}] is the Gibbs free energy for the chemical component, ∅ [V] is the potential and α is the transfer coefficient for reduction and oxidation reaction which is a ratio of the number of electrons transferred during the electrochemical process to

the number of times the rate-determining step must occur during one overall reaction. The value of PEFC anode transfer coefficient is generally 0.5 with 2 electrons involved, and the value for PEFC cathode transfer coefficient varies between 0.1 to 0.5; however, Newman et al. states that the transfer coefficient can increase up to 2 [283]. The net current density is obtained by substituting Equation (5.19) and Equation (5.20) into Equation (5.18) [258].

$$j = nF\left(k_{0,f}C_{Ox}exp\left[\frac{-\alpha_{Rd}F\emptyset}{RT}\right] - k_{0,b}C_{Rd}exp\left[\frac{\alpha_{Ox}F\emptyset}{RT}\right]\right) \quad (5.22)$$

At equilibrium, the forward and the backward reaction takes place simultaneously, generating zero net currents.

Based on exchange current density (j_0) and assuming only one electron transfer takes place.

$$\alpha_{Rd} = \alpha_{ox} = \alpha \quad (5.23)$$

$$j = j_0\left(exp\left[\frac{-\alpha F\eta_{rev}}{RT}\right] - exp\left[\frac{(1-\alpha)F\eta_{rev}}{RT}\right]\right) \quad (5.24)$$

This is known as the Butler-Volmer equation. η_{rev} is an equilibrium potential or a reversible potential. The reversible potential at the anode operating on pure hydrogen is 0 V, and that at the cathode is 1.229 V at 25 ˚C and atmospheric pressure. The net difference between electrode potential and reversible potential is commonly known as the overpotential (η). In the multi-step process, $\alpha_{red} \neq \alpha_{ox}$; hence, the generic form of the Butler-Volmer equation is used to define the electrochemical process.

$$j = j_0\left(exp\left[\frac{-\alpha_{Rd}F\eta}{RT}\right] - exp\left[\frac{(\alpha_{Ox}F\eta)}{RT}\right]\right) \quad (5.25)$$

The difference between electrode potential and the equilibrium potential is referred to as the overpotential, η, in Equation (5.25). As the Butler-Volmer equation is valid to represent both anode and the cathode electrochemical reaction,

$$j_a = j_{0,a}\left(exp\left[\frac{-\alpha_{Rd,a}F\eta_a}{RT}\right] - exp\left[\frac{(\alpha_{Ox,a}F\eta_a)}{RT}\right]\right) \quad (5.26)$$

and

$$j_c = j_{0,c}\left(exp\left[\frac{-\alpha_{Rd,c}F\eta_c}{RT}\right] - exp\left[\frac{(\alpha_{Ox,c}F\eta_c)}{RT}\right]\right) \quad (5.27)$$

The anode overpotential is positive, while cathode overpotential is negative. This makes the first term in the bracket of Equation (5.26) negligible, and leads to a negative anode current density, while the second term in the bracket of Equation (5.27) becomes negligible, obtaining positive cathode current density.

The exchange current density $(j_{0,a/c})$ is the function of the species concentration, operating temperature, and a function of the reference current density, electrode catalyst loading and ECSA.

$$j_{0,a/c} = j_{0,a/c}^{ref} a_{cl} L_{cl}\left(\frac{c_i}{c_i^{ref}}\right)^{\gamma} exp\left[-\frac{E_0}{RT}\left(1 - \frac{T}{T_{ref}}\right)\right] \quad (5.28)$$

Equation (5.28) derives the exchange current density (j_o) from the reference exchange current density (j_0^{ref}) [A cm^{-2}] per unit catalyst surface area, typically obtained at the room temperature and the atmospheric pressure. This is the measure of readiness of the electrode to start the electrochemical reaction. The electrode roughness is the function of a catalyst specific area (a_{cl}) and Pt loading on the catalyst electrode, denoted by L_{cl}. γ is the pressure coefficient that varies between 0.5 to 1.

The Tafel equation

In PEFCs, anode exchange current density is a few orders higher than the cathode exchange current density. This causes higher cathodic activation overpotential. Whilst considering overpotential at the cathode electrode α_{Ox} <<< α_{Rd}, the second term in Equation (5.25) can be neglected, and the net current density produced by the cell is obtained by the reduced Butler-Volmer equation. α_c is the reduction process at the cathode.

$$j = j_o exp\left[\frac{-\alpha_c F \eta}{RT}\right] \tag{5.29}$$

The reduced form of the Butler-Volmer equation gives an expression for the overpotential as the function of cathodic and anodic current.

$$\eta_{act,c} = \frac{RT}{\alpha_c F}\, ln\left(\frac{j}{j_{o,c}}\right);\ \eta_{act,a} = \frac{RT}{\alpha_a F}\, ln\left(\frac{j}{j_{o,a}}\right) \tag{5.30}$$

The equations above can be written in the simplified version as,

$$\eta_{act} = a + blog(j) \tag{5.31}$$

where,

$$a = -2.3\frac{RT}{\alpha F}\log(j_o);\ b = -2.3\frac{RT}{\alpha F} \tag{5.32}$$

b is known as Tafel slope that depends exclusively on transfer coefficient (α).

5.3.2 Agglomerate model

The agglomeration model treats the CL kinetics involving transport mechanisms of electrons, protons, and gas in most details. In this approach, the catalyst layers are

considered to be the compaction of CL agglomerates with the inter-agglomerate pore-spaces [218,289]. Nafion electrolyte, reactants and product water co-exist in the inter-agglomerate pore-spaces. Recently, the spherical agglomeration approach has gained much interest to model the continuum catalyst layer as this approach provides an additional parameter to modulate the transfer current density while providing better model predictions [218,258,289–293].

Hence, in order to provide the more appropriate representation of the CL structure, the spherical-agglomeration model has been adapted. This approach considers that each agglomerate consists of three phases, Pt dispersed on carbon, i.e. *Pt/C*, and ionomer electrolyte occupies inter-agglomerate spaces and the void space, i.e. CL porosity.

Figure 5.7 provides a schematic representation of the CL with an agglomerate structure. The overall electrochemical reaction at the CL is subdivided into multiple process steps, as described by Sun et al. [218]:

a. Step 1 – multicomponent diffusion of reactant species
b. Step 2 – reactant dissolution at the outer boundary of electrolyte/water film
c. Step 3 – diffusion of dissolve reactant species in the electrolyte film surrounding the agglomerate
d. Step 4 – diffusion of dissolve reactant gases within the agglomerate
e. Step 5 – electron conduction in the cathode, both in the GDL and CL
f. Step 6 – proton transport in the solid and electrolyte phases of the CL, respectively
g. Step 7 –Redox reaction on the CL surface

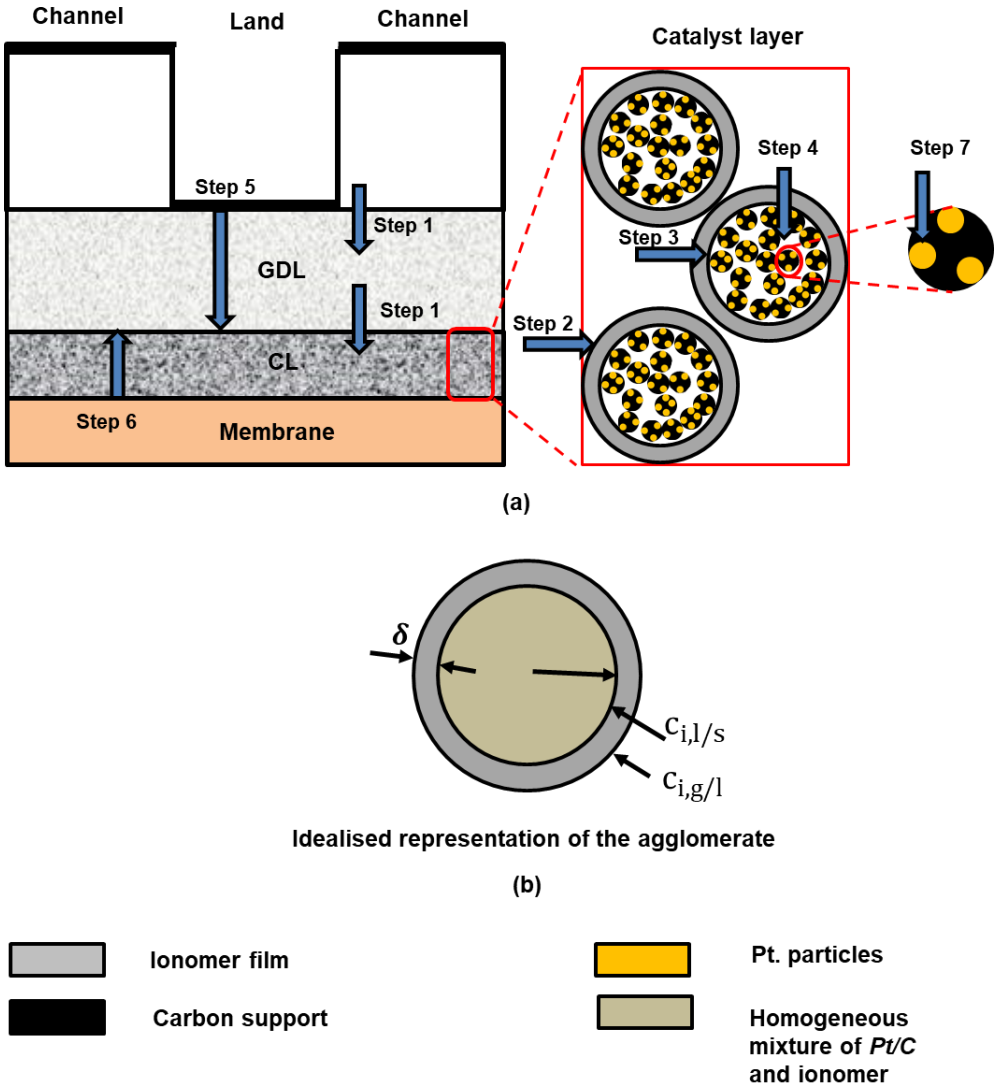

Figure 5.7– Schematic representation CL with an agglomerate structure, (a) diffusion of the reactant species through the ionomer film surrounding the agglomerate showing key processes, (b) idealised representation of *Pt/C* agglomerate

Hence, CL can be thought of as the cluster of individual carbon particles with Pt. catalyst dispersed on its surface, and the carbon-black particles are held together as a cluster by the electrolyte film surround the particles, as shown in Figure 5.7. The

concentration of the dissolved species at the gas/electrolyte interface is described by Henry's law

$$c_{i,g/l} = \frac{P_i}{H_i} \tag{5.33}$$

where $c_{i,g/l}$ [mol m^{-3}] is the concentration on the dissolved reactant species at gas/electrolyte interface, P_i [Pa] and H_i [Pa m^3 mol^{-1}] are the partial pressure and Henry's constant of the reactant species *i*, respectively.

Assuming that the transport of reactant species from high to low concentration, the diffusion of the reactant species from gas/electrolyte interface to the reaction sites, i.e. to the electrolyte/solid interface can be described by the Fick's law (Step 4).

$$N_i = -D_i^{eff} \frac{\partial c_i}{\partial r} \tag{5.34}$$

where N_i [mol m^{-2} s^{-1}] is the molar flux of the reactant through the ionomer electrolyte/water film surrounding the agglomerate, D_i^{eff} [m^2 s^{-1}] is the effective diffusion coefficient of the reactant, C_i [mol m^{-3}] is the reactant concentration, and *r* [m] is the radius.

By postulating that the Nafion ionomer/water film envelops the agglomerate uniformly and the size of the agglomerate is much larger than the film thickness, the flux of the dissolved species can be calculated as,

$$N_i = D_i^{eff} \frac{r_{agg}}{(r_{agg} + \delta)} \frac{(c_{i,g|l} - c_{i,l|s})}{\delta} \tag{5.35}$$

By applying mass balance, at steady state, the amount of species consumed in the electrochemical reaction equals to the species diffusing to the active surface.

$$R_{i,agg} = a_{agg} N_i \tag{5.36}$$

where a_{agg} [m^{-1}] is the specific area of the agglomerate that represents surface area per agglomerate volume, and R_i [mol m^3 s^{-1}] is the rate of the electrochemical reaction. By assuming that the overall ORR follows first-order kinetics with respect to the reactant concentration [289], gives:

$$R_{i,agg} = k_{agg} c_i \tag{5.37}$$

where k_{agg} [s^{-1}] is the reaction rate constant that represents the reactions occurred within the agglomerate. The overall reaction rate in the agglomerate can be expressed in terms of reactant concentration at electrolyte/solid interface, $c_{i,l|s}$; electrochemical reaction rate constant, k_{agg}; and an effectiveness factor of the electrode reaction, E_r:

$$R_{i,agg} = E_r k_{agg} c_{i,l|s} \tag{5.38}$$

The effectiveness factor represents the geometry of the agglomerate and the resistance to the reactant mass transport within the agglomerate. The effectiveness factor for the spherical agglomerates can be given as [250]

$$E_{r,sph} = \frac{1}{\emptyset_L}\left(\frac{1}{tanh(3\emptyset_L)} - \frac{1}{3\emptyset_L}\right) \tag{5.39}$$

where $\emptyset_L$ is a dimensionless group, commonly known as Thiele's modulus for the chemical reaction:

$$\emptyset_L = \frac{r_{agg}}{3}\sqrt{\frac{k_{agg}}{D_{agg}^{eff}}} \tag{5.40}$$

where D_{agg}^{eff} [m^2 s^{-1}] is the reactant effective diffusive coefficient inside the agglomerate, that can be represented as,

$$D_{agg}^{eff} = D\left(\varepsilon_{agg}\right)^{\tau_{agg}} \tag{5.41}$$

where D [m^2 s^{-1}] is the diffusivity of dissolved species in the electrolyte phase, ε_{agg} is the proportion of electrolyte phase in agglomerate and τ_{agg} is the tortuosity factor of the agglomerate that is assumed to be 1.5 [289].

According to Faraday's law, the volumetric current density is a function of the consumption rate of the reactants,

$$j_{i,agg} = nFE_r k_{agg} c_{i,g|l} \tag{5.42}$$

where $j_{i,agg}$ [A m^{-3}] is the volumetric current density based on the agglomerate volume, and the subscript *i* refers to anode or cathode, respectively. Combining equations from (5.35) to (5.42) the concentration of the dissolved species at electrolyte/solid interface is obtained as:

$$c_{i,g|l} = \left[1 + \frac{E_r k_{agg}\left(r_{agg} + \delta\right)\delta}{a_{agg} r_{agg} D_i^{eff}}\right]^{-1} c_{i,l|s} \tag{5.43}$$

Substituting Equation (5.43) into Equation (5.42) gives:

$$j_{i,agg} = nF\left[\frac{1}{E_r k_{agg}} + \frac{\left(r_{agg} + \delta\right)\delta}{a_{agg} r_{agg} D_i^{eff}}\right]^{-1} c_{i,l|s} \tag{5.44}$$

Substituting Equation (5.33), Henry's law into Equation (5.44),

$$j_{i,agg} = nF\frac{P_i}{H_i}\left[\frac{1}{E_r k_{agg}} + \frac{\left(r_{agg}+\delta\right)\delta}{a_{agg} r_{agg} D_i^{eff}}\right]^{-1} \quad (5.45)$$

Hence, the current density obtained from the Butler-Volmer equations (Equation (5.26) and Equation (5.27), could be transferred to the volumetric current density. Instead of defining exchange current density, j_0, on a geometric area basis, it can be based on the active or effective platinum surface area, a_{Pt}^{eff}. The approach allows effective scaling of the platinum loading on the electrode. Hence, to calculate the effective platinum surface area, the actual platinum surface area based on the Pt loading and Pt particle size is obtained.

$$a_{Pt}^{eff} = \varepsilon_l a_{pt} \quad (5.46)$$

where a_{pt} [$m^2\ m^{-3}$] is the specific Pt surface area per unit catalyst layer volume, i.e. equivalent to platinum loading divided by the catalyst layer thickness multiplied by the specific surface area of the platinum particles, S_{ac}:

$$a_{pt} = \frac{m_{pt}}{h_{cl}} S_{ac} \quad (5.47)$$

The surface area per unit mass of an individual Pt particle of radius, r_{pt}, is given as:

$$S_{ac} = \frac{3}{r_{pt}\rho_{pt}} \quad (5.48)$$

The specific area, of the agglomerate, a_{agg} [m^{-1}] represents surface area per agglomerate volume which can be calculated based on the Pt loading as:

$$a_{Pt}^{eff} = \frac{\varepsilon_l m_{pt} S}{h_{cl}(1-\varepsilon_{cl})} \quad (5.49)$$

where m_{pt} [mg cm^{-2}] is the Pt loading on the catalyst layer, S [cm^2 g^{-1}] is specific active surface area, ε_l is an effective platinum surface ratio, and h_{cl} [μm] is the thickness of the catalyst layer.

Therefore, the rate of electrochemical reaction at the cathode CL can be defined as ;

$$k_{c,agg} = \frac{\varepsilon_l m_{pt} S}{4F h_{cl}(1-\varepsilon_{cl})}\left(\frac{j_{0,c}^{ref}}{C_{O_2}^{ref}}\right)\left(exp\left[\frac{-\alpha_c F\eta}{RT}\right] - exp\left[\frac{((1-\alpha_c)F\eta)}{RT}\right]\right) \quad (5.50)$$

5.3.3 Charge transport

The charge balance equations are solved to obtain solid phase and electrolyte phase potentials. As the charge transport takes place in all the domains; the conservation of charge should be achieved at both anode and cathode domain and at the membrane. This was attained by

$$\nabla i^s + \nabla i^m = 0 \quad (5.51)$$

where superscript *s* and *m* stands for a solid phase in the domain, i.e. CL and electrolyte membrane; respectively. The charge balance in the domain can be achieved by balancing solid and electrolyte potential. Therefore, according to Ohms law:

$$\nabla i^s = \nabla \cdot (-\sigma_s^{eff} \nabla \varphi_s) \quad (5.52)$$

$$\nabla i^m = \nabla \cdot (-\sigma_m^{eff} \nabla \varphi_m) \quad (5.53)$$

where σ_s^{eff} and σ_m^{eff} [S m^{-1}] are effective conductivity for electrons and ions, respectively. While $\sigma_{gdl,through}^{eff}$ is a function of cell compression, σ_m^{eff} is a function of

membrane water content, as discussed in section 1.3.2.1, φ_s and φ_l [V] is the solid and electrolyte phase potentials respectively, which is defined as,

$$\eta^{a/c} = \varphi_s - \varphi_l - E_i^{eq} \tag{5.54}$$

Here, E_i^{eq} [V] is the equilibrium potential of the electrode. E_a^{eq}, i.e. anode equilibrium overpotential is zero at standard conditions (T = 25 °C, P_{H_2} = 1 atm, c_{H^+} = 1.0×10^{-7} M) and E_c^{eq} is cathode equilibrium cell potential. Due to the relatively high current conductivity of the electrode, the Ohmic resistance is neglected. Therefore, the cell voltage V_{cell} [V] is obtained from the membrane resistance, current density and overpotential shown as

$$V_{cell} = E^0 - \eta^a - |\eta^c| - j_m R_m \tag{5.55}$$

where E^0 [V] is the open-circuit voltage (OCV) of the fuel cell.

5.4 Mass transport in the porous domain

5.4.1 Viscous flow

In viscous flow, the gas behaves as the bulk fluid is driven under a pressure gradient. The molecular impact between neighbouring particles is more than the collision with the wall. Viscous flow in a porous media is defined by ‘Darcy’s law’ that solves for the pressure gradient. Being the bulk flow method, this does not include individual species in the gas mixture. The bulk velocity of the flow is

$$V_d = \frac{k}{\mu}(\nabla P - \rho g) \tag{5.56}$$

where V_d is Darcy's velocity, K is absolute permeability, μ is the dynamic viscosity of the fluid and ∇P is a pressure gradient.

5.4.2 Continuum diffusion

The different species of the mixture have interrelated concentration, temperature and electric gradients. In binary mixtures, the diffusive flux is directly proportional to the concentration.

$$N_i = -D_{ij}\nabla C_i \tag{5.57}$$

Here, N_i is the 'diffusion flux' [mol $m^{-2}s^{-1}$], D_{ij} is the binary diffusion coefficient [m^2s^{-1}] and the concentration gradient of the reactant species is given by ∇C_i. This is Fick's law of diffusion.

Equation (5.57) is appropriate for the binary species solution; however, it fails for a multi-component solution due to multiple concentration gradients and the individual species velocities. In PEFCs, the ternary species transport is observed; hence, this requires the multicomponent species model such as Stefan-Maxwell multicomponent diffusion that takes into an account the interdependent diffusivity of each species and solve for the concentration gradient.

$$\nabla C_i = \sum_{i \neq j}^{n} \frac{x_i N_j - N_i x_j}{C_T D_{ij}} \tag{5.58}$$

Using ideal gas law,

$$\mathrm{C_T} = \frac{p}{RT} \tag{5.59}$$

Hence, the Stefan-Maxwell transport equation is

$$\nabla C_i = RT \sum_{i \neq j}^{n} \frac{x_i N_j - N_i x_j}{p D_{ij}} \tag{5.60}$$

Here, *x* is the molar mass of individual species; *R* and *T* are universal gas constant, and temperature [K], respectively and p is the bulk density [kg m^{-3}]. For diffusion in the porous media, such as GDLs or MPLs, the binary diffusion coefficient D_{ij} should be modified to D_{ij}^{eff} using tortuosity, porosity, and pore saturation. Incorporating the effect of the porous structure of the GDL and the resistance offered by such blockages, the binary diffusivity is modified by accounting the effect of GDL porosity and the tortuosity. According to the Bruggeman correlation, the effective diffusivity in a porous GDL can be expressed as,

$$D_{ij}^{eff} = \varepsilon^{\tau} D_{ij} \tag{5.61}$$

where ε is the porosity of the structure that represents a ratio of pore volume to the total volume, and τ is the tortuosity that offers additional resistance to the diffusion due to the convoluted flow path within the porous medium. As has been seen in Chapter 4, the compression (from 20% to 60%) can change the porosity and tortuosity from 0.25 to 0.7 and 0.25 to 25, respectively, depending on the location of the porous structure.

5.4.3 Knudsen flow

Knudsen flow is observed where the frequency of gas molecule collision with the wall is much higher than the neighbouring molecule. Knudsen flow dominates with an increase in density of porous media, where a mean free path is 10 times greater than the pore radius. This suggests Knudsen flow might not be required for the GDL, but it's the preliminary diffusion process defining mass transport in CLs and MPLs.

$$N_{i,k} = -\left(\frac{2}{3}r\right)\sqrt{\frac{8RT}{\pi M}}\left(\frac{dc}{dz}\right) \tag{5.62}$$

Here, *r* is the pore radius of the structure. This can be obtained from experimental techniques such as X-ray CT or TEM [188,294]. *M* is the molar mass of gas species, and *dc/dz* is the concentration gradient of gas species. $\left(\frac{2}{3}r\right)\sqrt{\frac{8RT}{\pi M}}$ is known as Knudsen diffusivity (D_k), that is constant for the straight cylindrical pore, in case the of porous media,

$$D_{k,porous\ media} = -\frac{\varepsilon}{\tau}D_{k,single\ phase} \tag{5.63}$$

where ε is porosity and τ is tortuosity of the porous medium

5.4.4 Porous media conductivity

GDLs are made from carbon fibre, and the conductivity through carbon fibres need to consider in the model. Ohm's law is used to model GDL electrical conductivity [295].

$$i_i = -\sigma_o \varepsilon_{GDL}^{\tau} \nabla \phi_{gdl} \tag{5.64}$$

where σ_o is the electrical conductivity of the GDL. The effect of porosity and the tortuosity on the GDL conductivity is included in the equation through the Bruggeman correlation. *i* and ϕ are current and potential, respectively. Conducting and insulating phase co-exists in the GDLs. PTFE coating is the insulating phase; whereas carbon fibre is the conducting phase.

5.4.5 Vapour and gaseous species transport in PEFC ($\mathbf{X}_i^{a/c}$)

The velocity of the gaseous species (O_2, N_2, H_2, $H_2O_{(v)}$) was obtained by solving the continuity equation.

$$S_g = \nabla \cdot (\rho_g u_g) \tag{5.65}$$

where, ρ_g is the density of the gaseous mixture [kg m^{-3}] and u_g is the velocity of the gaseous phase in the porous domain [m s^{-1}]. The source term is S_g [kg m^3 s^{-1}]. The velocity of the gaseous phase was obtained by Darcy's law [71].

$$u_g = -\frac{k_p}{\mu_g}\nabla p \tag{5.66}$$

where, k_p [m^2] is the permeability of porous media. As discussed in the previous chapters, the GDL permeability is highly anisotropic in nature [216,235,296] and can be affected by the compression [45,297,298]. The spatial permeability of the GDL, i.e. in the in-plane and the through-plane orientation can be derived numerically, using the Carman-Kozeny equation or experimentally using the microstructural data. The permeability of the catalyst layer was assumed constant and not affected by the compression. μ_g is the viscosity of the gas mixture [Pa s], and was derived from Wilke's equation that uses kinetic theory extended to the multispecies mixture [299].

$$\mu_g = \sum_i \frac{X_i \mu_i}{X_i + \sum_{i \neq j}(X_j \cdot \phi_{ij})} \tag{5.67}$$

where X_i is the mole fraction of the species in a gaseous mixture, obtained using the concentration solution theory, and μ_i [Pa s] is the viscosity of the gas species.

ϕ_{ij} is the coefficient for each pair of the species in the gas mixture and depends on species viscosities and the molecular weight, M_i [kg mol^{-1}], given by

$$\mu_g = \sum_i \frac{X_i \mu_i}{X_i + \sum_{i \neq j} \left(X_j \cdot \phi_{ij} \right)} \tag{5.68}$$

The species conservation in the GDL/CL domains is given by

$$\frac{\partial (\varepsilon^{eff} C_i)}{\partial t} \nabla \cdot \left(u_g C_i \right) + \nabla \cdot \left(-D_i^{eff} \cdot \nabla C_i \right) = S_i \tag{5.69}$$

Here, as the model is solved in a steady-state, the first term on the left-hand side was assumed 0, C_i [kg m^{-3}] and D_i^{eff} [m^2 s^{-1}] are molar concentration and the effective diffusivity of the gaseous species, respectively [300]. Equations (5.65) through (5.69) are solved for both anode and cathode domains (GDL and CL).

5.5 Modelling framework - 2D single-phase electrochemical model

5.5.1 Formulation of the base-case model

The computational models comprising of five layers, namely cathode GDL (domain 1), cathode CL (CCL) (domain 2), polymer electrolyte membrane (domain 3), anode CL (ACL) (domain 4), anode GDL (domain 5), and bipolar plates on either side of the assembly, as shown in Figure 5.8. The geometric and material properties of each layer are listed in Table 5-1.

i. Reactant gas transport. Humidified feed gases (*RH* 100%) at both cathode and anode were treated as an ideal gas. The gases are transported through the GDL to CL, following the Stefan-Maxwell diffusion law. The membrane is

assumed to be non-permeable to reactant gases and separates the cathode domain from the anode.

ii. Catalyst layer. The base-case model solves the electrochemical reaction based on the concentration-dependent Butler-Volmer kinetics

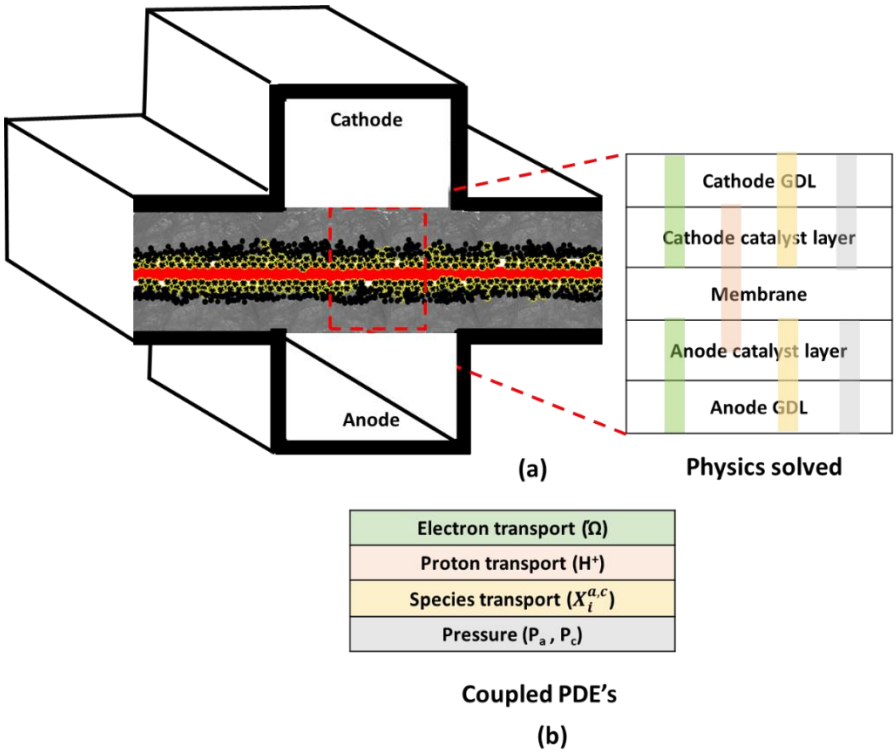

Figure 5.8– Schematics of the computational coupling and the solution methodology, various PDEs were solved at the colour coded computational domains.

5.5.2 Governing equations

By taking all the physical processes and the assumptions into consideration, the set of governing equations used for the base case model is presented in Figure 5.9

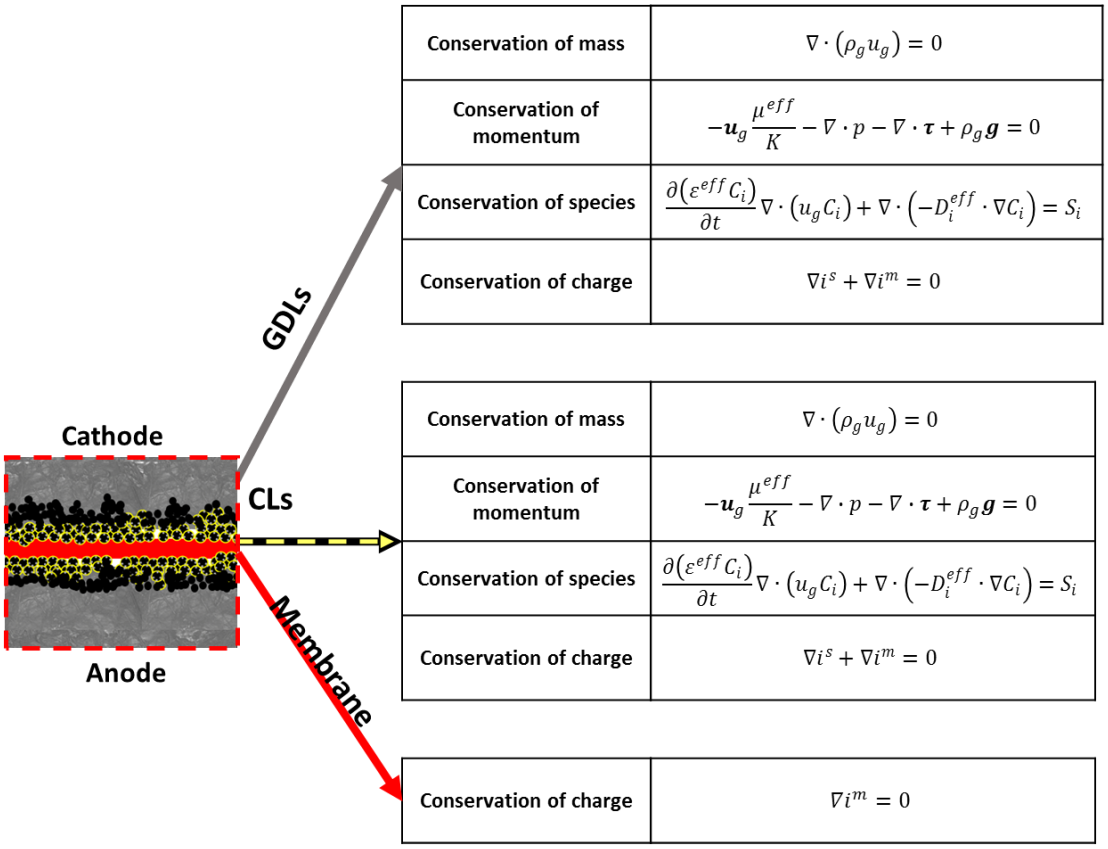

Figure 5.9– Schematic highlighting the governing equation solved in the domains

5.5.3 Boundary and initial conditions

This section presents the initial and boundary conditions used to build the electrochemical performance model. Fully humidified reactant gas at 333 K was specified at both inlets. The mole fraction of the species and pressure at the cathode inlet (boundary A) are given as,

$$X_{H_2O}^c = \frac{P_{sat} RH^c}{P^c}, \qquad X_{O_2}^c = 0.21\left(1 - X_{H_2O}^c\right), X_{N_2}^c = 0.79\left(1 - X_{H_2O}^c\right), \tag{5.70}$$
$$P = P^c$$

Similarly, the mole fraction of the species and pressure at the anode inlet, *i.e*. boundary H are given as,

$$X_{H_2O}^a = \frac{P_{sat} RH^a}{P^a}, \qquad X_{OH_2}^a = 1 - X_{H_2O}^{,c}, P = P^a \tag{5.71}$$

Temperature $T = T_{cell} = 313$ [K] was prescribed at boundaries A, B, H, and G. The boundary conditions for the electrochemical model are given as the fixed potential at GDL/land interface, *i.e.* boundaries B and G. At the cathode, $\varphi_s = V_{cell}$ [V] and the electrical ground condition is applied at the anode, *i.e*. $\varphi_s = 0$ [V].

Table 5-1 – Input parameters used in the model.

Parameters	Value	Ref.
Inlet pressure anode/cathode, P_{in} [atm]	1.1	
Reference temperature, T_{ref} [K]	333.15	
Inlet relative humidity, RH^a/RH^c	100% / 100%	assumed
Liquid water density, ρ_{liq} [kg m^{-3}]	1.0×10^3	
The viscosity of liquid water, μ_{liq} [Pa s]	3.56×10^{-4}	
Cell voltage, V_{cell} [V]	0.6	

Platinum loading, m_{pt} [mg cm^{-2}]	0.4	[218]
Agglomerate radius, r_{agg} [m]	10 × 10^{-6}	[218]
Henry's hydrogen constant, H_{H2} [Pa m^{-3} mol^{-1}]	4.56	[252]
Platinum surface area ratio, ε_l	0.75	[252]
The fraction of ionomer in the CL, ε_m^{agg}	0.2	[252]
The specific active surface area of platinum, *S* [cm^{-2} g^{-1}]	250,000	[252]
Equivalent molecular weight of the membrane EW_m [kg mol^{-1}]	1.1	[252]
Catalyst layer porosity, ε_{cl}	0.2	[250]
Initial GDL porosity, $\varepsilon_0^{No\ compression}$	0.75	Measured
Contact angle, θ	120°	[301]
Carbon density, ρ_c [kg m^{-3}]	1.80 × 10^3	[252]
Density of liquid water, ρ_{liq} [kg m^{-3}]	983	[252]
Density of dry membrane, ρ_m [kg m^{-3}]	2000	[252]
Density of Pt particles, ρ_{pt} [kg m^{-3}]	21.43 × 10^3	[252]
Density of GDL, ρ_{GDL} [kg m^{-3}]	440	[252]

Density of CL, ρ_{CL} [kg m^{-3}]	387	[252]
Through-plane electrical conductivity of GDL, $\sigma_{through-initial}^{gdl}$ [S m^{-1}]	240	[302]
In-plane electrical conductivity of GDL, σ_{in}^{gdl} [S m^{-1}]	1600	[302]
Electrical conductivity of CL, σ^{CL} [S m^{-1}]	500	

5.5.4 Numerical technique

All of the PDEs in this model were solved in the commercial software environment, COMSOL Multiphysics 5.4. Equations (5.52) - (5.54), and (5.65), (5.66), (5.69) are predefined in the COMSOL environment, while all remaining equations were added externally to the model. The details of PDE couplings are as shown in Figure 5.8. The iterative approach has been adopted to solve the modelling framework. The convergence criteria were set at 10^{-6}. The cell voltage, V_{cell} [V] was used as a variable parameter that ranges from 1 V to 0.3 V to generate the polarisation curve in steps of 0.01 V. The details of the solution procedure used is as shown in Figure 5.10.

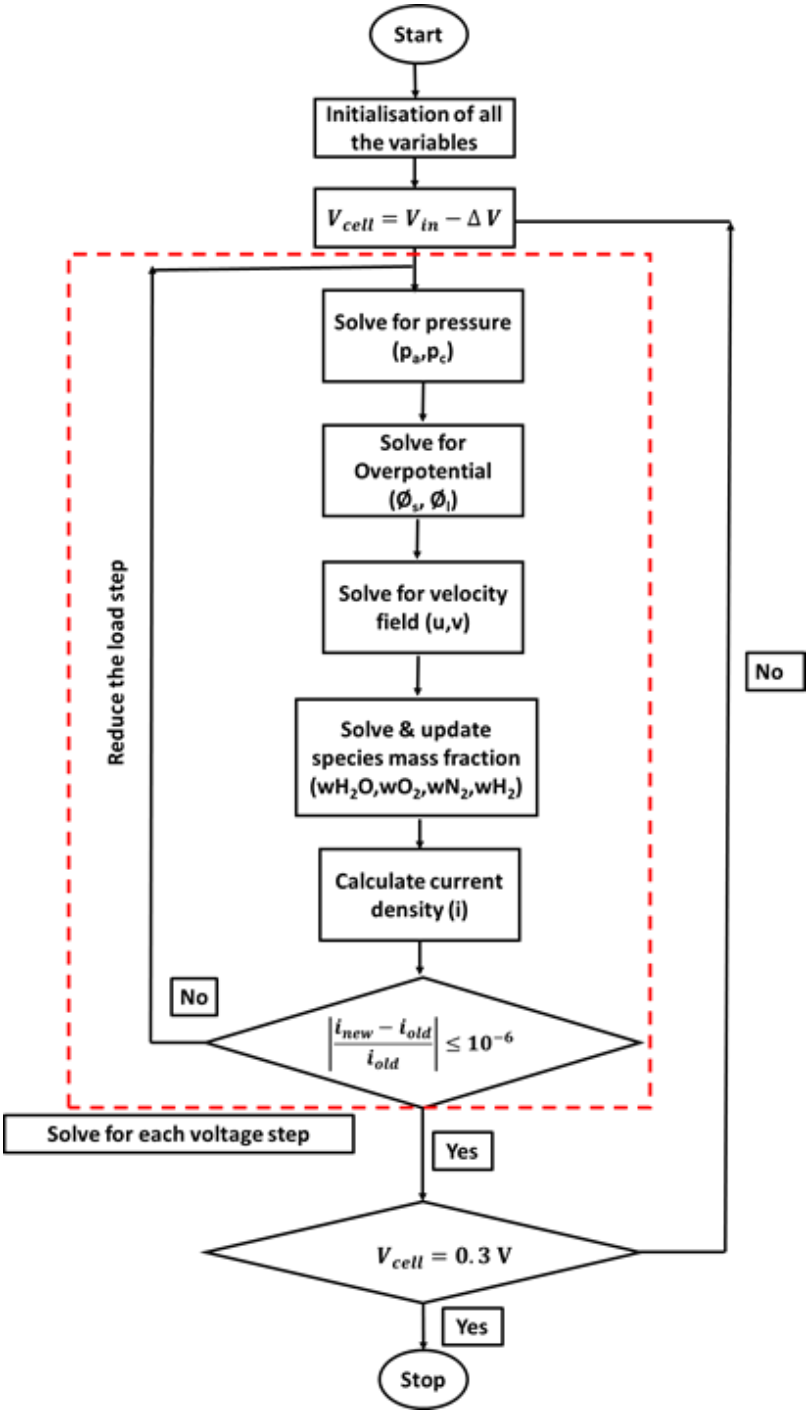

Figure 5.10– Iterative modelling algorithm was adapted where the analysis was performed at each cell voltage, V_{cell} [V], V_i = 1 V and ΔV = 0.01 V

Mesh independency was checked by solving a base-case study using three different mesh density; 2,000, 6,000, and 8,000, respectively. 1% deviation was observed in terms of the polarisation curve, pressure and species molar concentration. Thus, the mesh density of 8,000 was selected as a good trade-off between the result accuracy and computational time.

5.5.5 Results and discussions

5.5.5.1 Model validations

Figure 5.11 compares the experimental data with the results simulated by the agglomeration model. The parameters used for model validation and base case are listed in Table 5-2.

It is apparent from Figure 5.11 that the overall simulation results are in good agreement with the experimental data. The nominal deviation in results at a higher voltage from the experimental data is due to the variation in catalyst layer properties. At higher current densities there is a sudden loss in voltage which is caused by the increase in mass transport resistance. The deviation at higher current density is due to the strong dependence on the mass transport losses and the presence of liquid water. The agglomerate model accounts for the resistance of oxygen transport to the Pt surface; hence, the agglomerate film model gives a good correlation with the experimental data. This is in agreement with widely published literature [218,250,289,292,303].

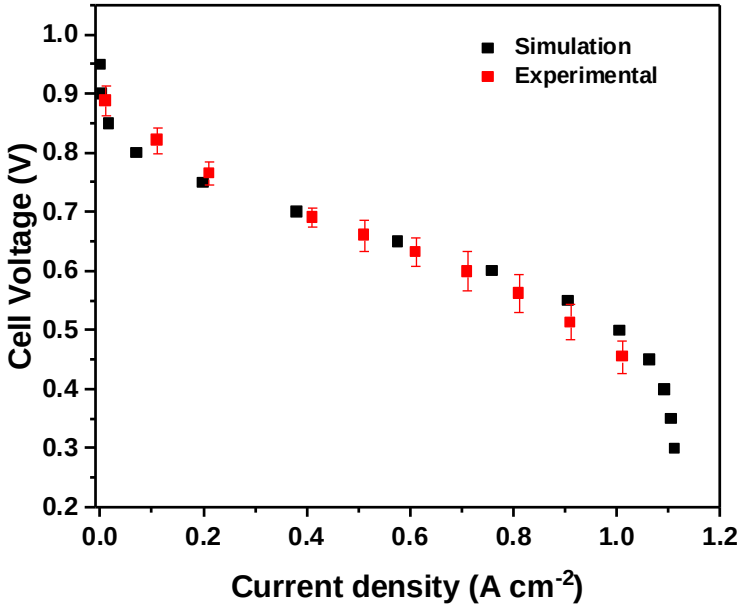

Figure 5.11– Comparison between the base case simulation model and the experimental results. the experimental details are provided in Table 5-2, the details of the cell used for the experiment are provided in section 3.1

Table 5-2 – Operating conditions, base-case simulation and experimental data

Parameters	Base-case simulation	Experimental data
Inlet pressure anode/cathode, P_{in} [atm]	1.1	
Inlet flow rate, $\dot{Q}$ [SLPM]		0.5/0.5
Reference temperature, T_{ref} [K]	333.15	333.15
Inlet relative humidity, RH^a/RH^c	100% / 100%	100% / 100%
Liquid water density, ρ_{liq}[kg m^{-3}]	1.0 × 10^3	
The viscosity of liquid water, μ_{liq} [Pa s]	3.56 × 10^{-4}	
Cell voltage, V_{cell} [V]	0.6	
Platinum loading, m_{pt}[mg cm^{-2}]	0.4 [218]	
Agglomerate radius, r_{agg}[m]	10 × 10^{-6} [218]	
Cell compression		25%

5.5.5.2 Effect of porosity of the performance

Polarisation curve

Figure 5.12 illustrates the impact of GDL porosity on the PEFC polarisation performance and the localised current density distribution. As shown in section 4.3.6.1,

GDL porosity varies between 0.75 at uncompressed state to 0.3 at highly compressed condition. Hence, for this analysis, four different porosities were chosen; 0.4, 0.5, 0.6, and 0.75. Notionally, a polarisation curve, as shown in Figure 5.12(a), can be partitioned into three regions, the activation dominant region, (V > 0.8 V), the Ohmic dominant region (0.5 V < V < 0.8 V) and the mass transport dominant region (V < 0.5 V).

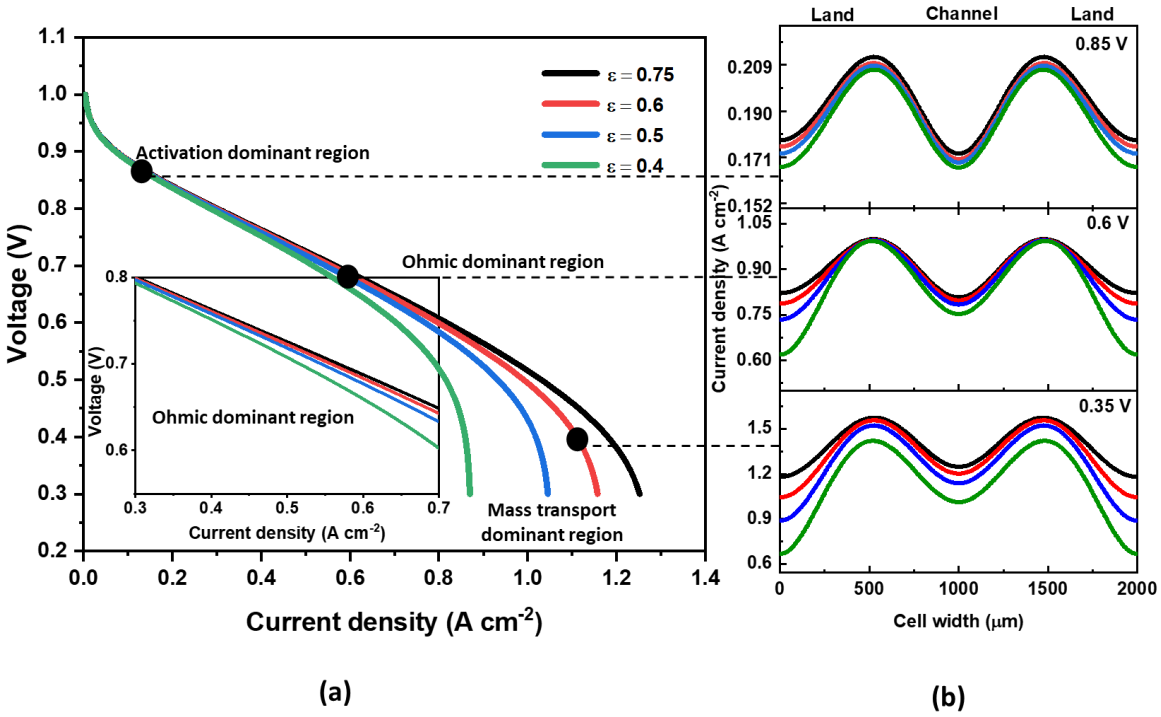

Figure 5.12– Schematics of the computational coupling and the solution methodology, various PDEs were solved at the colour coded computational domains.

It is evident that at low current densities, i.e. at the activation dominant region, the effect of porosity on the averaged current density is negligible. With an increase in the current density, the electrode kinetics demands for more reactant, and hence, the localised starvation zones emerge from the material limitations that cannot provide sufficient reactant to catalyst layers. This effect is predominantly observed in the

cathode domain. This is expressed by Equation (5.61), showing the relationship between gas diffusivity and the porosity. Hence, with an increase in the current density, the mass transport losses dominate the fuel cell performance, which is preliminarily defined by the resistance to the gas diffusivity. Thus; with an increase in the current density, the effect of porosity on the PEFC performance is substantial at the mass transport dominant region. However, it is essential to note that, at lowered porosity, the effect of mass transport losses could dominate the Ohmic region.

Figure 5.12 (b) depicts the distribution of current density at the interface between the catalyst layer and GDL for three load conditions and variable porosities. The key observations include: non-uniformity in the current density distribution, i.e. notional 'peaks' and 'valleys' become more defined with an increase in the operating load. The current density 'peaks' were observed at the interface edge between channel and land, and current density 'valleys' were observed towards the centre of the land region.

In the activation region, (V = 0.85 V), at ε = 0.75, the standard deviation in the localised current density was 0.013 A cm^{-2}, with local minima under the land region is 0.1725 A cm-2 , and local maxima reaching up to 0.2123 A cm^{-2}. With lowering the GDL porosity (ε) to 0.4, the standard deviation in the plotted current density distribution values reached up to 0.014 A cm^{-2}. Though lowering the GDL porosity has resulted in an increase in the standard deviation in local current density by 8.35%, the averaged current density remained virtually identical (maximum standard deviation is less than 1%). This result shows that even though the results obtained for four GDL porosity values yield identical data on the polarization curve, the local current distributions are different. This could be explained by the fact that the performance dynamics at the activation region is primarily based on the properties of CL, and GDL properties have minimal effect on the performance at the activation dominant region.

In the Ohmic dominant regions, i.e. V = 0.6 V, 'localised peaks' in the current density distribution were observed near the corner of the land, irrespective of the cell GDL

porosity. At higher porosity condition, i.e. ε = 0.75, the standard deviation was 0.03523 A cm^{-2}. The deviation increase in the Ohmic region by three folds compared to the activation region. With lowering the porosity to ε = 0.4, the standard deviation in the plotted current density distribution values reached up to 0.116 A cm^{-2}. Lowering the GDL porosity has resulted in an increase in the standard deviation by 77.17%. However, the change in the localised maxima (localised peak in the current density) was less than 1%; whereas the localised minima (valley) has lowered by 23%. This highlights that the GDL porosity has affected markedly under the land region in the Ohmic dominant region. However, the effect of change in contact resistance and the GDL through-plane conductivity with the change in the GDL porosity is not accounted in the present model (effect of porosity models). Therefore, the effect on the Ohmic resistance with respect to change in the GDL porosity has not impacted the localised maxima in the current density.

In the mass transport dominant region, i.e. V = 0.35 V, with the increased current density, the requirement of reactant increases. Also, increased current density results in the accumulation of water under the land region that increases mass transport resistance. Hence, with lowering GDL porosity from 0.75 to 0.4, the non-uniformity in the current density distribution has increased from 0.130 A cm^{-2} 0.228 A cm^{-2}. Lowering the GDL porosity has resulted in a 44 % reduction in ‘under the land’ current density while 18.5% reduction in under the channel current density. Therefore, in the mass transport dominant region, i.e. V = 0.35 V, the reduction in the GDL porosity has resulted in the deeper current density distribution valley while lowering overall performance.

The molar concentration of oxygen

The oxygen concentration at the cathode CL determines the fuel cell performance. The effect of cell compression and the operating load on the oxygen concentration inside the cathode domain, i.e. cathode GDL and CL are depicted in Figure 5.13. The

highest oxygen concentration exists under the channel region. With lowering GDL porosity, the oxygen transport resistance increases, lowering the oxygen concentration, preliminary affected in the region under the land.

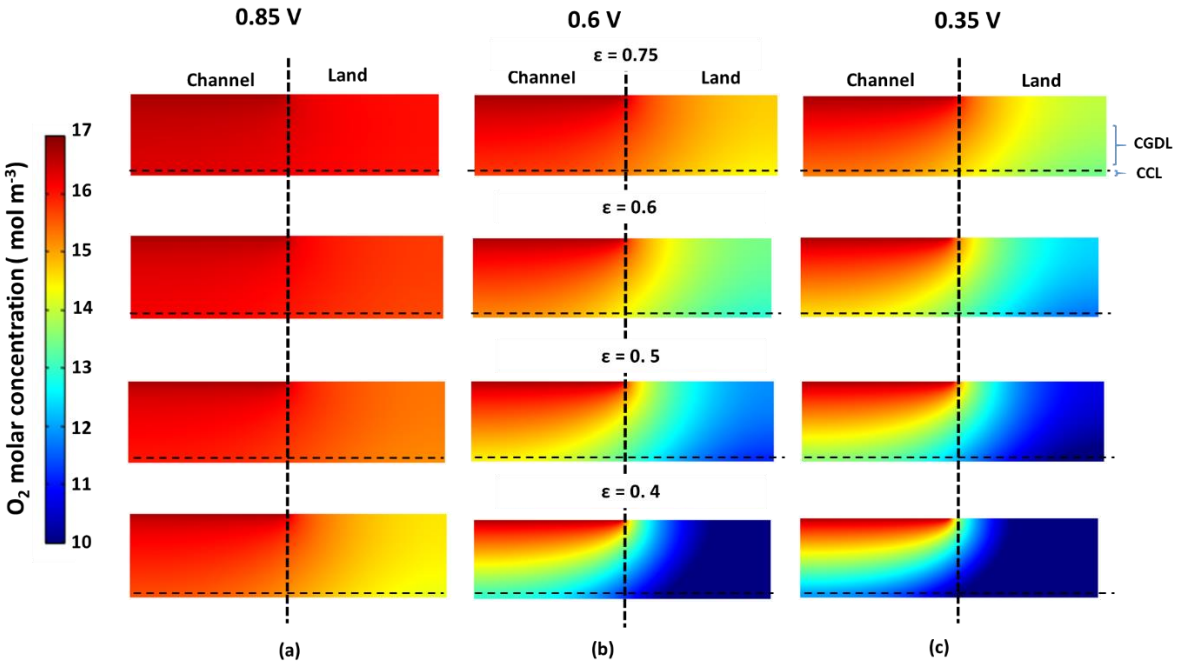

Figure 5.13– Effect of GDL porosity on the distribution of oxygen molar concentration, measured at ε = 0.75, 0.6, 0.5, and 0.4., (a) activation dominant region, V= 0.85 V, (b) Ohmic dominant region, V= 0.6 V, and (c) mass transport dominant region, V= 0.35 V,

At the activation dominant region, i.e. V = 0.85 V, lowering the GDL porosity has resulted in both the in-plane and the through-plane oxygen concentration gradient. At ε = 0.75, oxygen concentration under the channel region remains almost constant (variation less than 1%) when compared between the channel-GDL interface and CL-membrane interface. At lowered porosity, i.e. ε = 0.4, the concentration gradient between the channel-GDL and CL-membrane interface has increased to 11.76% when measured under the channel region; however, the same under the land region has reached up to 14.7%.

At the Ohmic dominant region, i.e. V = 0.6 V, lowering the GDL porosity has resulted in an evident oxygen concentration gradient, both the in-plane and the through-plane direction, with highest oxygen concentration at the inlet (channel-GDL interface) and the lowest concentration CL-membrane interface under the land region. Similarly, at the mass transport dominant region (V = 0.35 V), the oxygen concentration has been affected both the GDL porosity and the operating conditions. The effect of the operating condition, i.e. cell voltage is preliminary evident at the higher porosities. With lowering the GDL porosity, the oxygen concentration is virtually similar both at the Ohmic and the mass transport region.

In the lower voltage conditions, i.e. Ohmic and mass transport dominant region, the decrease in oxygen concentration, both in the in-plane and the through-plane direction can be explained by an increase in the rate of oxygen consumption due to enhanced ORR that increases the resistance to oxygen transport. The oxygen transport resistance is determined by the GDL microstructure and subsequently the effective transport properties of the GDL. Based on Equation (5.69), lowering the porosity resulted in lowering oxygen diffusivity and increase in oxygen mass transport resistance.

Cathode overpotential profile

Figure 5.14 represents the overpotential within the cathode catalyst layer. Overpotential is defined as a difference among the solid phase electrode potential (φ_s), electrolyte phase potential (φ_l), and the equilibrium potential of the electrode (E_c^{eq}), according to Equation 5.54. It represents the driving force of the electrochemical reaction. The negative cathode overpotential results in making the second term in the bracket of Equation 5.27 negative, leading to the positive cathode current.

The maximum absolute overpotential was observed under the land region compared to under the channel region, in case of all porosity conditions. The electrons take a longer path under the channel region to reach CL under the land region. This leads

the higher electrical resistance and results in higher solid-phase electrode potential (φ_s) and lowering absolute cathode overpotential under the channel region.

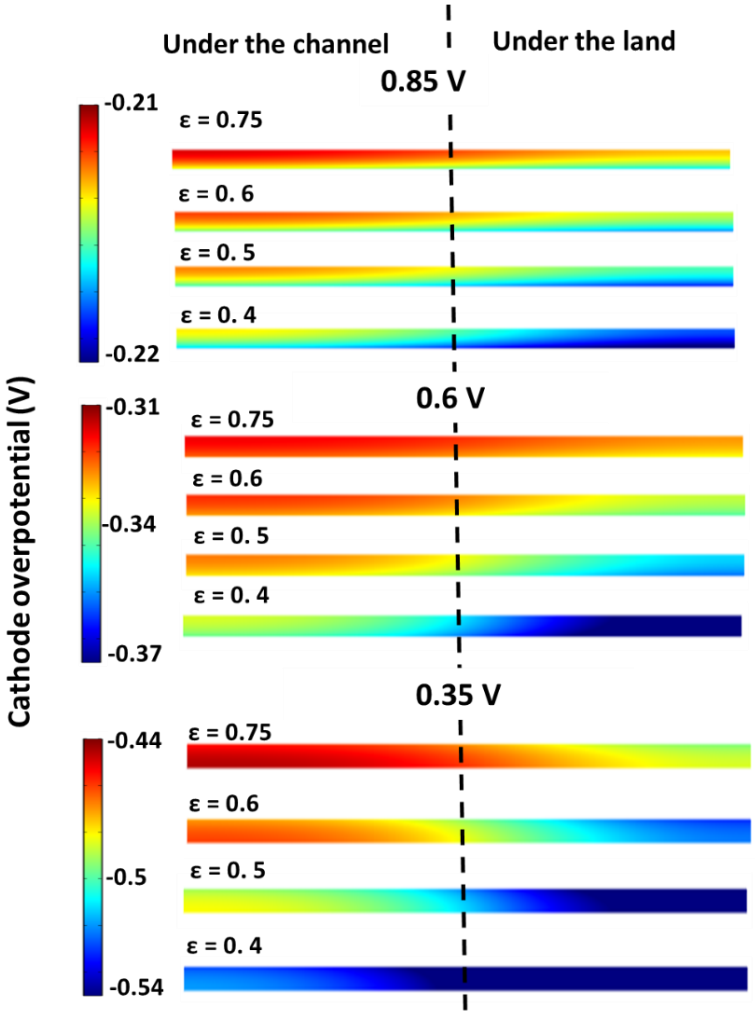

Figure 5.14– Half-symmetry contour plot showing the effect of porosity on the cathode overpotential (η_C), , measured at ε = 0.75, 0.6, 0.5, and 0.4., plotted at the activation (V = 0.85 V), Ohmic (V = 0.6 V) and mass transport (V = 0.35 V) operation

Lower GDL porosity results in enhance electronic conduction, both in the in-plane and in the through-plane direction, reducing Ohmic losses. Hence, reduction in the GDL porosity has resulted in higher absolute overpotential. This behaviour was observed over all the operating conditions. Hence, the GDL porosity and the operating load

leads to the non-uniform distribution of cathode current density and the rate of oxygen reduction reaction (ORR).

This section has presented the effects of the GDL porosity on the PEFC performance. Based on the constitutive relationships described in Section 5.4, the porosity affects mass transport in the GDL and CL, affecting fuel cell performance. As described in the previous chapters, GDL porosity is preliminarily affected by the cell compression that leads to the non-uniform porosity distribution across the active surface area. Chapter 4 collectively describes the effect of cell compression on the GDL porosity and other related effective parameters that affect fuel cell performance. Hence, to generate the comprehensive understanding of the in-situ fuel cell performance, it is important to develop the multi-phase fuel cell model considering the effect of cell compression on the porosity and related effective properties of the fuel cell components. Therefore, the present model stands as the framework to develop the multi-phase non-isothermal fuel cell model.

5.6 Conclusion

The objective of the present chapter was to develop the electrochemical modelling framework for low-temperature PEFCs. This chapter presents the overview of electrochemical modelling techniques for fuel cells, along with the particular challenges encounters during the model developments. Further, this chapter effectively delineates the electrochemical and physical processes governing the fuel cell performance. The series of equations that represents the chemical and physical behaviour of individual components of the fuel cell is developed. The membrane model based on the concentrated and dilute solution theory is presented with the focus on mass transport through the membrane and conservation of protons. This model forms the foundation for the membrane-water content model, and effectively the base of the multi-phase PEFC model, presented in Chapter 6. Both Butler-Volmer and

agglomerate structure-based equations are developed that adequately represent the reaction kinetics at the catalyst layers. Porous media in the fuel cell, i.e. mainly gas diffusion layers play a critical role in defining mass transport processes in the fuel cell. Hence, the chapter has described the mass transport processes that define flow through GDL.

Finally, the chapter presents the framework for a two-dimensional single-phase electrochemical model that presents the polarisation performance of PEFC, validated against the experimental data. The sensitivity analysis was focusing on the effect of GDL porosity highlights that the microstructural parameters affected by the cell compression alter the PEFC performance while emphasising on the importance of the multi-phase PEFC model. Hence, the single-phase model presented in this chapter forms the foundation of a structural-electrochemical multiphase PEFC model that collectively presents the effect of cell compression on the PEFC performance.

Chapter 6
Modelling the effect of non-uniform compression on PEFC performance

Abstract

The way in which a polymer electrolyte fuel cell (PEFC) is brought into mechanical compression has a significant effect on the structure of the membrane electrode assembly (MEA) and its operation. Adequate cell compression is required for effective current collection and gas sealing but can result in structural deformation of the MEA and limit reactant transport with adverse consequences to the electrochemical behaviour of the cell. The present study uses X-ray computed tomography (CT) to characterise the structure of MEAs under compression and determine key initial structural parameters (discussed in Chapter 4). A comprehensive multi-phase, a non-isothermal numerical model is then used to couple structural characteristics of the MEA under compression with the electrochemical performance. The structural model considers the deformation of the GDL's fibrous media under non-uniform (i.e. land and channel) compression, (15%, 25% and 35%), and describes the non-uniform distribution of the effective properties which are used as inputs to the electrochemical model. The effect of compression on performance is most marked in the mass transport region, and non-uniform compression effects are found to be important considerations for robust modelling studies.

Chapter 4has highlighted the effect non-uniform cell compression has on the effective properties on the fuel cell that defines the fuel cell performance. This chapter describes a comprehensive, a two dimensional, through-the-MEA continuum model of the fuel cell model that incorporates the non-linear mechanical behaviour of the GDL observed when subjected to inhomogeneous compression, and it is coupled with the two-phase flow, non-isothermal, steady state model. The present model is based on a spherical-agglomerate catalyst structure to predict the effect of non-uniform compression on water accumulation. The model provides guidance for optimisation of fuel cell compression and the water management for the low-temperature PEFCs having the symmetrically aligned flow-field architecture for the reactant transport.

6.1 Introduction

MEAs typically consists of a polymer electrolyte membrane (typically Nafion), microporous layer (MPL), GDLs and CLs are sandwiched between bipolar plates, in which flow-field channels are machined for transportation of gas and product water. While cell compression is required to provide good electrical contact and adequate sealing [109,110], the MEA components take the majority of the compressive dimension change, as presented in Chapter 4. The symmetrical flow-field architecture results in non-uniform compression of the GDL, leading to a loss of pore volume, primarily in the region under the land. This results in a loss of GDL porosity and permeability, and an increase in mass transport resistance [45,76]. A careful balance has to be struck in achieving effective water management and performance improvement in a fuel cell. The effect of compression on fuel cell performance was studied experimentally by Mason et al. using electrochemical impedance spectroscopy (EIS) [121]. They reported an improvement in contact resistance between the GDL and bipolar plate with an increase in compression. However, the

performance deteriorated with increased compression due to increased mass transport limitation. The effect of compression on water management was studied by Wu et al. using neutron radiography in the plane parallel to the MEA [125], the findings from which support the trade-off situation between electrical contact resistance and mass transport limitation due to flooding. While such experimental investigations provide great insight into fuel cell operation, the slow iterative nature of systematically varying design and operational conditions makes modelling a powerful design tool to examine the effect of such things as compression. The modelling study presented in 0 has highlighted the impact of effective properties such as porosity and conductivity on the fuel cell performance, which are altered non-uniformly under fuel cell compression.

Several classes of computational models have been developed in the last two decades with the aim of fully resolving reactants and liquid water transport, and heat management characteristics [30,255,304,305]. Models that capture water management aspects such as 2D multiphase flow models by Xing et al. [250,292] and water uptake by Chaudhary et al. [252] continue to be developed.

Despite significant efforts put into improving fuel cell models, the majority of models consider the MEA not to be compressed, or at least not to have a varying compression associated with lands and channels. The work of Hottinen et al. is among the first models to elucidate the importance of modelling cell compression to model realistic PEFC performance PEFC [231]. However, the effect of non-uniform compression across a regime of operation, expected to be limited by reactant access to the electrode (i.e., high current density, high relative humidity), could not be captured adequately due to the absence of liquid water. The half-cell MEA study by Mahmoudi et al. revealed that the increase in cell compression primarily affects the region dominated by mass transport. However, the model assumed isothermal operating conditions and the effect of compression on temperature distribution was not

investigated. Zhou et al. developed a compression deformation model and showed non-uniform cell compression affects the porosity of the GDL as well as the contact resistances. This study used the elastic-plastic deformation approach to obtain the porosity distribution across the GDL [227,228].

Currently, the most common approach to resolving fuel cell compression is to use empirical parameters obtained using ex-situ characterisation techniques such as X-ray CT and SEM, followed by implementation of electrochemical models [188]. This approach was taken and refined by Shimpalee et al. using a co-simulation approach where the flow-fields and the MEA were simulated using continuum modelling; whereas the diffusion media was simulated using the Lattice Boltzmann method (LBM) [306]. However, this combination of continuum-based and image-based modelling is computationally expensive and not always representative of the generic fuel cell due to the heterogeneity and variety of the commercially available fibrous materials.

Despite substantial efforts put into developing a compression model for the PEFC, a model that describes the localised effect of compression on liquid water accumulation, membrane hydration and temperature distribution is still not available.

6.2 Model formulation

The present work aims to delineate the effect of compression on the performance. The following methodology was adopted in this study.

Fuel cell geometry and the computational domain. The computational models comprising of five layers, namely cathode GDL (domain 1), cathode CL (CCL) (domain 2), polymer electrolyte membrane (domain 3), anode CL (ACL) (domain 4), anode GDL (domain 5), and bipolar plates on either side of the assembly, as shown in Figure

6.1. The geometric and material properties of each layer are listed in Table 6-1 and Table 6-2.

i. Structural properties. Three distinctive cell compressions, 15%, 25% and 35% are compared in this study, accounting for the change in the effective properties in the porous domain.
ii. Reactant gas transport. Humidified feed gases (RH 100%) at both cathode and anode were treated as an ideal gas. The gases are transported through the GDL to CL, following the Stefan-Maxwell diffusion law. The membrane is assumed to be non-permeable to reactant gases and separates the cathode domain from the anode.
iii. Water transport through the membrane. Membrane/ionomer was assumed to be permeable to the dissolved phase of water. The water dissolves into the ionomer in the vapour phase during water uptake. The dissolved water is assumed to leave the membrane in the liquid phase. Water is assumed to be generated in the vapour phase at the CCL.
iv. Liquid water transport. Liquid water is generated through condensation of water vapour and membrane/ionomer desorption. Liquid water was assumed to be present only in the cathode domain.
v. Membrane swelling. The effect of membrane swelling was not considered in this study.
vi. Catalyst layer. The present study adopted the spherical agglomerate model developed by Sun et al. [218]. The model assumes each agglomerate to consist of three main phases; Pt dispersed on carbon particles (Pt/C), ionomer and pores. Liquid water was assumed to fill the pores in the agglomerate structure.

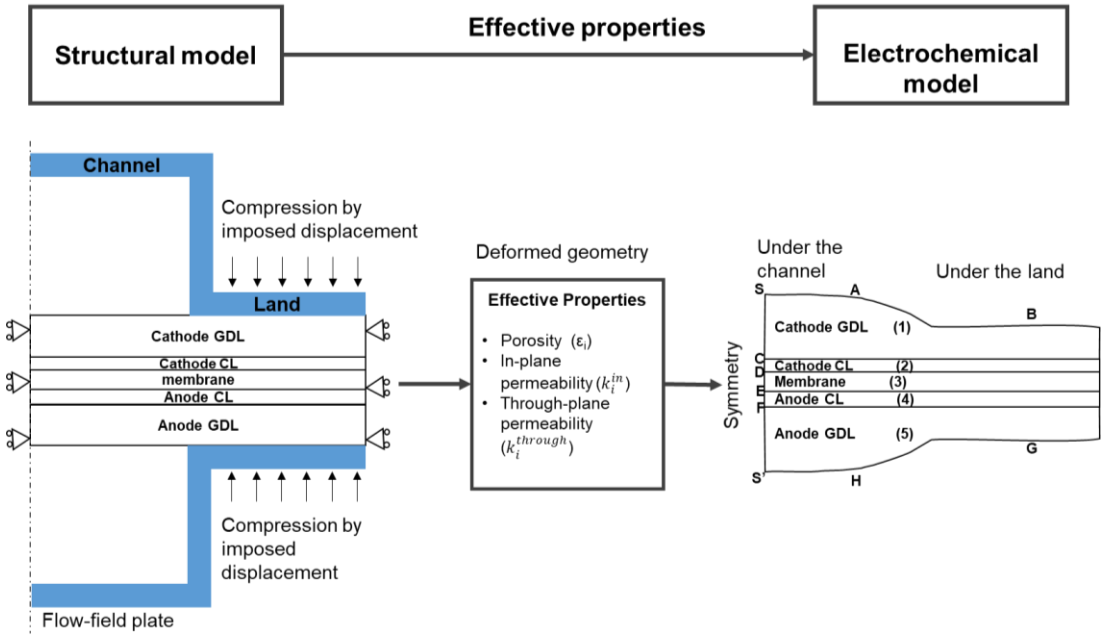

Figure 6.1–Schematic of the modelling methodology, where the results of the structural model act as the input for the electrochemical model

6.2.1 Governing equations

The present model combines structural and electrochemical models. Multiple coupled partial differential equations (PDEs) are solved to resolve the physical operation; the variables and physics-based approach are presented in this section.

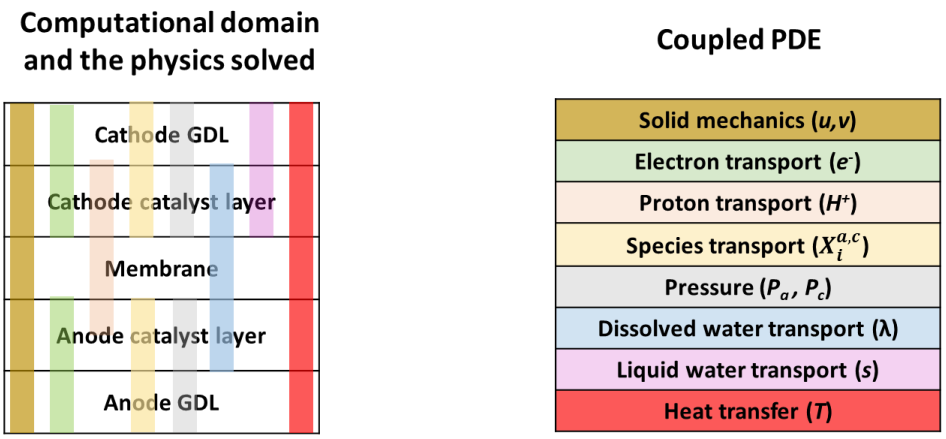

Figure 6.2– Schematics of the computational coupling and the solution methodology, various PDEs were solved at the colour coded computational domains.

6.2.1.1 Structural model (*u*, *v*)

The solid mechanics (*u*, *v*) physics were solved across all domains in the MEA as shown in Figure 6.2; the variables *u* and *v* represent the structural deformation in the *x* and *y*-direction, respectively. Geometrical and material properties of the component are listed in Table 6-1 and Table 6-2

The structural stresses on the fuel cell components subjected to cell compression can be obtained by a linear deformation approach [111,139,307], non-linear isotropic approach [308] or using more realistic nonlinear orthotropic models [213]. However, as the aim of the current modelling study is to investigate the effect of compression on the performance of the fuel cell, a simplified linear elastic model was used across the domain. The deformation of the GDL under compression was obtained by plane-strain theory.

$$\sigma = E\varepsilon_{elastic} \tag{6.1}$$

where σ is the principal stress [N m^{-2}], *E* is Young's modulus [GPa] and $\varepsilon_{elastic}$ is the elastic strain in the domain. The boundary conditions applied for the structural model are as shown in Figure 6.1. The deformation *u* and *v* indirectly represents the change in volume of the computational domain. The volumetric strain was further used to evaluate the non-uniform distribution of effective properties of the GDL under compression. The deformed geometry and the effective properties were used as the control domain and the material properties for the electrochemical model.

Table 6-1 – Geometric properties of the fuel cell component used in the computational domain

Parameters	Value	Ref.
GDL thickness, h_{GDL} [μm]	250	Measured
Membrane thickness, $h_{membrane}$ [μm]	50	Measured
Catalyst layer thickness, h_{CL} [μm]	15	Measured
Half channel width, $w_{channel}$ [μm]	500	Measured
Half land width, w_{land} [μm]	500	Measured

Table 6-2 Material properties of the fuel cell component used in the structural model

Component	Density [kg m^{-3}]	Young's Modulus [GPa]	Poisson's ratio	Ref.
GDL	400	10	0.25	[224]
CL	2000	0.19 [300 K, RH 35%]	0.25	[224]
Membrane	2000	0.200 [300 K, RH 35%]	0.25	[224]

6.2.1.2 Gaseous species transport ($\mathbf{X}_i^{a/c}$)

The species transport in the PEFC includes vapour and gaseous species transport. The transport of these species, H_2 and $H_2O_{(v)}$ in the anode domain and O_2, N_2 and $H_2O_{(v)}$ in the cathode domain was solved using the gaseous species transport model as discussed in 5.4.5

6.2.1.3 Dissolved water transport through the membrane ($\boldsymbol{\lambda}$)

Water transport through the membrane is defined by the migration of water from anode to cathode under electro-osmotic drag (EOD), back-diffusion of water from cathode to anode, and hydraulic permeation of the water. This can be modelled by three distinct approaches, diffusive models, chemical potential models, and the hydraulic models. According to the dilute solution theory, the Nafion membrane can be considered as the solvent, while protons and the dissolved water can be considered as the solute.

Hence, this approach assumes that the only interaction takes place in the membrane domain is between solute (proton and the dissolved water) and the solvent, i.e. the Nafion membrane. The effect of interactions between any other solute species is assumed negligible in this approach.

Adequate water transport through the Nafion membrane is essential for PEFC operation. The water content in a membrane (λ) is described as the ratio of the number of water molecules in the system to the number of charged ($SO^-_3H^+$) sites in the same domain. An experimental relationship for Nafion 117 membrane was presented by Zawodzinski et al. that shows membrane water content is the function of water activity, '*a*' [31]. This is derived by weighing membranes equilibrated above aqueous solutions of lithium chloride concentration at constant temperature 30 ˚C and constant pressure conditions. Water sorption isotherm as a function of water content λ and a water vapour activity, '*a'*, measured at the interface is shown in Figure 1.12. Water vapour activity can be calculated as,

$$\mathrm{a} = \frac{\mathrm{X}_{\mathrm{H_2O}} P}{P_{sat}} \; a \; \in \; [0 \ldots .3] \tag{6.2}$$

The equation relates the saturation ratio to the water vapour activity (*a*), measured at the membrane/CL interface. A molar fraction of water at the membrane interface represented as X_{H_2O}. *P* is the pressure at the anode / cathode interface and P_{sat} is a saturation pressure. In this case, water activity is assumed to be less than a unit. The water content is given as a function of water vapour activity, based on the water sorption curve.

$$\lambda_{H_2O/SO_3} = 0.043 + 17.81a - 39.85a^2 + 36.0a^3 \; 0 \leq a \leq 1 \tag{6.3}$$

As shown in Figure 1.12, at unit water vapour activity, when the measured value of water content is in the equilibrium with saturated water vapour, water content *λ* is equal to 14. Water content, *λ* increases linearly from 14 to 16.8 when the water activity is greater than 1.

The water transport through the membrane can be derived by the following form of the conservation equation [250]

$$\nabla \cdot \left(n_d \frac{i_m}{F}\right) - \nabla \cdot \left(D^m_{H_2O} \cdot \nabla C^d_{H_2O}\right) - \left(\frac{k^m_p C^d_{H_2O}}{\mu_{H_2O,l}} \nabla p\right) = S^d_{H_2O} \quad (6.4)$$

where n_d is the EOD coefficient, $D^m_{H_2O}$ [m^2 s^{-1}] is the diffusion coefficient of water through the membrane, k^m_p [m^2] is hydraulic permeability of water in the membrane, $\mu_{H_2O,l}$ [Pa s] is liquid water viscosity, and $C^d_{H_2O}$ [kg mol^{-1}] is the dissolved water concentration in the membrane, which is defined by the membrane water content (λ).

$$\lambda = \frac{C^d_{H_2O} EW_m}{\rho_m M_{H_2O}} \quad (6.5)$$

EW_m [g mol^{-1}] is the equivalent weight of the dry membrane/ionomer and ρ_m [kg m^{-3}] is the density of the membrane/ionomer. The source term $S^d_{H_2O}$ defines the phase transfer between dissolved water and the water vapour and constitutes two distinct phenomena; water uptake by membrane/ionomer and water desorption. Water uptake is defined as absorption when the equilibrium concentration of water is higher than the dissolved water concentration, and the phase is transferred from water vapour to dissolved water. Water desorption defines the phase transfer from dissolved water to liquid water when dissolved water concentration is higher than the equilibrium water concentration ($C^{eq}_{H_2O}$) The equilibrium water concentration is a function of water vapour activity (*a*). Using the empirical correlation between equilibrium concentration and

water vapour activity adjacent to the membrane described by Zawodzinski et al. [33], Equation (6.3), the equilibrium water concentration ($C_{H_2O}^{eq}$) can be calculated as

$$C_{H_2O}^{eq} = \frac{\rho_m M_{H_2O}}{EW_m}[(0.043 + 17.81a - 39.85a^2 + 36.0a^3)(1-s) + 16.8s] \quad (6.6)$$

where '*s*' is the level of liquid water saturation in the domain. Here, the source term $S_{H_2O}^{d}$ can be defined as

$$S_{H_2O}^{d} = S_{H_2O}^{vd} + S_{H_2O}^{dl} \quad (6.7)$$

$$S_{H_2O}^{vd} = \gamma_{ads}\left(C_{H_2O}^{eq} - C_{H_2O}^{d}\right) \quad C_{H_2O}^{d} < C_{H_2O}^{eq} \quad (6.8)$$

$$S_{H_2O}^{dl} = \gamma_{des}\left(C_{H_2O}^{d} - C_{H_2O}^{eq}\right) \quad C_{H_2O}^{d} \geq C_{H_2O}^{eq} \quad (6.9)$$

where superscript '*vd'* represents the phase change from water vapour to dissolved water, and superscript '*dl'* represents the phase change from dissolved water to liquid water. γ_{ads} and γ_{des} are water adsorption and desorption coefficient.

6.2.1.4 Electro-osmotic drag

For both water and proton, the conservation of mass can be represented by;

$$\frac{\partial c_i}{\partial t} = -\frac{\partial}{\partial z} N_i \quad (6.10)$$

The molar concentration is C_i and molar flux due to electro-osmotic force is N_i. Using diluted solution theory, N_i is given by Nernst-Plank equation, (Section 5.2)_

$$N_i = J_i + c_i u^m \quad (6.11)$$

The electro-osmotic drag is a rate at which water molecules are dragged by protons, migrated from anode CL to cathode CL through the membrane, under the influence of the electric field. $\boldsymbol{u}^m$ is the velocity of a membrane species, and J_i is the diffusive flux. Here, EOD represents the flux of water molecules.

$$N_{H2O} = -D_{\lambda,T}\frac{\partial c^m_{H_2O}}{\partial z} + n_{drag}\frac{i_{H^+}}{F} \tag{6.12}$$

where

$$n_{drag} = \begin{cases} 0.2\lambda & \lambda < 5 \\ 1 & 5 \le \lambda \le 14 \\ 0.1875\lambda - 1.625 & \lambda > 14 \end{cases} \tag{6.13}$$

6.2.1.5 Diffusion coefficient of water

Springer et al. defined the diffusion coefficient of water through the membrane, $D_{\lambda,T}$, as a function of water content in the membrane and the operating/membrane temperature [30].

$$D_{\lambda,T} = D'\left[exp\left[2416\left(\frac{1}{303} - \frac{1}{T}\right)\right]\lambda\ \frac{1}{a}\ \frac{1}{17.81 - 78.9a + 108a^2}\right] \tag{6.14}$$

where a is the water vapour activity and D' [$m^2\ s^{-1}$] is the diffusion coefficient measured at constant temperature and change in coordinate due to membrane swelling [30]. D' measured at 30 ˚C is written as,

$$D' = \begin{cases} 2.64227e^{-13}, \lambda < 1.23 \\ 7.75e^{-11}\lambda - 9.5e^{-11}, 1.23 \le \lambda \le 6 \\ 2.5625e^{-11}\lambda - 2.1625e^{-10}, \lambda < 14 \end{cases} \tag{6.15}$$

6.2.1.6 Membrane resistance

The water content in a membrane increases from the anode to cathode. Water is generated at the cathode CL. Generally, the quadratic profile of membrane hydration present along the thickness of the membrane is due to a higher rate of water generation at cathode CL compared to the water transport via EOD and back diffusion. An increase in water content affects the Ohmic and mass transport resistance. Membrane resistance is expressed as,

$$R_m = \int_0^{t_{mem}} \frac{dz}{\sigma_{Mem}(\lambda)} \tag{6.16}$$

where R_m is a membrane resistance [Ω cm^{-2}] and $\sigma_{mem}(\lambda)$ [S m^{-1}] is the proton conductivity of a membrane as a function of water content at cell operating temperature. The proton conductivity is calculated as,

$$\sigma_{Mem} = exp\left[1268\left(\frac{1}{303} - \frac{1}{T}\right)\right](0.5139\lambda - 0.326) \tag{6.17}$$

6.2.1.7 Liquid water transport (s)

In the two-phase flow through a porous medium, a saturation of the liquid phase is an important parameter, which indicates the volume of pore available for the gas phase to diffuse. The liquid water transport through porous media is defined by the following equation [252].

$$\frac{\partial\left(\varepsilon\rho_{H_2O}^{l}s\right)}{\partial \mathrm{t}} + \nabla\cdot\left(\rho_{\mathrm{H_2O}}^{l}D_c\nabla s - \frac{\rho_{\mathrm{H_2O}}^{\mathrm{l}}\mathrm{k}_{\mathrm{r}}^{\mathrm{l}}\mu_{\mathrm{H_2O}}^{\mathrm{g}}}{\mathrm{k}_{\mathrm{r}}^{\mathrm{g}}\mu_{\mathrm{H_2O}}^{\mathrm{l}}}\boldsymbol{u_{H_2O}}\right) = M_{H_2O}S_{H_2O}^{l} \tag{6.18}$$

where ε is the porosity of the domain, *s* is the extent of saturation, $\rho_{H_2O}^{l}$ [kg m^{-3}] is the density of liquid water, $\mu_{H_2O}^{l}$ and $\mu_{H_2O}^{g}$ [Pa s] are the dynamic viscosity of liquid water and water vapour respectively, k_r^l and k_r^g are the relative permeability of liquid water and water vapour, $\boldsymbol{u_{H_2O}}$ $[\mathrm{m\ s^{-1}}]$ is the velocity vector. M_{H_2O} [kg m^{-3}]is the molecular weight of water, and D_c [m^2 s^{-1}] is the capillary diffusion coefficient, calculated as [252],

$$D_c = \frac{k_r^l}{\mu_{H_2O}^{l}}\,\xi\,cos(\theta)\left(\sqrt{\varepsilon k_p}\right)\frac{dJ(s)}{ds} \tag{6.19}$$

Here, the relation between capillary pressure and the saturation is defined by $J(\mathrm{s})$, *i.e.* the Leverett-J function. However, it is essential to note that various different approaches have been used in the literature to describe water retention curves [243,309–314], while traditional Leverett-J approach is one of the most commonly used and well-established methods in the literature to describe water retention curves. This approach can be tailored according to GDL properties by accounting for parameters such as surface tension of liquid water ξ [N m^{-1}], contact angle θ [°], and PTFE content for better depiction of liquid water transport inside a fuel cell [310]. The form of Leverett-J function used in this study is [250,315];

$$J(\mathrm{s}) = \begin{cases} 1.417(1-\mathrm{s}) - 2.120(1-\mathrm{s})^2 + 1.263(1-\mathrm{s})^3 & \theta < 90° \\ 1.417\mathrm{s} - 2.120\mathrm{s}^2 + 1.263\mathrm{s}^3 & \theta > 90° \end{cases} \tag{6.20}$$

According to the assumption, liquid water transport was solved only in the cathode domain. $S_{H_2O}^{l}$ is the source term that defines the rate of phase transfer between water vapour and liquid water either by condensation or evaporation and defined as,

$$S_{H_2O}^{l} = \begin{cases} k_{con} \dfrac{\varepsilon(1-s)x_{H_2O}^{v}}{RT} & P_{sat} \le P_{H_2O}^{v} \\ k_{eva} \dfrac{\varepsilon s \rho_{H_2O}^{l}(P_{sat} - P_{H_2O}^{v})}{M_{H_2O}} & P_{sat} > P_{H_2O}^{v} \end{cases} \quad (6.21)$$

where k_{con} and k_{eva} is the rate coefficients of condensation [atm^{-1} s^{-1}] and the rate coefficient of evaporation [s^{-1}], respectively.

Table 6-3 – Input parameters used in model

Parameters	Value	Ref.
Inlet pressure anode/cathode, P_{in} [atm]	1.1	
Reference temperature, T_{ref} [K]	333.15	
Inlet relative humidity, RH^a/RH^c	100%/100%	assumed
Liquid water density, ρ_{liq} [kg m^{-3}]	1.0×10^3	
The viscosity of liquid water, μ_{liq} [Pa s]	3.56×10^{-4}	
Cell voltage, V_{cell} [V]	0.6	
Platinum loading, m_{pt}[mg cm^{-2}]	0.4	[218]
Agglomerate radius, r_{agg} [m]	1×10^{-6}	[218]
Henry's hydrogen constant, H_{H_2} [Pa m^3 mol^{-1}]	6.69×10^4	[251,316]

Henry's hydrogen constant, H_{O_2} [Pa m^3 mol^{-1}]	3.1664 × 10^4	[218,252]
Platinum surface area ratio, ε_l	0.75	[252]
The fraction of ionomer in the CL, ε_m^{agg}	0.2	[252]
The specific active surface area of platinum, *S* [cm^2 g^{-1}]	2.5 × 10^5	[252]
Equivalent molecular weight of the membrane EW_m [kg mol^{-1}]	1.1	[252]
Catalyst layer porosity, ε_{cl}	0.2	[250]
Initial GDL porosity, $\varepsilon_0^{No\ compression}$	0.75	Measured
Contact angle, θ	120°	[301]
Carbon density, ρ_c[kg m^{-3}]	1.8 × 10^3	[252]
Density of liquid water, ρ_{liq} [kg m^{-3}]	0.983 × 10^3	[252]
Density of dry membrane, ρ_m [kg m^{-3}]	1980	[252]
Density of Pt particles, ρ_{pt} [kg m^{-3}]	21.43 ×10^3	[252]
Through-plane electrical conductivity of GDL, $\sigma_{through-initial}^{gdl}$ [S m^{-1}]	240	[302]

In-plane electrical conductivity of GDL, σ_{in}^{gdl}[S m^{-1}]	1619.6	[302]
Electrical conductivity of CL, σ^{CL}[S m^{-1}]	500	

6.2.1.8 Electrochemical model ($\boldsymbol{H^+, e^-}$)

The proton (H^+) and charge (e^-) transport in the fuel cell was solved using the electrochemical model. The protonic transport was solved across the CL and the membrane, while the electron transport was solved across the CL and GDL domains on either side of the membrane. The electrochemical reaction was modelled at the catalyst layer using the agglomeration approach, as discussed in 5.3.2.

6.2.1.9 Energy model (T)

The multiphase heat transfer process is described by balancing the convective and the conductive heat fluxes. The equation is written as follows,

$$\nabla \cdot \left[\sum_{i=g,l} \left(\varepsilon \rho c_p u \right)_i T \right] - \nabla \left(\sum_{i=g,l,s} k_i \nabla T \right) = S_T \tag{6.22}$$

where '*i*' is the phase of the medium, which would be a gas or a liquid phase for the species and solid phase for CL, GDL and the membrane, c_p [J kg^{-1} K^{-1}] is the specific heat capacity at constant pressure, K_i [W m^{-1} K^{-1}], S_T [W m^{-3}] is the heat source that constitutes the heat generated during activation, Ohmic, phase transfer and reversible processes, and T is temperature [K]. The key assumption here is all the components and phases are in thermal equilibrium. The heat generated/depleted during fuel cell operation is due to four different sources, namely thermodynamic irreversibility ($S_T^{irreversible}$), reversible heat generated during the activation reaction ($S_T^{reversible}$),

Ohmic heating due to the resistance offered to electronic and protonic transport (S_T^{Ohmic}), and phase change of water ($S_T^{phase\ change}$). Therefore, the heat source S_T [W m^{-3}] is given by,

$$S_T = S_T^{reversible} + S_T^{irreversible} + S_T^{Ohmic} + S_T^{phase\ change} \tag{6.23}$$

$$S_T^{reversible} = -\left|i^{a/c}\right| \times \frac{T\nabla S^{a/c}}{n_{e^-}F} \tag{6.24}$$

$$S_T^{irreversible} = \left|i^{a/c}\right| \times \eta^{a/c} \tag{6.25}$$

$$S_T^{Ohmic} = \frac{\left(i^{a/c}\right)^2}{\sigma_{GDL/CL}^{eff}} + \frac{(i^{mem})^2}{\sigma_m^{eff}} \tag{6.26}$$

$$S_T^{phase\ change} = M_{H_2O} \times (S_{H_2O}^{l} \nabla h_{H_2O}^{con/eva} + S_{H_2O}^{vd} \nabla h_{H_2O}^{ads} + S_{H_2O}^{dl} \nabla h_{H_2O}^{des}) \tag{6.27}$$

The specific heat capacity (c_p) is obtained by an empirical equation as Wilke's equation,

$$\mathrm{c}_p^{mix} = \sum_i x_i \mathrm{c}_{p,i}^{g} \tag{6.28}$$

Table 6-4 – Constitutive relationships

Parameter	Value	Eq.	Ref
Thermal conductivities [W m^{-1} k^{-1}]			
Liquid water, $k_{H_2O.l}$	$-1.118 \times 10^{-5}T^2 + 8.388 \times 10^{-3}T - 9.004$	(6.29)	[317]
Water vapour, $k_{H_2O,v}$	$1.188 \times 10^{-4}T - 2.404 \times 10^{-2}$	(6.30)	[317]
Hydrogen, k_{H_2}	$3.777 \times 10^{-4}T + 7.444 \times 10^{-2}$	(6.31)	[317]
Nitrogen, k_{N_2}	$5.453 \times 10^{-5}T + 1.088 \times 10^{-2}$	(6.32)	[317]
Oxygen, k_{O_2}	$6.204 \times 10^{-5}T + 8.83 \times 10^{-3}$	(6.33)	[317]
Specific heat capacity [J mol k^{-1}]			
Water vapour, $C^{g}_{p,H_2o,v}$	$1.180 \times 10^{-6}\mathrm{T}^2 + 9.621 \times 10^{-3}\mathrm{T} + 30.33$	(6.34)	[317]

Hydrogen, C_{p,H_2}^{g}	$1.914 \times 10^{-6}\mathrm{T}^2 - 8.314 \times 10^{-4}\mathrm{T} + 28.89$	(6.35)	[317]
Nitrogen, C_{p,N_2}^{g}	$1.788 \times 10^{-5}\mathrm{T}^2 + 2.924 \times 10^{-3}\mathrm{T} + 27.85$	(6.36)	[317]
Oxygen, C_{p,O_2}^{g}	$-4.281 \times 10^{-6}\mathrm{T}^2 + 1.371 \times 10^{-2}\mathrm{T} + 25.4$	(6.37)	[317]
Relative permeability			
Liquid phase, K_r^l	s^3	(6.38)	[252]
Gas-phase, K_r^g	$(1-s)^3$	(6.39)	[252]
Properties dependent on dissolved water transport			
Electro-osmic drag coefficient, n_d	$\begin{cases} 0.2\lambda & \lambda < 5 \\ 1 & 5 \le \lambda \le 14 \\ 0.1875\lambda - 1.625 & \lambda > 14 \end{cases}$	(6.40)	[30,251,252]
Ionic conductivity of the membrane, σ_{Mem} [S m^{-1}]	$\sigma_{Mem} = exp\left[1268\left(\frac{1}{303} - \frac{1}{T}\right)\right](0.5139\lambda - 0.326)$	(6.41)	[30,251,252]
Effective ionic conductivity of the membrane, σ_{Mem}^{eff} [S m^{-1}]	${\sigma_{CL/ionomer}}^{1.5} \times \sigma_{Mem}$	(6.42)	

Volume fraction of water in the membrane, $f_{H_2O,d}$	$\frac{\lambda V_{H_2O}}{V_{H_2O} + \lambda V_{H_2O}}$	(6.43)	[30,251,252]
Adsorption rate coefficient, γ_{ads} [s^{-1}]	$\frac{1.14 \times 10^{-5} f_{H_2O,d}}{h_{\mathrm{CL}}} exp\left[2416\left(\frac{1}{303} - \frac{1}{T}\right)\right]$	(6.44)	[30,251,252]
Desorption rate coefficient, γ_{des} [s^{-1}]	$\frac{4.59 \times 10^{-5} f_{H_2O,d}}{h_{\mathrm{CL}}} exp\left[2416\left(\frac{1}{303} - \frac{1}{T}\right)\right]$	(6.45)	[30,251,252]
Effective diffusivity of oxygen in ionomer phase, $D_{O_2}^{mem}$[$m^2\ s^{-1}$]	$\begin{cases} D_0(2.563 - 0.33\lambda + 0.0264\lambda^2 - 0.00067 \\ D_0(-1.25\lambda + 6.65) \\ D_0(2.05\lambda - 3.25) \end{cases}$	(6.46)	[30,251,252]
Diffusivity of oxygen in ionomer, D_0 [$m^2\ s^{-1}$]	$10^{-10} exp\left[2416\left(\frac{1}{303} - \frac{1}{T}\right)\right]$	(6.47)	[30,251,252]
Local water vapour activity, *a*	$a = \frac{P_{H_2O,v}}{P_v^{sat}}$	(6.48)	[30,251,252]
Initial membrane water content, λ_0	$\begin{cases} 0.043 + 17.80\mathrm{a} - 39.85a^2 + 36a^3 & a < 1 \\ 14 + 1.4(\mathrm{a} - 1) & 1 \le a \le 3 \\ 16.8 & a > 3 \end{cases}$	(6.49)	
Saturation pressure of water vapour, P_v^{sat}[Pa]	$exp\left[73.648 - \frac{7258.2}{T} - 7.3037 logT + 4.1653 \times 10^{-6}\mathrm{T}^2\right]$	(6.50)	

6.2.2 Boundary conditions

The boundary conditions for the structural model are as shown in Figure 6.1– Schematic of the modelling methodology, where the results of the structural model act as the input for the electrochemical model. For the fuel cell performance model, fully humidified reactant gas at 333 K was specified at both inlets. The mole fraction of the species and pressure at the cathode inlet (boundary A) are given as,

$$X_{H_2O}^{c} = \frac{P_{sat} RH^{c}}{P^{c}}, \qquad X_{O_2}^{c} = 0.21\left(1 - X_{H_2O}^{c}\right), X_{N_2}^{c} = 0.79\left(1 - X_{H_2O}^{c}\right), \qquad P = P^{c} \tag{6.51}$$

Similarly, the mole fraction of the species and pressure at the anode inlet, i.e. boundary H are given as,

$$X_{H_2O}^{a} = \frac{P_{sat} RH^{a}}{P^{a}}, \qquad X_{OH_2}^{a} = 1 - X_{H_2O}^{,c}, \qquad P = P^{a} \tag{6.52}$$

Temperature $T = T_{cell} = 313$ [K] was prescribed at boundaries A, B, H, and G. Water content at CL/membrane ionomer interface, *i.e.* boundaries D and E was defined by the Dirichlet boundary condition as the initial membrane water content (λ_0), given in Table 6-4. Assuming no presence of liquid water in the flow channels, the saturation at boundaries A and H, as prescribed by no flux boundary condition and the Dirichlet boundary condition, as $s = 0$, respectively. The boundary conditions for the electrochemical model are given as the fixed potential at GDL/land interface, i.e. boundaries B and G. At the cathode, $\varphi_s = V_{cell}$ [V] and the electrical ground condition is applied at the anode, *i.e.* $\varphi_s = 0$ [V]. Table 6-5 provides the details of sources and sinks used in the model to adequately represent the water transport in the fuel cell. Here $S_{H_2O}^{g}$represents water generated at the cathode CL, given by ($S_{H_2O}^{g} = \frac{j_c}{2F}$), $S_{H_2O}^{dl}$

and $S_{H_2O}^{vl}$ represents water transport from dissolved water to liquid water and vapour to liquid water respectively, and $S_{H_2O}^{vd}$ and $S_{H_2O}^{ld}$ represents water uptake from vapour dissolved water and liquid water to dissolved water, respectively.

Table 6-5 – Sources and sinks used in the model to represent water transport in the fuel cell

Source	**Anode GDL**	**Anode CL**	**Membrane**	**Cathode CL**	**Cathode GDL**
Water Vapour (S_{H_2O})	0	$-S_{H_2O}^{vd}$	0	$S_{H_2O}^{g}$-($S_{H_2O}^{vd}$ + $S_{H_2O}^{ld}$)	$-S_{H_2O}^{vl}$
Dissolved water ($S_{H_2O}^{d}$)	0	$S_{H_2O}^{vd}$	0	$S_{H_2O}^{vd} - S_{H_2O}^{dl}$	0
Liquid water ($S_{H_2O}^{l}$)	0	0	0	$S_{H_2O}^{dl} + S_{H_2O}^{vl}$	$S_{H_2O}^{vl}$

6.2.3 Numerical technique

The solution procedure comprises of two steps; firstly, solving for the volumetric strain and deformation under the cell compression to generate effective properties for the GDL, which are required to solve the electrochemical species transport model in step II Figure 6.1. The deformed geometry was then used in the second step as the control domain, as shown in Figure 6.2. All of the PDEs in this model were solved in the commercial software environment, COMSOL Multiphysics 5.4. Equations (5.52) - (5.54), and (5.65), (5.66), (5.69) are predefined in the COMSOL environment, while all

remaining equations were added externally to the model. The convergence criteria were set at 10^{-6}. The cell voltage, V_{cell}, was used as a variable parameter that ranges from 1 V to 0.3 V to generate the polarisation curve in steps of 0.01 V. The details of the solution procedure used in the second step are provided in the 5.5.4.

6.3 Results and discussion

6.3.1 Effective property distribution

Knowledge of the effective properties is crucial in the two-phase models where liquid water generation and accumulation is predicted with the saturation term. Effective properties are directly affected by the compression. Figure 6.3 illustrates the effect of compression on the vertical deformation of the GDL bulk porosity, the in-plane and the through-plane permeability of the GDL.

The vertical deformation of the GDL agrees with the well-known 'tenting' behaviour of the GDL under the channel region that results in partial blocking of the active channels [62]. Mechanical compression results in a change in volume (i.e., volumetric strain (ϵ_v) of the fibrous GDL). Therefore, the modified porosity, due to a change in volumetric strain, was calculated from the following equation.

$$\varepsilon = \varepsilon_{\text{new}}^{Compressed} = \varepsilon_0^{No\ compression}(1 + \epsilon_v) \tag{6.53}$$

where ε is the GDL porosity after compression. The change in porosity leads to a change in permeability. The permeability of the porous material, as a function of porosity, is calculated using the Carman-Kozeny equation [235,300],

$$K = \frac{D_{fibre}^2 \varepsilon^3}{16 k_{ck}(1-\varepsilon)^2} \tag{6.54}$$

where D_{fibre} [μm] is the fibre diameter obtained from the X-ray CT analysis, ε is the porosity obtained from Equation (6.53), k_{ck} is the Carman-Kozeny constant that depends on the type of media [235] and the fibre orientation [300]. The X-ray CT images showed in Chapter 4, Figure 4.2 shows that the fibres are randomly aligned in the *xz* plane, while uniformly oriented in the *y*-direction, providing distinct in-plane and through-plane permeability. Therefore, the effective permeability is given by,

$$\mathrm{K_{in-plane}} = \frac{\mathrm{D_{fibre}^2 \varepsilon^3}}{16 \mathrm{k_{ck,IP}}(1-\varepsilon)^2} \tag{6.55}$$

$$\mathrm{K_{through-plane}} = \frac{\mathrm{D_{fibre}^2 \varepsilon^3}}{8 \mathrm{k_{ck,TP}}(1-\varepsilon)^2} \tag{6.56}$$

Figure 6.3 shows the contours of inhomogeneous distribution of the effective properties plotted at 15%, 25% and 35% compression. Non-uniform compression exerted by the flow-fields results in non-uniform distribution of porosity. The inherent initial 76% GDL porosity (at 0% compression) was obtained from the X-ray CT analysis. The porosity under the land lowered with compression by 19%, 28% and 38%, at 15%, 25% and 35% compression, respectively. In contrast, the domain under the channel was retained at the initial porosity. X-ray CT studies observed the opening of fibres under the channel that results in an increase in the porosity [62]. As the GDL was modelled as a continuum domain, fibre opening phenomenon was not accounted for; hence, the porosity under the channel remained at the initial porosity. Similarly, an increase in compression affected the in-plane and the through-plane permeability; however, the permeability (both the in in-plane and the through-plane) under the

channel region was not affected by the compression while the permeability under the land region lowered with the compression.

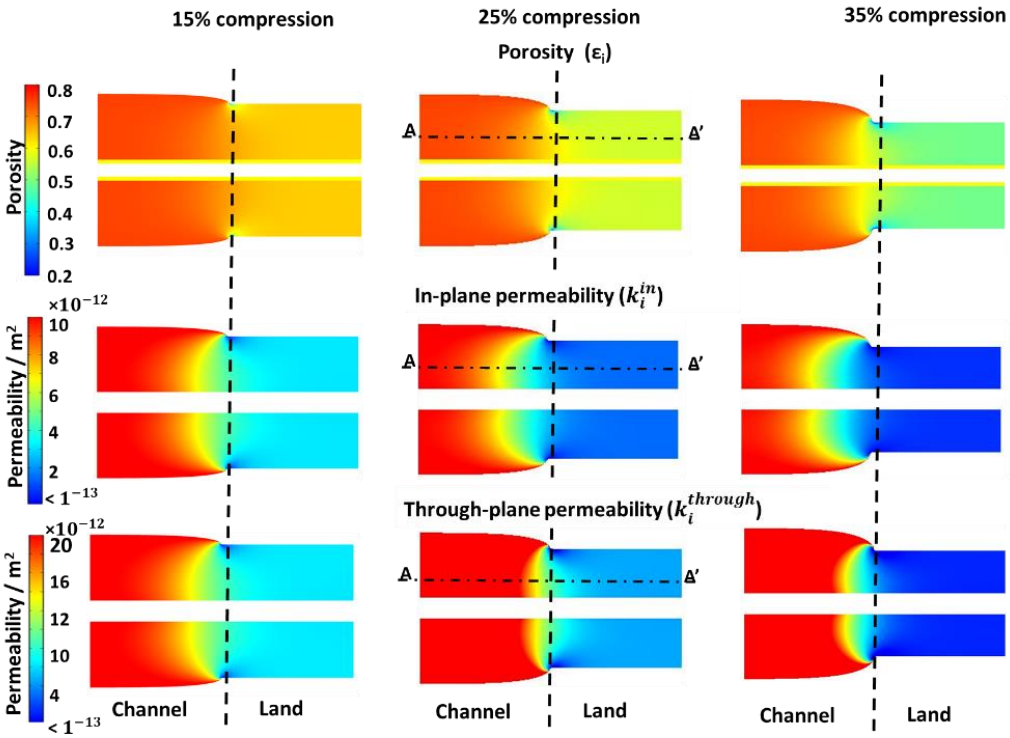

Figure 6.3– Effect of compression on the effective properties , contour plots of the porosity, the in-plane and the through-plane permeability (from top to bottom) plotted at 15 %, 25% and 35% cell compression (from left to right, the dashed (- - -) line represents the land and the channel domain.

Comparative illustrations of the change in effective properties across the cell width are shown in Figure 6.4; this highlights the non-linear distribution of the effective properties. Both the in-plane and the through-plane permeability are the function of $\frac{\varepsilon^3}{(1-\varepsilon)^2}$, as presented in equations (6.55) and (6.56). Therefore, the permeability lowered under the land by 67%, 85% and 93% with an increase in compression to 15 %, 25% and 35%, respectively. This suggests that if the cell is compressed by 35%, the non-

linearity in the permeability increases to almost an order of magnitude, significantly affecting the removal of accumulated liquid water under the land [82].

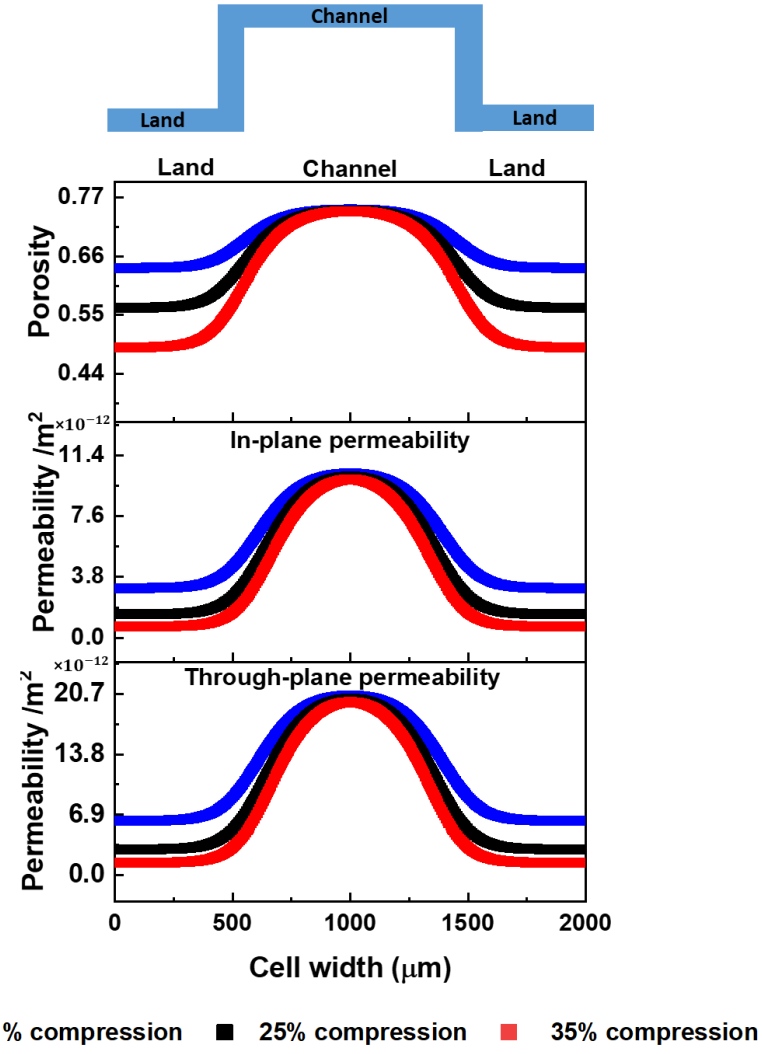

Figure 6.4– Effective property distribution in the middle of the cathode GDL (along A-A' shown in Figure 6.3) plotted at 15% , 25% and 35% cell compression

6.3.2 Polarisation curve

Figure 6.5 illustrates the effect of non-homogeneous compression on the polarisation performance and the localised current density distribution. Notionally, a polarisation curve, as shown in Figure 6.5(a), can be partitioned into three regions, the activation dominant region, (V > 0.8 V), the Ohmic dominant region (0.5 V < V < 0.8 V) and the mass transport dominant region (V < 0.5 V).

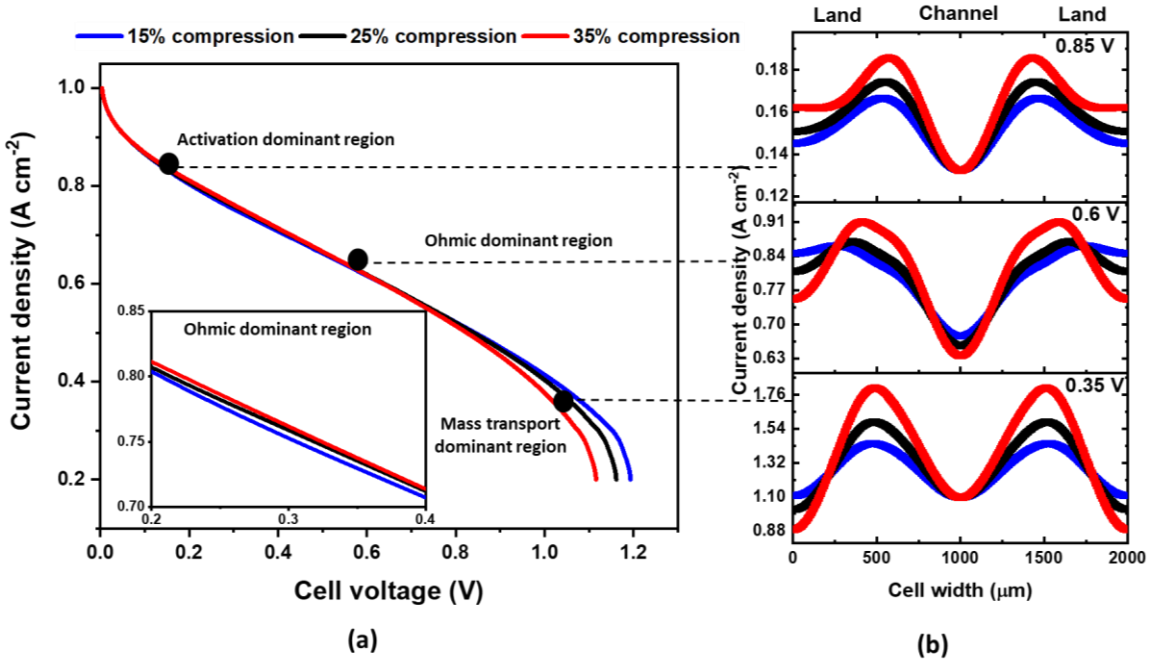

Figure 6.5– Effect of compression on the fuel cell performance, (a) polarisation curve, the detailed view gives a close-up look into the Ohmic region and (b) localised current density distribution along the cathode CL and GDL interface plotted as a function of compression at activation dominant region (V = 0.85 V), Ohmic dominant region (V = 0.6 V) and the mass transport dominant region (V = 0.35 V).

The activation kinetics are primarily dependent on the properties of the catalyst layers given in Table 6-3 – Input parameters used in model. Therefore, as identical catalyst

layer properties were used, the overall activation performance remained unaffected with compression. At the Ohmic dominant region, the performance improved marginally (with increased compression, i.e. by 1% and 2% at 0.65 V) when compression increased to 25% and 35%, respectively (detailed view of Figure 6.5(a)). Increase in compression improves electrical conductivity as an increased contact between the conductive phases and reduction in the pore sizes, which results in lowering Ohmic losses [46,109,125].

With further increases in current density, the effect of compression on the cell performance was apparent. In the mass transport region (V = 0.35 V), 25% compression lowered the performance by 3% and 35% compression lowered it by 6% (in comparison with 15% compression case). This indicates that two contradicting behaviours are influencing fuel cell performance, i.e. improved electrical conductivity with compression aids performance, while lowering the porosity and the permeability of the GDL under the land region, adversely affecting mass transport and effective water management.

The localised current density is affected not only by the effective properties, such as porosity and diffusivity [222] but also by the cell architecture such as channel/land ratio and cell compression [138,289,307].

Figure 6.5(b) depicts the distribution of current density at the interface between the catalyst layer and GDL for three load conditions and compressions. The key observations include: non-uniformity in the current density distribution, i.e. notional ‘peaks’ and ‘valleys’ become more defined with an increase in the operating load, the current density ‘peaks’ were observed at the interface edge between channel and land, and current density ‘valleys’ were observed towards the centre of the land and the centre of the channel. However, it is important to note that at all the operating conditions and the compressions, the ‘notional valleys’ at the centre of the under-the-

channel region are virtually unchanged with respect to the global current density shown in Figure 6.5(a). This phenomenon is in agreement with the previously published literature [222,246,289,318–321].

In the activation and Ohmic dominant regions, i.e. V = 0.85 V and V = 0.6 V, respectively, more profound 'localised peaks' in the current density distribution were observed near the corner of the land, irrespective of the cell compression. This is due to the balance of mass transfer resistance in the GDL and the electrical resistance in the GDL [138].

However, with an increase in average current density, the accumulation of liquid water under the land affects the available porosity, increasing the mass transport resistance. Therefore, in the mass transport dominant region, i.e. V = 0.35 V, the deeper current density distribution valley was shifted towards the centre of the land, while the current density under the channel remains virtually unchanged as that of global current density.

The non-uniformity in the distribution is further affected by the level of compression. In the activation dominant region, the current density distribution was non-uniform with a difference of 21%, 24% and 29% between the peak and the valley, measured at 15%, 25%, and 35% compression, respectively. With the increase in the operating load to V = 0.6 V, i.e. the Ohmic dominant region, the non-uniformity in the current distribution marginally increased to 22%, 25%, and 30%, at 15%, 25%, and 35% compression (in comparison with the activation dominant region), respectively. However, in the mass transport dominant region, the effects of compression on the non-uniformity of the current distribution were evident. At V = 0.35 V, the localised current maxima were reached to 1.44 A cm^{-2}, 1.58 A cm^{-2}, 1.80 A cm^{-2} at the edge between a channel and the land on the bi-polar plate at 15%, 25% and 35% cell compression, respectively. This emphasises the inherent non-uniformity in the current density distribution was

intensified by an increase in the compression. Also, an essential factor to note here is that although the polarisation performance at 0.85 V and 0.6 V marginally differ with an increase in compression, the current density distribution is not the same. This highlights that trying to validate a model exclusively based on polarisation performance can be misleading and introduce errors in the validation process, as described by Pharaoh et al. [222]. So, as water distribution is a factor in this study, the model was validated with the aid of neutron imaging results, presented in Chapter 7.

6.3.3 Cathode overpotential

The overpotential inside the cathode CL is affected both by compression and the operating load, as shown in Figure 6.6. The negative overpotential at cathode results in the positive cathode current density; therefore, higher negative overpotential results in higher current density.

The maximum absolute value of cathode overpotential increases from 0.2 to 0.5, with an increase in the operating load, according to Equation (5.54), when measured at 15% cell compression. At the activation dominant region, the uniform cathode overpotential distribution was observed, irrespective of the cell compression. With further increase in the operating load, the non-uniformity in the cathode overpotential distribution is evident, and it leads to the higher absolute cathode overpotential under the land region. The maximum absolute value of cathode overpotential was observed under the land region adjacent to the membrane, where the highest oxygen transport resistance exists. An increase in the cell compression results in increasing the non-uniformity in the cathode overpotential distribution, which is predominantly affected in the mass transport region.

The negative cathode overpotential (η_c) makes the second term in the bracket of Equation (5.27) negligible, leading to the positive cathode current density. Hence, the

non-uniformity in the cathode overpotential distribution, which is affected both by the extent of cell compression and the operating load leads to the non-uniform distribution of cathode current density and the rate of oxygen reduction reaction (ORR).

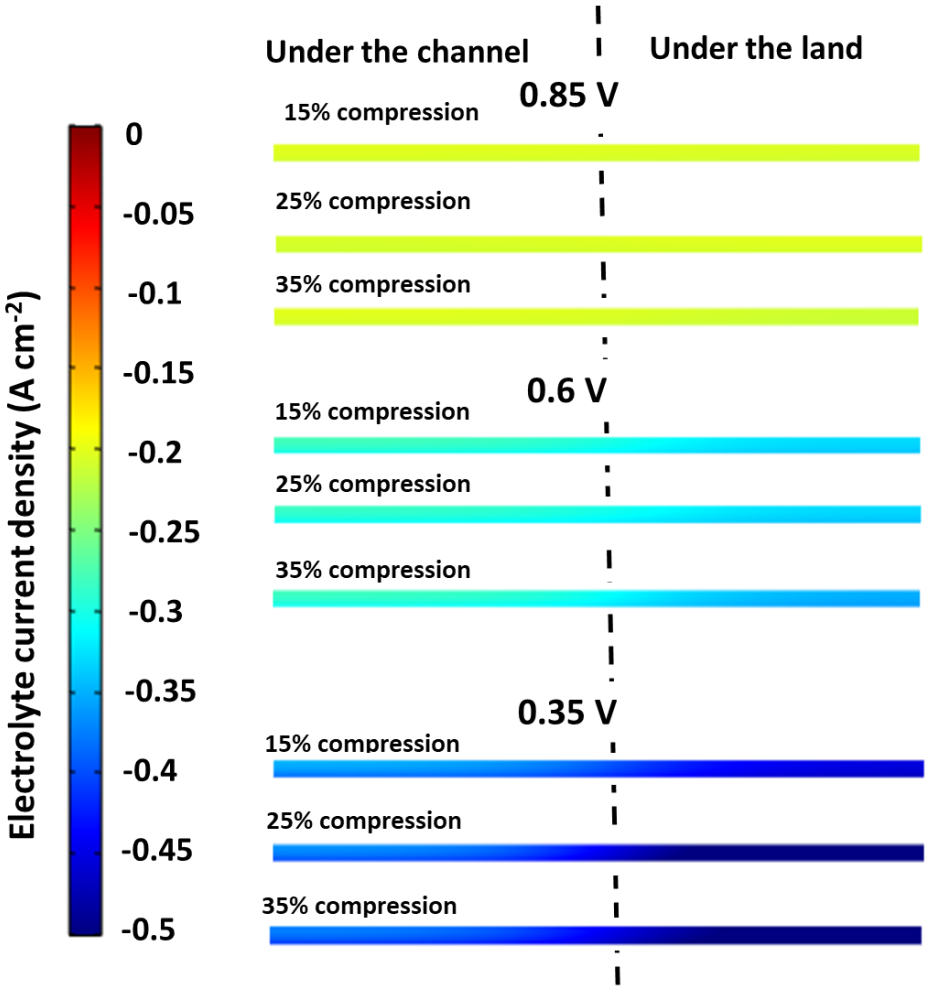

Figure 6.6–Half-symmetry contour plot showing the effect of compression on the cathode overpotential (η_C), plotted at the activation (V = 0.85 V), Ohmic (V = 0.6 V) and mass transport (V = 0.35 V) operation at 15% compression, 25% compression, and 35% compression

6.3.4 Membrane/ionomer water content

Figure 6.7 shows the membrane/ionomer water content profile shown with the dimensionless quantity λ that defines a ratio of the number of water molecules to the number of charge sites, at varying load conditions, plotted for 15%, 25% and 35% cell compression. It is generally found that the membrane/ionomer water content increases with the operating load (average current density). The influence of compression on the water content is clearly apparent. The higher membrane/ionomer water content under the cathode land and comparatively lower water content towards the anode (anode CL) suggest a link between compression and EOD. In the activation dominant region, the effect of compression on the water content was apparent at 35% compression. The average water content under the land was 3.6, 6.19, and 8.3, at 15%, 25%, and 35% compression, respectively. With an increase in the load to the Ohmic region, average water content under the land increased to 8.9, 13.4, and 13.9 with an increase in the compression. Further increase in the load to the mass transport region increases the water content under the land to 9.7, 14.3, and 15, at 15%, 25% and 35% compression, respectively. This emphasizes the increase in the net water diffusion flux with compression and operating load. While overall membrane/ionomer water content under the land region increases, the increase under the channel region is not significant. This highlight the nonlinear humidification of the membrane and CL. Hence, for transient operation, areas with lower membrane/ionomer water content would dry out, leading to in-plane (cross-diffusion) and through-plane (back-diffusion) water transport. This phenomenon is apparent at higher cell compression and lower saturation conditions.

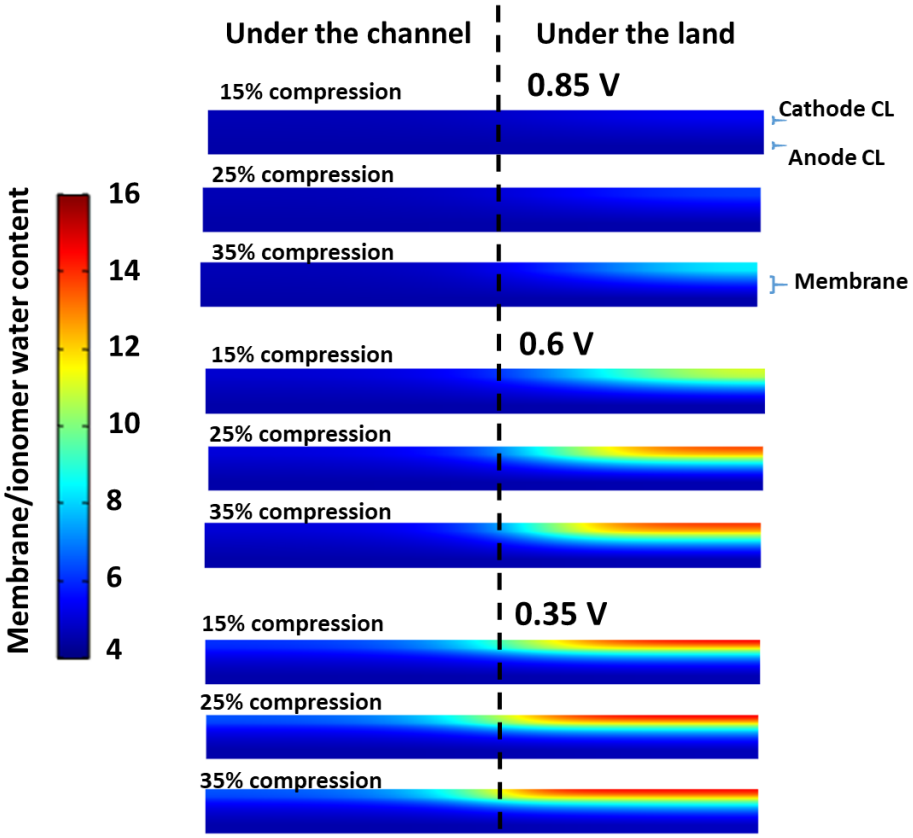

Figure 6.7–Half-symmetry contour plot showing the effect of compression on the membrane/ionomer water content shown with the dimensionless quantity (λ), plotted at the activation (V = 0.85 V), Ohmic (V = 0.6 V) and the mass transport (V = 0.35 V) operation. The compression varies from 15%, 25% to 35%

6.3.5 The molar concentration of oxygen

The oxygen concentration at the cathode CL determines the fuel cell performance. The effect of cell compression and the operating load on the oxygen concentration inside the cathode domain, i.e. cathode GDL and CL are depicted in Figure 6.8. The highest oxygen concentration exists under the channel region. With an increase in the non-uniform cell compression, the water saturation under the land increases, increasing the oxygen transport resistance under the land region.

At the activation dominant region, i.e. V = 0.85 V, the oxygen concentration profile is almost uniform at 15% cell compression. However, with an increase in compression, the oxygen concentration under the land region lowered by approximately 5% (measured at 35% compression).

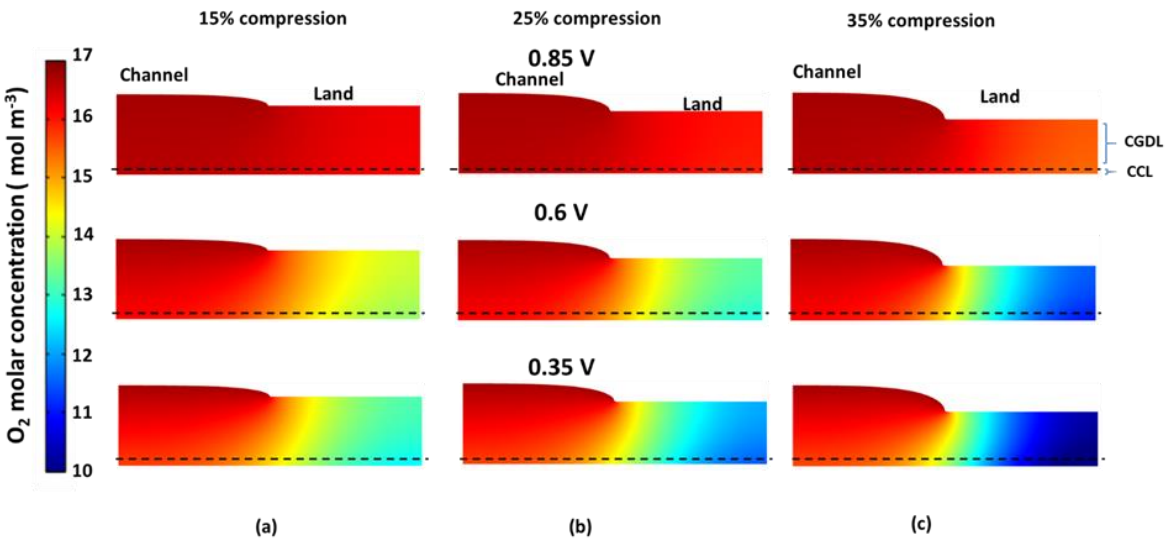

Figure 6.8–Half-symmetry contour plot showing the effect of compression on the oxygen concentration in the cathode domain plotted at the activation (V = 0.85 V), Ohmic (V = 0.6 V) and mass transport (V = 0.35 V) operation. (a) 15% compression, (b) 25% compression, and (c) 35% compression

At higher operating load, the rate of water generation and the propensity of water accumulation under the land region increase, increasing the water saturation under the land. Hence; with an increase in compression to 35%, the non-uniformity in the oxygen concentration has increased to 23% at the ohmic [V= 0.65 V] and to 41% at the mass transport dominant region [V = 0.35V]. This analysis suggests higher compression will act to promote the nonuniformity in the oxygen concentration that could further affect the current density distribution

6.3.6 Liquid water saturation

The effect of cell compression and the operating load on the liquid water saturation, and consequently, the propensity for flooding, in the cathode domain, are depicted in Figure 6.9. With an increase in the load, the rate of water generation elevates. However, it can be seen from the contours that the accumulation of liquid water increases with an increase in compression. Due to the loss of porosity under the land with an increase in compression, more considerable water accumulation and higher resistance to reactant transport (lower oxygen diffusivity and a lower rate of water removal) were observed under the land. Further, in the present model, liquid water is generated by two main phenomena, water vapour condensation and membrane/ionomer water desorption. Membrane/ionomer water desorption dominates the liquid water saturation phenomenon, enhancing the accumulation of liquid water under the land domain with local maxima towards the cathode CL. These results are in agreement with previously published models [250,252,322] and experimental results [167,173,323]. The polarisation performance at 0.85 V suggests a similar rate of water generation, irrespective of compression. However, the difference in the saturation profile at 35% compression clearly shows that with an increase in the operating load, the net water accumulation increases at all compressions, with the tendency to accumulate water under the land and localised

maxima towards the cathode CL. In the mass transport dominant region, an increase in the compression resulted in an increase in the saturation and lowering of the limiting current by 3% and 7% at 25% and 35% cell compression, respectively (in comparison with the 15% cell compression). This analysis suggests higher compression will act to promote water flooding conditions in the cell.

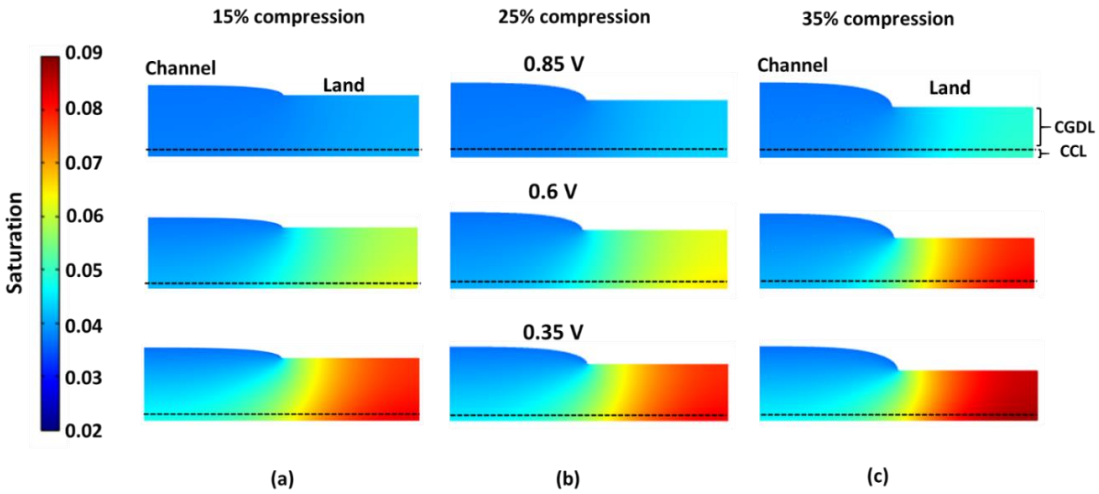

Figure 6.9 – Half-symmetry contour plot showing the effect of compression on the liquid water saturation in the cathode domain plotted at the activation (V = 0.85 V), Ohmic (V = 0.6 V) and mass transport (V = 0.35 V) operation. (a) 15% compression, (b) 25% compression, and (c) 35% compression

6.3.7 Temperature distribution

Figure 6.10 shows the temperature distribution across the computational domain with an increase in both the compression from 15% to 35% and the operating load from 0.85 V (low current density/activation dominant region) to 0.3 V (high current/mass transport dominant region). At the activation dominant region (V = 0.85 V), the average current density at all the compressions was identical, as shown in Figure 6.5 At these

operating conditions, the exothermic ORR is the main contributor to the heat source at all the compressions (> 98 %), as shown in Figure 6.11.

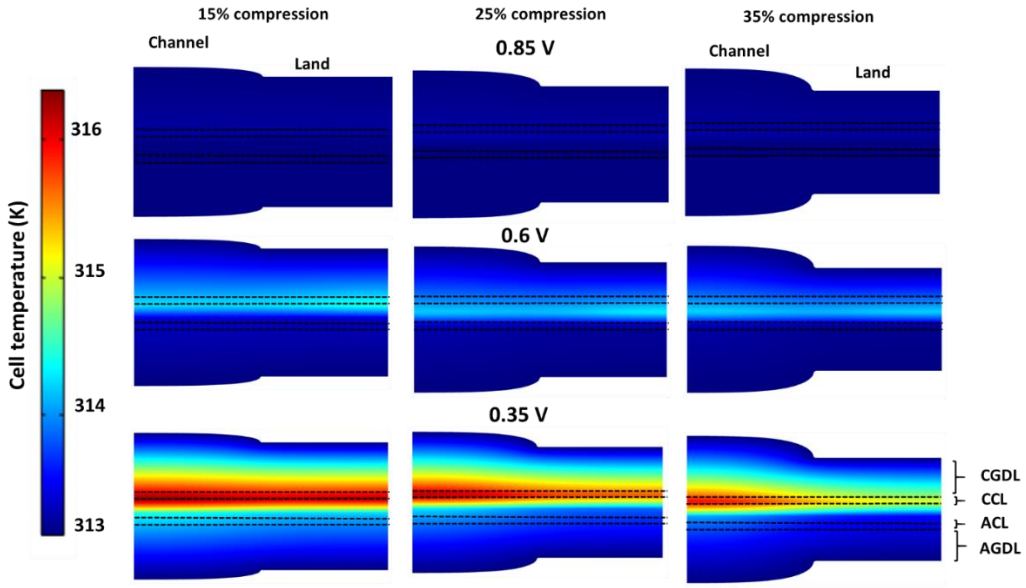

Figure 6.10 –Effect of compression on the energy transport at 15%, 25 %, and 35% compression depicted in the half-symmetry contour plots, showing the temperature distribution at the activation (V = 0.85 V), Ohmic (V = 0.6 V) and the mass transport (V = 0.35 V) operation

With an increase in the operating load to the Ohmic operation, the cell temperature elevates in the cathode region with a noticeable temperature gradient in the through-plane direction (Figure 6.10). Among the heat sources, the Ohmic heating accounts for less than 1% of the total heat released. Moreover, an increase in the compression improves the electrical conductivity of the GDL and lowers the contact resistance between the adjacent layers. Hence, the Ohmic contribution to the heat source further reduces with compression, as shown in Figure 6.11. Furthermore, the heat release from the phase change operation has also elevated, accounting for 7%, 9% and 11% of the total heat source (S_T). This delineates the presence of mass-transport limiting phenomenon at the Ohmic operation region, which is altered by the compression.

As anticipated, the non-uniformity in temperature profile intensifies with the operating load reaching V = 0.35 V. The highest temperature was observed towards the centre of cathode catalyst layer under the channel, which is approximately 3.2% higher than the temperature at the inlet boundary, measured at 15% compression. These results are in agreement with previous modelling efforts [250,252,307]. The effect of compression at the mass transport dominant region (at the fixed voltage) was unequivocal (Figure 6.10). Besides the heat released by the ORR, the heat released during the phase change of water contributes approximately 9%, 9.8% and 11% of the heat at 15%, 25% and 35% compression, respectively. It is important to note that the results are presented at the fixed voltage where the current density was approximately 6% lower at 35% compression compared to 15% cell compression (Figure 6.5(a)). Therefore, the absolute heat released due to ORR at 35% compression was lower than that at 15% compression; hence, the change in the temperature maxima is subjective to limiting current density.

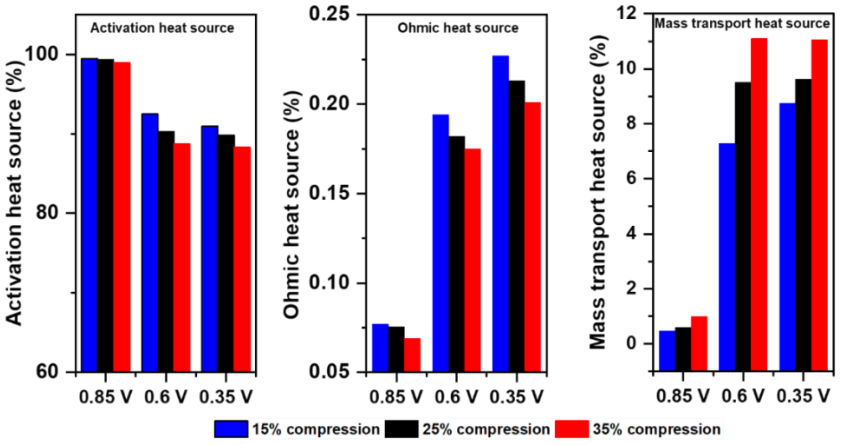

Figure 6.11 – Contribution of activation, Ohmic, and mass transport heat sources to the total heat source

6.4 Conclusion

The non-uniform compression exerted by the channel/land arrangement results in lowering of the porosity and directional permeability while improving the thermal and electrical conductivity of the GDL under the land region. The non-linear distribution of these properties, including structural deformation of GDL under the channel (tenting), was achieved by solving a structural model.

The electrochemical model predicts the polarisation performance at three compressions, 15%, 25% and 35%, with the focus on the three operating regions of the fuel cell. Compression showed a marginal effect on the averaged activation and the Ohmic performance of the fuel cell; however, results differ on the localised scale. The results also showed that an increase in compression increases the mass transport dominance in the Ohmic region, fostering early mass transport losses.

Reactant transport in the GDL is mainly a function of porosity. The loss of empty pore spaces with an increase in the compression, primarily under the land, have an undesirable impact on the performance. The formation and accumulation of liquid water occupying the empty pores in the GDL and further reduces the GDL porosity, increasing mass transport resistance. This results in reaching the limiting current earlier as compression increases.

Hence, the present study effectively combines the use of X-ray CT for the initial parameterisation (Chapter 4) and the numerical modelling to describe the effect of channel/land geometry on fuel cell performance, while highlighting the strong dependence of cell compression on the water saturation and temperature distribution, particularly under mass transport dominant conditions. The experimental validation of the model using neutron imaging is provides in Chapter 7, Figure 7.8.

Chapter 7
In-operando water dynamics of a PEFC

Abstract

Water dynamics in the membrane electrode assembly (MEA) and flow channels of polymer electrolyte fuel cells (PEFCs) is governed by the complex interplay of many physical and operational factors. The chemical nature and structure of the gas diffusion layer (GDL) plays a large part in this and is affected by the extent to which it is mechanically compressed. Here, multi-orientation neutron radiography reveals the effect of compression on the way in which water accumulates and is transported between land and channel and between cathode and anode. By performing neutron imaging in both the in-plane and through-plane directions, it is possible to determine what constitutes a given ‘thickness’ of water mapped across the extent of an MEA. Changing MEA compression from 25% to 35% has a significant effect on water distribution and dynamics in operational cells. The effect of compression on performance is most marked in the mass transport region, and there are consequences for liquid accumulation in channels and back-diffusion of water from the cathode to the anode.

7.1 Introduction

The advancement in PEFC technology towards commercialisation demands for a detailed understanding of how fuel cell operate *in operando*; this insight can then inform improved engineering design, assembly, materials selection and operating conditions [315,324] As discussed in the previous chapters, water transport in porous domains of the fuel cell, such as the GDL, MPL and CL, is one of the critical parameters that impact water management and subsequently fuel cell performance [315,324]. The non-uniform compression, detailed in Chapter 4 confirms the heterogeneous distribution of the effective properties that define water management and hence the performance.

High-resolution neutron imaging is a particularly powerful technique for probing water in fuel cells. The neutron beam is strongly attenuated by hydrogen-containing compounds such as water while being relatively transparent to heavier atoms that constitute the remainder of fuel cell components, (bipolar plates, gaskets, etc.) (Detailed discussion is provided in Chapter 3). These properties make the technique particularly versatile for visualising water dynamics across a fuel cell [88,152,166,167,179,183,325–327]. While this technique can resolve water at higher resolution, the fundamental limitation is a smaller field-of-view [169,180,328–330]. Hence, a careful balance between resolution, exposure time and the field-of-view or size of the active area has to be met to generate adequate data from the neutron imaging.

Neutron imaging can be applied in the in-plane orientation, where the MEA is parallel to the neutron beam or in the through-plane orientation, where the MEA is perpendicular to the beam. The in-plane radiographs of operating cells provide information regarding the water content in different layers of the MEA but do not give an indication of where the water is distributed spatially across the entire fuel cell active area [18,168,331]. The through-plane radiographs provide water retention profile

along the channel length, but cannot identify in which layer of the cell the water resides. [131,133,149]. The relationship between cell compression and the fuel cell performance was evaluated by Wu *et al.* using through-plane neutron imaging, showing an overall increase in water content in the channel with increasing compressions; however, no information was provided regarding the effect of cell compression on the water accumulation in the MEA layers [125].

In this work, multi-orientation in-operando neutron radiography, both in the in-plane and the through-plane orientation is used to investigate the effects of cell compression on the water dynamics of the fuel cell. This allows for a detailed analysis of the effect of compression on membrane hydration, water distribution under the land and across the channel domains, and back-diffusion of water across the membrane, from the cathode to the anode domain. The neutron imaging performed in both the in-plane and through-plain allows determining what constitutes a given 'thickness' of water mapped across the as a validation tool for the 2D non-isothermal multiphase model discussed in Chapter 6.

7.2 Experimental set-up

7.2.1 Cell design and compression

A closed-cathode PEFC with an active area of 10 cm^2 was used in the study. The cell comprised of aluminium end-plates, current collectors and flow-fields, as shown in Figure 7.1(a). The end-plates, current collectors and flow-fields were gold-coated to increase corrosion resistance and decrease electrical resistance. PTFE gasket sheets were used to seal the perimeter of the MEA on either side of the membrane. Tygaflor gasket sheet (70 µm thickness) was used for electrical insulation between the current collector and the end-plate. VITON rubber O-rings were used to provide a gas/liquid seal at the interface between current collectors and flow-fields. A parallel flow-field

arrangement was used to give a clear visualisation of water emerging into the channel. This is not possible with a serpentine configuration where meanders overlap in the in-plane direction. The bifurcating reactant delivery channels were designed on the back of the flow-field to ensure uniform gas distribution across individual parallel gas channels, as shown in Figure 7.1(c) [131,148,154].

The MEAs were assembled from commercial carbon fibre GDEs with a platinum catalyst loading of 0.4 mg cm^{-2} (HyPlat, South Africa) and a 50 µm thick ionomer membrane (GORE, USA). The MEAs were hot-pressed as per the conditions described in section 3.1.1.

PTFE sheets of 50 µm and 75 µm were laser-cut to the cell's dimension. Multiple sheets stacked together were used to achieve the required degree of compression. The GDL thickness and details of the gaskets used are presented in 3.1.2. The particular compression levels were chosen to evaluate the typical range of cell compression that assures proper sealing and the performance of the fuel cell. The initial torque of 1.5 Nm was used to tighten the bolts. A micrometre (RS Pro, accuracy ±5 µm) was used to reassure the changes in GDL thickness with compression. A laboratory X-ray CT system, ZEISS Xradia 520 Versa (Carl Zeiss, USA) was used to examine the structural behaviour of the MEA under compression. (Figure 7.1(b)).

With an increase in cell compression, the fibre density of the GDL has increased in the region under the land, causing the loss of porosity, as presented in Section 4.3.6.1. However, the region under the channel undergoes 'tenting'. This results in the non-uniform structural and effective mass transport properties in the fuel cell.

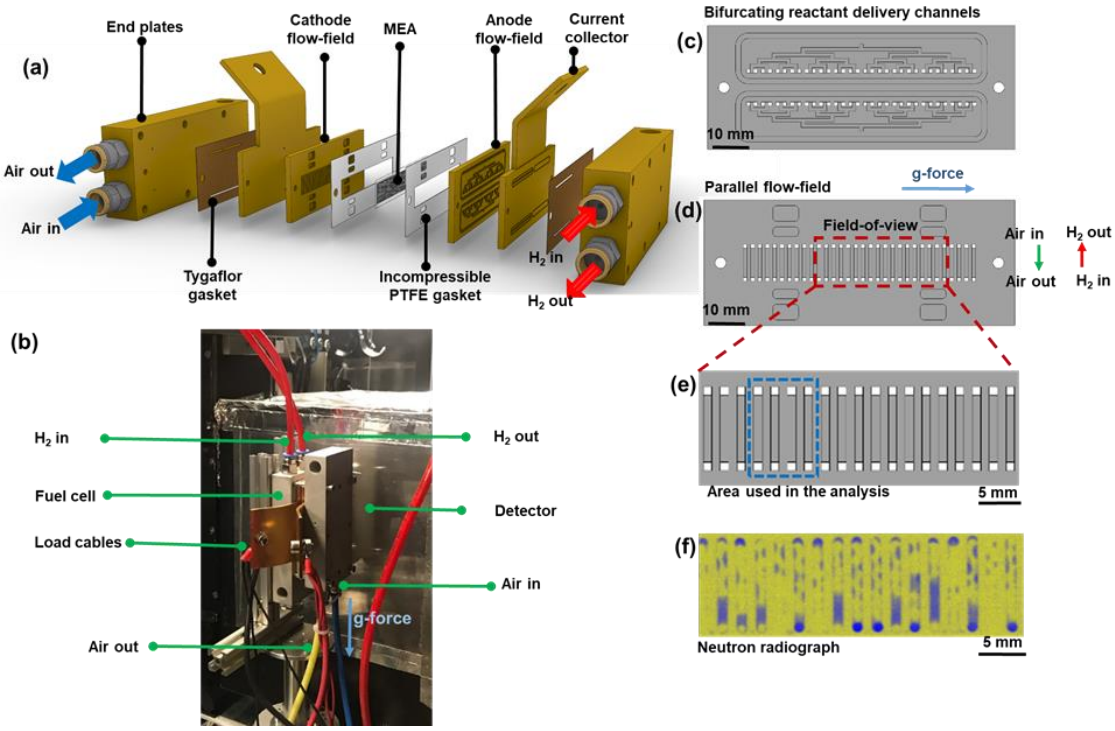

Figure 7.1– (a) Exploded view of the fuel cell showing individual components, (b) neutron radiography set-up at CONARD to generate in-operando radiographs in the in-plane and the through-plane orientation, The cell was held in the vertical orientation (c) bifurcating reactant delivery channels on the back-side of the flow-field to ensure uniform reactant delivery to individual parallel gas channels, (d) the parallel gas channels where the highlighted region in red indicates the field-of-view used in this study, (e) highlighted region in blue shows the area used in the analysis. The particular area of interest includes four channels in the centre of the fuel cell. (f) Generated radiograph in the through-plane orientation masked with yellow and blue colour, yellow representing the dry region and blue representing the higher water content

Table 7-1 – GDL thickness achieved using PTFE gaskets

Gasket thickness (µm)	GDL thickness (µm)	Cell compression (%)
	238	0%
50 + 50 + 75	175	~25%
50 + 50 + 50	150	~35%

7.2.2 Experimental procedure

In-house fuel cell test rig and control software based on LabVIEW (National Instruments, USA) was used to operate the PEFC. (refer to Figure 3.4 for the schematic of the setup). The experimental data were acquired with a data acquisition card (DAQ card, USB 6363, - National Instruments, USA). The cell was operated under dry gas conditions to evaluate the water dynamics in isolation from the water present in a humidified reactant stream. Dry reactant delivery allows evaluation of back-diffusion of the water during operation. The cell was tested under ambient temperature conditions.

The cell was operated at a fixed flow condition where both anode and cathode flow-rates were set at 0.5 L min^{-1} during neutron imaging. The cell was flushed with argon (Ar), high flow rates, 1 L min^{-1}, before changing the operating conditions, ensuring the removal of accumulated water from the previous experiment. The reactant gas flow was controlled using digital mass flow controllers (Bronkhorst, UK). The current was drawn from the fuel cell using a DC electronic load (PLZ664WA, Kikusui).

Table 7-2 – Cell conditioning parameters before the neutron radiography experiments.

Operation	Conditions
Polarisation range	OCV to 0.4 V
Cell conditioning	10 min
Hold time per current increment (0.1 A cm^{-2})	1 min
Flushing time	5 mins

Separate experiments were carried out for the in-plane and the through-plane orientation for each compression. The current load was increased from 0.01 to 1.1 A cm^{-2} in steps of 0.1 A cm^{-2} until the voltage reached 0.4 V. Three fast polarisation curves were generated before holding the current at 0.1, 0.6, and 1 A cm^{-2} for 300 s each. The same current sweep procedure was repeated after each change in the orientation and compression. The details of the fast-polarisation curve are as presented in Table 7-2.

7.2.3 Neutron radiography

Neutron radiographs were generated at low energetic (cold) neutron radiography (CONRAD) beamline facility at Helmholtz-Zentrum Berlin (HZB). The neutron radiography setup is shown in Figure 7.1(b).The details of HZB CONRAD are provided in Chapter 3, Section 3.1.4.2. The cell mounted on a fixture was placed on a rotating table, allowing radiographs in both the in-plane and through-plane orientation. An imaging field-of-view of 40 × 34 mm^2 with 15.2 µm $pixel^{-1}$ resolution was achieved

using the imaging set-up previously developed by Kardjilov *et al*. [180]. In-plane imaging at a resolution of 15.2 μm pixel^{-1} cannot unequivocally separate the GORE membrane from the catalyst layers and are thus grouped and referred to as the 'membrane electrode assembly (MEA). Each image was taken with an exposure time of 5 s. The liquid water image was generated by normalising the wet image to the dry fuel cell image taken at the beginning of each experiment and any non-uniformity in the beam-intensity was corrected with an open-beam image. The quantification of the water thickness from neutron images was performed using the Beer-Lambert law (Equation (3.2)). The radiographs presented were originally grey-scale images which were masked with a yellow-to-blue 'parula' colour-map, blue representing the presence of higher levels of water.

7.3 Results and discussions

7.3.1 Polarisation performance

Figure 7.2 shows the effect of cell compression on the polarisation and the power density curves. A polarisation curve can notionally be divided into three regions, the activation region, (V > 0.8 V), the Ohmic region (0.5 V < V < 0.8 V), and the mass transport region (V < 0.5 V). The activation kinetics is primarily reliant on catalyst properties and particularly sensitive to operational temperature. Therefore, the compression did not show any notable difference in the activation performance. With increases in current density, the effect of compression on the cell performance was apparent [46,109,125]. In the Ohmic region, the 25% compressed cell showed better performance. At j = 0.6 A cm^{-2}, the cell performance of the 35% compressed cell was reduced by 4% compared with the 25% cell compression. In the mass transport region (j = 1 A cm^{-2}), 25% compression showed 11% increase in performance. The maximum power density achieved at 25% compression was 0.49 W cm^{-2}; whereas the maximum power density reached at 35% compression, was 0.47 W cm^{-2}.

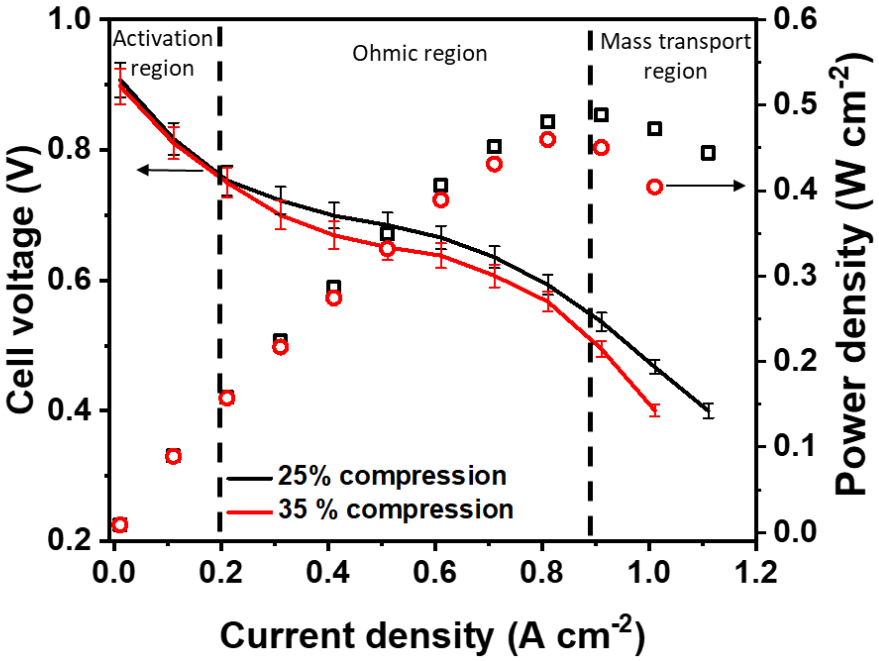

Figure 7.2– Comparison of polarization performance with a change in compression. Error bars indicate the difference between three repeat runs; Solid lines (-) are cell voltage, hollow shapes (□) are power density

In the present case, the porosity under the land region lowered by 13% and 25 % with an increase in compression to 25% and 35%, respectively. Lowered GDL porosity under the land region lowers the contact resistance [62]. The EIS study by Mason et al. shows that the increase in cell compression to 25% (i.e. dimensional change of 60 μm) lowered the Ohmic resistance from 29 mΩ cm^2 (at no compression) to 14 mΩ cm^2. Furthermore, an increase in the compression to 35% (i.e. dimensional change of 83 μm) lowered the Ohmic resistance to 10 mΩ cm^2 [121]. Therefore, though the increase in cell compression is an effective method for reducing Ohmic losses associated with the contact resistance [109], this leads to a loss of GDL porosity under the land region (please refer to Figure 4.12) which affects the water management in the Ohmic region.

This strongly suggests that an increase in cell compression increases the mass transport dominance in the Ohmic region and promotes early mass transport due to the limitations in water management. Hence, to maximise the performance, an optimal compression needs to be determined, which is a trade-off between electrical and mass transport factors.

7.3.2 Neutron radiographs

The polarisation data can be coupled with the neutron imaging that provides detailed and instantaneous information regarding the water dynamics in the fuel cell, which can obtain a better picture of an operating fuel cell.

7.3.2.1 Activation region

At open circuit voltage, no water is produced electrochemically. Hence, the cell is in dry condition. With an increase in current density, water is produced across the active area. Figure 7.3 shows the radiographs taken over 300 s in separate in-plane and through-plane experiments, with all the operating conditions identical.

The in-plane radiographs for both compressions are shown in Figure 7.3(a). At 0.1 A cm^{-2}, the cell at 25% compression appeared to be almost dry (average $\delta_{water\ -\ membrane}$ < 13 μm). Although the same amount of water was being generated at a given current density, at 35% cell compression the presence of water was seen in the MEA (in Figure 7.3(a) - blue region) with average water thickness increased to 42 μm. Moreover, the tendency to accumulate water under the land is evident at 35% cell compression with distinctive ‘peak’ and ‘valley’ profiles in the CL-membrane that correspond to the land and channel regions, respectively (Figure 7.3(b)). This suggests that the compression affects the condensation of liquid water under the land region; whereas water evaporation is promoted under the channels [307,326].

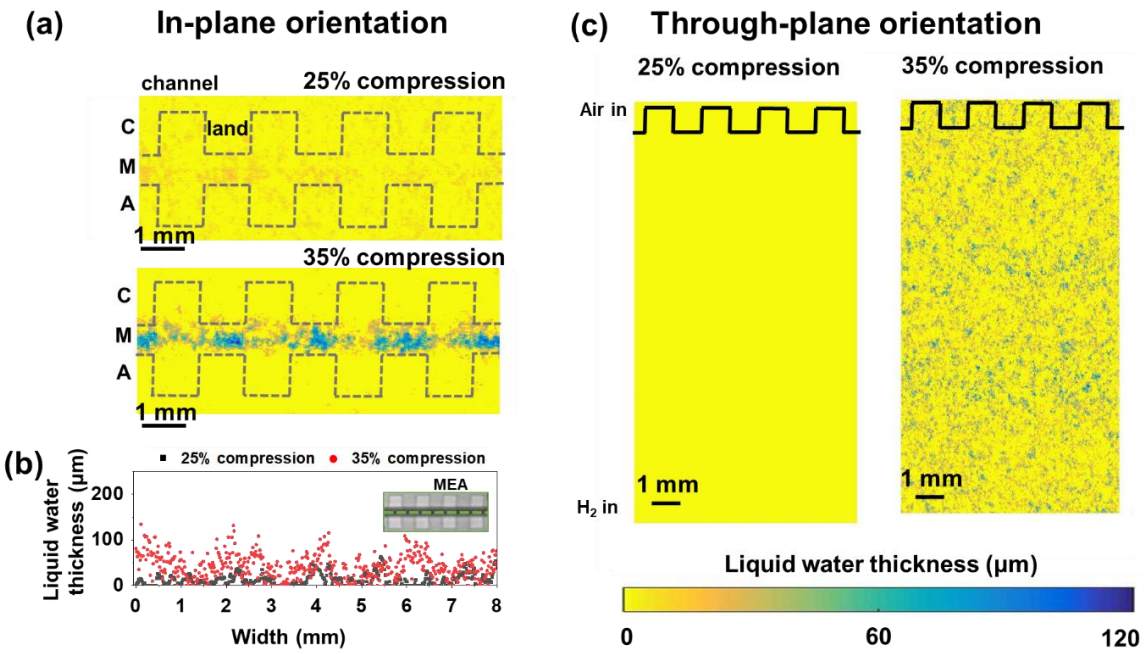

Figure 7.3– Effect of compression on the water distribution in the activation region, j = 0.1 A cm^{-2} when the flow of the reactants was fixed to 0.5 L min^{-1}, equating to >10 air stoichiometry. (a) in-plane radiographs measured at t = 300 s, 'C' is the cathode flow-channels, 'M' is MEA (GDLs + CLs + membrane) and 'A' is an anode flow-channels, Grey dashed line showing the flow-field outline is included as a guide to the eye (b) liquid water thickness profile in the in-plane orientation measured at the membrane/CL showing the effect of channel/land geometry on the water retention. Green dashed line at membrane/CL shows the schematic location where the liquid water thickness was measured, and (c) through-plane radiographs measured at t = 300 s. (a) and (c) share the same colour bar.

The through-plane radiographs are shown in Figure 7.3(c). No significant water signal was observed for the 25% compression, with a relatively uniform water distribution for the 35% compression with no clear demarcation between land and channel zones. This is clearly in contrast to the in-plane representation. This could be due to higher signal-to-noise is achieved for the in-plane analysis as the neutron probe integrates a much larger sample through the length of a channel. The collective analysis of the

voltage profile and radiographs at the activation region strongly suggest that the compression has a marginal effect on voltage performance, though the water accumulation in the cell became noticeable with an increase in the compression. However, the stable performance indicates the balance between water generation, capillary transport, forced convection and accumulation.

7.3.2.2 Ohmic region

In the ‘notional’ Ohmic region, an increase in the current density elevates water production. As the name suggests, the voltage loss in the Ohmic region is typically considered to be dominated by ionic and electronic losses. However, it has been shown that an increase in cell compression increases the mass transport resistance in the Ohmic region which leads to the accumulation of liquid water in the MEA, amplifying the voltage loss [109,332]. The radiographs presented in Figure 7.4 compare the galvanostatic cell performances at both compressions in the Ohmic region (j = 0.6 Acm^{-2}).

The in-plane radiographs for Ohmic operation for each cell compression are shown in Figure 7.4(a) obtained at t = 300 s. Irrespective of the compression, the overall water content has increased with the current density showing the presence of the water at 25% cell compression (blue region in the MEA). The average water thickness at 25% compression was 225 μm, with a standard deviation of 101 μm, while at 35% compression, the average water thickness increased to 291 μm with a standard deviation of 101 μm (Figure 7.4(b)). The comparative analysis of water accumulation implied that the increase in the cell compression to 35% increases the water accumulation by 27%, with clear ‘peaks’ and ‘valleys’ that correspond to the land and channel regions, respectively. Moreover, almost constant standard deviation suggests that the probability of the water accumulation at a particular location was the same for both the compressions, while the water content differed. Water transport in the GDL is governed by capillary action. Lowered GDL pore diameter under the land region

alters the capillary pressure, which further promotes the water vapour condensation under the land, increasing water retention in the GDL under the land region [160,165,166,326,333]. Therefore, an increase in compression to 35% results in lowering the porosity under the land region and an increase in the local water thickness maxima to 580 µm compared to 500 µm at 25% compression. The non-uniform liquid water distribution in the MEA promotes non-uniform current generation when operated in a galvanostatic mode [207,334]. Non-uniform current generation leads to the local hot spots and alters the durability of the cell in the long run.

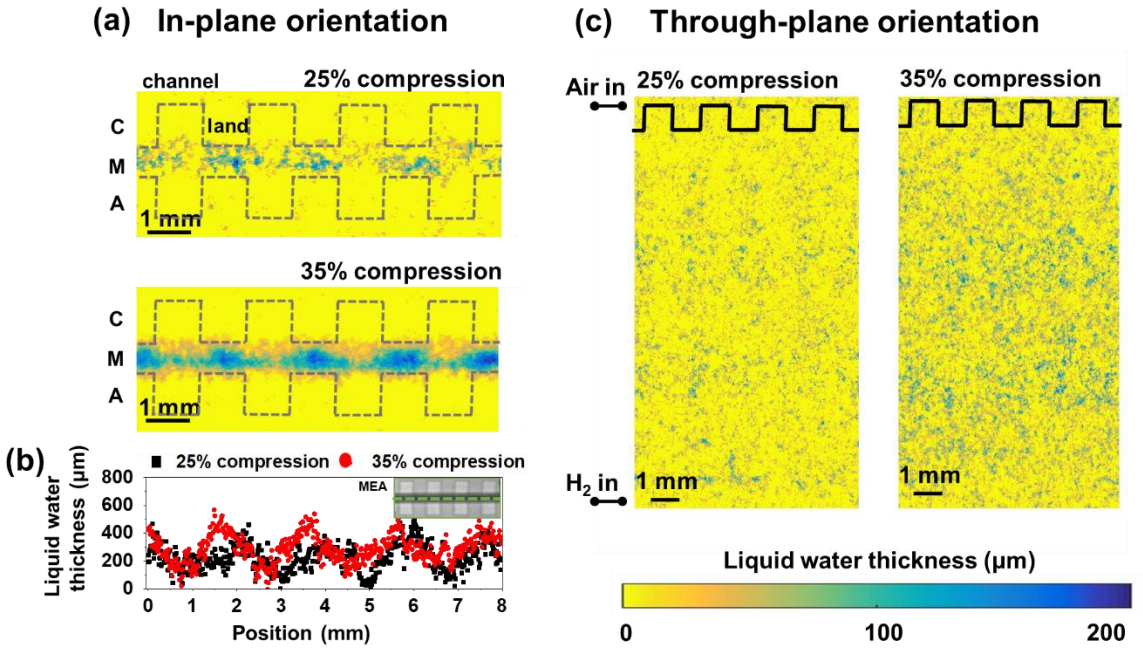

Figure 7.4– Effect of compression on the water distribution in the Ohmic region, j = 0.6 A cm^{-2} ((a) in-plane radiographs at t = 300 s, 'C' is the cathode flow-channels, 'M' is MEA (GDLs + CLs + membrane) and 'A' is an anode flow-channels, Grey dashed line showing the flow-field outline is included as a guide to the eye (b) liquid water thickness profile in the in-plane orientation measured at the membrane/CL showing the effect of channel/land geometry on the water retention. Green dashed line at membrane/CL shows the schematic location, where the liquid water thickness was measured, and (c) through-plane radiographs at t = 300 s. (a) and (c) share the same colour bar

The water profile shown in the through-plane radiographs indicates the presence of water in the form of droplets spread across the active area (Figure 7.4(c)). Though larger water droplets were seen at 35% compression, neither water accumulation in the channels or the dry-out areas were observed in the Ohmic region. Therefore, whilst all other operating parameters were constant, the change in liquid water retention and voltage decay at j = 0.6 A cm^{-2} was due to cell compression. The increase in cell compression leads to a noticeable variation in water accumulation and water retention under the land region. The dry cell operation at a high flow rate (air stoichiometry ~ 7.5) resulted in the removal of the product water through evaporation under the channel region, while providing adequate membrane hydration. The increase in compression lowers the electrical contact resistance and increases water accumulation under the land. Accumulated water hinders the reactant transport to the active layers, increasing reactant transport resistance [109]. As the reactant transport resistance is higher than the contact resistance, an increase in compression promotes mass transport in the 'Ohmic' region.

7.3.2.3 Mass transport region

Figure 7.5 displays the liquid water profile at each cell compression, operated in the mass transport region (j = 1 A cm^{-2}) with the flow rate fixed at 0.5 L min^{-1} equating to air stoichiometry of ~4.44. The in-plane radiographs shown in Figure 7.5(a) reveal the combined, yet distinct, effect that land/channel geometries and cell compression have on water accumulation. In general, an increase in compression resulted in the increased propensity of water accumulation in the cell during the mass transport operation (in comparison with the Ohmic operation). These results are in agreement with previous studies [163,166,334,335]. The discernible feature of mass transport operation was the back-diffusion of water, observed at both compressions. The water vapour condenses under the land region and saturates the GDL. The liquid water starts 'bulging' into the channel, forming water droplets, while some water back-

diffuses to the anode domain. This behaviour can be clearly seen in the in-plane radiographs. The behaviour agrees with the previously reported experimental and modelling studies [18,244,251,252,332,336]. The hydrophilic contact angle observed between water droplets and the channel wall (θ = 84°, highlighted by the red arrow in Figure 7.5(c)), was due to the gold coating on the aluminium plate [22,166].

The water content in the MEA depicted in Figure 7.5(b) shows increased water thickness with flooded ‘peaks’ and relatively dry ‘valleys’. This confirms non-uniform accumulation and retention of the liquid water. The average water thickness at 25% compression was 350 µm with a standard deviation of 124 µm. Increase in compression resulted in a 7% increase in average water thickness, reaching 373 µm with a standard deviation of 104 µm.

The through-plane hydrographs in Figure 7.5(c) provides vital information regarding the effect of compression on water retention, water spread, and droplet/slug formations. In general, the through-plane radiographs in the mass transport region revealed well-defined channel/land profiles, highlighting the accumulation of liquid water in the channel. This result agrees with previously published studies [104,125,131,149,167].

The through-plane hydrographs revealed that the overall water content in the channel has increased with compression in the form of three main water retention profiles, namely, water droplets, slugs, and films. The hydrophilic nature of the channel walls leads to the formation of water droplets and further develops into slugs [140,337]. Large and elongated water droplets (length >1000 µm) highlighted in ‘red’, were observed on the channel wall, while ‘isolated’ droplets were observed across the active area of the cell.

The present cell was operated in counter-flow mode, but results will be a function of the flow-field design. The net flux of water between electrodes can vary locally depending on the flow arrangement and local relative humidity at the anode and

cathode. For example, in counter-flow with dry anode feed, the net flow of water from cathode to anode is likely, with back-diffusion being dominant. Whereas at the exit of the anode, where the stream has become fully humidified, net water flux could be in the opposite direction due to electro-osmotic drag outweighing back-diffusion as a result of lower hydraulic gradient from cathode to anode. As the present cell was operated at low temperature and relatively high feed gas velocity, the effect of relative humidity gradients along channels is minimised [338,339]. The increased saturation towards the cathode channel outlet reduces the effectiveness of water removal and forms the larger and more elongated water droplets/slugs. The increase in compression resulted in a 34% increase in the average slug size. Increase in the slug density results in partial blocking of the channel that could lead to the non-uniform reactant distribution to the active sites on the catalyst layer [75,337,340]. Furthermore, water spreads in the channel, forming the thin water film, as highlighted in 'dashed black'. The hydrophilic channel wall fosters water adherence to the channel under the surface tension; whereas higher gas velocity across the channel (0.5 m s^{-1}) results in convective water removal under higher drag forces. These two phenomena collectively result in forming the thin water film on the channel walls [340]. Increase in compression from 25% to 35% resulted in a 31% increase in the average water film thickness.

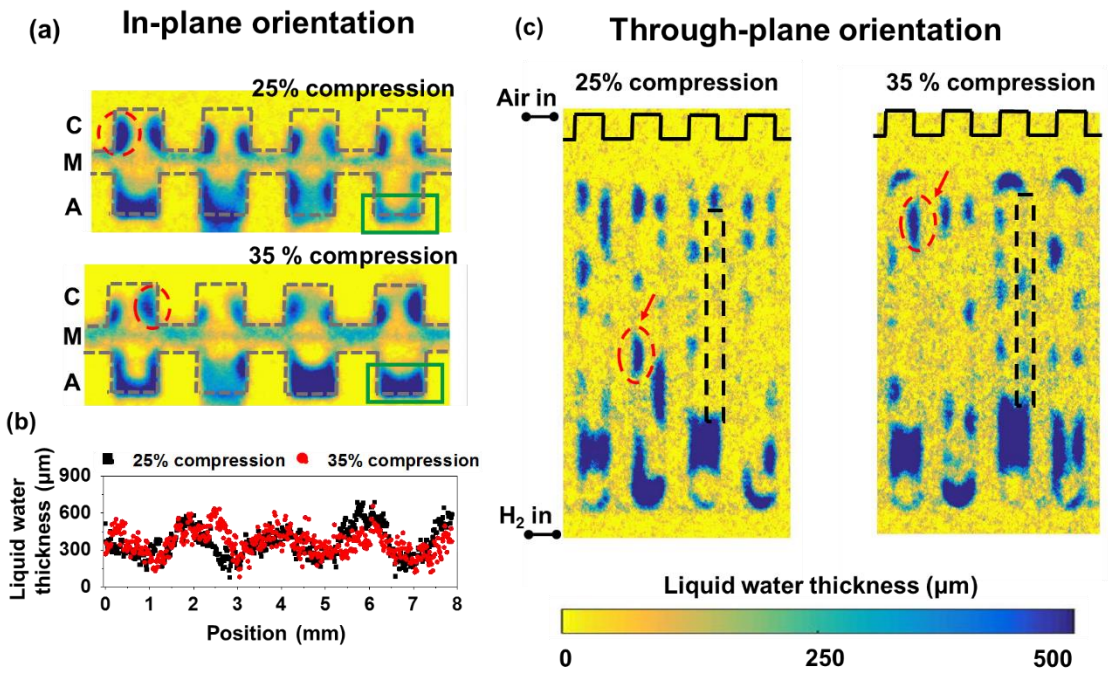

Figure 7.5– Effect of compression on the water distribution in the mass transport region, j = 1 A cm^{-2} (a) in-plane radiographs measured at t = 300 s, 'C' is the cathode flow-channels, 'M' is MEA (GDLs + CLs + membrane) and 'A' is an anode flow-channels, Grey dashed line showing the flow-field outline is included as a guide to the eye (b) liquid water thickness profile in the in-plane orientation measured at the membrane/CL showing the effect of channel/land geometry on the water retention. (c) through-plane radiographs measured at t = 300 s. (a) and (c) share the same colour bar

Hence, while the cell architecture and operating conditions were identical in both the compression cases and the same amount of water was being generated at the given current densities, it can be concluded that the difference in the water content in the cell was solely due to the increased compression. Moreover, the radiographs of the galvanostatic operation confirmed that the voltage loss at increased compression (observed in 7.3.1) was associated with increased water retention that leads to flooding and the tendency to back-diffuse water to the anode domain.

7.3.3 Water transport dynamics

Effective water management, required for the optimal cell operation, can be achieved by attaining a balance between the rate of water generation due to electrochemical reaction and the rate of water removal. The radiographs presented in Figure 7.3 (activation region) Figure 7.4 (Ohmic region) suggest that the membrane was adequately hydrated without channel flooding. However, with an increase in current density (mass transport region), the presence of liquid water in the channel suggests that the rate of water generation exceeds the rate of water removal.

Therefore, the rate of water retention influences the propensity for water flooding. The performance comparison between the cell compressions can be determined by calculating the rate of water retention within the cell [g s^{-1}], following the increase in current density. The amount of water generation, m_{gen} [mg] is theoretically calculated using Faraday's law, Equation (7.1)

$$m_{gen} = \frac{M_{H_2O} \cdot j \cdot A \cdot t}{2F} \tag{7.1}$$

where M_{H_2O} is the molecular weight of water, *A* is the area under analysis, *j* is the current density, and *t* is the duration of the galvanostatic operation, which is 300 s, *F* is the Faraday constant (96485 C mol^{-1}). The same amount of water was generated electrochemically under identical operating conditions, irrespective of the cell compression. The liquid water retention for different compressions was calculated by integrating the local water thickness across the area under analysis using Equation (7.2).

$$m_{rtn} = \rho_{H_2O} \int_0^A \delta_{water} \cdot dA \tag{7.2}$$

where ρ_{H_2O} is the density of the liquid water, *A* is the area under analysis, δ_{water} is the thickness of the liquid water.

Figure 7.6 shows the dynamic performance, under galvanostatic operation, of water retention and cell voltage, measured at 25% and 35% compression. In the activation region, the water profile was almost invariant over the duration; however, it was influenced by compression with an increase in the compression doubling the mean water retention, which was mainly observed under the anode land region (Figure 7.3). The compressive effect on the anode MPL may be the reason for increased water retention, as the hydrophobic MPL resists removal of water to the anode exit.

At 0.6 A cm^{-2}, water retention is affected by both the compression and the duration of the galvanostatic operation. A transient water retention profile is observed with the higher compression resulting in more rapid water accumulation, before reaching a plateau above that of the 25% compression. This higher water retention of the 35% case is manifest in a reducing voltage with time, compared to a relatively stable potential profile for the 25% case.

The dynamic water retention profile in the mass transport region (1 A cm^{-2}) is affected by the higher rate of water generation with the new water accumulation/retention reaching equilibrium faster than the 0.6 A cm^{-2} case.

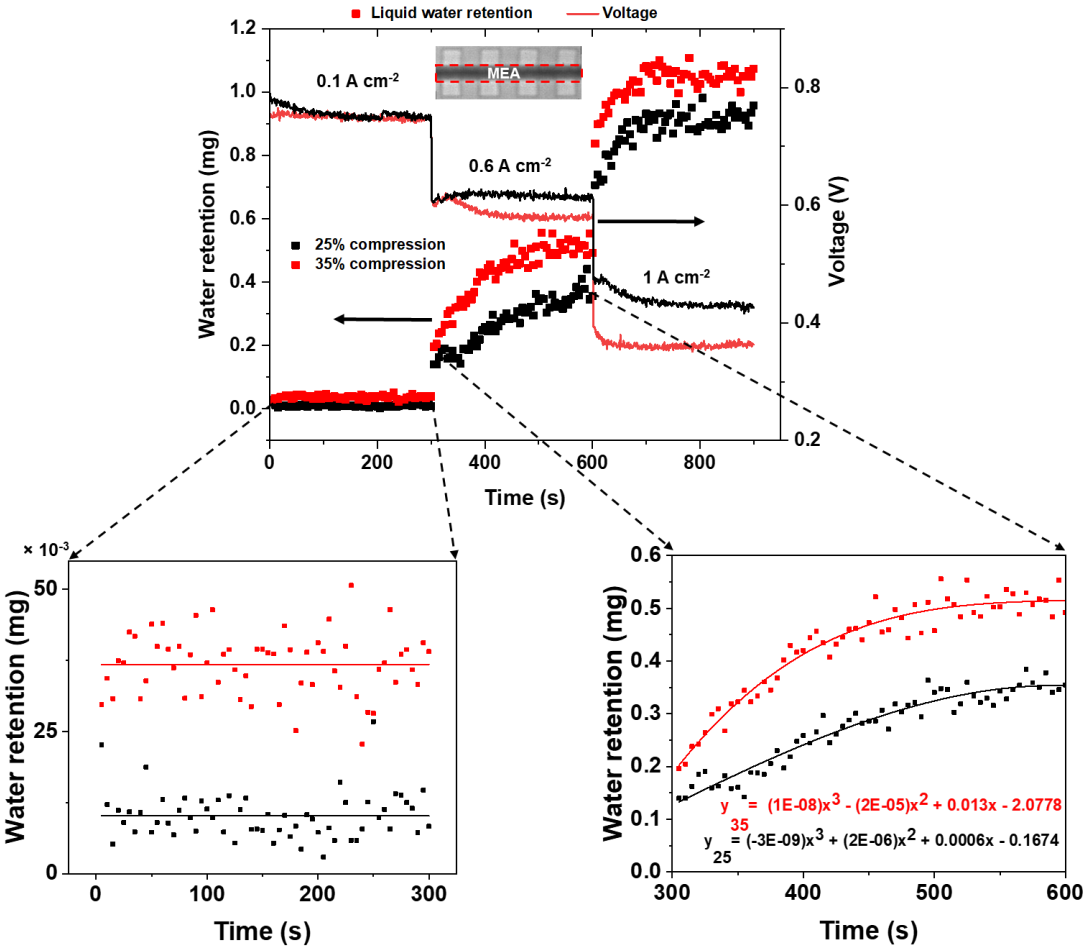

Figure 7.6– The dynamic effect of compression on the liquid water retention in the MEA (GDL + CL + Membrane) measured from the in-plane neutron radiographs and the voltage profile during the galvanostatic operation over 300 s

The effectiveness of water removal is calculated as the difference between the amount of water generation and the amount of water retention. Figure 7.7(a) shows the effect of compression and current density on the rate of water retention and efficiency of water removal measured at 300 s. An increase in the current density results in increased water generation. With fixed inlet flow conditions, the water removal efficiency was affected by the current density. Increase in current density to j = 1 A cm^{-2}, reduced water removal efficiency by 11% and 19%, for the 25% and 35%

compressions, respectively. As the water removal efficiency decreases with compression, the rate of water retention in the cell increased. Increase in current density from 0.6 to 1 A cm^{-2}, resulted in an increase in the rate of water retention by 84% and 80% when measured at 25 % and 35%, respectively. Moreover, cell compression affects the rate of water retention in a similar manner. The water retention in the Ohmic region (j = 0.6 A cm^{-2}) increased by 80% with an increase in compression, and the same in the mass transport region (j = 1 A cm^{-2}) which increased by 88%. This confirms that the compression exacerbates the effect of current density on water retention by lowering the water removal efficiency.

Increased water retention in the cell leads to the flooding conditions, as shown in previous radiographs. Active water removal mechanisms such as the electroosmotic pump effect [341], high stoichiometric open cathode PEFC designs [220], long and serpentine oxidant channels [342], anode water removal [255], etc. help to lower the effect of flooding at the cost of associated parasitic losses [202]. With no active water removal mechanism in place, like in the present cell, the generated/accumulated water under the land is either transported laterally under capillary action to the flow-channel and evacuated by the convective flux or back-diffuses to the anode (Figure 7.7(b)). The in-plane radiographs shown previously confirm that both the water transport mechanisms were apparent in the present case and the water content in the anode resulted from back-diffusion.

Figure 7.7(c) shows the characteristic effect of compression and operating load on the rate of back-diffusion plotted against the polarisation curves. The propensity of the water to back-diffuse into the anode was minimal at the low current region but increased with current density. The back-diffusion was marginally affected by compression throughout the current range with fixed flow conditions. The results presented here are in agreement with previous neutron imaging studies [167]. At identical reactant pressure and dry inlet conditions at the cathode and the anode, the net rate of water transport through the membrane is preliminarily controlled by the

water concentration gradient between the anode and cathode domain and the electro-osmotic drag [84,343]. Anode water thickness map presented in Figure 7.7(d) visually confirms that the water accumulation in the anode is in agreement with previous studies [84,167,344], and was due to water back-diffusion from the cathode to the anode. However, it is essential to note that the present results are provided in the central channels of the fuel cell and the effect of gravitational forces on the water accumulation and removal from the channel is not considered in the analysis.

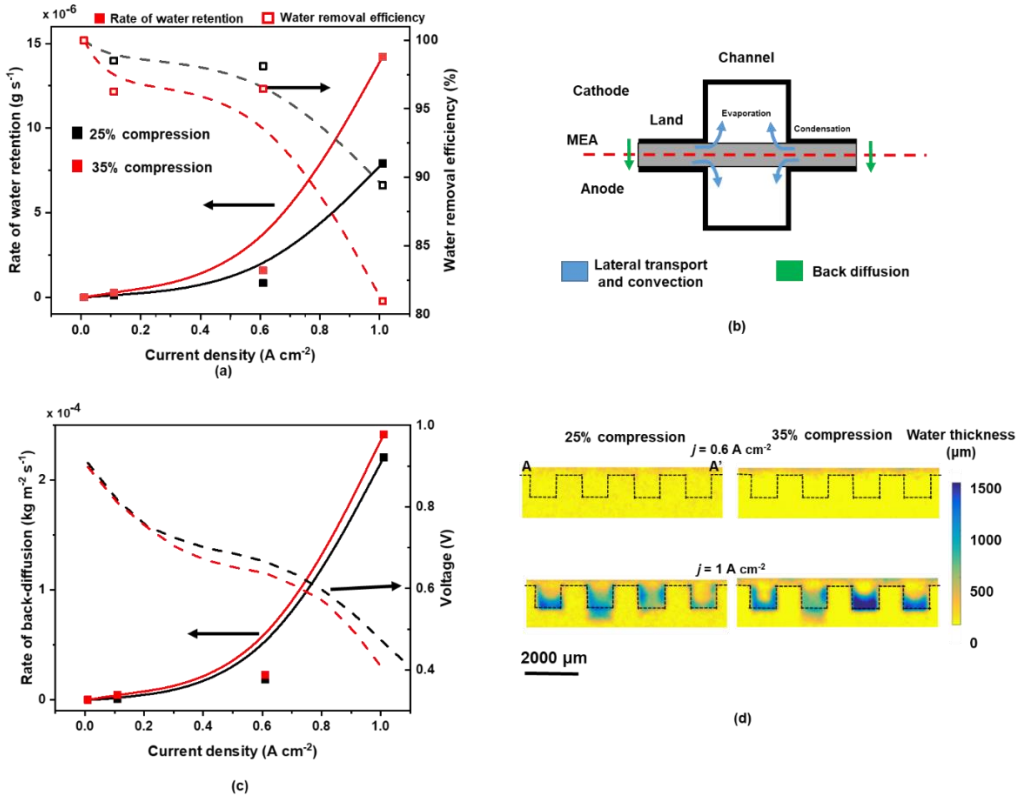

Figure 7.7– Effect of compression on liquid water dynamics, (a) effect of compression on the rate of water retention and water removal efficiency in the cell. B-spline passing through the data points included as a guide to the eye; (b) schematic of the water transport in the operating fuel cell; (c) rate of back-diffusion of water through the membrane as a function of current density and cell compression; and (d) radiographs showing averaged liquid water thickness distribution in the anode domain.

7.3.4 Validation of the numerical model

One of the objectives of this project is to develop a comprehensive model that describes the effect of compression on cell performance and water management. As discussed in the previously in 5.1.4, the use of only polarisation curve as a model validation tool could lead to the errors by not capturing the localised behaviour of the PEFC. Hence, neutron imaging was used to provide better insight into the localised water distribution and to validate the modelling results discussed in 6.3.5.

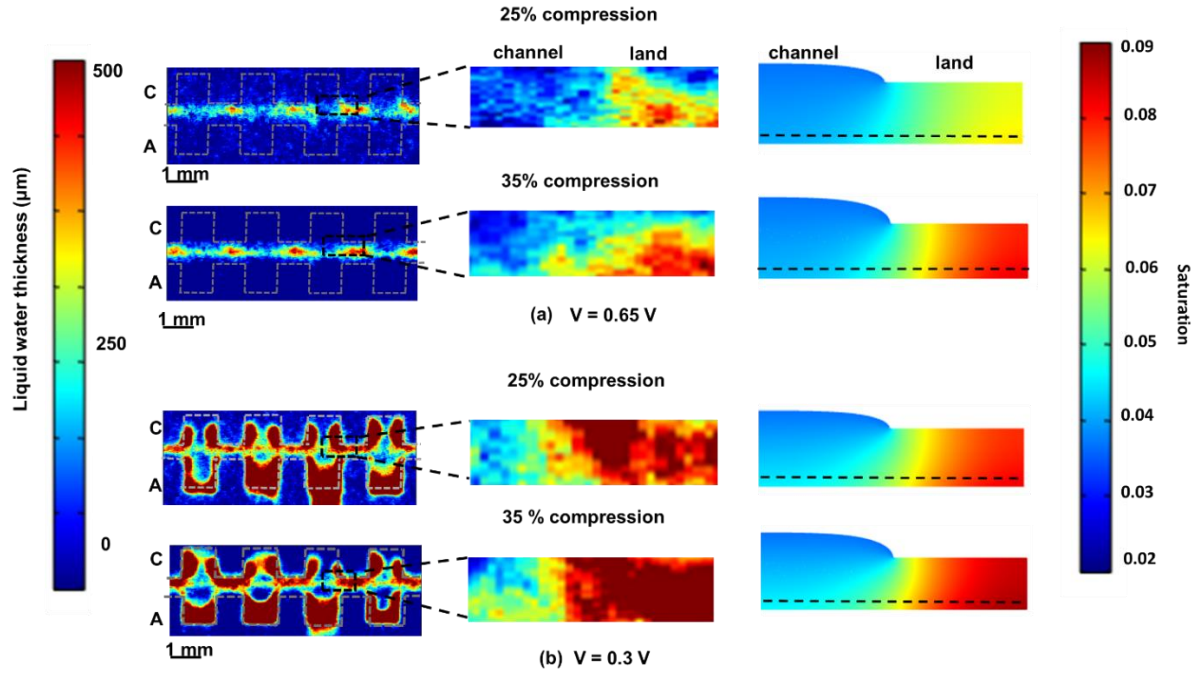

Figure 7.8– Neutron radiographs in the *xy*-orientation at 25% and 35% cell compression of the parallel channel PEFC. (a) saturation/liquid water profile at the Ohmic dominant operation (V = 0.65 V), (b) saturation/liquid water profile at the mass transport dominant operation (V = 0.35 V).

Figure 7.8(a) shows the neutron radiographs at the Ohmic operation region, masked in JET colour-map for the better representation, highlighting the marginal presence of liquid water at 25% cell compression and accumulation of liquid water under the land at 35% cell compression. The presence of liquid water was amplified at the mass-

transport dominant region, promoting flooding conditions, as shown in Figure 7.8(b). The cell design used shares the channel/land arrangement of the model, with 1 mm wide parallel channels. The results support the water accumulation and retention under the land region in the cathode domain, agreeing with the liquid water saturation profile obtained under identical operating load (Figure 6.9).

7.4 Conclusion

Water distribution and accumulation have been investigated at different levels of MEA compressions for a self-humidifying PEFC using neutron imaging in both the in-plane and through-plane orientation. The in-plane radiographs showed the water distribution within the layers of the MEA highlighting the effect of land and channel pattern on the non-uniform retention of the liquid water, fluctuating between the peaks underneath lands and valleys under the channels. The through-plane radiographs provided the information about water accumulation along the channel length and across the active area of the cell, highlighting the retention profiles such as water droplets, water film and slugs. Therefore, the combined analysis of the in-plane and the through-plane radiographs made it possible to determine what constitutes a given ‘thickness’ of water mapped across the extent of an MEA.

The effect of compression on the PEFC performance and on the water transport dynamics was investigated at three operating regions of the fuel cell. Compression has a marginal effect on the cell performance and water retention at the activation region; however, the notable effect of compression on the water dynamics in the PEFC was observed in the Ohmic and the mass transport regions. Increase in compression not only resulted in an increase in mass transport dominance in the Ohmic region, promoting early mass transport losses, but also increased flooding in the mass transport region.

Under identical cell architecture and the operating conditions, the extent of water retention in the cell and water removal efficiency is principally affected by the cell compression. Increase in compression worsens the water removal efficiency of the cell and increases the back diffusion of water.

Hence, the present study effectively delineates the effect of channel/land geometry on the liquid water transport mechanism, while highlighting the strong dependence of cell compression on the water accumulation and retention in fuel cells using multi-orientation neutron radiography. Furthermore, the results presented in this study would be useful to simulation studies by providing input parameters for models used to develop advanced fuel cell stack architectures and MEAs'.

The neutron imaging results at 25% and 35% cell compression obtained at the Ohmic and the mass transport dominant region agree with the localised saturation profile obtained from the electrochemical model presented in Chapter 6.

Chapter 8
Secondary flow-field architecture

Abstract

Flow-fields are critical factors in determining the operation of fuel cells. While extensive work has been conducted to develop and optimise the reactant flow and current collection performance of PEFC components, there is a factor that remains mostly unaccounted for. Depending on how a membrane electrode assembly is GDL and the seal or bipolar plate. This gap acts as a ‘secondary flow-field’ (SFF) that can bypass or affect/augment the conventional or ‘primary flow-field’. Understanding how this affects performance (either positively or adversely) is essential for holistic flow-field design. This chapter describes the issues associated with the SFF, examines how cell compression affects its width due to lateral expansion of the GDL and discusses the results of a 3D computational model that investigates the effect of the SFF during dead-ended anode (DEA) operation for a fuel cell without a macroscopic (conventional) anode flow-field.

8.1 Introduction

The existence of the secondary flow-field is discussed briefly in 2.4.2.2. In this chapter, the effects of SFF on fuel cell performance are discussed in detail. In the case of bipolar plate designs without a macroscopic (conventional) flow-field, the SFF offers a path of low resistance to reactant transport through the GDL [103]. In such designs, the reactant diffuses laterally through the GDL, and the SFF may act as a primary flow-field [103]. As an example of how this is seen in technologically well-developed fuel cells, Figure 8.1 shows an X-ray radiograph of the internal structure of a commercial open-cathode fuel cell used in the UPP fuel-cell charger developed by Intelligent Energy, UK. A gap between the GDL and outer structure of the stack, i.e. 1.5 mm wide SFF, is clearly visible and has been incorporated in the design architecture while dispensing with the conventional primary flow-field on the anode side. The presence and extent of the SFF depend on the cell design, fabrication and assembly, GDL material, component positioning accuracy and the compression process.

The optimal compression for a fuel cell depends on a range of factors, and the effect of cell compression on the fuel cell performance is discussed in details in the previous chapters. However, though the standard compression range is considered to be between 10 - 40%, some designs go beyond this. The effect of non-uniform cell compression on the non-uniform cell compression results in the vertical deformation of GDL in the primary flow-field as discussed in 4.3.3, the GDL compression leads to a certain amount of lateral deformation. In the case of SFF, as shown in Figure 2.19, the lateral deformation of the GDL could potentially narrow the SFF width, with GDL fibres protruding into the gap. This might result in the reduction of free convection path in the SFF, and thus affect the reactant distribution to the active area. The extent of GDL intrusion into the SFF due to cell compression should be known to properly size the MEA/GDL to either fill the SFF or control it and take advantage of SFF effects to improve the performance.

The cell operating modes and purge processes are critical factors affecting the performance of a fuel cell and has been the subject of research [102,103,327]. Dead-ended anode (DEA) is extensively used in commercial fuel cells where pressurised hydrogen is fed to the anode inlet, while the downstream anode valve is closed. This ensures the system operates at unit hydrogen stoichiometry [104,345–347]. The simplicity in operation and higher fuel utilization makes the DEA mode cost-effective and potentially more efficient than through-flow operation [348]. However, in practice, the DEA operation can lead to the accumulation of back-diffused water and/or build-up of N_2 due to its crossover from the cathode to the anode domain [327,348–350]. The areas of the anode lowest hydrogen concentration result in the nitrogen blanket build-up of N_2. This results in hydrogen starvation at the anode, voltage drop with time and uneven current density distribution [93,103,220]. The hydrogen humidification is the critical water management parameter during the DEA operation. While humid hydrogen stream results in water accumulation in the anode [327,350], the dry hydrogen inlet could result in drying out of the membrane [94,220]. Hence, it is essential to understand the cell drying process during the DEA operation, which would be affected by SFF design.

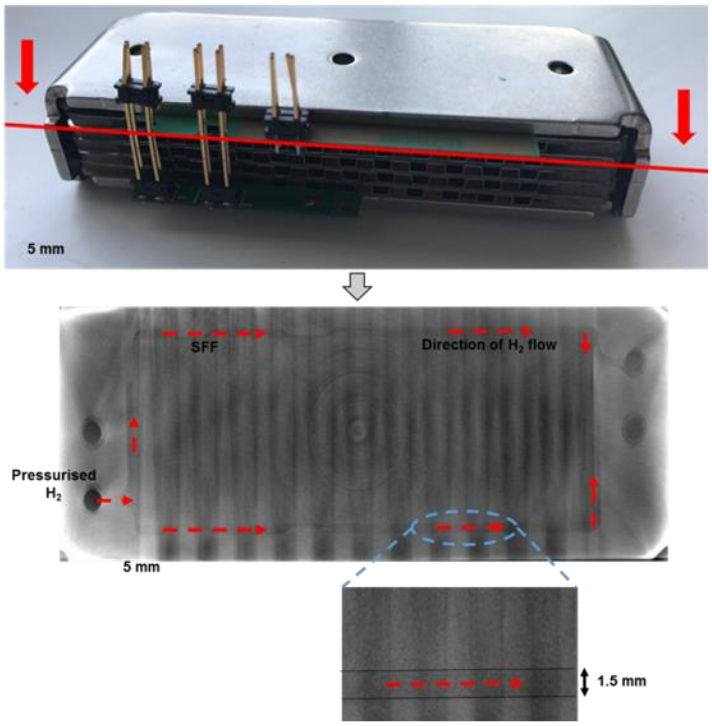

Figure 8.1– X-ray computed radiographs of a commercial fuel cell showing the gap between gasket and membrane electrode assembly

Yang et al. studied the effect of anode flow-field arrangement on the DEA performance of the fuel cell, pointing out the type of anode flow-field arrangements impact the fuel cell performance in the DEA operation [351]. Flow-fields for the DEA operation may, or may not, adopt a conventional ‘primary’ flow-field. The effect of an SFF on the DEA operation is particularly pertinent, as when the exit valve is closed, access of reactant to the electrode is based on diffusion from the entrance point and not the convective flow of gas through the flow-field. Systems that dispense with a flow-field altogether, such as the commercial fuel cell shown in Figure 8.1, rely on the lateral diffusion of gas through the GDL alone; therefore, the presence of the SFF provides a lower resistance flow path around the circumference of the electrode, potentially improving reactant access.

Traditional experimental techniques, such as polarisation curves, offer useful insight into the overall fuel cell operation but do not capture localised behaviour that can be achieved through numerical modelling. Recently numerous modelling studies focused on the DEA operation and nitrogen and water build-up have been published [95,96,327,349,352] . Mainly these studies are 1D through the cell thickness or 2D where parallel channels are considered. These models provide the quantitative information regarding voltage performance, water accumulation and nitrogen blanketing in the DEA operation; however, they cannot predict the effect of the flow-field arrangement, including SFF on in-plane reactant distribution. Hence the simplistic model that shows the effect of SFF in isolation from primary flow-field on the reactant distribution during the DEA operation is needed [104]. The results can be validated using real-time visualisation techniques such as neutron imaging that identifies the water distribution in both the in-plane and through-plane directions [18,152,275,353]. The hydrographs developed shows the potential flooded and dry-out areas in the membrane. The neutron imaging performed by Meyer et al. [103] to study water distribution in transient DEA operation of the cell with SFF showed non-uniform water accumulation in the anode and non-uniform current and temperature distribution at the centre of electrodes.

This chapter intends to identify the SFF as a potential design feature of fuel cells and highlights that it can potentially have an effect on performance. Secondly, the effect of compression on the lateral deformation of GDL has been studied using X-ray radiography that would influence the width of the SFF channel. Thirdly, a simplistic steady-state half-cell CFD model is developed to investigate the effect of the presence and size of the SFF on flow and reactant distribution during the DEA operation. This model is further correlated with the experimental evidence available in the published literature.

8.2 Effect of compression on the lateral expansion of MEA

8.2.1 X-ray radiography

X-ray radiographs of the MEA during cell compression were obtained using a laboratory-based X-ray CT system, (Zeiss Xradia 520 Versa, Carl Zeiss X-ray Microscopy Inc., CA) The material used to build the MEA ample and the imaging parameters used in to obtain the radiographs are presented in Table 8-1. The imaging methodology, postprocessing techniques and the details of Deben compression rig offering compression by displacement are discussed in Chapter 3.

Table 8-1 – X-ray radiography parameters and MEA materials properties

Materials	
GDL	Carbon fibre GDL , ELE0201 (Johnson Matthey GDE)
CL	0.4 mg cm^{-2} Pt loading
Membrane	Nafion NRE-212 membrane (Dupont, USA)
Imaging parameters	
Source voltage	80 kV
Field-of-view	2 × 2 mm^2
Compression ratio	0% - 80%, in steps of 10%.
Resolution	0.85 µm
Exposure time	50 s
Magnification	0.4×

A photograph of the compression stage and a compression sample holder is shown in Figure 8.2(a and b), respectively. Figure 8.2(c) shows the radiograph obtained in the uncompressed state.

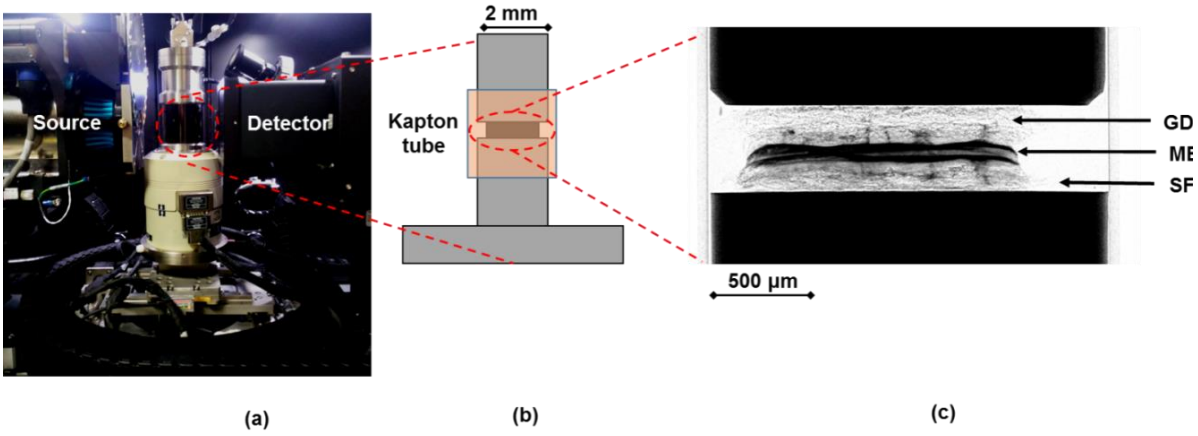

Figure 8.2– Set-up for imaging of GDL compression, (a) compression stage, (b) the circular pins of 2 mm diameter enclosed in a Kapton tube was used for the compression with the GDL sample placed at the centre; and (c) X-ray radiograph of the uncompressed sample.

8.2.2 Lateral expansion of MEA

The amount of GDL intrusion into the perimeter channel when under compression should be known in order to properly size the MEA/GDL to either fill the space or control it and take advantage of SFF effects to improve performance. The radiographic images of four different levels of cell compression are shown in Figure 8.3. The radiographs show the increase in material density in the cell with increased compression.

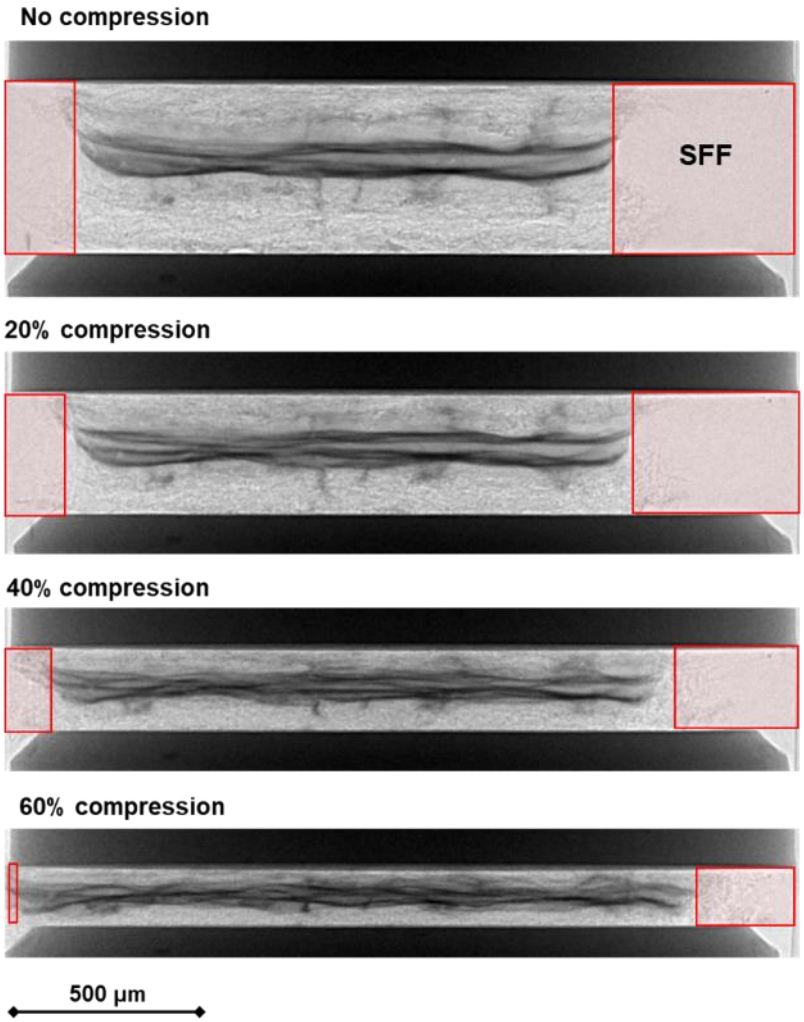

Figure 8.3–Radiographs of the cell compression at variable cell compression from 0% to 60% showing the intrusion of GDL into the SFF

Figure 8.4 shows the extent of lateral deformation into the SFF space under uniform cell compression. The results show that the uniformly compressed GDLs deform laterally, leading to reduced free-path of reactant. To serve as an approximate design parameter, a linear fit to these data over the range of 0 – 60% (the range over which a GDL would typically be compressed) gives a value of 0.1086% μm^{-1} lateral deformation of the GDL.

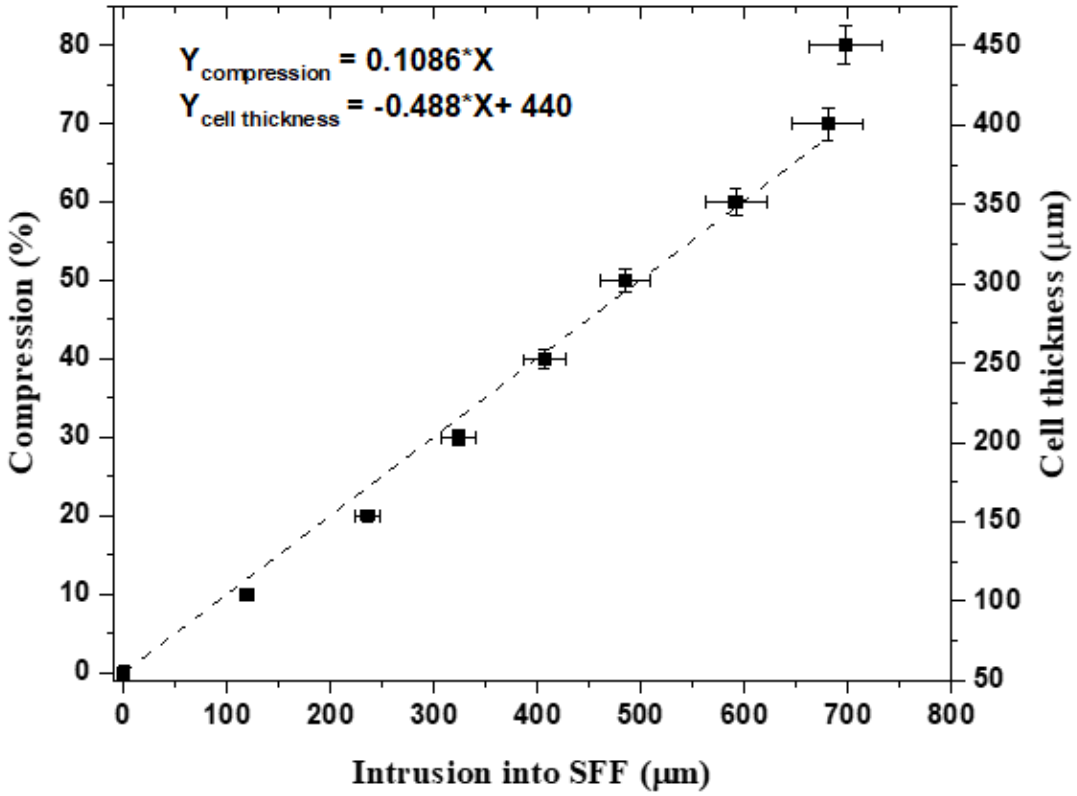

Figure 8.4–Quantitative representation of intrusion of GDL/MEA into the SFF (calibration graph).

8.3 Computational modelling

The performance of a fuel cell strongly depends upon the operating conditions, transport phenomena and electrochemical reaction kinetics. Reactant distribution is crucial in deciding species transport in a cell, which is primarily affected by the flow-field design. In this work, the 3D computational anode-only model is developed to understand and optimise the use of the SFF to improve fuel cell design and operation.

8.3.1 Computational domains and assumption

The computational domains used for the study, along with the boundary labels, are shown in Figure 8.5. The assumption made in the model are listed as follow,

- The low-temperature PEFC operates under the steady-state isothermal condition at 60 °C (as is typical for open-cathode PEFCs).
- The current model solves mass, momentum and energy conservation equations, along with species conservation.
- The anode domain has a fixed average current density '*j*' that acts as the reactant sink, modelled using the Butler-Volmer equation.
- The single-phase flow in the (secondary) flow-field was laminar.
- The momentum interactions between the fluid and porous phases were modelled using Darcy's law and the species diffusion modelled using Maxwell-Stefan's law.
- GDL, CL, and the membrane were assumed isotropic and homogeneous.
- The membrane was considered impermeable for reactant gases; hence, the accumulation of back diffused water and the effect of the gas crossover was neglected.
- The model assumes dry H_2 supplied at the inlet at constant pressure and unit stoichiometry.
- The fuel cell is open-cathode with high cathode stoichiometry; hence, the effect of cathode oxygen depletion is not solved in the model.
- The effect of cell compression on the morphological properties such as permeability, porosity, tortuosity, etc. of the porous domains is not considered in the model.

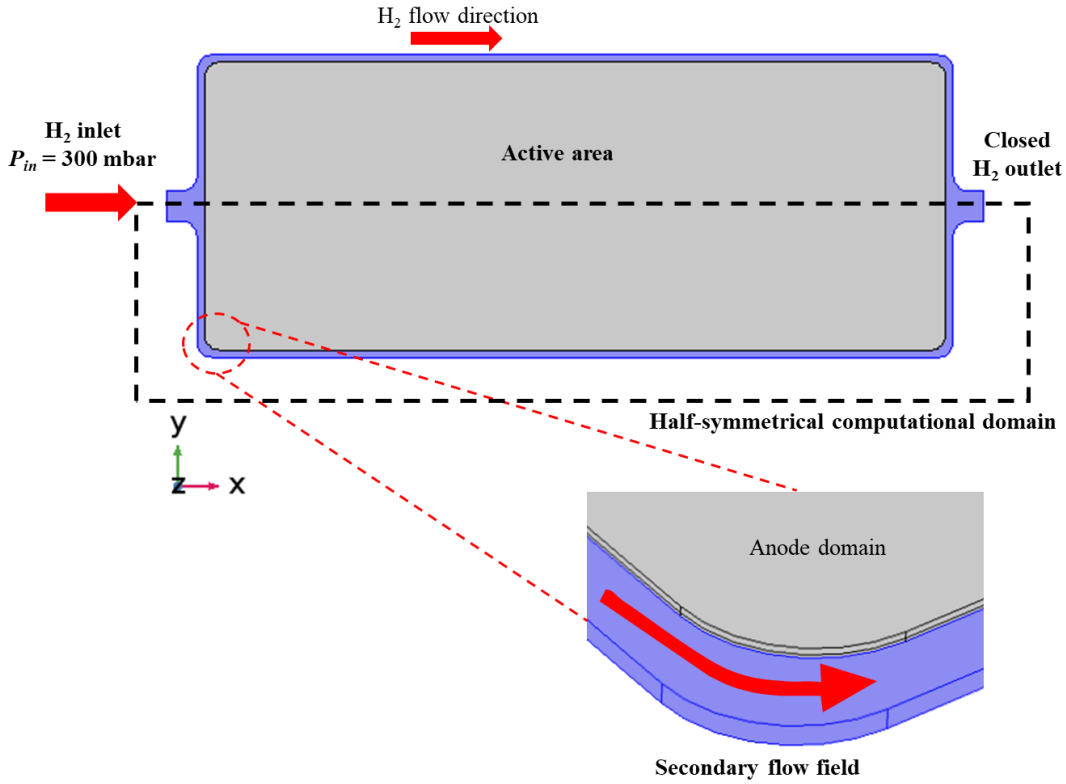

Figure 8.5– 3D computational domain from *x-y* planar view and detailed view of the SFF

8.3.2 Boundary conditions

Table 8-2 lists the parameters used in the model. The anode was supplied with dry pressurised H_2 at 300 mbar. The DEA condition, i.e. purge valve closed condition, was mimicked with a wall boundary condition at the anode outlet. The rectangular geometry of the anode domain offered symmetrical anode flow behaviour. Hence, *xz* plane symmetry was applied to optimise the computational time.

Table 8-2 – Modelling parameters and operating conditions

Property	Value	Ref.
Current density, j [A cm^{-2}]	0.1, 0.6, 1	
GDL Thickness – 40% compression, $h_{GDL}^{Compressed}$ [m]	1×10^{-4}	
GDL Thickness – 60% compression, $h_{GDL}^{Compressed}$ [m]	0.55×10^{-4}	
GDL Thickness – 70% compression, $h_{GDL}^{Compressed}$ [m]	0.4×10^{-4}	
Membrane thickness, h_{mem} [m]	40×10^{-6}	
Catalyst layer thickness, h_{cl} [m]	15×10^{-6}	
GDL porosity – 20% compression, $\varepsilon_{GDL}^{Compressed}$	0.75	Measured
GDL porosity – 40% compression, $\varepsilon_{GDL}^{Compressed}$	0.6	Measured
GDL porosity – 60% compression, $\varepsilon_{GDL}^{Compressed}$	0.5	Measured
Catalyst layer porosity, ε_{cl}	0.3	[354]
Catalyst layer permeability, K_{cl} [m^2]	1.0×10^{-13}	[355]
GDL permeability, K_{gdl} [m^2]	1.76×10^{-11}	[252]
GDL electrical conductivity, σ_{gdl} [S m^{-1}]	570	[252]
Electrolyte conductivity, σ_{mem} [S m^{-1}]	9	[252]

H_2 viscosity, μ [Pa s]	1.19×10^{-5}	
H_2 inlet pressure, P_{in} [mbar]	300	
Cell operating temperature, T_{cell} [°K]	333	
Reference H_2 concentration, $C_{H_2}^{ref}$ [mol m^{-3}]	40.89	
Anode exchange current density, J_o^a [A m^{-2}]	1×10^{-4}	[252]
Anodic transfer coefficient, α_a	0.5	[252]
Cathodic transfer coefficient, α_c	0.5	[252]

The no-slip boundary condition was applied to the flow-field walls and slip-wall boundary condition to the porous walls. The parametric investigation solves for four SFF design cases: case (i) design without the SFF, i.e. either no primary anode flow-field is used, and the SFF is blocked due to the lateral deformation of GDL fibres (corresponding to 70% compression); case (ii) design with 0.1 mm SFF is available (corresponding to 60% compression); case (iii) design where 0.25 mm SFF is available (corresponding to 40% compression), and case (iv) design with 1 mm wide SFF is available for the reactant transport. The model was tested under various operating current densities ranging from 0.1 A cm^{-2} to 1 A cm^{-2}. The current work discusses the results for three average current densities, i.e. 0.1 A cm^{-2}, 0.6 A cm^{-2} and 1 A cm^{-2}. These current densities were carefully chosen as fuel cell reactant transport dynamics typically become important over 0.6 A cm^{-2} and lead to voltage decay during DEA operation [103]. All the cases are initialised at 0.6 V for computational stability.

8.3.3 Governing equations

The computational model consists of the following governing equations with respect to individual components in the computational domain.

8.3.3.1 Secondary flow-field

Based on the assumptions made in the current model, the reactant, i.e. pressurised hydrogen flowing through the SFF, is governed by the continuity equation. The steady-state Navier-Stokes equation describes the momentum conservation for an incompressible fluid.

$$\rho(u \cdot \nabla)u = \nabla \cdot [-PI + \mu(\nabla u + \nabla u^T)] \tag{8.1}$$

$$\nabla \cdot u = 0 \tag{8.2}$$

Here, u is the velocity vector, [m s^{-1}]; μ is the dynamic viscosity, [kg $m^{-1}s^{-1}$]; *P* is the pressure,[Pa]; ρ is the density of the gas mixture, [kg m^{-3}]. It is described by,

$$\rho = \frac{P \cdot \sum_i x_i M_i}{RT} \tag{8.3}$$

where x_i is the mole fraction, R is the universal gas constant, 8.314 [J $mol^{-1}K^{-1}$] *T* is the cell operating temperature [°K]. The subscript *i* represents species used in the model, i.e. hydrogen and water. The species diffusion and conservation in the SFF were defined using the Maxwell-Stefan diffusivity equation. This solves for the mass fraction fluxes.

$$j_i = -\left(\rho D_i^m \nabla \omega_i + \rho D_i^m \omega_i \frac{\nabla m_n}{m_n}\right) \nabla \cdot j_i + \rho(u \cdot \nabla)\omega_i = R_i \tag{8.4}$$

where $D_i^m = \frac{1-\omega_i}{\sum_{k\neq i}\frac{x_k}{D_{ik}}}$ and D_{ik} is the diffusion coefficient, [$m^2\ s^{-1}$], R_i is the reaction rate, [kg $m^{-3}s^{-1}$]. As no reaction takes place in the flow-field, $R_i = 0$. *x*, the mass fraction, and *M* is the molecular mass of the species ($\mathrm{kg\ mol^{-1}}$).

8.3.3.2 GDL and CL

GDL and catalyst layers are considered porous domains. Hence, the velocity distribution is solved using Darcy's mass conservation equation.

$$-\frac{k}{\mu}\nabla \cdot p = u \tag{8.5}$$

where *k* is the permeability (m^2). The continuity equation is given by,

$$\nabla \cdot (\rho u) = S \tag{8.6}$$

Here, *S* is the source term [kg m^{-3} s^{-1}]. The continuity equation for gas flow in the anode domain was defined by the sum of hydrogen and water present at the anode. The source term, *S*, defines the total production and consumption of the species during the electrochemical reactions. The reaction rate, R_i, is defined in the catalyst layer. This was solved using Faraday's law.

$$R_{H_2} = -\frac{j_a}{2F} M_{H_2} \tag{8.7}$$

8.3.3.3 Electrochemical reaction

The electrochemical reaction (species sink equivalent to current) at the anode catalyst layer is formulated by the anodic Butler-Volmer expression.

$$j_a = j_o^a \left(exp\left(\frac{\alpha_a F\eta}{RT}\right) - exp\left(\frac{-\alpha_c F\eta}{RT}\right)\right) \quad (8.8)$$

where j_o^a [A cm^{-2}] is the anode exchange current density; (α_a and α_c are anodic and cathodic transfer coefficients respectively. η is electrochemical overpotential (V); which is expressed by the potential difference between the solid phase responsible for electron transport and electrolyte phase responsible for proton transport. The anode side electrochemical overpotential is defined as,

$$\eta = \phi_s - \phi_l \quad (8.9)$$

The current model performs parametric analysis at average current density boundary condition set at 0.1, 0.6 and 1 A cm^{-2}.

8.3.4 Numerical solution

The system of coupled nonlinear equations contains five dependent variables, electrolyte potential (ϕ_l), an electric potential (ϕ_s), velocity (u,), pressure (P), and a mass fraction (ω_i) at the anode. All the partial differential equations in this model were solved in the commercial software environment, COMSOL Multiphysics 5.2a. All PDEs were solved using a direct solver, MUMPS, with undamped Newton and relative tolerance of 10^{-6} was used as the convergence criteria. Due to the small curvatures in the geometry, in the present work, a triangle grid based on the Lagrange shape function was generated for finite-element calculation with average mesh quality of 0.54. Mesh size was determined based on the application of minimum 10 elements on the smallest edge length. This ensures appropriate resolution of the boundary layers at computational walls. Therefore, the mesh independency study was restricted to solving a base-case analysis using three different mesh densities (approximately 10% variation in the mesh size). For the channel-level study, three SFF channel sizes consisting of 411,800, 457,555 and 503,310 elements were implemented. 1%

deviation was observed in terms of local velocity, pressure and species molar concentration. Hence, the grid-independent mesh density of 457,555 was selected as a good trade-off between the result accuracy and computational time.

8.3.5 Modelling results

The objective of the numerical modelling was to predict the effect of the available SFF on the localised reactant distribution at the anode. This work focuses on the system with no macroscopic (primary) flow-field. The current model shows the effect of available SFF on the localised reactant velocity and the molar concentration.

8.3.5.1 Effect available SFF on the localised velocity distribution

Figure 8.6 shows a matrix of results describing the effect of the width of SFF on the localised planar velocity at the GDL mid-plane (*xy* plane) at varying current densities. During DEA operation, the system works at unit stoichiometry; hence, the H_2 mass flux increases with an increase in the current density, manifest here by an increase in diffusion velocity.

For Case (i), design without SFF, at a lower current density region, refereeing to the activation dominant region (j = 0.1 A cm^{-2}), the planar velocity at the GDL mid-plane is comparatively even. Increasing to j = 0.6 A cm^{-2}, i.e. Ohmic dominant region, linear velocity gradient across the GDL was observed to accommodate the increased consumption of H_2. At a mass transport dominant region, j = 1 A cm^{-2}, velocity gradient across the GDL has further increased. This shows that H_2 is diffusing through the GDL from the point of entry.

Case (ii) describes a 0.1 mm wide SFF. Though the results show a similar trend as for Case (i) at lower current density, with an increase in current density, a transition from a ‘diffusion-driven flow’ regime to the convective mass transport around the perimeter of the cell and diffusive mass transport into the GDL becomes increasingly apparent.

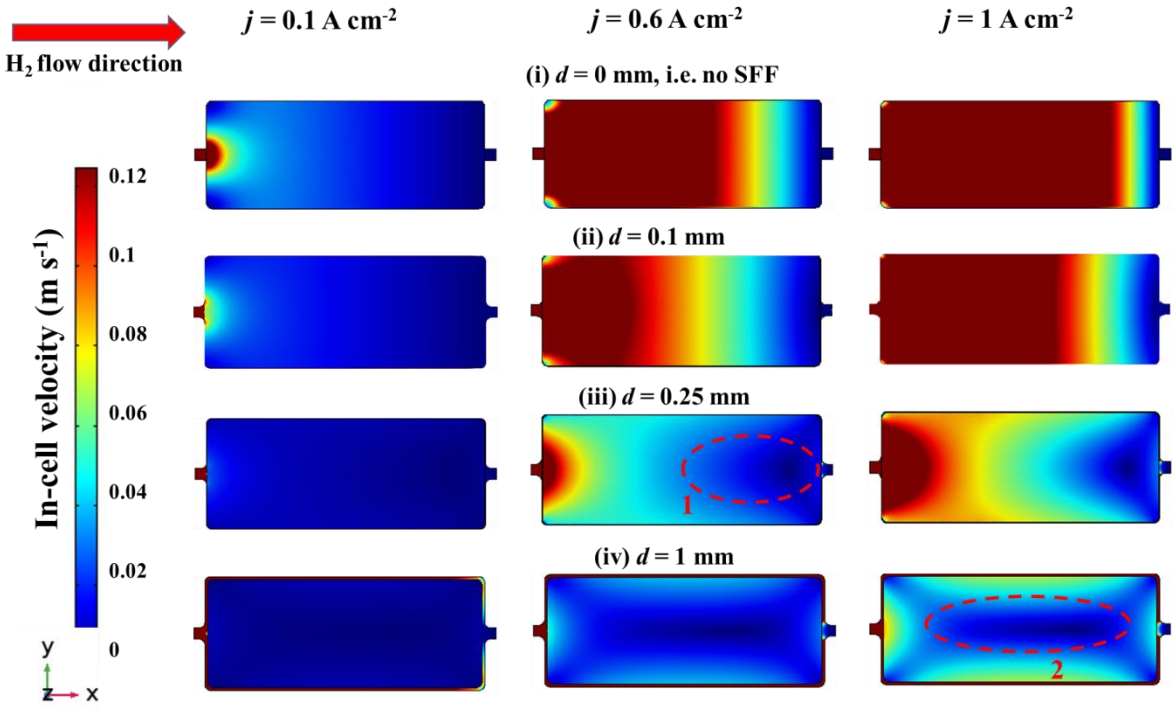

Figure 8.6– Effect of current density and SFF design on in-cell hydrogen velocity distribution at the GDL-mid-plane while operating in dead-ended mode for: (i) design without SFF; (ii) SFF width, d = 0.1 mm; (iii) SFF width, d = 0.25 mm, and (iv) SFF width, d = 1 mm.

For Case (iii), i.e. 0.25 mm wide SFF, an approximately constant convective velocity in the SFF is observed, servicing the H_2 sink within the active electrode area. At higher current density, this design shows the shift in lower diffusion velocity region towards the centre of the electrode, as highlighted in Figure 8.6(1) and Figure 8.7(1).

Case (iv) shows the design with a 1 mm SFF. At lower current density, this design shows similar planar velocity distribution to Case (iii). With the increase in the average current density, the effect of the SFF is evident. At j = 1 A cm^{-2}, higher velocity gradient into the centre of the electrode was observed. This results in the lower diffusion velocity region at the centre, highlighted in Figure 8.6 (2) and Figure 8.7(2).

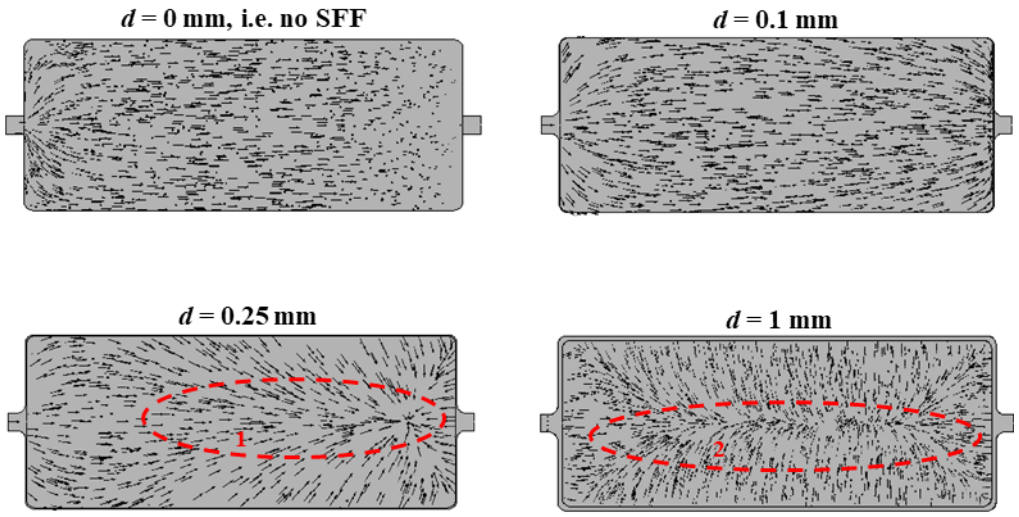

Figure 8.7– Effect of SFF width on the in-cell hydrogen velocity vectors plotted at the mass transport dominant region (j = 1 A cm^{-2}).

The velocity vector plots are at mass transport dominant region, i.e. j = 1 A cm^{-2} are shown in Figure 8.7. The orientation velocity vector changes with the width of SFF and supports the findings from the planar velocity contour plots emphasising the effect of the SFF not only on the reactant transport but also on the direction of reactant diffusion.

8.3.5.2 Effect available SFF on localised reactant concentration

The current fuel cell design relies on the lateral flow of reactant through the anode GDL, the SFF effectively acts as the 'primary' flow-field, ensuring reactant distribution from all the sides of the GDL. The effect of the width of SFF during high averaged current density DEA operation, i.e. j = 1 A cm^{-2}, is plotted at the global concentration gradient in Figure 8.8(a). The contour plots against the global colour legend show the presence of the SFF has a significant effect on the localised hydrogen concentration. The hydrogen concentration gradient is defined as the ratio of the difference between concentration ($C_{inlet}^{Max} - C^{min}$) at the GDL mid-plane to the maximum concentration at

the inlet (C_{inlet}^{Max}) and acts as an indication of how evenly the reactant is distributed across the electrode Figure 8.8(b).

$$Hydrogen\ concentration\ gradient\ (\%) = \frac{(C_{inlet}^{Max} - C^{min})}{C_{inlet}^{Max}} \tag{8.10}$$

The fuel cell where the entire SFF is blocked, i.e. no free path is available for the reactant transport is shown in Case (i). This condition / design have the highest hydrogen concentration gradient among all the designs, i.e. 38.0% implying an uneven reactant distribution. In case (ii), 0.1 mm wide SFF, a hydrogen concentration gradient of 15.8% was observed. This design particularly highlights the concentration depletion from the inlet (highest concentration) to 'exhaust' location (lowest concentration). For case (iii), though the results show a similar trend as that of the case (ii), this design shows the effect of the combined convective – diffusive flow on the localised hydrogen concentration distribution, with the reduction in concentration gradient to 5.6%. In this case, the localised reactant concentration minima slightly shift from the exhaust location towards the centre (to the 'left') of the electrode (Figure 8.8(a)). Case (iv) describes the reactant distribution behaviour of the cell with a 1 mm wide SFF channel. This design shows comparatively even reactant distribution with the reduction in concentration gradient to 1.1% when compared at the global colour scale.

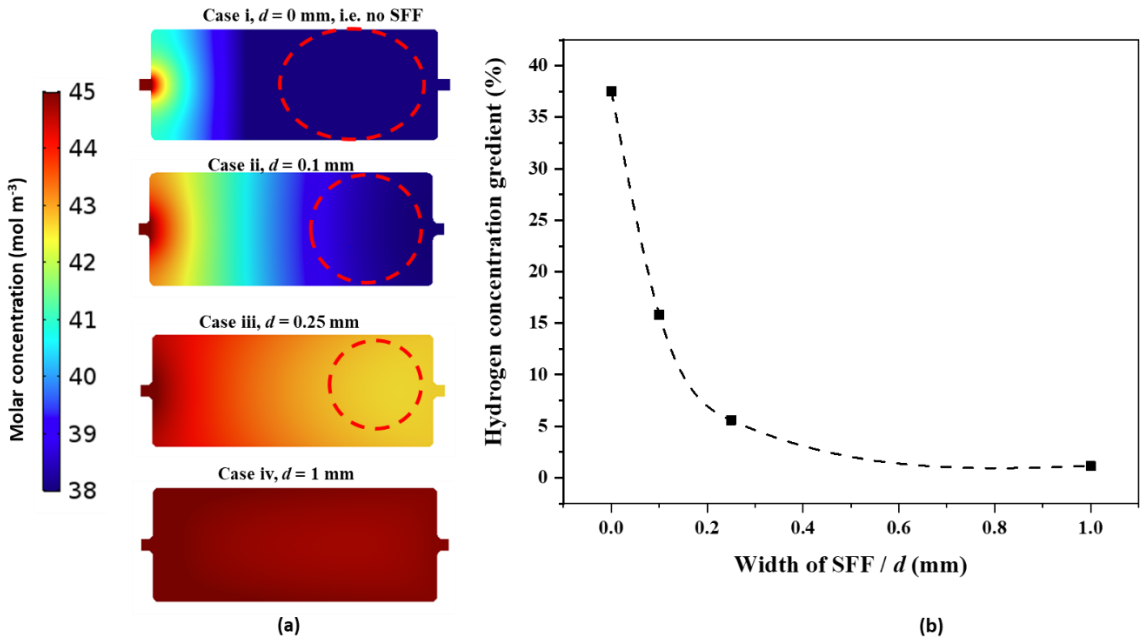

Figure 8.8 Effect of the width of secondary flow-field on (a) hydrogen molar concentration [mol m^{-3}] at the GDL mid-plane when measured at j =1 A cm^{-2}, plotted at the global colour scale. Circled areas highlight the area of minimal hydrogen concentration, (b) hydrogen concentration gradient,

As the global colour bar fails to show the interesting localised concentration features, case iv with local concentration legend shows that the local minima of hydrogen concentration have moved to the centre of the cell, as shown in Figure 8.9(a). The *yz* and *zy* planar concentration shows that concentration varies mainly in the in-plane direction, with a constant concentration in the through-plane direction, as shown in the detailed view of in Figure 8.9(b).

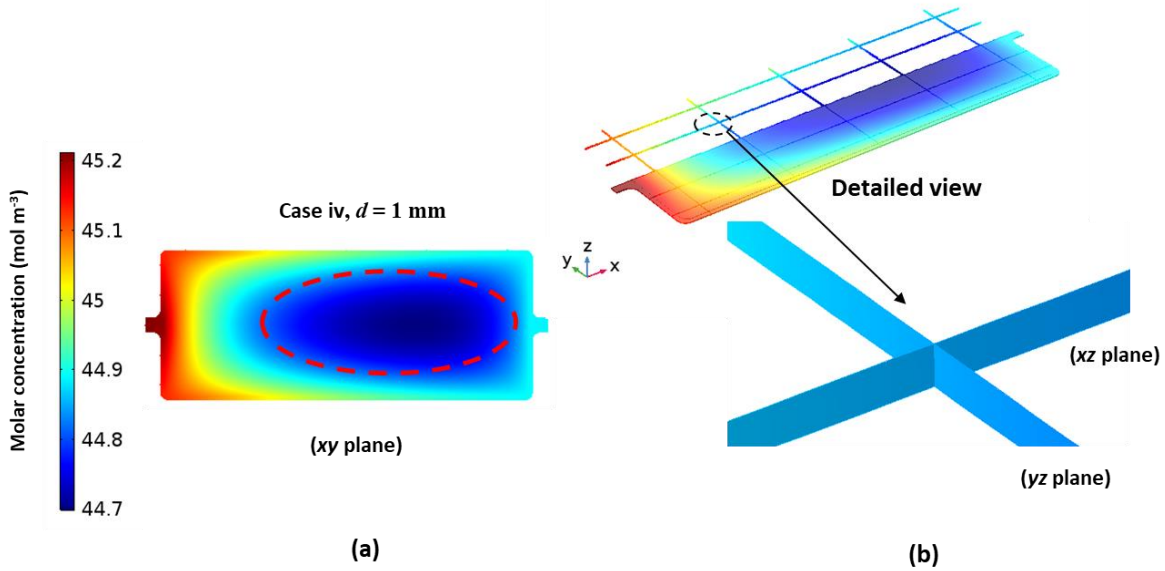

Figure 8.9 (a) localised hydrogen concentration for Case iv, SFF width 1 mm, (b) in-plane and through-plane hydrogen concentration plot, the detailed view showing the uniform through-plane concentration.

8.3.5.3 Correlation with experimental evidence

Recently, Watanabe et al. used a visualisation technique to investigate localised hydrogen concentration distribution for a 'wraparound flow path' [203]. The result suggests that lateral diffusion of hydrogen from the perimeter leads to a lower hydrogen concentration at the central area of the cell, in agreement with the hydrogen concentration gradient obtained from the modelling (Figure 8.9(a)).

Figure 8.10(a) shows the distribution of liquid water obtained from the neutron imaging of a fuel cell with the similar cell architecture as that used in the present SFF model, i.e.no conventional flow-field at the anode and the presence of a 1 mm wide SFF and operating under DEA conditions [103]. The radiograph obtained at the beginning of the experiment where the exhaust valve was open, i.e. the through-flow anode operation. Shows comparatively uniform water distribution pattern observed under the

land region (Figure 8.10(a)). During the dead-ended anode operation, the uniformity in the water distribution pattern has lowered with the potential dried region in the centre of the fuel cell, as highlighted in Figure 8.10(b). The cell drying location obtained from the neutron imaging correlated with the region with the lower hydrogen concentration (Figure 8.9(a)). Lowered hydrogen concentration, results in the fuel starvation at the centre of the cell leading to lowered current production from the particular sites.

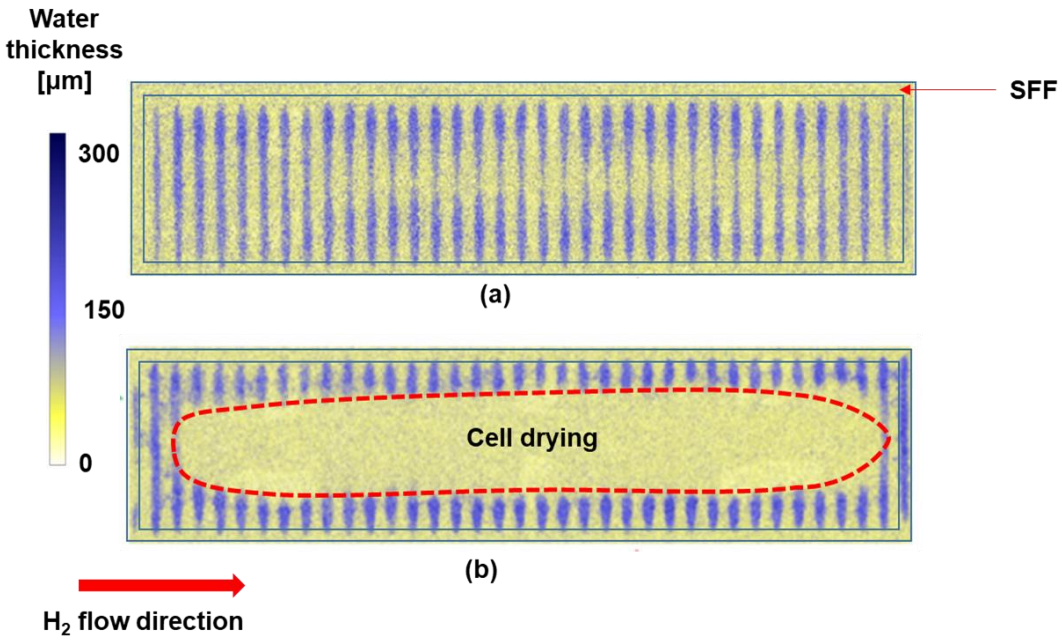

Figure 8.10 Neutron hydrographs in *xy* plane at the centre of the cells with no conventional flow-field at the anode, where the SFF acts as a primary flow-field and cross-flow at the cathode, j = 0.56 Acm^{-2}. (a) the through-flow operation, (b) DEA operation results in depletion of water in the middle of the electrode, resulting in subsequent cell drying and H_2 starvation, Adapted from [103]

8.4 Conclusion

This work identifies the gap that may exist at the perimeter of a GDL as a ‘secondary’ flow-field. The way in which an MEA is put into compression, causes the GDL to expand laterally by different amounts and will determine the width of the SFF channel. X-ray radiography of an MEA has shown the almost linear lateral intrusion of the GDL into the gap with increasing compression.

The influence of the SFF dimension on reactant distribution in an operating fuel cell is explored by applying a simplistic flow model. It is important to note that the present model solves steady-state, dead-ended operation, with constant current output. In reality, PEFC operation is transient, and the anode will suffer from N_2 crossover from the cathode. Such multiphase and transient response factors are likely to lead to more complex operation in practice.

In the specific case of a fuel cell operating without a conventional anode flow-field in dead-ended mode, the presence of SFF is predicted to improve reactant distribution and consequently current density distribution. In the cell where both primary and secondary flow-fields are available, the SFF may enhance the overall reactant distribution and complement the behaviour of primary or conventional flow-fields or could act as a by-pass of the primary flow-field. This will very much depend on the type and size of the primary flow-field, the electrode and the operating mode (i.e. through-flow or dead-ended).

The way that the SFF forms will depend on the compression of the fuel cell and the manufacturing and component tolerances. There is scope for optimising the SFF for operation and modifying its structure by, for example, incorporating baffle features or tapering the channel width to facilitate reactant access to the active electrode area.

Chapter 9
Research summary and future scope

The last couple of decades have seen tremendous growth in the development of fuel cell technology with the aim of large scale commercialisation. The focussed efforts have achieved the progress in the membrane quality, reduction of the platinum loading and overall material system cost. However, to achieve broad-scale commercialisation and deep market penetration, a significant improvement in fuel cell operation, durability and architecture are essential. Various studies provided throughout this thesis present a strategy towards the advancement of fuel cell performance and architecture.

9.1 Research summary and conclusion

The primary goal of the thesis was to identify and understand the architectural factors that define the structural and electrochemical performance of the fuel cell. The understanding generated from the present research will enable improvements in PEFC performance and efficiency while potentially enhancing cell designs, architecture and durability. Electrochemical modelling framework and advance characterisation techniques developed in this work are also directly applicable to the broader fuel cell as well as electrochemical community. Many of the features of structural and morphological findings are relevant to other fuel cell technologies and concepts, such as the determination of the effective property distributions, distribution of material fractions across the cell thickness, water dynamics, etc.

The novelty of this work is the combined use of three systematic approaches to analyse the architectural and electrochemical factors affecting the fuel cell performance, which are

(1) X-ray characterisation.- The in-situ characterisation technique evaluates and quantifies the effective parameters that affect the fuel cell performance,
(2) Numerical modelling- The detailed mechanistic models that couples structural deformations of the cell with electrochemical behaviour

(3) Neutron imaging - The novel in-situ, in-operando performance evaluation and liquid water visualisation techniques providing qualitative model validations while commenting on water transport mechanism in low-temperature PEFCs.

X-ray CT characterisation highlights the inherent morphological heterogeneities in the entire MEA and quantifies the effect of non-uniform fuel cell compression and cell architecture on the cell microstructure that determine the fuel cell performance. The key findings presented by X-ray CT analysis are,

(1) The non-uniform cell compression promotes partial blocking of the active flow-fields. This would adversely affect the reactant transport within the flow-field and thermal management of the fuel cell.
(2) Inherent heterogeneity in the membrane thickness could aggravate by the non-uniform compression of the fuel cell. This leads to non-uniform structural thinning of the membrane. Non-uniform thinner membranes could promote higher crossover losses and adversely affect cell durability.
(3) The fuel cell performance is determined by the strong interdependence between the cell architecture, non-uniform compression, accuracy of cell assembly process and the resultant effective parameters.

The numerical models developed in this study are preliminary 2-D mechanistic non-isothermal multiphase models. The outstanding aspects of these models are,

(1) Coupled structural-electrochemical modelling approach considers the effect of cell architecture and the extent of cell compression on the distribution of effective properties within the fuel cell layers. This approach uses the initial porosity and fibre diameter that can be obtained from X-ray CT studies.
(2) The agglomeration approach was opted to model catalyst layers. This approach considers the CL microstructure based on the input parameters such as CL porosity, Pt. particle size, Platinum surface area ratio, ionomer fraction and film thickness.

(3) Complex water transport mechanism across all the layers of the fuel cell was described by a combination of water phase transfer between water vapour, dissolved water and liquid water, water transport in the porous media through capillary action and water transport across the ionomer membrane under EOD and back diffusion.
(4) Constitutive equations based on operating parameters of the fuel cells define the input parameters and boundary conditions required to solve the model.

Hence, the key aspects of the model result in a comprehensive, robust and experimentally validate modelling framework that could be used to design, solve, analyse, and predict PEFC performance with various cell architectures, operating conditions and fuel cell materials.

In present study, the developed modelling framework effectively delineate the strong dependence of cell compression on the water saturation and temperature distribution, particularly under mass transport dominant conditions. The model highlights the key processes affecting the fuel cell performance on both global and local scale, such as at the low-temperature PEFC operation, the exothermic ORR is the main contributor to the non-uniform cell heating at all the compressions, contributing to more than 98 % of the heat source. Hence, the thermal performance of the cell is not preliminarily affected by the compression and can be enhanced by improving the catalytic properties of the electrode.

The present model highlights that an increase in compression results in increased mass transport dominance in the Ohmic region, fostering early mass transport losses. Hence, in order to improve the efficiency and the useful operating range of the fuel cell, the dominance of mass transport losses during the Ohmic operation has to be minimised. Hence, the present model successfully delineates multi-phase modelling environment while commenting on the water formation, phase change and transport. The developed models are believed to be useful tools to analyse the transport and

electrochemical reaction processes involved in the fuel cell operation and predict cell performance.

In this research work, the dynamics of fuel cell operation was investigated by studying the effect of cell compression on the water transport behaviour using in-plane and through-plane in-operando neutron radiography. The key features of the multi-orientation neutron radiography are,

(1) The in-plane neutron radiography enables to evaluate the water retention and accumulation within the layers of the MEA highlighting the effect of land and channel pattern on the non-uniform distribution of the liquid water, fluctuating between the peaks underneath lands and valleys under the channels. The in-plane radiographs provided vital information regarding how the dynamic behaviour of water transport is affected by cell compression while commenting on the rate of water back-diffusion, water retention in the system and water removal efficiency.
(2) The through-plane hydrographs help explore the water dynamics over the active area of the cell with a key-focus on the water retention along the channel length and form of water retention such as droplet, film or a slug.
(3) The in-plane neutron radiographs could be used to validate 2-D multi-phase fuel cell models qualitatively.

Neutron radiography study results in an enhanced understanding of the water transport process in the fuel cell while augmenting the knowledge of how the non-uniform compression affects the mass-transport losses in the fuel cell. Additionally, the combined in-plane and the through-plane radiographs provided the baseline to determine what constitutes the in-situ water thickness in an operating fuel cell. The neutron radiographs validate the computational models developed in this work and agree well with the fuel cell literature.

This research also presents a highly neglected feature in fuel cell design that may exist at the perimeter of a GDL, referred to as the ‘secondary flow-field’. The developed characterisation and the modelling framework highlighted that the secondary flow-field would play a critical role in determining the performance and durability of the fuel cell while operated in the dead-ended anode mode. In addition, the secondary flow-field architecture is closely linked with cell compression, and the manufacturing and component tolerances, highlighting the importance of design for manufacturing (DFM) on the fuel cell performance.

Altogether, this work has produced an enhanced knowledge of the fuel cell designs and the architectural factors defining the morphological, electrochemical-thermal behaviour of this low-temperature fuel cell. Additionally, this thesis contributes to a better understanding of the extent by which physical and electrochemical processes within a PEFC, especially the water formation, phase change and transport are affected by fuel cell architecture, compression and operating conditions.

9.2 The future direction of the research

In terms of future work, three main routes are considered: increasing the knowledge of the in-situ behaviour by multi-scale characterisation through further advanced diagnosis, development of an extensive high-fidelity electrochemical model of the cell capable of solving the porous morphology in the fuel cell while effectively predicting the effect of architectural factors, and enhancement in the understanding of the effect of fuel cell assembly process and errors on the performance.

9.2.1 Morphological correlations for in-situ X-ray CT and in-operando studies

The morphological approach presented in this study focusses mainly on GDLs and membranes while the pixel resolution is restricted to 1.64 μm. In order to evaluate the fuel cell microstructure and its effects on the performance, X-ray nano-computed tomography could be adapted in future for 3D investigations of electrode microstructures. However, the scanning should facilitate access to a larger sampled volume, thus providing more representative characterisation of the entire MEA. The lab-based instrument, Zeiss Xradia 810 Ultra (Carl Zeiss X-ray Microscopy, 157 Pleasanton, USA), could be used for the initial understanding of the electrode nano-morphology. However due to FOV restriction of the lab-based instruments, (typically no more than tens or hundreds of micrometres in dimension), the synchrotron-based instruments could be adopted for the entire MEA scanning. This experiments should give the defined direction towards the evaluation of the effects of cell architecture on electrode crack-formation, crack-growth, and cell degradation.

Additionally, the combined effect of cell architecture, compression and operating conditions such as variable temperature and humidity on the mechanical thinning of the membrane could further be analysed using micro and nano X-ray CT. This should provide the direction towards developing structural non-degradable membranes.

Neutron radiography technique discussed in the current research could be used to characterise water transport mechanisms and two-phase flow in PEFC. The local water transport mechanism and rate of exchanges inside the PEFC materials can be visualised using Hydrogen–Deuterium (H-D) contrast neutron radiography. The contract in attenuation strength between hydrogen and deuterium allows understanding the rate at which the accumulated water is exchanged with newly generated water. Therefore, the impact of architectural and operating parameters on

the stationary application fuel cell can be analysed, with a particular focus on water management.

The diagnostic techniques such as morphology correlation can segment water from the tomography with extreme precision when operated at higher humidity conditions. Hence, morphology correlation can be used to conjugate X-ray CT and the neutron imaging studies, for the advancements in PEFC architecture, performance improvement and high-fidelity numerical model validation suite.

Additionally, the combined effect of cell architecture, compression and operating conditions, such as variable temperature and humidity on the mechanical thinning of the membrane, could be further analysed using micro and nano X-ray CT and H-D neutron imaging. This should provide the direction towards developing structural non-degradable membranes.

9.2.2 Development of an extensive high-fidelity 3D models

The modelling reliability and compatibility can be improved with several aspects. The present modelling framework effectively predicts the performance in two-dimensional aspect. For a better understanding and the representation of real-world behaviour, the model should be extended to three-dimensions. This would facilitate the prediction of the of non-linear compressions and localised stresses arising from the flow-field channels geometries, such as parallel, interdigitated, serpentine and/or mixed-types, as well as reactant distribution and water management during the parallel and cross-flow arrangements

The present steady-state continuum models have to be extended to predict the dynamic behaviour of water generation, accumulation and transport. The model can also be coupled with the degradation models briefly mentioned in this thesis. The models can be validated with the dynamic water management presented.

The present model can also be extended to predict the effect of carbon (catalyst support) corrosion, catalyst degradation, and membrane degradation. The effect of membrane thinning on the species crossover is pivotal in determining the fuel cell performance, preliminarily when operated in the dead-ended mode. This would impact the fuel cell durability; hence, the operating cost of the system. The current work could also be used as the baseline in developing the dynamic electrochemical multispecies models predicting the effect of species-crossover during DEA operation.

The present continuum-based model and the morphological images can be used to develop the high-fidelity three-dimensional models considering the representative structure of the gas-diffusion and microporous layers. The LBM approach could be used to solve the GDL, and the MPL structure with the present agglomeration based model could be used to solve the continuum-based electrochemical processes. However, the model will be sensitive to the morphological images used.

9.2.3 Effects of the stack assembly process on PEFC performance.

The potential impact of the stack assembly process and the manufacturing tolerances on the fuel cell morphology has to be addressed. The use of X-ray CT on micro and nano level, in conjunction with in-situ mapping of the fuel cell behaviour, such as electro-thermal mapping using the high-resolution sensor plates, water mapping using neutron imaging and the multiphase modelling would provide great insight into the real-life fuel cell challenges. This would allow the research focus in attaining the effect of external factors on the performance, durability and on commercialisation.

One of the ways that could be used to assess the impact of manufacturing and assembly errors is to build a stack with ‘intentional’ deformities such as channel misalignment or extreme compressions. X-ray CT could be effectively used to understand the changes in the internal structure of the MEA under unwanted cell deformities such as extreme manufacturing tolerances, over-compression, and

membrane delamination and stresses on the GDLs. The modelling framework discussed in Chapter 4 and further enhancement in the model discussed in Chapter 6 can be used to numerically predict the performance of the cell with deformities and sensitivity analysis can then be conducted to assess the means of mitigating the undesirable effects.

The in-situ diagnosis of the cell with the ‘intentional’ deformities can be focussed on understanding the effect on start-up and shut-down cycles while monitoring carbon corrosion. The membrane and GDL could be investigated in post-mortem analysis to monitor the structural changes and particle size related to carbon corrosion.

The proposed framework comprising of the morphological characterisation, numerical modelling, and the neutron imaging is not limited to low-temperature PEFCs but should lead to performance advancements in other electrochemical systems as well. Redox flow batteries, electrolysers, and different types of fuel cells (alkaline, high temperature, direct methanol, etc.) could thus benefit from the proposed approach. Therefore, the understanding of architectural factors using advanced diagnostics would benefit the development of reliable and robust ‘green’ energy systems integrated with sustainable development.

References

[1] AR6 Synthesis Report: Climate Change 2022 — IPCC, (n.d.). https://www.ipcc.ch/report/sixth-assessment-report-cycle/ (accessed April 22, 2020).

[2] S.H. Mohr, J. Wang, G. Ellem, J. Ward, D. Giurco, Projection of world fossil fuels by country, Fuel. 141 (2015) 120–135. doi:10.1016/j.fuel.2014.10.030.

[3] M. Höök, X. Tang, Depletion of fossil fuels and anthropogenic climate change-A review, Energy Policy. 52 (2013) 797–809. doi:10.1016/j.enpol.2012.10.046.

[4] Intergovernmental Panel on Climate Change, AR5 - Working Group 3, Mitigation of Climate Change - Contribution of Working Group III, 2014. https://www.ipcc.ch/report/ar5/wg3/.

[5] Intergovernmental Panel on Climate Change, Climate Change 2007: Mitigation. Contribution of Working Group III to the Fourth Assessment Report of the Intergovernmental Panel on Climate Change, 2007. https://www.ipcc.ch/report/ar4/wg3/.

[6] Intergovernmental Panel on Climate Change, Climate Change 2014 Synthesis Report Summary Chapter for Policymakers, (2014) 31. doi:10.1017/CBO9781107415324.

[7] A. Chapman, K. Itaoka, K. Hirose, F.T. Davidson, K. Nagasawa, A.C. Lloyd, M.E. Webber, Z. Kurban, S. Managi, T. Tamaki, M.C. Lewis, R.E. Hebner, Y. Fujii, A review of four case studies assessing the potential for hydrogen penetration of the future energy system, Int. J. Hydrogen Energy. 44 (2019) 6371–6382. doi:10.1016/j.ijhydene.2019.01.168.

[8] International Energy Agency, Renewables 2019: Analysis and forecast to 2024, (2019) 184. https://webstore.iea.org/market-report-series-gas-2019.

[9] S.G. Chalk, J.F. Miller, Key challenges and recent progress in batteries, fuel

cells, and hydrogen storage for clean energy systems, J. Power Sources. 159 (2006) 73–80. doi:10.1016/j.jpowsour.2006.04.058.

[10] S.J. Peighambardoust, S. Rowshanzamir, M. Amjadi, Review of the proton exchange membranes for fuel cell applications, Int. J. Hydrogen Energy. 35 (2010) 9349–9384. doi:10.1016/j.ijhydene.2010.05.017.

[11] P.P. Edwards, V.L. Kuznetsov, W.I.F. David, N.P. Brandon, Hydrogen and fuel cells: Towards a sustainable energy future, Energy Policy. 36 (2008) 4356–4362. doi:10.1016/j.enpol.2008.09.036.

[12] B. Tanç, H.T. Arat, E. Baltacıoğlu, K. Aydın, Overview of the next quarter century vision of hydrogen fuel cell electric vehicles, Int. J. Hydrogen Energy. 44 (2019) 10120–10128. doi:10.1016/j.ijhydene.2018.10.112.

[13] F. Barbir, PEM Fuel Cells: Theory and Practice, Strateg. Manag. J. 22 (2005) 314. doi:10.1016/B978-0-12-387710-9.00012-6.

[14] US Department of Energy, Comparison of Fuel Cell Technologies, (2011) 3463.

[15] F. Laurencelle, R.Chahine, J. Hamelin, K. Agbossou, M. Fournier, T.K. Bose, A. Laperrière, Characterization of a Ballard MK5-E proton exchange membrane fuel cell stack, Fuel Cells. 1 (2001) 66–71. doi:10.1002/1615-6854(200105)1:1<66::AID-FUCE66>3.0.CO;2-3.

[16] A. Fly, R.H. Thring, A comparison of evaporative and liquid cooling methods for fuel cell vehicles, Int. J. Hydrogen Energy. 41 (2016) 14217–14229. doi:10.1016/j.ijhydene.2016.06.089.

[17] Y. Sohn, G. Park, T. Yang, Y. Yoon, W. Lee, S. Yim, C. Kim, Operating characteristics of an air-cooling PEMFC for portable applications, J. Power Sources. 145 (2005) 604–609. doi:10.1016/j.jpowsour.2005.02.062.

References

[18] Q. Meyer, S. Ashton, P. Boillat, M. Cochet, E. Engebretsen, D.P. Finegan, X. Lu, J.J. Bailey, N. Mansor, R. Abdulaziz, O.O. Taiwo, R. Jervis, S. Torija, P. Benson, S. Foster, P. Adcock, P.R. Shearing, D.J.L. Brett, Effect of gas diffusion layer properties on water distribution across air-cooled, open-cathode polymer electrolyte fuel cells: A combined ex-situ X-ray tomography and in-operando neutron imaging study, Electrochim. Acta. 211 (2016) 478–487. doi:10.1016/j.electacta.2016.06.068.

[19] A.P. Sasmito, E. Birgersson, A.S. Mujumdar, Numerical evaluation of various thermal management strategies for polymer electrolyte fuel cell stacks, Int. J. Hydrogen Energy. 36 (2011) 12991–13007. doi:10.1016/j.ijhydene.2011.07.028.

[20] D.T.S. Rosa, D.G. Pinto, V.S. Silva, R.A. Silva, C.M. Rangel, High performance PEMFC stack with open-cathode at ambient pressure and temperature conditions, Int. J. Hydrogen Energy. 32 (2007) 4350–4357. doi:10.1016/j.ijhydene.2007.05.042.

[21] S. Strahl, A. Husar, J. Riera, Experimental study of hydrogen purge effects on performance and efficiency of an open-cathode proton exchange membrane fuel cell system, 248 (2014) 474–482.

[22] J.I.S. Cho, T.P. Neville, P. Trogadas, J. Bailey, P. Shearing, D.J.L. Brett, M.-O. Coppens, Capillaries for water management in polymer electrolyte membrane fuel cells, Int. J. Hydrogen Energy. 43 (2018) 21949–21958. doi:10.1016/j.ijhydene.2018.10.030.

[23] T.A. Zawodzlnski, T.E. Springer, F. Urlbe, S. Gottesfeld, Solid state characterization of polymer electrolytes for fuel cell applications, Ionics (Kiel). 60 (1993) 199–211.

[24] C. Heitner-wirguin, Recent advances in perfluorinated ionomer membranes :

structure , properties and applications, J. Memb. Sci. 120 (1996).

[25] J.T. Hinatsu, Water Uptake of Perfluorosulfonic Acid Membranes from Liquid Water and Water Vapor, J. Electrochem. Soc. 141 (2006) 1493. doi:10.1149/1.2054951.

[26] N.S. Vasile, A.H.A. Monteverde Videla, S. Specchia, Effects of the current density distribution on a single-cell DMFC by tuning the anode catalyst in layers of gradual loadings: Modelling and experimental approach, Chem. Eng. J. 322 (2017) 722–741. doi:10.1016/j.cej.2017.04.060.

[27] L. Dubau, L. Castanheira, F. Maillard, M. Chatenet, O. Lottin, G. Maranzana, J. Dillet, A. Lamibrac, J.-C. Perrin, E. Moukheiber, A. ElKaddouri, G. De Moor, C. Bas, L. Flandin, N. Caqué, A review of PEM fuel cell durability: materials degradation, local heterogeneities of aging and possible mitigation strategies, Wiley Interdiscip. Rev. Energy Environ. 3 (2014) 540–560. doi:10.1002/wene.113.

[28] K.A. Mauritz, R.B. Moore, State of understanding of Nafion, Chem. Rev. 104 (2004) 4535–4585. doi:10.1021/cr0207123.

[29] Y. Wang, K.S. Chen, J. Mishler, S.C. Cho, X.C. Adroher, A review of polymer electrolyte membrane fuel cells: Technology, applications, and needs on fundamental research, Appl. Energy. 88 (2011) 981–1007. doi:10.1016/j.apenergy.2010.09.030.

[30] T.E. Springer, T.A. Zawodzinski, S. Gottesfeld, Polymer electrolyte fuel cell model, J. Electrochem. Soc., Vol. 138, No. 8, August 1991. 138 (1993) 2334–2342.

[31] S. Gottesfeld, T.A. Zawodzinski, Polymer electrolyte fuel cells, Los Alamos, 1997.

References

[32] T.A. Zawodzinski, S. Gottesfeld, M.W. Verbrugge, M.W. Verbrugge, R.E. White, Literature Models Synthesis 5.1. 50, 37 (1992) 2178–2186.

[33] T.A. Zawodzinski, A Comparative Study of Water Uptake By and Transport Through Ionomeric Fuel Cell Membranes, J. Electrochem. Soc. 140 (1993) 1981. doi:10.1149/1.2220749.

[34] A. Biyikoglu, Review of proton exchange membrane fuel cell models, Int. J. Hydrogen Energy. 30 (2005) 1181–1212. doi:10.1016/j.ijhydene.2005.05.010.

[35] H.A. Gasteiger, S.S. Kocha, B. Sompalli, F.T. Wagner, Activity benchmarks and requirements for Pt, Pt-alloy, and non-Pt oxygen reduction catalysts for PEMFCs, Appl. Catal. B Environ. 56 (2005) 9–35. doi:10.1016/j.apcatb.2004.06.021.

[36] J. Zhang, PEM fuel cell electrocatalysts and catalyst layers, Fundamentals and Applications, 2008.

[37] R. O'Hayre, D.M. Barnett, F.B. Prinz, The Triple Phase Boundary, J. Electrochem. Soc. 152 (2005) A439. doi:10.1149/1.1851054.

[38] P.K. Das, X. Li, Z.S. Liu, A three-dimensional agglomerate model for the cathode catalyst layer of PEM fuel cells, J. Power Sources. 179 (2008) 186–199. doi:10.1016/j.jpowsour.2007.12.085.

[39] A. Ozden, S. Shahgaldi, X. Li, F. Hamdullahpur, A review of gas diffusion layers for proton exchange membrane fuel cells—With a focus on characteristics, characterization techniques, materials and designs, Prog. Energy Combust. Sci. 74 (2019) 50–102. doi:10.1016/j.pecs.2019.05.002.

[40] N. Rajalakshmi, K.S. Dhathathreyan, Catalyst layer in PEMFC electrodes-fabrication, characterisation and analysis, Chem. Eng. J. 129 (2007) 31–40. doi:10.1016/j.cej.2006.10.035.

References

[41] S. Litster, G. McLean, PEM fuel cell electrodes, J. Power Sources. 130 (2004) 61–76. doi:10.1016/j.jpowsour.2003.12.055.

[42] P.R. Challa, X-ray investigations of PEMFC gas diffusion layers (GDLs), University of Toronto, 2012.

[43] G. Park, Y. Sohn, T. Yang, Y. Yoon, W. Lee, C. Kim, Effect of PTFE contents in the gas diffusion media on the performance of PEMFC, J. Power Sources. 131 (2004) 182–187. doi:10.1016/j.jpowsour.2003.12.037.

[44] S. Shimpalee, U. Beuscher, J.W. Van Zee, Analysis of GDL flooding effects on PEMFC performance, Electrochim. Acta. 52 (2007) 6748–6754. doi:10.1016/j.electacta.2007.04.115.

[45] I. Nitta, T. Hottinen, O. Himanen, M. Mikkola, Inhomogeneous compression of PEMFC gas diffusion layer, J. Power Sources. 171 (2007) 26–36. doi:10.1016/j.jpowsour.2006.11.018.

[46] J. Ge, A. Higier, H. Liu, Effect of gas diffusion layer compression on PEM fuel cell performance, J. Power Sources. 159 (2006) 922–927. doi:10.1016/j.jpowsour.2005.11.069.

[47] J.P. James, H.-W. Choi, J.G. Pharoah, X-ray computed tomography reconstruction and analysis of polymer electrolyte membrane fuel cell porous transport layers, Int. J. Hydrogen Energy. 37 (2012) 18216–18230. doi:10.1016/j.ijhydene.2012.08.077.

[48] H. Li, Y. Tang, Z. Wang, Z. Shi, S. Wu, D. Song, J. Zhang, K. Fatih, J. Zhang, H. Wang, Z. Liu, R. Abouatallah, A. Mazza, A review of water flooding issues in the proton exchange membrane fuel cell, J. Power Sources. 178 (2008) 103–117. doi:10.1016/j.jpowsour.2007.12.068.

[49] Z. Qi, A. Kaufman, Improvement of water management by a microporous

sublayer for PEM fuel cells, J. Power Sources. 109 (2002) 38–46. doi:10.1016/S0378-7753(02)00058-7.

[50] R. Ramasamy, E. Kumbur, M. Mench, W. Liu, D. Moore, M. Murthy, Investigation of macro- and micro-porous layer interaction in polymer electrolyte fuel cells, Int. J. Hydrogen Energy. 33 (2008) 3351–3367. doi:10.1016/j.ijhydene.2008.03.053.

[51] S. Shimpalee, U. Beuscher, J.W. Van Zee, Investigation of gas diffusion media inside PEMFC using CFD modeling, J. Power Sources. 163 (2006) 480–489. doi:10.1016/j.jpowsour.2006.09.038.

[52] J. Ma, X. Zhang, Z. Jiang, H. Ostadi, K. Jiang, R. Chen, Flow properties of an intact MPL from nano-tomography and pore network modelling, Fuel. 136 (2014) 307–315. doi:10.1016/j.fuel.2014.07.040.

[53] Z. Fishman, J. Hinebaugh, A. Bazylak, Microscale Tomography Investigations of Heterogeneous Porosity Distributions of PEMFC GDLs, J. Electrochem. Soc. 157 (2010) B1643. doi:10.1149/1.3481443.

[54] R. Omrani, B. Shabani, Gas diffusion layer modifications and treatments for improving the performance of proton exchange membrane fuel cells and electrolysers: A review, Int. J. Hydrogen Energy. 42 (2017) 28515–28536. doi:10.1016/j.ijhydene.2017.09.132.

[55] A. Hermann, T. Chaudhuri, P. Spagnol, Bipolar plates for PEM fuel cells: A review, Int. J. Hydrogen Energy. 30 (2005) 1297–1302. doi:10.1016/j.ijhydene.2005.04.016.

[56] D.J.L. Brett, N.P. Brandon, Review of Materials and Characterization Methods for Polymer Electrolyte Fuel Cell Flow-Field Plates, J. Fuel Cell Sci. Technol. 4 (2007) 29. doi:10.1115/1.2393303.

References

[57] J.S. Cooper, Design analysis of PEMFC bipolar plates considering stack manufacturing and environment impact, J. Power Sources. 129 (2004) 152–169. doi:10.1016/j.jpowsour.2003.11.037.

[58] A.A. Kulikovsky, Voltage loss in bipolar plates in a fuel cell stack, J. Power Sources. 160 (2006) 431–435. doi:10.1016/j.jpowsour.2006.01.058.

[59] T. Maiyalagan, S. Pasupathi, Components for PEM fuel cells: An overview, 2010. doi:10.4028/www.scientific.net/MSF.657.143.

[60] F.B. O'Hayre, R., Cha, S.W., Colella, W., Prinz, Fuel cell fundamentals, Second, John Wiley & Sons, Inc., New York, 2006. http://books.google.co.uk/books/about/Fuel_cell_fundamentals.html?id=Cr0QAQAAMAAJ&pgis=1.

[61] J. Lipkowski, P.N. Ross, eds., Recent advances in the kinetics of oxygen reaction, in: Electrocatalysis, WILEY-VCH, 1998: pp. 197–200.

[62] N. Kulkarni, M.D.R. Kok, R. Jervis, F. Iacoviello, Q. Meyer, P.R. Shearing, D.J.L. Brett, The effect of non-uniform compression and flow-field arrangements on membrane electrode assemblies - X-ray computed tomography characterisation and effective parameter determination, J. Power Sources. 426 (2019) 97–110. doi:10.1016/j.jpowsour.2019.04.018.

[63] N. Kulkarni, J.I.S. Cho, L. Rasha, R.E. Owen, Y. Wu, R. Ziesche, J. Hack, T. Neville, M. Whiteley, N. Kardjilov, H. Markötter, I. Manke, P.R. Shearing, D.J.L. Brett, Effect of cell compression on the water dynamics of a polymer electrolyte fuel cell using in-plane and through-plane in-operando neutron radiography, J. Power Sources. 439 (2019) 227074. doi:10.1016/j.jpowsour.2019.227074.

[64] N. Kulkarni, Q. Meyer, J. Hack, R. Jervis, F. Iacoviello, K. Ronaszegi, P. Adcock, P.R. Shearing, D.J.L. Brett, Examining the effect of the secondary flow-field on

polymer electrolyte fuel cells using X-ray computed radiography and computational modelling, Int. J. Hydrogen Energy. 44 (2019) 1139–1150. doi:10.1016/j.ijhydene.2018.11.038.

[65] Y. Wang, D.F. Ruiz Diaz, K.S. Chen, Z. Wang, X.C. Adroher, Materials, technological status, and fundamentals of PEM fuel cells – A review, Mater. Today. (2019). doi:10.1016/j.mattod.2019.06.005.

[66] T. Abdel-Baset, T. Benjamin, R. Borup, K.E. Martin, N. Garland, S. Hirano, J. Kopasz, B. Lakshmanmn, D. Masten, M. Mehall, D. Myers, D. Papageorgopoulos, W. Podolski, T. Trabold, B. Vermeersch, J. Waldecker, The. US Deparment of Energy (DOE). Energy Efficiency and Renewable Energy https://energy.gov/eere/fuelcells/doe-technical-targets-polymer-electrolyte-membrane-fuel-cell-components, (2017) 30. doi:10.2172/1220127.

[67] US Department of Energy (DOE), Multi-Year Research, Development, and Demonstration Plan: 3.4 Fuel Cells, Fuel Cell Technol. Off. 2015 (2017) 3.4.1-3.4.58. doi:Department of Energy.

[68] D.N. Ozen, B. Timurkutluk, K. Altinisik, Effects of operation temperature and reactant gas humidity levels on performance of PEM fuel cells, Renew. Sustain. Energy Rev. 59 (2016) 1298–1306. doi:10.1016/j.rser.2016.01.040.

[69] M. Amirinejad, S. Rowshanzamir, M.H. Eikani, Effects of operating parameters on performance of a proton exchange membrane fuel cell, J. Power Sources. 161 (2006) 872–875. doi:10.1016/j.jpowsour.2006.04.144.

[70] M. V. Williams, H.R. Kunz, J.M. Fenton, Operation of Nafion®-based PEM fuel cells with no external humidification: influence of operating conditions and gas diffusion layers, J. Power Sources. 135 (2004) 122–134. doi:10.1016/j.jpowsour.2004.04.010.

References

[71] D. Natarajan, T. Van Nguyen, A Two-Dimensional, Two-Phase, Multicomponent, Transient Model for the Cathode of a Proton Exchange Membrane Fuel Cell Using Conventional Gas Distributors, J. Electrochem. Soc. 148 (2001) A1324. doi:10.1149/1.1415032.

[72] Q. Yan, H. Toghiani, H. Causey, Steady state and dynamic performance of proton exchange membrane fuel cells (PEMFCs) under various operating conditions and load changes, J. Power Sources. 161 (2006) 492–502. doi:10.1016/j.jpowsour.2006.03.077.

[73] H.K. Esfeh, M.K.A. Hamid, Temperature Effect on Proton Exchange Membrane Fuel Cell Performance Part II: Parametric Study, Energy Procedia. 61 (2014) 2617–2620. doi:10.1016/j.egypro.2014.12.261.

[74] S. Shimpalee, S. Dutta, Numerical Prediction of Temperature Distribution in Pem Fuel Cells, Numer. Heat Transf. 38 (2000) 111–128. doi:10.1080/10407780050135360.

[75] T. Ous, C. Arcoumanis, Visualisation of water accumulation in the flow channels of PEMFC under various operating conditions, J. Power Sources. 187 (2009) 182–189. doi:10.1016/j.jpowsour.2008.10.072.

[76] T. Hottinen, O. Himanen, PEMFC temperature distribution caused by inhomogeneous compression of GDL, 2007. doi:10.1016/j.elecom.2006.12.018.

[77] L. Wang, A. Husar, T. Zhou, H. Liu, A parametric study of PEM fuel cell performances, Int. J. Hydrogen Energy. 28 (2003) 1263–1272. doi:10.1016/S0360-3199(02)00284-7.

[78] M. Santarelli, M. Torchio, M. Cali, V. Giaretto, Experimental analysis of cathode flow stoichiometry on the electrical performance of a PEMFC stack, Int. J. Hydrogen Energy. 32 (2007) 710–716. doi:10.1016/j.ijhydene.2006.08.008.

References

[79] R.C. Dante, J.L. Escamilla, V. Madrigal, T. Theuss, J. de Dios Calderón, O. Solorza, R. Rivera, Fractional factorial design of experiments for PEM fuel cell performances improvement, Int. J. Hydrogen Energy. 28 (2003) 343–348. doi:10.1016/S0360-3199(02)00069-1.

[80] A. Kazim, P. Forges, H.T. Liu, Effects of cathode operating conditions on performance of a PEM fuel cell with interdigitated flow fields, Int. J. Energy Res. 27 (2003) 401–414. doi:10.1002/er.884.

[81] S. Kim, S. Shimpalee, J.W. Van Zee, The effect of stoichiometry on dynamic behavior of a proton exchange membrane fuel cell (PEMFC) during load change, J. Power Sources. 135 (2004) 110–121. doi:10.1016/j.jpowsour.2004.03.060.

[82] A. Turhan, K. Heller, J.S. Brenizer, M.M. Mench, Quantification of liquid water accumulation and distribution in a polymer electrolyte fuel cell using neutron imaging, J. Power Sources. 160 (2006) 1195–1203. doi:10.1016/j.jpowsour.2006.03.027.

[83] DOE Technical Targets for Polymer Electrolyte Membrane Fuel Cell Components | Department of Energy, (n.d.). https://www.energy.gov/eere/fuelcells/doe-technical-targets-polymer-electrolyte-membrane-fuel-cell-components (accessed April 22, 2020).

[84] F. Liu, G. Lu, C. Wang, Water transport coefficient distribution through the membrane in a polymer electrolyte fuel cell, J. Memb. Sci. 287 (2007) 126–131. doi:10.1016/j.memsci.2006.10.030.

[85] S.-J. Cheng, J.-M. Miao, S.-J. Wu, Investigating the effects of operational factors on PEMFC performance based on CFD simulations using a three-level full-factorial design, Renew. Energy. 39 (2012) 250–260. doi:10.1016/j.renene.2011.08.009.

References

[86] D.H. Jeon, K.N. Kim, S.M. Baek, J.H. Nam, The effect of relative humidity of the cathode on the performance and the uniformity of PEM fuel cells, Int. J. Hydrogen Energy. 36 (2011) 12499–12511. doi:10.1016/j.ijhydene.2011.06.136.

[87] S.G. Kandlikar, E.J. See, R. Banerjee, Modeling Two-Phase Pressure Drop along PEM Fuel Cell Reactant Channels, J. Electrochem. Soc. 162 (2015) F772–F782. doi:10.1149/2.0831507jes.

[88] A. Iranzo, A. Salva, P. Boillat, J. Biesdorf, E. Tapia, F. Rosa, Water build-up and evolution during the start-up of a PEMFC: Visualization by means of Neutron Imaging, Int. J. Hydrogen Energy. 42 (2017) 13839–13849. doi:10.1016/j.ijhydene.2016.11.076.

[89] L. Wang, A. Husar, T. Zhou, H. Liu, A parametric study of PEM fuel cell performances, 28 (2003) 1263–1272. doi:10.1016/S0360-3199(02)00284-7.

[90] T. Fabian, J.D. Posner, R. O'Hayre, S.W. Cha, J.K. Eaton, F.B. Prinz, J.G. Santiago, The role of ambient conditions on the performance of a planar, air-breathing hydrogen PEM fuel cell, J. Power Sources. 161 (2006) 168–182.

[91] D. JEON, The effect of serpentine flow-field designs on PEM fuel cell performance, Int. J. Hydrogen Energy. 33 (2008) 1052–1066. doi:10.1016/j.ijhydene.2007.11.015.

[92] A. Iranzo, P. Boillat, A. Salva, J. Biesdorf, PEM Fuel Cell Operation under Air and O2Feed: Analysis of Cell Performance and Liquid Water Distributions, Fuel Cells. 16 (2016) 463–468. doi:10.1002/fuce.201500145.

[93] J. Chen, J.B. Siegel, A.G. Stefanopoulou, J.R. Waldecker, Optimization of purge cycle for dead-ended anode fuel cell operation, Int. J. Hydrogen Energy. 38 (2013) 5092–5105. doi:10.1016/j.ijhydene.2013.02.022.

[94] Y. Yang, X. Zhang, L. Guo, H. Liu, Different flow fields, operation modes and designs for proton exchange membrane fuel cells with dead-ended anode, Int. J. Hydrogen Energy. 43 (2018) 1769–1780. doi:10.1016/j.ijhydene.2017.10.137.

[95] E.A. Müller, F. Kolb, L. Guzzella, A.G. Stefanopoulou, D.A. McKay, Correlating Nitrogen Accumulation With Temporal Fuel Cell Performance, J. Fuel Cell Sci. Technol. 7 (2010) 021013. doi:10.1115/1.3177447.

[96] Y. Hou, C. Shen, Z. Yang, Y. He, A dynamic voltage model of a fuel cell stack considering the effects of hydrogen purge operation, Renew. Energy. 44 (2012) 246–251. doi:10.1016/j.renene.2012.01.088.

[97] O.A. Obeisun, Q. Meyer, C.W. Gibbs, J.B. Robinson, P.R. Shearing, Bret, Advanced diagnostics applied to a self-breathing fuel cell, ECS Trans. 61 (2014) 249–258.

[98] Q. Meyer, A. Himeur, S. Ashton, O. Curnick, R. Clague, T. Reisch, P. Adcock, P.R. Shearing, D.J.L. Brett, System-level electro-thermal optimisation of air-cooled open-cathode polymer electrolyte fuel cells: Air blower parasitic load and schemes for dynamic operation, Int. J. Hydrogen Energy. 40 (2015) 1–7. doi:10.1016/j.ijhydene.2015.07.040.

[99] R.K. Ahluwalia, X. Wang, Buildup of nitrogen in direct hydrogen polymer-electrolyte fuel cell stacks, J. Power Sources. 171 (2007) 63–71. doi:10.1016/j.jpowsour.2007.01.032.

[100] K.D. Baik, M.S. Kim, Characterization of nitrogen gas crossover through the membrane in proton-exchange membrane fuel cells, Int. J. Hydrogen Energy. 36 (2011) 732–739. doi:10.1016/j.ijhydene.2010.09.046.

[101] A. Rabbani, M. Rokni, Effect of nitrogen crossover on purging strategy in PEM

fuel cell systems, Appl. Energy. 111 (2013) 1061–1070. doi:10.1016/j.apenergy.2013.06.057.

[102] A.P. Sasmito, A.S. Mujumdar, Performance evaluation of a polymer electrolyte fuel cell with a dead-end anode: A computational fluid dynamic study, Int. J. Hydrogen Energy. 36 (2011) 10917–10933. doi:10.1016/j.ijhydene.2011.05.171.

[103] Q. Meyer, S. Ashton, S. Torija, C. Gurney, P. Boillat, M. Cochet, E. Engebretsen, D.P. Finegan, P. Adcock, P.R. Shearing, D.J.L. Brett, Nitrogen Blanketing and Hydrogen Starvation in Dead-Ended-Anode Polymer Electrolyte Fuel Cells Revealed by Hydro-Electro-Thermal Analysis, Electrochim. Acta. 203 (2016) 198–205. doi:10.1016/j.electacta.2016.04.018.

[104] Q. Meyer, S. Ashton, O. Curnick, T. Reisch, P. Adcock, K. Ronaszegi, J.B. Robinson, D.J.L. Brett, Dead-ended anode polymer electrolyte fuel cell stack operation investigated using electrochemical impedance spectroscopy, off-gas analysis and thermal imaging, J. Power Sources. 254 (2014) 1–9. doi:10.1016/j.jpowsour.2013.11.125.

[105] J. Millichamp, T.J. Mason, T.P. Neville, N. Rajalakshmi, R. Jervis, P.R. Shearing, D.J.L. Brett, Mechanisms and effects of mechanical compression and dimensional change in polymer electrolyte fuel cells – A review, J. Power Sources. 284 (2015) 305–320. doi:10.1016/j.jpowsour.2015.02.111.

[106] J. Ihonen, F. Jaouen, G. Lindbergh, G. Sundholm, A novel polymer electrolyte fuel cell for laboratory investigations and in-situ contact resistance measurements, Electrochim. Acta. 46 (2001) 2899–2911. doi:10.1016/S0013-4686(01)00510-2.

[107] R. Montanini, G. Squadrito, G. Giacoppo, Measurement of the clamping pressure distribution in polymer electrolyte fuel cells using piezoresistive sensor

arrays and digital image correlation techniques, J. Power Sources. 196 (2011) 8484–8493. doi:10.1016/j.jpowsour.2011.06.017.

[108] F. Alcaide, G. Alvarez, A. Querejeta, O. Miguel, I. Boyano, Effect of Gas Diffusion Layer Composition on the Performance of Liquid Direct Methanol Fuel Cells, in: ECS Trans., ECS, 2009: pp. 891–897. doi:10.1149/1.3210643.

[109] T.J. Mason, J. Millichamp, T.P. Neville, A. El-kharouf, B.G. Pollet, D.J.L. Brett, Effect of clamping pressure on ohmic resistance and compression of gas diffusion layers for polymer electrolyte fuel cells, J. Power Sources. 219 (2012) 52–59. https://www.sciencedirect.com/science/article/pii/S0378775312011469#fig5 (accessed March 21, 2018).

[110] E. Carcadea, M. Varlam, D.B. Ingham, L.G. Patularu, A. Marinoiu, D. Ion-Ebrasu, I. Stefanescu, Effect of Gdl(+MPL) Compression on the PEM Fuel Cell Performance, Meet. Abstr. MA2016-02 (2016) 2742–2742. http://ma.ecsdl.org/content/MA2016-02/38/2742.

[111] A.H. Mahmoudi, A. Ramiar, Q. Esmaili, Effect of inhomogeneous compression of gas diffusion layer on the performance of PEMFC with interdigitated flow field, Energy Convers. Manag. 110 (2016) 78–89. doi:10.1016/j.enconman.2015.12.012.

[112] R. Banerjee, J. Hinebaugh, H. Liu, R. Yip, N. Ge, A. Bazylak, Heterogeneous porosity distributions of polymer electrolyte membrane fuel cell gas diffusion layer materials with rib-channel compression, Int. J. Hydrogen Energy. 41 (2016) 14885–14896. doi:10.1016/j.ijhydene.2016.06.147.

[113] C. Tötzke, G. Gaiselmann, M. Osenberg, T. Arlt, H. Markötter, A. Hilger, A. Kupsch, B.R. Müller, V. Schmidt, W. Lehnert, I. Manke, Influence of hydrophobic treatment on the structure of compressed gas diffusion layers, J. Power

Sources. 324 (2016) 625–636. doi:10.1016/j.jpowsour.2016.05.118.

[114] S. Thiele, R. Zengerle, C. Ziegler, Nano-morphology of a polymer electrolyte fuel cell catalyst layer-imaging, reconstruction and analysis, Nano Res. 4 (2011) 849–860. doi:10.1007/s12274-011-0141-x.

[115] A. Therdthianwong, P. Manomayidthikarn, S. Therdthianwong, Investigation of membrane electrode assembly (MEA) hot-pressing parameters for proton exchange membrane fuel cell, Energy. 32 (2007) 2401–2411. doi:10.1016/j.energy.2007.07.005.

[116] A. Bazylak, D. Sinton, Z.-S. Liu, N. Djilali, Effect of compression on liquid water transport and microstructure of PEMFC gas diffusion layers, J. Power Sources. 163 (2007) 784–792. doi:10.1016/j.jpowsour.2006.09.045.

[117] S. Prass, S. Hasanpour, P.K. Sow, A.B. Phillion, W. Mérida, Microscale X-ray tomographic investigation of the interfacial morphology between the catalyst and micro porous layers in proton exchange membrane fuel cells, J. Power Sources. 319 (2016) 82–89. doi:10.1016/j.jpowsour.2016.04.031.

[118] P.A. García-Salaberri, I. V. Zenyuk, A.D. Shum, G. Hwang, M. Vera, A.Z. Weber, J.T. Gostick, Analysis of representative elementary volume and through-plane regional characteristics of carbon-fiber papers: diffusivity, permeability and electrical/thermal conductivity, Int. J. Heat Mass Transf. 127 (2018) 687–703. doi:10.1016/j.ijheatmasstransfer.2018.07.030.

[119] C. Tötzke, G. Gaiselmann, M. Osenberg, J. Bohner, T. Arlt, H. Markötter, A. Hilger, F. Wieder, A. Kupsch, B.R. Müller, M.P. Hentschel, J. Banhart, V. Schmidt, W. Lehnert, I. Manke, Three-dimensional study of compressed gas diffusion layers using synchrotron X-ray imaging, J. Power Sources. 253 (2014) 123–131. doi:10.1016/j.jpowsour.2013.12.062.

References

[120] J.-H. Lin, W.-H. Chen, Y.-J. Su, T.-H. Ko, Effect of gas diffusion layer compression on the performance in a proton exchange membrane fuel cell, Fuel. 87 (2008) 2420–2424. doi:10.1016/J.FUEL.2008.03.001.

[121] T.J. Mason, J. Millichamp, T.P. Neville, P.R. Shearing, S. Simons, D.J.L. Brett, A study of the effect of water management and electrode flooding on the dimensional change of polymer electrolyte fuel cells, J. Power Sources. 242 (2013) 70–77. doi:10.1016/j.jpowsour.2013.05.045.

[122] R.W. Atkinson, Y. Garsany, B.D. Gould, K.E. Swider-Lyons, I. V. Zenyuk, The Role of Compressive Stress on Gas Diffusion Media Morphology and Fuel Cell Performance, ACS Appl. Energy Mater. (2017) acsaem.7b00077. doi:10.1021/acsaem.7b00077.

[123] J. Kleemann, F. Finsterwalder, W. Tillmetz, Characterisation of mechanical behaviour and coupled electrical properties of polymer electrolyte membrane fuel cell gas diffusion layers, J. Power Sources. 190 (2009) 92–102. doi:10.1016/j.jpowsour.2008.09.026.

[124] E.M. Khetabi, K. Bouziane, N. Zamel, X. François, Y. Meyer, D. Candusso, Effects of mechanical compression on the performance of polymer electrolyte fuel cells and analysis through in-situ characterisation techniques - A review, J. Power Sources. (2019). doi:10.1016/j.jpowsour.2019.03.071.

[125] Y. Wu, J.I.S. Cho, X. Lu, L. Rasha, T.P. Neville, J. Millichamp, R. Ziesche, N. Kardjilov, H. Markötter, P. Shearing, D.J.L. Brett, Effect of compression on the water management of polymer electrolyte fuel cells: An in-operando neutron radiography study, J. Power Sources. 412 (2019) 597–605. doi:10.1016/j.jpowsour.2018.11.048.

[126] I. Nitta, O. Himanen, M. Mikkola, Contact resistance between gas diffusion layer and catalyst layer of PEM fuel cell, 2008. doi:10.1016/j.elecom.2007.10.029.

References

[127] C.M. Baca, R. Travis, M. Bang, Three-dimensional, single-phase, non-isothermal CFD model of a PEM fuel cell, J. Power Sources. 178 (2008) 269–281. doi:10.1016/j.jpowsour.2007.12.023.

[128] V.K. Krastev, G. Falcucci, E. Jannelli, M. Minutillo, R. Cozzolino, 3D CFD modeling and experimental characterization of HT PEM fuel cells at different anode gas compositions, Int. J. Hydrogen Energy. 39 (2014) 21663–21672. doi:10.1016/j.ijhydene.2014.09.015.

[129] C. Fink, N. Fouquet, Three-dimensional simulation of polymer electrolyte membrane fuel cells with experimental validation, Electrochim. Acta. 56 (2011) 10820–10831. doi:10.1016/j.electacta.2011.05.041.

[130] J.I.S. Cho, T.P. Neville, P. Trogadas, J. Bailey, P. Shearing, D.J.L. Brett, M.O. Coppens, Capillaries for water management in polymer electrolyte membrane fuel cells, Int. J. Hydrogen Energy. 43 (2018) 21949–21958. doi:10.1016/j.ijhydene.2018.10.030.

[131] J.I.S. Cho, T.P. Neville, P. Trogadas, Q. Meyer, Y. Wu, R. Ziesche, P. Boillat, M. Cochet, V. Manzi-Orezzoli, P. Shearing, D.J.L. Brett, M.-O. Coppens, Visualization of liquid water in a lung-inspired flow-field based polymer electrolyte membrane fuel cell via neutron radiography, Energy. 170 (2019) 14–21. doi:10.1016/j.energy.2018.12.143.

[132] X. Li, I. Sabir, Review of bipolar plates in PEM fuel cells: Flow-field designs, Int. J. Hydrogen Energy. 30 (2005) 359–371. doi:10.1016/j.ijhydene.2004.09.019.

[133] A. Iranzo, M. Muñoz, J. Pino, F. Rosa, Update on numerical model for the performance prediction of a PEM Fuel Cell, Int. J. Hydrogen Energy. 36 (2011) 9123–9127. doi:10.1016/j.ijhydene.2011.04.102.

[134] Y. Ferng, A. Su, A three-dimensional full-cell CFD model used to investigate the

effects of different flow channel designs on PEMFC performance, Int. J. Hydrogen Energy. 32 (2007) 4466–4476. doi:10.1016/j.ijhydene.2007.05.012.

[135] V.B. Oliveira, C.M. Rangel, A.M.F.R. Pinto, Effect of anode and cathode flow field design on the performance of a direct methanol fuel cell, Chem. Eng. J. 157 (2010) 174–180. doi:10.1016/j.cej.2009.11.033.

[136] T. V. Reshetenko, G. Bender, K. Bethune, R. Rocheleau, A segmented cell approach for studying the effects of serpentine flow field parameters on PEMFC current distribution, Electrochim. Acta. 88 (2013) 571–579. doi:10.1016/j.electacta.2012.10.103.

[137] P.T. Nguyen, T. Berning, N. Djilali, Computational model of a PEM fuel cell with serpentine gas flow channels, J. Power Sources. 130 (2004) 149–157. doi:10.1016/j.jpowsour.2003.12.027.

[138] D.H. Ahmed, H.J. Sung, Effects of channel geometrical configuration and shoulder width on PEMFC performance at high current density, J. Power Sources. 162 (2006) 327–339. doi:10.1016/j.jpowsour.2006.06.083.

[139] Z. Lu, C. Kim, A.M. Karlsson, J.C. Cross, M.H. Santare, Effect of gas diffusion layer modulus and land–groove geometry on membrane stresses in proton exchange membrane fuel cells, J. Power Sources. 196 (2011) 4646–4654. doi:10.1016/j.jpowsour.2011.01.028.

[140] D. Lorenzini-Gutierrez, S.G. Kandlikar, A. Hernandez-Guerrero, F. Elizalde-Blancas, Residence time of water film and slug flow features in fuel cell gas channels and their effect on instantaneous area coverage ratio, J. Power Sources. 279 (2015) 567–580. doi:10.1016/j.jpowsour.2015.01.041.

[141] X. Zhu, Q. Liao, P.C. Sui, N. Djilali, Numerical investigation of water droplet dynamics in a low-temperature fuel cell microchannel: Effect of channel

geometry, J. Power Sources. 195 (2010) 801–812. doi:10.1016/J.JPOWSOUR.2009.08.021.

[142] A.D. Santamaria, N.J. Cooper, M.K. Becton, J.W. Park, Effect of channel length on interdigitated flow-field PEMFC performance: A computational and experimental study, Int. J. Hydrogen Energy. 38 (2013) 16253–16263. doi:10.1016/j.ijhydene.2013.09.081.

[143] L. Yu, G. Ren, M. Qin, X. Jiang, Transport mechanisms and performance simulations of a PEM fuel cell with interdigitated flow field, Renew. Energy. 34 (2009) 530–543. doi:10.1016/j.renene.2008.05.048.

[144] S. Shimpalee, J.W. Van Zee, Numerical studies on rib & channel dimension of flow-field on PEMFC performance, Int. J. Hydrogen Energy. 32 (2007) 842–856. doi:10.1016/j.ijhydene.2006.11.032.

[145] J. Scholta, G. Escher, W. Zhang, L. Küppers, L. Jörissen, W. Lehnert, Investigation on the influence of channel geometries on PEMFC performance, J. Power Sources. 155 (2006) 66–71. doi:10.1016/j.jpowsour.2005.05.099.

[146] N. Akhtar, A. Qureshi, J. Scholta, C. Hartnig, M. Messerschmidt, W. Lehnert, Investigation of water droplet kinetics and optimization of channel geometry for PEM fuel cell cathodes, Int. J. Hydrogen Energy. 34 (2009) 3104–3111. doi:10.1016/j.ijhydene.2009.01.022.

[147] A.A. Kornyshev, A.A. Kulikovsky, Characteristic length of fuel and oxygen consumption in feed channels of polymer electrolyte fuel cells, Electrochim. Acta. 46 (2001) 4389–4395. doi:10.1016/S0013-4686(01)00662-4.

[148] H. Liu, P. Li, D. Juarez-Robles, K. Wang, A. Hernandez-Guerrero, Experimental Study and Comparison of Various Designs of Gas Flow Fields to PEM Fuel Cells and Cell Stack Performance, Front. Energy Res. 2 (2014) 1–8.

doi:10.3389/fenrg.2014.00002.

[149] Y. Wu, J.I.S. Cho, T.P. Neville, Q. Meyer, R. Ziesche, P. Boillat, M. Cochet, P.R. Shearing, D.J.L. Brett, Effect of serpentine flow-field design on the water management of polymer electrolyte fuel cells: An in-operando neutron radiography study, J. Power Sources. 399 (2018) 254–263. doi:10.1016/j.jpowsour.2018.07.085.

[150] H. Dohle, A.A. Kornyshev, A.A. Kulikovsky, J. Mergel, D. Stolten, The current voltage plot of PEM fuel cell with long feed channels, Electrochem. Commun. 3 (2001) 73–80. doi:10.1016/S1388-2481(01)00108-4.

[151] C.J. Bapat, S.T. Thynell, Effect of anisotropic thermal conductivity of the GDL and current collector rib width on two-phase transport in a PEM fuel cell, J. Power Sources. 179 (2008) 240–251. doi:10.1016/j.jpowsour.2007.12.033.

[152] P. Stahl, J. Biesdorf, P. Boillat, J. Kraft, K. a. Friedrich, Water Distribution Analysis in the Outer Perimeter Region of Technical PEFC Based on Neutron Radiography, J. Electrochem. Soc. 162 (2015) F677–F685. doi:10.1149/2.0351507jes.

[153] Q. Meyer, N. Mansor, F. Iacoviello, P.L. Cullen, R. Jervis, D. Finegan, C. Tan, J. Bailey, P.R. Shearing, D.J.L. Brett, Investigation of Hot Pressed Polymer Electrolyte Fuel Cell Assemblies via X-ray Computed Tomography, Electrochim. Acta. 242 (2017) 125–136. doi:10.1016/j.electacta.2017.05.028.

[154] H. Liu, P. Li, J. Van Lew, CFD study on flow distribution uniformity in fuel distributors having multiple structural bifurcations of flow channels, Int. J. Hydrogen Energy. 35 (2010) 9186–9198. doi:10.1016/j.ijhydene.2010.06.043.

[155] D.J.. Brett, S. Atkins, N.P. Brandon, V. Vesovic, N. Vasileiadis, A.R. Kucernak, Measurement of the current distribution along a single flow channel of a solid

polymer fuel cell, Electrochem. Commun. 3 (2001) 628–632. doi:10.1016/S1388-2481(01)00234-X.

[156] K. Scott, S. Pilditch, M. Mamlouk, Modelling and experimental validation of a high temperature polymer electrolyte fuel cell, J. Appl. Electrochem. 37 (2007) 1245–1259. doi:10.1007/s10800-007-9414-1.

[157] T. Kurz, A. Hakenjos, J. Krämer, M. Zedda, C. Agert, An impedance-based predictive control strategy for the state-of-health of PEM fuel cell stacks, J. Power Sources. 180 (2008) 742–747. doi:10.1016/j.jpowsour.2008.02.062.

[158] a Kulikovsky, Performance of catalyst layers of polymer electrolyte fuel cells: exact solutions, Electrochem. Commun. 4 (2002) 318–323. doi:10.1016/S1388-2481(02)00275-8.

[159] D.A. McKahn, Influence of gas channel depth in self-humidified miniature PEM fuel cells with dead-ended anode, Int. J. Hydrogen Energy. 40 (2015) 7168–7181. doi:10.1016/j.ijhydene.2015.02.132.

[160] S. Litster, D. Sinton, N. Djilali, Ex situ visualization of liquid water transport in PEM fuel cell gas diffusion layers, J. Power Sources. 154 (2006) 95–105. doi:10.1016/j.jpowsour.2005.03.199.

[161] A. Bazylak, D. Sinton, Z.-S. Liu, N. Djilali, Effect of compression on liquid water transport and microstructure of PEMFC gas diffusion layers, J. Power Sources. 163 (2007) 784–792. doi:10.1016/j.jpowsour.2006.09.045.

[162] J. Haußmann, H. Markötter, R. Alink, A. Bauder, K. Dittmann, I. Manke, J. Scholta, Synchrotron radiography and tomography of water transport in perforated gas diffusion media, J. Power Sources. 239 (2013) 611–622. doi:10.1016/j.jpowsour.2013.02.014.

[163] D. Muirhead, R. Banerjee, J. Lee, M.G. George, N. Ge, H. Liu, S. Chevalier, J.

Hinebaugh, K. Han, A. Bazylak, Simultaneous characterization of oxygen transport resistance and spatially resolved liquid water saturation at high-current density of polymer electrolyte membrane fuel cells with varied cathode relative humidity, Int. J. Hydrogen Energy. 42 (2017) 29472–29483. doi:10.1016/j.ijhydene.2017.10.031.

[164] T. Sasabe, P. Deevanhxay, S. Tsushima, S. Hirai, Soft X-ray visualization of the liquid water transport within the cracks of micro porous layer in PEMFC, Electrochem. Commun. 13 (2011) 638–641. doi:10.1016/j.elecom.2011.03.033.

[165] S. Chevalier, J. Lee, N. Ge, R. Yip, P. Antonacci, Y. Tabuchi, T. Kotaka, A. Bazylak, In operando measurements of liquid water saturation distributions and effective diffusivities of polymer electrolyte membrane fuel cell gas diffusion layers, Electrochim. Acta. 210 (2016) 792–803. doi:10.1016/j.electacta.2016.05.180.

[166] A. Turhan, S. Kim, M. Hatzell, M.M. Mench, Impact of channel wall hydrophobicity on through-plane water distribution and flooding behavior in a polymer electrolyte fuel cell, Electrochim. Acta. 55 (2010) 2734–2745. doi:10.1016/j.electacta.2009.11.095.

[167] A. Iranzo, P. Boillat, Liquid water distribution patterns featuring back-diffusion transport in a PEM fuel cell with neutron imaging, Int. J. Hydrogen Energy. 39 (2014) 17240–17245. doi:10.1016/j.ijhydene.2014.08.042.

[168] A. Iranzo, P. Boillat, P. Oberholzer, J. Guerra, A novel approach coupling neutron imaging and numerical modelling for the analysis of the impact of water on fuel cell performance, Energy. 68 (2014) 971–981. doi:10.1016/j.energy.2014.03.014.

[169] N. Kardjilov, I. Manke, R. Woracek, A. Hilger, J. Banhart, Advances in neutron imaging, Mater. Today. 21 (2018) 652–672. doi:10.1016/j.mattod.2018.03.001.

References

[170] P. Boillat, E.H. Lehmann, P. Trtik, M. Cochet, Neutron imaging of fuel cells – Recent trends and future prospects, Curr. Opin. Electrochem. 5 (2017) 3–10. doi:10.1016/j.coelec.2017.07.012.

[171] M. Weiland, P. Boillat, P. Oberholzer, A. Kaestner, E.H. Lehmann, T.J. Schmidt, G.G. Scherer, H. Reichl, High resolution neutron imaging for pulsed and constant load operation of passive self-breathing polymer electrolyte fuel cells, Electrochim. Acta. 87 (2013) 567–574. doi:10.1016/j.electacta.2012.09.091.

[172] N. Kardjilov, I. Manke, A. Hilger, M. Strobl, J. Banhart, Neutron imaging in materials science, Mater. Today. 14 (2011) 248–256. doi:10.1016/S1369-7021(11)70139-0.

[173] J.P. Owejan, T.A. Trabold, D.L. Jacobson, D.R. Baker, D.S. Hussey, M. Arif, In situ investigation of water transport in an operating PEM fuel cell using neutron radiography: Part 2 – Transient water accumulation in an interdigitated cathode flow field, Int. J. Heat Mass Transf. 49 (2006) 4721–4731. doi:10.1016/j.ijheatmasstransfer.2006.07.004.

[174] A. Forner-Cuenca, J. Biesdorf, V. Manzi-Orezzoli, L. Gubler, T.J. Schmidt, P. Boillat, Advanced water management in PEFCs: Diffusion layers with patterned wettability: III. Operando characterization with neutron imaging, J. Electrochem. Soc. 163 (2016) F1389–F1398. doi:10.1149/2.0891613jes.

[175] A. Forner-Cuenca, J. Biesdorf, L. Gubler, P.M. Kristiansen, T.J. Schmidt, P. Boillat, Engineered Water Highways in Fuel Cells: Radiation Grafting of Gas Diffusion Layers, Adv. Mater. 27 (2015) 6317–6322. doi:10.1002/adma.201503557.

[176] M.A. Hickner, N.P. Siegel, K.S. Chen, D.N. McBrayer, D.S. Hussey, D.L. Jacobson, M. Arif, Real-time imaging of liquid water in an operating proton exchange membrane fuel cell, J. Electrochem. Soc. 153 (2006) 902–908.

doi:10.1149/1.2184893.

[177] M.A. Hickner, N.P. Siegel, K.S. Chen, D.S. Hussey, D.L. Jacobson, Observations of transient flooding in a proton exchange membrane fuel cell using time-resolved neutron radiography, J. Electrochem. Soc. 157 (2010) 32–38. doi:10.1149/1.3250864.

[178] J.D. Fairweather, D. Spernjak, A.Z. Weber, D. Harvey, S. Wessel, D.S. Hussey, D.L. Jacobson, K. Artyushkova, R. Mukundan, R.L. Borup, Effects of cathode corrosion on through-planewater transport in proton exchange membrane fuel cells, J. Electrochem. Soc. 160 (2013) 980–993. doi:10.1149/2.024309jes.

[179] J. Kätzel, H. Markötter, T. Arlt, M. Klages, J. Haußmann, M. Messerschmidt, N. Kardjilov, J. Scholta, J. Banhart, I. Manke, Effect of ageing of gas diffusion layers on the water distribution in flow field channels of polymer electrolyte membrane fuel cells, J. Power Sources. 301 (2016) 386–391. doi:10.1016/j.jpowsour.2015.10.004.

[180] N. Kardjilov, A. Hilger, I. Manke, CONRAD-2: Cold Neutron Tomography and Radiography at BER II (V7), J. Large-Scale Res. Facil. JLSRF. 2 (2016) 98. doi:10.17815/jlsrf-2-108.

[181] N. Kardjilov, A. Hilger, I. Manke, M. Strobl, M. Dawson, S. Williams, J. Banhart, Neutron tomography instrument CONRAD at HZB, Nucl. Instruments Methods Phys. Res. Sect. A Accel. Spectrometers, Detect. Assoc. Equip. 651 (2011) 47–52. doi:10.1016/j.nima.2011.01.067.

[182] N. Kardjilov, M. Dawson, A. Hilger, I. Manke, M. Strobl, D. Penumadu, F.H. Kim, F. Garcia-Moreno, J. Banhart, A highly adaptive detector system for high resolution neutron imaging, Nucl. Instruments Methods Phys. Res. Sect. A Accel. Spectrometers, Detect. Assoc. Equip. 651 (2011) 95–99. doi:10.1016/j.nima.2011.02.084.

References

[183] H. Markötter, I. Manke, R. Kuhn, T. Arlt, N. Kardjilov, M.P. Hentschel, A. Kupsch, A. Lange, C. Hartnig, J. Scholta, J. Banhart, Neutron tomographic investigations of water distributions in polymer electrolyte membrane fuel cell stacks, J. Power Sources. 219 (2012) 120–125. doi:10.1016/j.jpowsour.2012.07.043.

[184] W.C.Rontgen, Über eine neue Art von Strahlen, Ann. Phys.,. 300 (1898) 1–11. doi:10.1002/piuz.201090005.

[185] H. Markötter, I. Manke, P. Krüger, T. Arlt, J. Haussmann, M. Klages, H. Riesemeier, C. Hartnig, J. Scholta, J. Banhart, Investigation of 3D water transport paths in gas diffusion layers by combined in-situ synchrotron X-ray radiography and tomography, Electrochem. Commun. 13 (2011) 1001–1004. doi:10.1016/j.elecom.2011.06.023.

[186] M. Di Michiel, J.M. Merino, D. Fernandez-Carreiras, T. Buslaps, V. Honkimäki, P. Falus, T. Martins, O. Svensson, Fast microtomography using high energy synchrotron radiation, Rev. Sci. Instrum. 76 (2005). doi:10.1063/1.1884194.

[187] H. Ostadi, K. Jiang, P.D. Prewett, Micro/nano X-ray tomography reconstruction fine-tuning using scanning electron microscope images, Micro Nano Lett. 3 (2008) 106. doi:10.1049/mnl:20080030.

[188] H. Ostadi, P. Rama, Y. Liu, R. Chen, X.X. Zhang, K. Jiang, Influence of threshold variation on determining the properties of a polymer electrolyte fuel cell gas diffusion layer in X-ray nano-tomography, Chem. Eng. Sci. 65 (2010) 2213–2217. doi:10.1016/j.ces.2009.12.019.

[189] S. Hasanpour, M. Hoorfar, A.B. Phillion, Characterization of transport phenomena in porous transport layers using X-ray microtomography, J. Power Sources. 353 (2017) 221–229. doi:10.1016/j.jpowsour.2017.03.153.

[190] J. Hack, T.M.M. Heenan, F. Iacoviello, N. Mansor, Q. Meyer, P. Shearing, N.

Brandon, D.J.L. Brett, A Structure and Durability Comparison of Membrane Electrode Assembly Fabrication Methods: Self-Assembled Versus Hot-Pressed, J. Electrochem. Soc. 165 (2018) F3045–F3052. doi:10.1149/2.0051806jes.

[191] C.A. Schneider, W.S. Rasband, K.W. Eliceiri, NIH Image to ImageJ: 25 years of image analysis, Nat. Methods. 9 (2012) 671–675. doi:10.1038/nmeth.2089.

[192] J. Schindelin, I. Arganda-Carreras, E. Frise, V. Kaynig, M. Longair, T. Pietzsch, S. Preibisch, C. Rueden, S. Saalfeld, B. Schmid, J.Y. Tinevez, D.J. White, V. Hartenstein, K. Eliceiri, P. Tomancak, A. Cardona, Fiji: An open-source platform for biological-image analysis, Nat. Methods. 9 (2012) 676–682. doi:10.1038/nmeth.2019.

[193] A. Buades, B. Coll, J.-M. Morel, A Non-Local Algorithm for Image Denoising, in: 2005 IEEE Comput. Soc. Conf. Comput. Vis. Pattern Recognit., IEEE, 2005: pp. 60–65. doi:10.1109/CVPR.2005.38.

[194] N. Kwok, H. Shi, Design of unsharp masking filter kernel and gain using particle swarm optimization, in: 2014 7th Int. Congr. Image Signal Process., IEEE, 2014: pp. 217–222. doi:10.1109/CISP.2014.7003780.

[195] T. F. Scientific, Thermo Scientific Avizo Software 9 User's Guide, (2018) 1–915.

[196] S.J. Cooper, D.S. Eastwood, J. Gelb, G. Damblanc, D.J.L. Brett, R.S. Bradley, P.J. Withers, P.D. Lee, A.J. Marquis, N.P. Brandon, P.R. Shearing, Image based modelling of microstructural heterogeneity in LiFePO4 electrodes for Li-ion batteries, J. Power Sources. 247 (2014) 1033–1039. doi:10.1016/J.JPOWSOUR.2013.04.156.

[197] S.J. Cooper, A. Bertei, P.R. Shearing, J.A. Kilner, N.P. Brandon, TauFactor: An open-source application for calculating tortuosity factors from tomographic data, SoftwareX. 5 (2016) 203–210. doi:10.1016/j.softx.2016.09.002.

References

[198] R. Jervis, M.D.R. Kok, T.P. Neville, Q. Meyer, L.D. Brown, F. Iacoviello, J.T. Gostick, D.J.L. Brett, P.R. Shearing, In situ compression and X-ray computed tomography of flow battery electrodes, J. Energy Chem. (2018). doi:10.1016/J.JECHEM.2018.03.022.

[199] S.J. Cooper, A. Bertei, D.P. Finegan, N.P. Brandon, Simulated impedance of diffusion in porous media, Electrochim. Acta. 251 (2017) 681–689. doi:10.1016/j.electacta.2017.07.152.

[200] D. Candusso, F. Harel, A. De Bernardinis, X. Francois, M. Pera, D. Hissel, P. Schott, G. Coquery, J. Kauffmann, Characterisation and modelling of a 5kW PEMFC for transportation applications, Int. J. Hydrogen Energy. 31 (2006) 1019–1030. doi:10.1016/j.ijhydene.2005.11.010.

[201] R.K. Ahluwalia, X. Wang, Fuel cell systems for transportation: Status and trends, J. Power Sources. 177 (2008) 167–176. doi:10.1016/j.jpowsour.2007.10.026.

[202] R. Anderson, L. Zhang, Y. Ding, M. Blanco, X. Bi, D.P. Wilkinson, A critical review of two-phase flow in gas flow channels of proton exchange membrane fuel cells, J. Power Sources. 195 (2010) 4531–4553. doi:10.1016/j.jpowsour.2009.12.123.

[203] K. Watanabe, K. Hamada, T. Araki, Visualization technique for time-variant hydrogen concentration distribution in porous materials using hydrogen storage alloy thin film, Int. J. Hydrogen Energy. 43 (2018) 12377–12385. doi:10.1016/j.ijhydene.2018.04.180.

[204] B. Sompalli, B.A. Litteer, W. Gu, H.A. Gasteiger, Membrane Degradation at Catalyst Layer Edges in PEMFC MEAs, J. Electrochem. Soc. 154 (2007) B1349. doi:10.1149/1.2789791.

[205] I. V. Zenyuk, D.Y. Parkinson, L.G. Connolly, A.Z. Weber, Gas-diffusion-layer

structural properties under compression via X-ray tomography, J. Power Sources. 328 (2016) 364–376. doi:10.1016/j.jpowsour.2016.08.020.

[206] C. Tötzke, I. Manke, T. Arlt, H. Markötter, N. Kardjilov, A. Hilger, S.H. Williams, P. Krüger, R. Kuhn, C. Hartnig, J. Scholta, J. Banhart, Investigation of fuel cells using scanning neutron imaging and a focusing neutron guide, Nucl. Instruments Methods Phys. Res. Sect. A Accel. Spectrometers, Detect. Assoc. Equip. 663 (2012) 48–54. doi:10.1016/j.nima.2011.09.054.

[207] T. Hottinen, O. Himanen, S. Karvonen, I. Nitta, Inhomogeneous compression of PEMFC gas diffusion layer, J. Power Sources. 171 (2007) 113–121. doi:10.1016/j.jpowsour.2006.10.076.

[208] N. Parikh, J. Allen, R.S. Yassar, Effect of deformation on electrical properties of carbon fibers used in gas diffusion layer of proton exchange membrane fuel cells, J. Power Sources. 193 (2009) 766–768. doi:10.1016/j.jpowsour.2009.04.061.

[209] N. Ge, S. Chevalier, J. Lee, R. Yip, R. Banerjee, M.G. George, H. Liu, C. Lee, M. Fazeli, P. Antonacci, T. Kotaka, Y. Tabuchi, A. Bazylak, Non-isothermal two-phase transport in a polymer electrolyte membrane fuel cell with crack-free microporous layers, Int. J. Heat Mass Transf. 107 (2017) 418–431. doi:10.1016/j.ijheatmasstransfer.2016.11.045.

[210] S. Odaya, R.K. Phillips, Y. Sharma, J. Bellerive, A.B. Phillion, M. Hoorfar, X-ray Tomographic Analysis of Porosity Distributions in Gas Diffusion Layers of Proton Exchange Membrane Fuel Cells, Electrochim. Acta. 152 (2015) 464–472. doi:10.1016/j.electacta.2014.11.143.

[211] R. Kamal, S.H. Chan, Sensitivity analysis of anode overpotential during start-up process of a high temperature proton exchange membrane fuel cell, Electrochim. Acta. 176 (2015) 965–975. doi:10.1016/j.electacta.2015.07.090.

References

[212] T. Koido, T. Furusawa, K. Moriyama, An approach to modeling two-phase transport in the gas diffusion layer of a proton exchange membrane fuel cell, J. Power Sources. 175 (2008) 127–136. doi:10.1016/j.jpowsour.2007.09.029.

[213] P.A. García-Salaberri, M. Vera, R. Zaera, Nonlinear orthotropic model of the inhomogeneous assembly compression of PEM fuel cell gas diffusion layers, Int. J. Hydrogen Energy. 36 (2011) 11856–11870. doi:10.1016/j.ijhydene.2011.05.152.

[214] R. Lin, Y.S. Ren, X.W. Lin, Z.H. Jiang, Z. Yang, Y.T. Chang, Investigation of the internal behavior in segmented PEMFCs of different flow fields during cold start process, Energy. 123 (2017) 367–377. doi:10.1016/j.energy.2017.01.138.

[215] Z. Fishman, A. Bazylak, Heterogeneous Through-Plane Porosity Distributions for Treated PEMFC GDLs. II. Effect of MPL Cracks, J. Electrochem. Soc. 158 (2011) B846. doi:10.1149/1.3594636.

[216] L. Holzer, O. Pecho, J. Schumacher, P. Marmet, O. Stenzel, F.N. Büchi, A. Lamibrac, B. Münch, Microstructure-property relationships in a gas diffusion layer (GDL) for Polymer Electrolyte Fuel Cells, Part I: effect of compression and anisotropy of dry GDL, Electrochim. Acta. 227 (2017) 419–434. doi:10.1016/J.ELECTACTA.2017.01.030.

[217] Q. Meyer, S. Ashton, R. Jervis, D.P. Finegan, P. Boillat, M. Cochet, O. Curnick, T. Reisch, P. Adcock, P.R. Shearing, D.J.L. Brett, The hydro-electro-thermal performance of air-cooled, open-cathode polymer electrolyte fuel cells: Combined localised current density, temperature and water mapping, Electrochim. Acta. 180 (2015) 307–315. doi:10.1016/j.electacta.2015.08.106.

[218] W. Sun, B.A. Peppley, K. Karan, An improved two-dimensional agglomerate cathode model to study the influence of catalyst layer structural parameters, Electrochim. Acta. 50 (2005) 3359–3374. doi:10.1016/j.electacta.2004.12.009.

References

[219] R. Satija, D.L. Jacobson, M. Arif, S.A. Werner, In situ neutron imaging technique for evaluation of water management systems in operating PEM fuel cells, J. Power Sources. 129 (2004) 238–245. doi:10.1016/j.jpowsour.2003.11.068.

[220] Q. Meyer, K. Ronaszegi, J.B. Robinson, M. Noorkami, O. Curnick, S. Ashton, A. Danelyan, T. Reisch, P. Adcock, R. Kraume, P.R. Shearing, D.J.L. Brett, Combined current and temperature mapping in an air-cooled, open-cathode polymer electrolyte fuel cell under steady-state and dynamic conditions, J. Power Sources. 297 (2015) 315–322. doi:10.1016/j.jpowsour.2015.07.069.

[221] N. Khajeh-Hosseini-Dalasm, T. Sasabe, T. Tokumasu, U. Pasaogullari, Effects of polytetrafluoroethylene treatment and compression on gas diffusion layer microstructure using high-resolution X-ray computed tomography, J. Power Sources. 266 (2014) 213–221. doi:10.1016/j.jpowsour.2014.05.004.

[222] J.G. Pharoah, K. Karan, W. Sun, On effective transport coefficients in PEM fuel cell electrodes: Anisotropy of the porous transport layers, J. Power Sources. 161 (2006) 214–224. doi:10.1016/j.jpowsour.2006.03.093.

[223] R. Flückiger, S.A. Freunberger, D. Kramer, A. Wokaun, G.G. Scherer, F.N. Büchi, Anisotropic, effective diffusivity of porous gas diffusion layer materials for PEFC, Electrochim. Acta. 54 (2008) 551–559. doi:10.1016/j.electacta.2008.07.034.

[224] A. Kusoglu, A.M. Karlsson, M.H. Santare, S. Cleghorn, W.B. Johnson, Mechanical response of fuel cell membranes subjected to a hygro-thermal cycle, J. Power Sources. (2006). doi:10.1016/j.jpowsour.2006.05.020.

[225] Y. Tang, M.H. Santare, A.M. Karlsson, S. Cleghorn, W.B. Johnson, Stresses in Proton Exchange Membranes Due to Hygro-Thermal Loading, J. Fuel Cell Sci. Technol. 3 (2006) 119. doi:10.1115/1.2173666.

References

[226] M.D.R. Kok, R. Jervis, T.G. Tranter, M.A. Sadeghi, D.J.L. Brett, P.R. Shearing, J.T. Gostick, Mass transfer in fibrous media with varying anisotropy for flow battery electrodes: Direct numerical simulations with 3D X-ray computed tomography, Chem. Eng. Sci. 196 (2019) 104–115. doi:10.1016/j.ces.2018.10.049.

[227] P. Zhou, C.W. Wu, G.J. Ma, Contact resistance prediction and structure optimization of bipolar plates, J. Power Sources. 159 (2006) 1115–1122. doi:10.1016/j.jpowsour.2005.12.080.

[228] P. Zhou, C.W. Wu, G.J. Ma, Influence of clamping force on the performance of PEMFCs, J. Power Sources. 163 (2007) 874–881. doi:10.1016/j.jpowsour.2006.09.068.

[229] H. Sadeghifar, In-plane and through-plane electrical conductivities and contact resistances of a Mercedes-Benz catalyst-coated membrane, gas diffusion and micro-porous layers and a Ballard graphite bipolar plate: Impact of humidity, compressive load and polytetrafluoroethylene, Energy Convers. Manag. 154 (2017) 191–202. doi:10.1016/j.enconman.2017.10.060.

[230] Y. Zhou, G. Lin, A.J. Shih, S.J. Hu, A micro-scale model for predicting contact resistance between bipolar plate and gas diffusion layer in PEM fuel cells, 163 (2007) 777–783. doi:10.1016/j.jpowsour.2006.09.019.

[231] T. Hottinen, O. Himanen, S. Karvonen, I. Nitta, Inhomogeneous compression of PEMFC gas diffusion layer, J. Power Sources. 171 (2007) 113–121. doi:10.1016/j.jpowsour.2006.10.076.

[232] L. Hao, P. Cheng, Lattice Boltzmann simulations of anisotropic permeabilities in carbon paper gas diffusion layers, J. Power Sources. 186 (2009) 104–114. doi:10.1016/j.jpowsour.2008.09.086.

References

[233] D. Froning, J. Brinkmann, U. Reimer, V. Schmidt, W. Lehnert, D. Stolten, 3D analysis, modeling and simulation of transport processes in compressed fibrous microstructures, using the Lattice Boltzmann method, Electrochim. Acta. 110 (2013) 325–334. doi:10.1016/j.electacta.2013.04.071.

[234] A. Nabovati, J. Hinebaugh, A. Bazylak, C.H. Amon, Effect of porosity heterogeneity on the permeability and tortuosity of gas diffusion layers in polymer electrolyte membrane fuel cells, J. Power Sources. 248 (2014) 83–90. doi:10.1016/j.jpowsour.2013.09.061.

[235] J.T. Gostick, M.W. Fowler, M.D. Pritzker, M.A. Ioannidis, L.M. Behra, In-plane and through-plane gas permeability of carbon fiber electrode backing layers, J. Power Sources. 162 (2006) 228–238. doi:10.1016/j.jpowsour.2006.06.096.

[236] Y. Gao, X. Zhang, P. Rama, R. Chen, H. Ostadi, K. Jiang, Lattice Boltzmann simulation of water and gas flow in porous gas diffusion layers in fuel cells reconstructed from micro-tomography, Comput. Math. with Appl. 65 (2013) 891–900. doi:10.1016/j.camwa.2012.08.006.

[237] T. Koido, T. Furusawa, K. Moriyama, An approach to modeling two-phase transport in the gas diffusion layer of a proton exchange membrane fuel cell, J. Power Sources. 175 (2008) 127–136. doi:10.1016/j.jpowsour.2007.09.029.

[238] J. Lobato, P. Cañizares, M.A. Rodrigo, F.J. Pinar, E. Mena, D. Úbeda, Three-dimensional model of a 50 cm2 high temperature PEM fuel cell. Study of the flow channel geometry influence, Int. J. Hydrogen Energy. 35 (2010) 5510–5520. doi:10.1016/j.ijhydene.2010.02.089.

[239] M. Januszewski, M. Kostur, Sailfish: A flexible multi-GPU implementation of the lattice Boltzmann method, Comput. Phys. Commun. 185 (2014) 2350–2368. doi:10.1016/j.cpc.2014.04.018.

References

[240] N. Djilali, Computational modelling of polymer electrolyte membrane (PEM) fuel cells: Challenges and opportunities, Energy. 32 (2007) 269–280. doi:10.1016/j.energy.2006.08.007.

[241] A.A. Shah, K.H. Luo, T.R. Ralph, F.C. Walsh, Recent trends and developments in polymer electrolyte membrane fuel cell modelling, Electrochim. Acta. 56 (2011) 3731–3757. doi:10.1016/j.electacta.2010.10.046.

[242] A. Boucetta, H. Ghodbane, M.Y. Ayad, M. Bahri, A review on the performance and modelling of proton exchange membrane fuel cells, AIP Conf. Proc. 1758 (2016). doi:10.1063/1.4959415.

[243] L. Xing, Y. Xu, P.K. Das, B. Mao, Q. Xu, H. Su, X. Wu, W. Shi, Numerical matching of anisotropic transport processes in porous electrodes of proton exchange membrane fuel cells, Chem. Eng. Sci. 195 (2019) 127–140. doi:10.1016/J.CES.2018.11.034.

[244] P.K. Das, A. Grippin, A. Kwong, A.Z. Weber, Liquid-Water-Droplet Adhesion-Force Measurements on Fresh and Aged Fuel-Cell Gas-Diffusion Layers, J. Electrochem. Soc. 159 (2012) B489–B496. doi:10.1149/2.052205jes.

[245] P.K. Das, X. Li, Z.S. Liu, Analysis of liquid water transport in cathode catalyst layer of PEM fuel cells, Int. J. Hydrogen Energy. (2010). doi:10.1016/j.ijhydene.2009.12.160.

[246] B. Sivertsen, N. Djilali, CFD-based modelling of proton exchange membrane fuel cells, J. Power Sources. 141 (2005) 65–78. doi:10.1016/j.jpowsour.2004.08.054.

[247] D. Singh, D.M. Lu, N. Djilali, A two-dimensional analysis of mass transport in proton exchange membrane fuel cells, Int. J. Eng. Sci. 37 (1999) 431–452. doi:10.1016/S0020-7225(98)00079-2.

References

[248] W.H.J. Hogarth, J. Steiner, J.B. Benziger, A. Hakenjos, Spatially-resolved current and impedance analysis of a stirred tank reactor and serpentine fuel cell flow-field at low relative humidity, J. Power Sources. 164 (2007) 464–471. doi:10.1016/j.jpowsour.2006.10.103.

[249] C. Siegel, Review of computational heat and mass transfer modeling in polymer-electrolyte-membrane (PEM) fuel cells, Energy. 33 (2008) 1331–1352. doi:10.1016/j.energy.2008.04.015.

[250] L. Xing, X. Liu, T. Alaje, R. Kumar, M. Mamlouk, K. Scott, A two-phase flow and non-isothermal agglomerate model for a proton exchange membrane (PEM) fuel cell, Energy. 73 (2014) 618–634. doi:10.1016/j.energy.2014.06.065.

[251] L. Xing, M. Mamlouk, K. Scott, A two dimensional agglomerate model for a proton exchange membrane fuel cell, Energy. 61 (2013) 196–210. doi:10.1016/j.energy.2013.08.026.

[252] S. Chaudhary, V.K. Sachan, P.K. Bhattacharya, Two dimensional modelling of water uptake in proton exchange membrane fuel cell, Int. J. Hydrogen Energy. 39 (2014) 17802–17818. doi:10.1016/j.ijhydene.2014.08.128.

[253] N. Fouquet, C. Boulet, C. Nouillant, G. Dauphin-Tanguy, B. Oulb-Bouamama, Model based PEM fuel cell state-of-health monitoring via AC impedance measurements, J. Power Sources. 159 (2006) 905–913.

[254] C. Brunetto, A. Moschetto, G. Tina, PEM fuel cell testing by electrochemical impedance spectroscopy, Electr. Power Syst. Res. 79 (2009) 17–26. doi:10.1016/j.epsr.2008.05.012.

[255] D.M. Bernardi, M.W. Verbrugge, Mathematical model of a gas diffusion electrode bonded to a polymer electrolyte, AIChE J. 37 (1991) 1151–1163. http://www.scopus.com/inward/record.url?eid=2-s2.0-

0026204251&partnerID=tZOtx3y1.

[256] J.J. Baschuk, X. Li, A general formulation for a mathematical PEM fuel cell model, J. Power Sources. 142 (2005) 134–153. doi:10.1016/j.jpowsour.2004.09.027.

[257] A.A. Kulikovsky, The effect of non–uniform aging of a polymer electrolyte fuel cell on the polarization curve: A modeling study, Electrochim. Acta. 49 (2004) 617–625. doi:10.1016/j.electacta.2003.09.016.

[258] A.Z. Weber, R.L. Borup, R.M. Darling, P.K. Das, T.J. Dursch, W. Gu, D. Harvey, A. Kusoglu, S. Litster, M.M. Mench, R. Mukundan, J.P. Owejan, J.G. Pharoah, M. Secanell, I. V. Zenyuk, A Critical Review of Modeling Transport Phenomena in Polymer-Electrolyte Fuel Cells, J. Electrochem. Soc. 161 (2014) F1254–F1299. doi:10.1149/2.0751412jes.

[259] J.. Baschuk, X. Li, Modelling of polymer electrolyte membrane fuel cells with variable degrees of water flooding, J. Power Sources. 86 (2000) 181–196. doi:10.1016/S0378-7753(99)00426-7.

[260] E.M. Scattergood, E.N. Lightfoot, Diffusional interaction in an ion-exchange membrane, Trans. Faraday Soc. 64 (1968) 1135. doi:10.1039/tf9686401135.

[261] C. Marr, X. Li, Composition and performance modelling of catalyst layer in a proton exchange membrane fuel cell, J. Power Sources. 77 (1999) 17–27. doi:10.1016/S0378-7753(98)00161-X.

[262] N. Djilali, D. Lu, Influence of heat transfer on gas and water transport in fuel cells, Int. J. Therm. Sci. 41 (2002) 29–40. doi:10.1016/S1290-0729(01)01301-1.

[263] D.S. Falcão, V.B. Oliveira, C.M. Rangel, C. Pinho, A.M.F.R. Pinto, Water transport through a PEM fuel cell: A one-dimensional model with heat transfer

effects, Chem. Eng. Sci. 64 (2009) 2216–2225. doi:10.1016/j.ces.2009.01.049.

[264] D.S. Falcão, P.J. Gomes, V.B. Oliveira, C. Pinho, A.M.F.R. Pinto, 1D and 3D numerical simulations in PEM fuel cells, Int. J. Hydrogen Energy. 36 (2011) 12486–12498. doi:10.1016/j.ijhydene.2011.06.133.

[265] A.A. Kulikovsky, Semi-analytical 1D+1D model of a polymer electrolyte fuel cell, Electrochem. Commun. 6 (2004) 969–977. doi:10.1016/j.elecom.2004.07.009.

[266] T. V. Nguyen, R.E. White, A Water and Heat Management Model for Proton-Exchanae-Membrane Fuel Cells, J. Electrochem. Soc. 140 (1993) 2178–2186. doi:10.1149/1.2220792.

[267] T.F. Fuller, J. Newman, Water and Thermal Management in Solid-Polymer-Electrolyte Fuel Cells, J. Electrochem. Soc. 140 (1993) 1218–1225. doi:10.1149/1.2220960.

[268] J.S. Yi, An Along-the-Channel Model for Proton Exchange Membrane Fuel Cells, J. Electrochem. Soc. 145 (1998) 1149. doi:10.1149/1.1838431.

[269] A. Iranzo, M. Muñoz, F. Rosa, J. Pino, Numerical model for the performance prediction of a PEM fuel cell. Model results and experimental validation, Int. J. Hydrogen Energy. 35 (2010) 11533–11550. doi:10.1016/j.ijhydene.2010.04.129.

[270] A.D. Le, B. Zhou, A general model of proton exchange membrane fuel cell, J. Power Sources. 182 (2008) 197–222. doi:10.1016/j.jpowsour.2008.03.047.

[271] A. Santafé-Moros, Nanofiltration modeling based on the extended Nernst-Planck equation under different physical modes, in: Proc. COMSOL Conf. 2008 Hann., 2008.

[272] P. Mina, P. Schott, J. Pauchet, Computational Analysis of Transport Phenomena

in PEM Fuel Cells with Comsol Multiphysics, (2007).

[273] M.A.R. Sadiq Al-Baghdadi, H.A.K. Shahad Al-Janabi, Parametric and optimization study of a PEM fuel cell performance using three-dimensional computational fluid dynamics model, Renew. Energy. 32 (2007) 1077–1101. doi:10.1016/j.renene.2006.04.018.

[274] M.A.R. Sadiq Al-Baghdadi, A CFD study of hygro–thermal stresses distribution in PEM fuel cell during regular cell operation, Renew. Energy. 34 (2009) 674–682. doi:10.1016/j.renene.2008.05.023.

[275] A. Iranzo, P. Boillat, F. Rosa, Validation of a three dimensional PEM fuel cell CFD model using local liquid water distributions measured with neutron imaging, Int. J. Hydrogen Energy. 39 (2014) 7089–7099. doi:10.1016/j.ijhydene.2014.02.115.

[276] S. Dutta, S. Shimpalee, J.W. Van Zee, Numerical prediction of mass-exchange between cathode and anode channels in a PEM fuel cell, Int. J. Heat Mass Transf. 44 (2001) 2029–2042. doi:10.1016/S0017-9310(00)00257-X.

[277] K.W. Lum, J.J. McGuirk, Three-dimensional model of a complete polymer electrolyte membrane fuel cell – model formulation, validation and parametric studies, J. Power Sources. 143 (2005) 103–124. doi:10.1016/j.jpowsour.2004.11.032.

[278] T. Berning, D.M. Lu, N. Djilali, Three-dimensional computational analysis of transport phenomena in a PEM fuel cell, J. Power Sources. 106 (2002) 284–294. doi:10.1016/S0378-7753(01)01057-6.

[279] M.A.R.S. Al-Baghdadi, H.A.K.S. Al-Janabi, Modeling optimizes PEM fuel cell performance using three-dimensional multi-phase computational fluid dynamics model, Energy Convers. Manag. 48 (2007) 3102–3119.

doi:10.1016/j.enconman.2007.05.007.

[280] B. Dadda, S. Abboudi, A. Ghezal, Transient two-dimensional model of heat and mass transfer in a PEM fuel cell membrane, Int. J. Hydrogen Energy. 38 (2013) 7092–7101. doi:10.1016/j.ijhydene.2013.03.142.

[281] F. Tiss, R. Chouikh, A. Guizani, A numerical investigation of the effects of membrane swelling in polymer electrolyte fuel cells, Energy Convers. Manag. 67 (2013) 318–324. doi:10.1016/j.enconman.2012.12.006.

[282] L. Xing, M. Mamlouk, R. Kumar, K. Scott, Numerical investigation of the optimal Nafion®ionomer content in cathode catalyst layer: An agglomerate two-phase flow modelling, Int. J. Hydrogen Energy. 39 (2014) 9087–9104. doi:10.1016/j.ijhydene.2014.03.225.

[283] A.Z. Weber, J. Newman, Modeling transport in polymer-electrolyte fuel cells, Chem. Rev. 104 (2004) 4679–4726. doi:10.1021/cr020729l.

[284] A.Z. Weber, J. Newman, Transport in Polymer-Electrolyte Membranes I . Physical Model, (2003) 1008–1015. doi:10.1149/1.1580822.

[285] A.Z. Weber, J. Newman, Coupled Thermal and Water Management in Polymer Electrolyte Fuel Cells, (2006). doi:10.1149/1.2352039.

[286] C. Bao, W.G. Bessler, Two-dimensional modeling of a polymer electrolyte membrane fuel cell with long flow channel. Part I. Model development, J. Power Sources. 275 (2015) 922–934. doi:10.1016/j.jpowsour.2014.11.058.

[287] D. Fofana, J. Hamelin, P. Bénard, Modelling and experimental validation of high performance low platinum multilayer cathode for polymer electrolyte membrane fuel cells (PEMFCs), Int. J. Hydrogen Energy. 38 (2013) 10050–10062. doi:10.1016/j.ijhydene.2013.05.175.

References

[288] K. Broka, P. Ekdunge, Modelling the PEM fuel cell cathode, J. Appl. Electrochem. 27 (1997) 281–289. doi:10.1023/A:1018476612810.

[289] W. Sun, B.A. Peppley, K. Karan, Modeling the Influence of GDL and flow-field plate parameters on the reaction distribution in the PEMFC cathode catalyst layer, J. Power Sources. 144 (2005) 42–53. doi:10.1016/j.jpowsour.2004.11.035.

[290] L. Xing, Q. Cai, X. Liu, C. Liu, K. Scott, Y. Yan, Anode partial flooding modelling of proton exchange membrane fuel cells: Optimisation of electrode properties and channel geometries, Chem. Eng. Sci. 146 (2016) 88–103. doi:10.1016/j.ces.2016.02.029.

[291] K.J. Lange, P.-C. Sui, N. Djilali, Determination of effective transport properties in a PEMFC catalyst layer using different reconstruction algorithms, J. Power Sources. 208 (2012) 354–365. doi:10.1016/j.jpowsour.2011.11.001.

[292] L. Xing, P.K. Das, X. Song, M. Mamlouk, K. Scott, Numerical analysis of the optimum membrane/ionomer water content of PEMFCs: The interaction of Nafion® ionomer content and cathode relative humidity, Appl. Energy. 138 (2015) 242–257. doi:10.1016/j.apenergy.2014.10.011.

[293] J. Marquis, M.O. Coppens, Achieving ultra-high platinum utilization via optimization of PEM fuel cell cathode catalyst layer microstructure, Chem. Eng. Sci. 102 (2013) 151–162. doi:10.1016/j.ces.2013.08.003.

[294] H. Ostadi, P. Rama, Y. Liu, R. Chen, X.X. Zhang, K. Jiang, 3D reconstruction of a gas diffusion layer and a microporous layer, J. Memb. Sci. 351 (2010) 69–74. doi:10.1016/j.memsci.2010.01.031.

[295] N. Zamel, X. Li, Effective transport properties for polymer electrolyte membrane fuel cells – With a focus on the gas diffusion layer, Prog. Energy Combust. Sci.

39 (2013) 111–146. doi:10.1016/j.pecs.2012.07.002.

[296] M.S. Ismail, T. Damjanovic, D.B. Ingham, M. Pourkashanian, A. Westwood, Effect of polytetrafluoroethylene-treatment and microporous layer-coating on the electrical conductivity of gas diffusion layers used in proton exchange membrane fuel cells, J. Power Sources. 195 (2010) 2700–2708. doi:10.1016/j.jpowsour.2009.11.069.

[297] J. Becker, R. Flückiger, M. Reum, F.N. Büchi, F. Marone, M. Stampanoni, Determination of Material Properties of Gas Diffusion Layers: Experiments and Simulations Using Phase Contrast Tomograzutatenphic Microscopy, J. Electrochem. Soc. 156 (2009) B1175. doi:10.1149/1.3176876.

[298] Z.Y. Su, C.T. Liu, H.P. Chang, C.H. Li, K.J. Huang, P.C. Sui, A numerical investigation of the effects of compression force on PEM fuel cell performance, J. Power Sources. 183 (2008) 182–192. doi:10.1016/j.jpowsour.2008.04.060.

[299] J.W. Buddenberg, C.R. Wilke, Calculation of Gas Mixture Viscosities., Ind. Eng. Chem. 41 (2005) 1345–1347. doi:10.1021/ie50475a011.

[300] M.M. Tomadakis, T.J. Robertson, Viscous permeability of random fiber structures: Comparison of electrical and diffusional estimates with experimental and analytical results, J. Compos. Mater. 39 (2005) 163–188. doi:10.1177/0021998305046438.

[301] D. Gerteisen, T. Heilmann, C. Ziegler, Modeling the phenomena of dehydration and flooding of a polymer electrolyte membrane fuel cell, J. Power Sources. 187 (2009) 165–181. doi:10.1016/J.JPOWSOUR.2008.10.102.

[302] M. Bosomoiu, G. Tsotridis, T. Bednarek, Study of effective transport properties of fresh and aged gas diffusion layers, J. Power Sources. 285 (2015) 568–579. doi:10.1016/j.jpowsour.2015.03.132.

References

[303] F.C. Cetinbas, S.G. Advani, A.K. Prasad, Optimization of polymer electrolyte membrane fuel cell catalyst layer with bidirectionally-graded composition, Electrochim. Acta. 174 (2015) 787–798. doi:10.1016/j.electacta.2015.06.056.

[304] G. He, Y. Yamazaki, A. Abudula, A three-dimensional analysis of the effect of anisotropic gas diffusion layer(GDL) thermal conductivity on the heat transfer and two-phase behavior in a proton exchange membrane fuel cell(PEMFC), J. Power Sources. 195 (2010) 1551–1560. doi:10.1016/j.jpowsour.2009.09.059.

[305] S. Mazumder, J.V. Cole, Rigorous 3-D Mathematical Modeling of PEM Fuel Cells, J. Electrochem. Soc. 150 (2003) A1510. doi:10.1149/1.1615609.

[306] S. Shimpalee, P. Satjaritanun, S. Hirano, N. Tippayawong, J.W. Weidner, Multiscale Modeling of PEMFC Using Co-Simulation Approach, J. Electrochem. Soc. 166 (2019) F534–F543. doi:10.1149/2.0291911jes.

[307] M. Mehrtash, I. Tari, S. Yesilyurt, Impacts of inhomogeneous clamping force on local performance and liquid water formation in polymer electrolyte fuel cells, Int. J. Hydrogen Energy. 42 (2017) 19227–19245. doi:10.1016/j.ijhydene.2017.06.139.

[308] Y. Zhou, G. Lin, A.J. Shih, S.J. Hu, Assembly pressure and membrane swelling in PEM fuel cells, J. Power Sources. 192 (2009) 544–551. doi:10.1016/j.jpowsour.2009.01.085.

[309] E.C. Kumbur, K.V. Sharp, M.M. Mench, On the effectiveness of Leverett approach for describing the water transport in fuel cell diffusion media, J. Power Sources. 168 (2007) 356–368. doi:10.1016/j.jpowsour.2007.02.054.

[310] E.C. Kumbur, K. V. Sharp, M.M. Mench, Validated Leverett Approach for Multiphase Flow in PEFC Diffusion Media, J. Electrochem. Soc. 154 (2007) B1315. doi:10.1149/1.2784286.

References

[311] J.T. Gostick, M.A. Ioannidis, M.W. Fowler, M.D. Pritzker, Pore network modeling of fibrous gas diffusion layers for polymer electrolyte membrane fuel cells, J. Power Sources. 173 (2007) 277–290. doi:10.1016/j.jpowsour.2007.04.059.

[312] Y. Wang, C.-Y. Wang, A Nonisothermal, Two-Phase Model for Polymer Electrolyte Fuel Cells, J. Electrochem. Soc. 153 (2006) A1193. doi:10.1149/1.2193403.

[313] P.K. Sinha, C.-Y. Wang, Pore-network modeling of liquid water transport in gas diffusion layer of a polymer electrolyte fuel cell, Electrochim. Acta. 52 (2007) 7936–7945. doi:10.1016/j.electacta.2007.06.061.

[314] X. Wang, T. Van Nguyen, Modeling the Effects of Capillary Property of Porous Media on the Performance of the Cathode of a PEMFC, J. Electrochem. Soc. 155 (2008) B1085. doi:10.1149/1.2965512.

[315] P.K. Das, X. Li, Z.S. Liu, Analysis of liquid water transport in cathode catalyst layer of PEM fuel cells, Int. J. Hydrogen Energy. 35 (2010) 2403–2416. doi:10.1016/j.ijhydene.2009.12.160.

[316] C.-Y. Jung, W.-J. Kim, S.-C. Yi, Computational analysis of mixed potential effect in proton exchange membrane fuel cells, Int. J. Hydrogen Energy. 37 (2012) 7654–7668. doi:10.1016/J.IJHYDENE.2012.01.102.

[317] L. Xing, Modelling and Simulation of the Laboratory Low Temperature Proton Exchange Membrane and Direct Methanol Fuel Cells, (2014).

[318] M.-S. Chiang, H.-S. Chu, Numerical investigation of transport component design effect on a proton exchange membrane fuel cell, J. Power Sources. 160 (2006) 340–352. doi:10.1016/j.jpowsour.2006.01.086.

[319] F. Hashemi, S. Rowshanzamir, M. Rezakazemi, CFD simulation of PEM fuel cell performance: Effect of straight and serpentine flow fields, Math. Comput. Model.

55 (2012) 1540–1557. doi:10.1016/j.mcm.2011.10.047.

[320] H.K. Esfeh, A. Azarafza, M.K.A. Hamid, On the computational fluid dynamics of PEM fuel cells (PEMFCs): an investigation on mesh independence analysis, RSC Adv. 7 (2017) 32893–32902. doi:10.1039/C7RA03236F.

[321] J. Wang, J. Yuan, B. Sundén, Modeling of inhomogeneous compression effects of porous GDL on transport phenomena and performance in PEM fuel cells, Int. J. Energy Res. 41 (2017) 985–1003. doi:10.1002/er.3687.

[322] S. Basu, C.-Y. Wang, K.S. Chen, Phase Change in a Polymer Electrolyte Fuel Cell, J. Electrochem. Soc. 156 (2009) B748. doi:10.1149/1.3115470.

[323] Y. Wang, K.S. Chen, Effect of Spatially-Varying GDL Properties and Land Compression on Water Distribution in PEM Fuel Cells, J. Electrochem. Soc. 158 (2011) B1292. doi:10.1149/2.015111jes.

[324] P.K. Das, X. Li, Z.S. Liu, Effective transport coefficients in PEM fuel cell catalyst and gas diffusion layers: Beyond Bruggeman approximation, Appl. Energy. 87 (2010) 2785–2796. doi:10.1016/j.apenergy.2009.05.006.

[325] T.A. Trabold, J.P. Owejan, D.L. Jacobson, M. Arif, P.R. Huffman, In situ investigation of water transport in an operating PEM fuel cell using neutron radiography: Part 1 – Experimental method and serpentine flow field results, Int. J. Heat Mass Transf. 49 (2006) 4712–4720. doi:10.1016/j.ijheatmasstransfer.2006.07.003.

[326] S. Gößling, M. Klages, J. Haußmann, P. Beckhaus, M. Messerschmidt, T. Arlt, N. Kardjilov, I. Manke, J. Scholta, A. Heinzel, Analysis of liquid water formation in polymer electrolyte membrane (PEM) fuel cell flow fields with a dry cathode supply, J. Power Sources. 306 (2016) 658–665. doi:10.1016/j.jpowsour.2015.12.060.

References

[327] J.B. Siegel, S. V. Bohac, A.G. Stefanopoulou, S. Yesilyurt, Nitrogen front evolution in purged polymer electrolyte membrane fuel cell with dead-ended anode, J. Electrochem. Soc. 157 (2010) B1081. doi:10.1149/1.3425743.

[328] C. Tötzke, I. Manke, A. Hilger, G. Choinka, N. Kardjilov, T. Arlt, H. Markötter, A. Schröder, K. Wippermann, D. Stolten, C. Hartnig, P. Krüger, R. Kuhn, J. Banhart, Large area high resolution neutron imaging detector for fuel cell research, J. Power Sources. 196 (2011) 4631–4637. doi:10.1016/j.jpowsour.2011.01.049.

[329] A. Bazylak, Liquid water visualization in PEM fuel cells: A review, Int. J. Hydrogen Energy. 34 (2009) 3845–3857. doi:10.1016/j.ijhydene.2009.02.084.

[330] N. Kardjilov, A. Hilger, I. Manke, R. Woracek, J. Banhart, CONRAD-2: the new neutron imaging instrument at the Helmholtz-Zentrum Berlin, J. Appl. Crystallogr. 49 (2016) 195–202. doi:10.1107/s1600576715023353.

[331] P. Boillat, D. Kramer, B.C. Seyfang, G. Frei, E. Lehmann, G.G. Scherer, A. Wokaun, Y. Ichikawa, Y. Tasaki, K. Shinohara, In situ observation of the water distribution across a PEFC using high resolution neutron radiography, Electrochem. Commun. 10 (2008) 546–550. doi:10.1016/j.elecom.2008.01.018.

[332] D. Muirhead, R. Banerjee, M.G. George, N. Ge, P. Shrestha, H. Liu, J. Lee, A. Bazylak, Liquid water saturation and oxygen transport resistance in polymer electrolyte membrane fuel cell gas diffusion layers, Electrochim. Acta. 274 (2018) 250–265. doi:10.1016/j.electacta.2018.04.050.

[333] J. Lee, S. Chevalier, R. Banerjee, P. Antonacci, N. Ge, R. Yip, T. Kotaka, Y. Tabuchi, A. Bazylak, Investigating the effects of gas diffusion layer substrate thickness on polymer electrolyte membrane fuel cell performance via synchrotron X-ray radiography, Electrochim. Acta. 236 (2017) 161–170. doi:10.1016/j.electacta.2017.03.162.

[334] C. Hartnig, I. Manke, N. Kardjilov, A. Hilger, M. Grünerbel, J. Kaczerowski, J. Banhart, W. Lehnert, Combined neutron radiography and locally resolved current density measurements of operating PEM fuel cells, J. Power Sources. 176 (2008) 452–459. doi:10.1016/j.jpowsour.2007.08.058.

[335] M. Klages, S. Enz, H. Markötter, I. Manke, N. Kardjilov, J. Scholta, Investigations on dynamic water transport characteristics in flow field channels using neutron imaging techniques, J. Power Sources. 239 (2013) 596–603. doi:10.1016/j.jpowsour.2013.01.196.

[336] J.M. LaManna, S. Chakraborty, J.J. Gagliardo, M.M. Mench, Isolation of transport mechanisms in PEFCs using high resolution neutron imaging, Int. J. Hydrogen Energy. 39 (2014) 3387–3396. doi:10.1016/j.ijhydene.2013.12.021.

[337] T. Hellstern, E. Gauthier, M.J. Cheah, J.B. Benziger, The role of the gas diffusion layer on slug formation in gas flow channels of fuel cells, Int. J. Hydrogen Energy. 38 (2013) 15414–15427. doi:10.1016/j.ijhydene.2013.09.073.

[338] B.S. Machado, N. Chakraborty, P.K. Das, Influences of flow direction, temperature and relative humidity on the performance of a representative anion exchange membrane fuel cell: A computational analysis, Int. J. Hydrogen Energy. 42 (2017) 6310–6323. doi:10.1016/j.ijhydene.2016.12.003.

[339] S.-H. Ge, B.-L. Yi, A mathematical model for PEMFC in different flow modes, J. Power Sources. 124 (2003) 1–11. doi:10.1016/S0378-7753(03)00584-6.

[340] Z. Lu, C. Rath, G. Zhang, S.G. Kandlikar, Water management studies in PEM fuel cells, part IV: Effects of channel surface wettability, geometry and orientation on the two-phase flow in parallel gas channels, Int. J. Hydrogen Energy. 36 (2011) 9864–9875. doi:10.1016/j.ijhydene.2011.04.226.

[341] C.R. Buie, J.D. Posner, T. Fabian, S.-W. Cha, D. Kim, F.B. Prinz, J.K. Eaton,

J.G. Santiago, Water management in proton exchange membrane fuel cells using integrated electroosmotic pumping, J. Power Sources. 161 (2006) 191–202. doi:10.1016/j.jpowsour.2006.03.021.

[342] S. Shahsavari, A. Desouza, M. Bahrami, E. Kjeang, Thermal analysis of air-cooled PEM fuel cells, Int. J. Hydrogen Energy. 37 (2012) 18261–18271. doi:10.1016/j.ijhydene.2012.09.075.

[343] D.J.L. Brett, S. Atkins, N.P. Brandon, N. Vasileiadis, V. Vesovic, A.R. Kucernak, Membrane resistance and current distribution measurements under various operating conditions in a polymer electrolyte fuel cell, J. Power Sources. 172 (2007) 2–13. doi:10.1016/j.jpowsour.2007.05.071.

[344] V.N. Duy, J. Lee, K. Kim, J. Ahn, S. Park, T. Kim, H.M. Kim, Dynamic simulations of under-rib convection-driven flow-field configurations and comparison with experiment in polymer electrolyte membrane fuel cells, J. Power Sources. 293 (2015) 447–457. doi:10.1016/j.jpowsour.2015.05.107.

[345] A. Manokaran, S. Pushpavanam, P. Sridhar, S. Pitchumani, Experimental analysis of spatio-temporal behavior of anodic dead-end mode operated polymer electrolyte fuel cell, J. Power Sources. 196 (2011) 9931–9938. doi:10.1016/j.jpowsour.2011.06.103.

[346] J.B. Siegel, Experiments and Modeling of PEM Fuel Cells for Dead-Ended Anode Operation, (2010).

[347] H. Mahyari, H. Hassanzadeh, M. Shams, Three dimensional transient multiphase fl ow simulation in a dead end anode polymer electrolyte fuel cell, J. Mol. Liq. 225 (2017) 391–405. doi:10.1016/j.molliq.2016.11.063.

[348] Y.S. Chen, C.W. Yang, J.Y. Lee, Implementation and evaluation for anode purging of a fuel cell based on nitrogen concentration, Appl. Energy. 113 (2014)

1519–1524. doi:10.1016/j.apenergy.2013.09.028.

[349] J. Chen, J.B. Siegel, A.G. Stefanopoulou, Nitrogen blanketing front equilibria in dead end anode fuel cell operation, Proc. 2011 Am. Control Conf. (2011) 1524–1529. http://ieeexplore.ieee.org/stamp/stamp.jsp?arnumber=5991552.

[350] S. Abbou, J. Dillet, G. Maranzana, S. Didierjean, O. Lottin, Local potential evolutions during proton exchange membrane fuel cell operation with dead-ended anode – Part I: Impact of water diffusion and nitrogen crossover, J. Power Sources. 340 (2017) 337–346. doi:10.1016/j.jpowsour.2016.11.079.

[351] K.K. Poornesh, Y.-J. Sohn, G.-G. Park, T.-H. Yang, Gas-diffusion layer's structural anisotropy induced localized instability of nafion membrane in polymer electrolyte fuel cell, Int. J. Hydrogen Energy. 37 (2012) 15339–15349. doi:10.1016/j.ijhydene.2012.04.154.

[352] J.B. Siegel, A.G. Stefanopoulou, Modeling and experiments of voltage transients of polymer electrolyte membrane fuel cells with the dead-ended anode, 9 (2012) 1–7. doi:10.1115/1.4005626.

[353] M. Klages, S. Enz, H. Markötter, I. Manke, N. Kardjilov, J. Scholta, Investigations on dynamic water transport characteristics in flow field channels using neutron imaging techniques, J. Power Sources. 239 (2013) 596–603. doi:10.1016/j.jpowsour.2013.01.196.

[354] C.Y. Jung, C.S. Lee, S.C. Yi, Computational analysis of transport phenomena in proton exchange membrane for polymer electrolyte fuel cells, J. Memb. Sci. 309 (2008) 1–6. doi:10.1016/j.memsci.2007.10.017.

[355] G.-S. Kim, P.C. Sui, A.A. Shah, N. Djilali, Reduced-dimensional models for straight-channel proton exchange membrane fuel cells, J. Power Sources. 195 (2010) 3240–3249. doi:10.1016/j.jpowsour.2009.11.110.

References

[356] J. Zhang, PEM fuel cell electrocatalysts and catalyst layers: Fundamentals and applications, PEM Fuel Cell Electrocatal. Catal. Layers Fundam. Appl. (2008) 1–1137. doi:10.1007/978-1-84800-936-3.

[357] N. Jung, D.Y. Chung, J. Ryu, S.J. Yoo, Y.-E. Sung, Pt-based nanoarchitecture and catalyst design for fuel cell applications, Nano Today. 9 (2014) 433–456. doi:10.1016/j.nantod.2014.06.006.

[358] D. Voiry, M. Chhowalla, Y. Gogotsi, N.A. Kotov, Y. Li, R.M. Penner, R.E. Schaak, P.S. Weiss, Best Practices for Reporting Electrocatalytic Performance of Nanomaterials, ACS Nano. 12 (2018) 9635–9638. doi:10.1021/acsnano.8b07700.

[359] A. Pozio, M. De Francesco, A. Cemmi, F. Cardellini, L. Giorgi, Comparison of high surface Pt/C catalysts by cyclic voltammetry, J. Power Sources. 105 (2002) 13–19. doi:10.1016/S0378-7753(01)00921-1.

[360] Z. Wu, P. Pei, H. Xu, X. Jia, P. Ren, B. Wang, Study on the effect of membrane electrode assembly parameters on polymer electrolyte membrane fuel cell performance by galvanostatic charging method, Appl. Energy. 251 (2019) 113320. doi:10.1016/j.apenergy.2019.113320.

[361] R. Borup, J. Meyers, B. Pivovar, Y.S. Kim, R. Mukundan, N. Garland, D. Myers, M. Wilson, F. Garzon, D. Wood, P. Zelenay, K. More, K. Stroh, T. Zawodzinski, J. Boncella, J.E. McGrath, M. Inaba, K. Miyatake, M. Hori, K. Ota, Z. Ogumi, S. Miyata, A. Nishikata, Z. Siroma, Y. Uchimoto, K. Yasuda, K.I. Kimijima, N. Iwashita, Scientific aspects of polymer electrolyte fuel cell durability and degradation, Chem. Rev. 107 (2007) 3904–3951. doi:10.1021/cr050182l.

[362] R.L. Borup, J.R. Davey, F.H. Garzon, D.L. Wood, M.A. Inbody, PEM fuel cell electrocatalyst durability measurements, J. Power Sources. 163 (2006) 76–81. doi:10.1016/j.jpowsour.2006.03.009.

References

[363] J. Xie, D.L. Wood, D.M. Wayne, T.A. Zawodzinski, P. Atanassov, R.L. Borup, Durability of PEFCs at High Humidity Conditions, J. Electrochem. Soc. 152 (2005) A104. doi:10.1149/1.1830355.

[364] J. Xie, D.L. Wood, K.L. More, P. Atanassov, R.L. Borup, Microstructural Changes of Membrane Electrode Assemblies during PEFC Durability Testing at High Humidity Conditions, J. Electrochem. Soc. 152 (2005) A1011. doi:10.1149/1.1873492.

[365] J.C. Meier, C. Galeano, I. Katsounaros, J. Witte, H.J. Bongard, A.A. Topalov, C. Baldizzone, S. Mezzavilla, F. Schüth, K.J.J. Mayrhofer, Design criteria for stable Pt/C fuel cell catalysts, Beilstein J. Nanotechnol. 5 (2014) 44–67. doi:10.3762/bjnano.5.5.

[366] R.T. White, A. Wu, M. Najm, F.P. Orfino, M. Dutta, E. Kjeang, 4D in situ visualization of electrode morphology changes during accelerated degradation in fuel cells by X-ray computed tomography, J. Power Sources. 350 (2017) 94–102. doi:10.1016/j.jpowsour.2017.03.058.

[367] L. Castanheira, L. Dubau, M. Mermoux, G. Berthomé, N. Caqué, E. Rossinot, M. Chatenet, F. Maillard, Carbon corrosion in proton-exchange membrane fuel cells: From model experiments to real-life operation in membrane electrode assemblies, ACS Catal. 4 (2014) 2258–2267. doi:10.1021/cs500449q.

[368] N. Macauley, D.D. Papadias, J. Fairweather, D. Spernjak, D. Langlois, R. Ahluwalia, K.L. More, R. Mukundan, R.L. Borup, Carbon corrosion in PEM fuel cells and the development of accelerated stress tests, J. Electrochem. Soc. 165 (2018) F3148–F3160. doi:10.1149/2.0061806jes.

[369] X. Zhang, Y. Yang, L. Guo, H. Liu, Effects of carbon corrosion on mass transfer losses in proton exchange membrane fuel cells, Int. J. Hydrogen Energy. 42 (2017) 4699–4705. doi:10.1016/j.ijhydene.2016.08.223.

References

[370] T.W. Patterson, R.M. Darling, Damage to the cathode catalyst of a PEM fuel cell caused by localized fuel starvation, Electrochem. Solid-State Lett. 9 (2006) 183–185. doi:10.1149/1.2167930.

[371] M.F. Chinannai, J. Lee, H. Ju, Numerical study for diagnosing various malfunctioning modes in PEM fuel cell systems, Int. J. Hydrogen Energy. (2019). doi:10.1016/j.ijhydene.2019.07.126.

[372] D.A. Stevens, M.T. Hicks, G.M. Haugen, J.R. Dahn, Ex situ and in situ stability studies of PEMFC catalysts effect of carbon type and humidification on degradation of the carbon, J. Electrochem. Soc. 152 (2005) 2309–2315. doi:10.1149/1.2097361.

[373] X. Cheng, Z. Shi, N. Glass, L. Zhang, J. Zhang, D. Song, Z.-S. Liu, H. Wang, J. Shen, A review of PEM hydrogen fuel cell contamination: Impacts, mechanisms, and mitigation, J. Power Sources. 165 (2007) 739–756. doi:10.1016/j.jpowsour.2006.12.012.

[374] G.A. Camara, E.A. Ticianelli, S. Mukerjee, S.J. Lee, J. McBreen, The CO poisoning mechanism of the hydrogen oxidation reaction in proton exchange membrane fuel cells, J. Electrochem. Soc. 149 (2002) 748–753. doi:10.1149/1.1473775.

[375] R.K. Ahluwalia, X. Wang, Effect of CO and CO2 impurities on performance of direct hydrogen polymer-electrolyte fuel cells, J. Power Sources. 180 (2008) 122–131. doi:10.1016/j.jpowsour.2008.01.087.

[376] D.H. Ye, Z.G. Zhan, Y.J. Lee, Z.K. Tu, Y. Zhang, M. Pan, Effects of frame materials and structures on stress concentration of membrane electrode assembly of PEMFCs, Fuel Cells. 13 (2013) 1205–1212. doi:10.1002/fuce.201300073.

References

[377] D. Liu, X. Lai, J. Ni, L. Peng, S. Lan, Z. Lin, Robust design of assembly parameters on membrane electrode assembly pressure distribution, J. Power Sources. 172 (2007) 760–767. doi:10.1016/j.jpowsour.2007.05.066.

[378] L. Peng, P. Yi, X. Lai, Design and manufacturing of stainless steel bipolar plates for proton exchange membrane fuel cells, Int. J. Hydrogen Energy. 39 (2014) 21127–21153. doi:10.1016/j.ijhydene.2014.08.113.

[379] D. Qiu, P. Yi, L. Peng, X. Lai, Channel Dimensional Error Effect of Stamped Bipolar Plates on the Characteristics of Gas Diffusion Layer Contact Pressure for Proton Exchange Membrane Fuel Cell Stacks, J. Fuel Cell Sci. Technol. 12 (2015) 041002. doi:10.1115/1.4030513.

[380] F. Dundar, E. Dur, S. Mahabunphachai, M. Koç, Corrosion resistance characteristics of stamped and hydroformed proton exchange membrane fuel cell metallic bipolar plates, J. Power Sources. 195 (2010) 3546–3552. doi:10.1016/j.jpowsour.2009.12.040.

[381] R. Banan, J. Zu, A. Bazylak, Humidity and temperature cycling effects on cracks and delaminations in PEMFCs, Fuel Cells. 15 (2015) 327–336. doi:10.1002/fuce.201400118.

[382] D. Qiu, P. Yi, L. Peng, X. Lai, Assembly design of proton exchange membrane fuel cell stack with stamped metallic bipolar plates, Int. J. Hydrogen Energy. 40 (2015) 11559–11568. doi:10.1016/j.ijhydene.2015.03.064.

[383] J. Wang, H. Wang, Y. Fan, Techno-Economic Challenges of Fuel Cell Commercialization, Engineering. 4 (2018) 352–360. doi:10.1016/j.eng.2018.05.007.

[384] R. Solasi, Y. Zou, X. Huang, K. Reifsnider, D. Condit, On mechanical behavior and in-plane modeling of constrained PEM fuel cell membranes subjected to

hydration and temperature cycles, J. Power Sources. 167 (2007) 366–377. doi:10.1016/j.jpowsour.2007.02.025.

[385] D. Liu, L. Peng, X. Lai, Effect of assembly error of bipolar plate on the contact pressure distribution and stress failure of membrane electrode assembly in proton exchange membrane fuel cell, J. Power Sources. 195 (2010) 4213–4221. doi:10.1016/j.jpowsour.2009.12.113.

Appendix A: The effect of catalytic factors on PEFC performance

The catalytic factors define the electrochemical performance of the fuel cell. This section discusses the critical catalytic factors and how they alter/impact fuel cell operations.

A.1 Activation barrier and electrode materials

To reduce activation losses, the activation energy barrier (E_0) has to be reduced by offering an adequate surface for reaction and stabilising the transition state. The strength of bonds between the catalyst and the absorbed species is the key factor while selecting the suitable catalyst (Figure A-1(b)). The bond strength needs to be strong enough to hold the reactant species to the catalyst layer, increasing reaction sites, but weak enough to break to form the product. This phenomenon is known as the 'Sabatier principle', which is often illustrated by the volcano plot with Pt group metals, generally having the optimal medium-strength bonds. For example, for Pt/C electrode HOR exchange current density is several orders larger than ORR; however, ORR shows higher exchange current density on Pt/C electrode than on Au electrode. Therefore, electrode material and/on catalysts have a substantial effect on the ORR.

Table A-1- ORR exchange current densities on various electrode material. Adapted from [356]

Electrode material/ catalyst	**ORR exchange current density, [A cm^{-2}]**	**Electron transfer co-efficiency**
Pt	2.8× 10^{-7}	0.48
PtO/Pt	1.7× 10^{-10}	0.46
PtFe/C	2.15× 10^{-7}	0.55

PtW_2C/C	4.7×10^{-5}	0.47

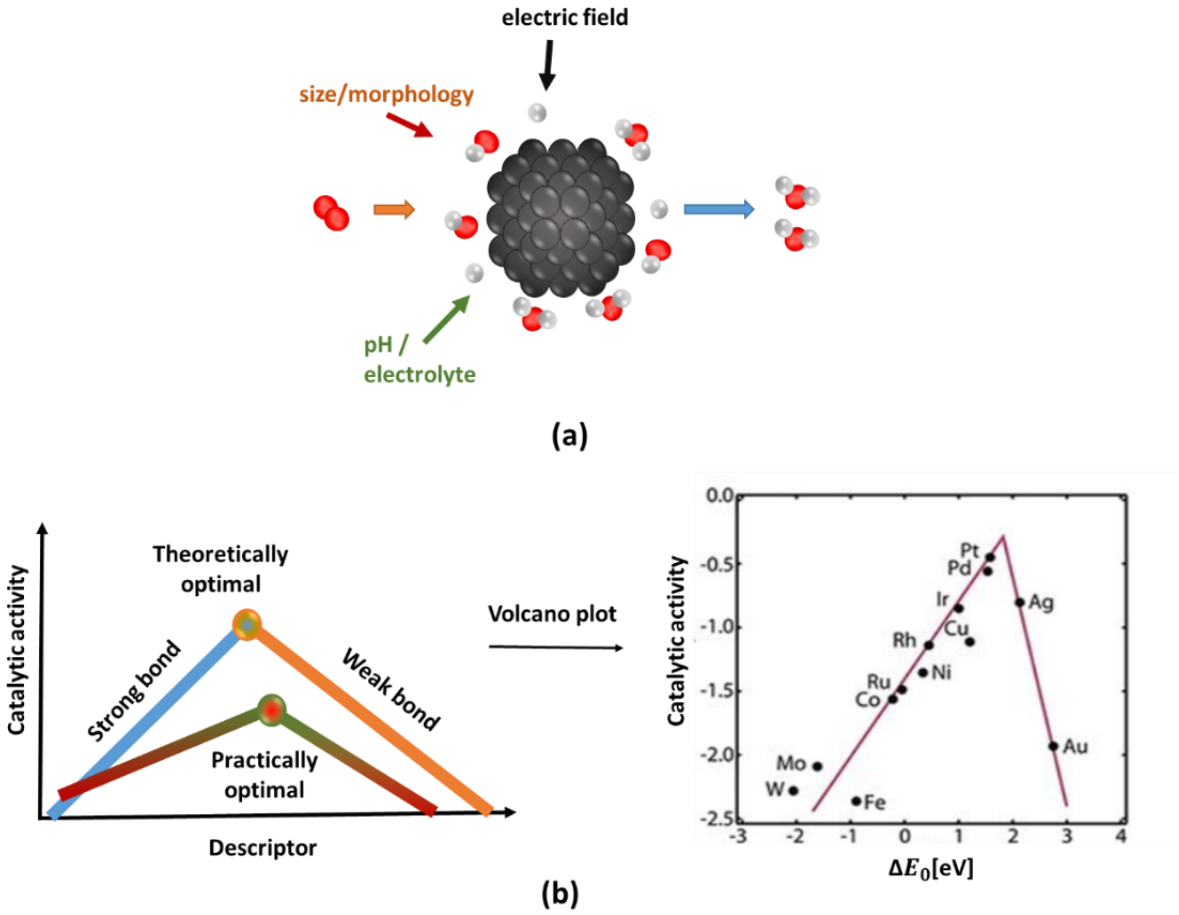

Figure A-1 (a) Schematic of catalyst morphology with respect to the Sabatier principle, (b) Sabatier-type volcano plots. The blue and orange lines represent the theoretical approach based only on the adsorption strength of the reactant species to the catalyst surface. The red-green lines represent the practical approach considering the effect of catalyst composition and morphology, environment, and (c) volcano plot of the activity of various transition metals for the ORR, as a function of the binding energy of oxygen atom to the catalyst. From [357]

A.2 Surface roughness

The catalytic activity of Pt is generally characterised by electrochemically active surface area (ECSA) [358,359]. ECSA is associated with charges of hydrogen adsorption, Q_h $[\mathrm{m^2 g^{-1}}]$, and calculated as [360],

$$ECSA = \frac{Q_H}{0.21 \times m_{pt} \times A_{MEA}} \quad \text{(A.1)}$$

Where 0.21 is hydrogen adsorption charges on the smooth Pt electrode $[\mathrm{mC\ cm^{-2}}]$, m_{pt} $[\mathrm{mg\ cm^{-2}}]$ is the Pt loading on the catalyst layer, A_{MEA} $[\mathrm{cm^2}]$; is the geometric area of the MEA. Increase in electrochemically active surface area (ECSA) of the catalyst is equivalent to increasing surface roughness factor, *RF*. With an increase in surface roughness, the number of active surface sites for the electrochemical reaction increases, increasing exchange-current density.

The catalytic activity, RF, and durability can be enhanced by evenly dispersing fine nano-particles of Pt or Pt group alloys (PGM) over the carbon support structure such as carbon nanotubes (CNTs), carbon nanofibers (CNFs), and graphene [357]. Typically, the optimum Pt particle size reported in the literature varies between 2 to 6 nm [361]. The study by Borup et al. showed that the Pt particle grows in size during cyclic testing. X-ray diffraction (XRD) analysis to evaluate the degree of electrocatalyst sintering showed that the growth of cathode Pt particle size depends on operating temperature, test length and the potential. During steady-state testing, the particle size grew from about 1.9 nm to 3.1 nm over 3500 h testing; whereas, the durability test showed the growth of Pt particles from 1.9 nm to 3.5 nm during the drive cycle experiment of 1200 h [362]. The morphological changes within the CLs lead on to a gradual decrease in the ECSA. Though this phenomenon is observed at both the anode and the cathode CLs, presence of liquid water at the cathode CL facilitate the

primary corrosion and promotes extensive degradation of CLs [363,364] as shown in Figure A-2.

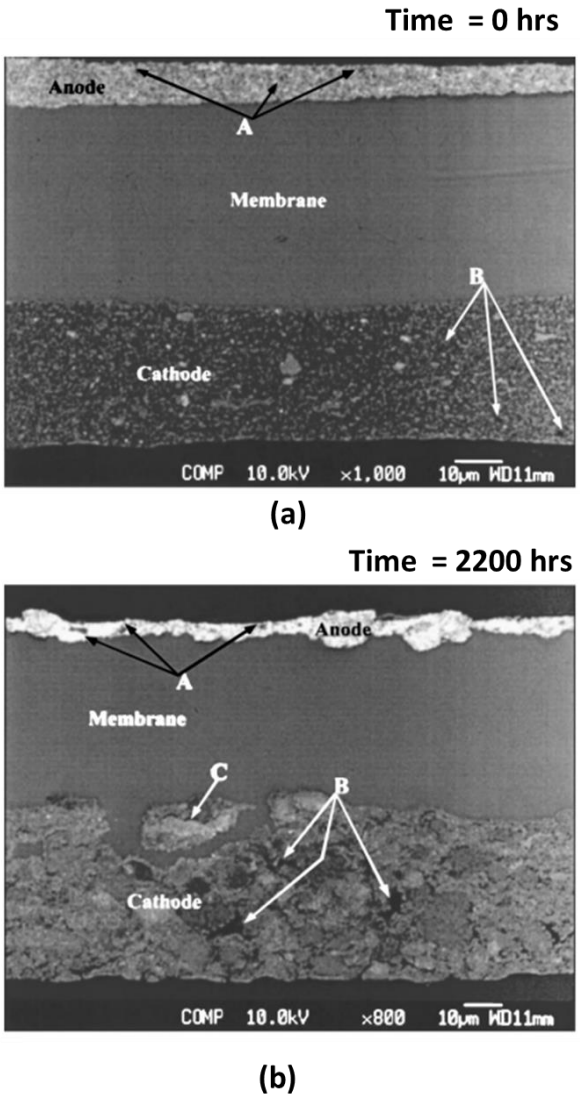

Figure A-2–SEM image of CL cross-section for Pt/C CL and Nafion membrane, (a) cross-section of fresh MEA before testing, (b) cross-section of MEA after 2200 h life test with arrows denoted as ‘A’ and ‘B’ showing catalyst agglomeration/growth in the anode and cathode catalyst layers, respectively. Arrow denoted as C shows a segment of the catalyst layer that has been detached. [363]

The mechanisms for nanoparticle growth include local coalescence of agglomerated particles [301], agglomeration of nonadjacent crystallites via Pt particle migration [364], Ostwald ripening [27], Particle detachment [363,364] and dissolution of the catalyst and subsequent precipitation of platinum[27]. (Figure A-3)

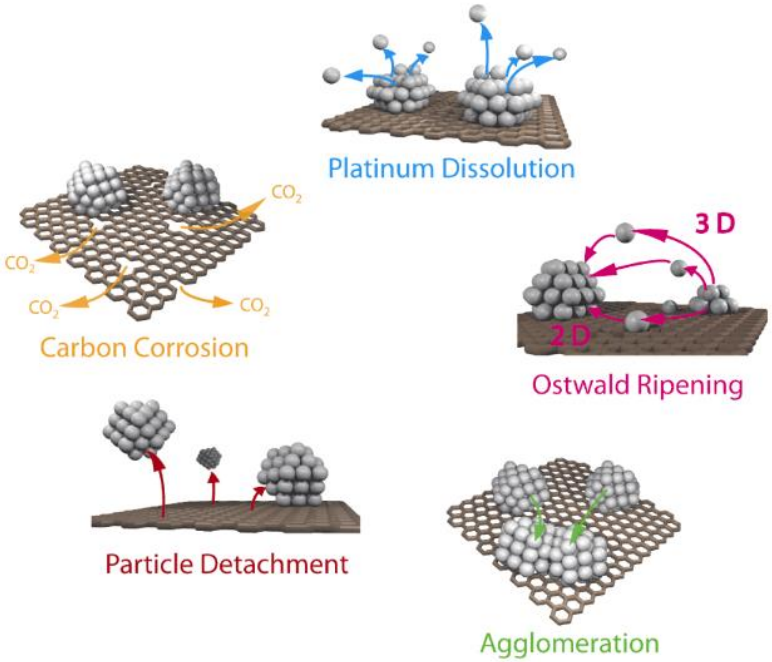

Figure A-3–Simplified schematic showing the degradation mechanism for Pt particles on carbon support in fuel cells. [365]

A.3 Catalytic corrosion

Carbon corrosion in Pt/C catalyst layers has been recognized as one of significant fuel cell degradation mechanisms, and much effort has been devoted to understanding the

process of carbon corrosion and its detrimental consequences [93,366,367]. The cathode CL is particularly susceptible to carbon corrosion causing performance degradation due to both losses in the kinetics of the oxygen reduction reaction (ORR) and losses in oxygen mass transport [368].

The standard potential for the corrosion of carbon is 0.207 V. Reactant gases (H_2 in this case) is utilised to draw the current when the anode potential is below 0.207 V; however, when it grows above 0.207 V, carbon corrosion in the anode catalyst layer occurs to supply protons to support the current requirement [369]. The chemical equation for carbon corrosion is as follows,

$$C + 2H_2O \rightarrow CO_2 + 4H^+ + 4e^- \quad \text{(A.2)}$$

The key factors initiating and promoting carbon corrosion is a reverse current that occurs during frequent start-up and shutdown of the device [27,367], localised anode flooding, i.e. water management, fuel starvation due to uneven reactant distribution and the mode of operation (see section 2.3.5 discussing the effect of mode of operation) [370]. Corrosion of carbon support in CL causes detachment of Pt nanoparticles (Figure A-4), migration, agglomeration and severe reduction in ECSA [363]. Therefore, the carbon corrosion in the cathode can lead to performance loss due to loss of ECSA [371], decreased electrical connectivity of the catalyst support structure within the electrode [368], and alteration of pore morphology and pore surface characteristics [365]. 4D X-ray CT study by White et al. highlighted the change on mud-crack morphology of Pt/C catalyst layer and an increase in the crack width, over the 550 operating cycles and a gradual loss of catalyst layer thickness up to 60% highlighting the extent of carbon corrosion (Figure A-4) [366].

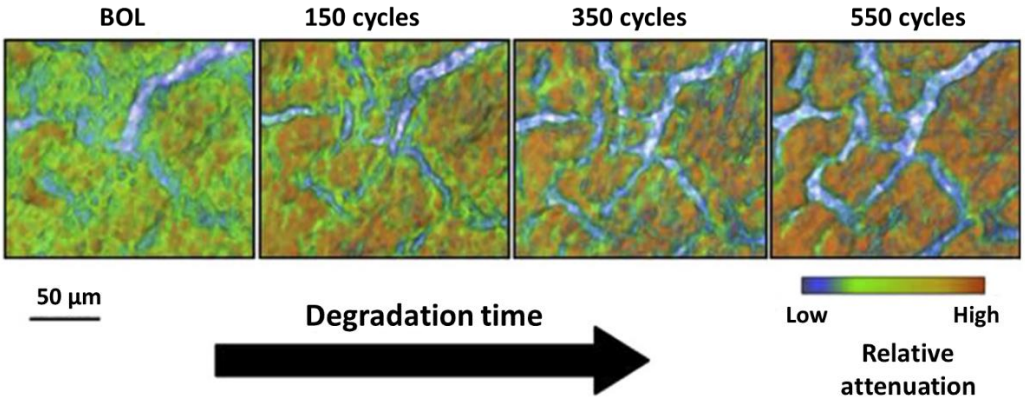

Figure A-4– Crack propagation in Pt/C cathode CL over 550 accelerated cell testing (AST) cycles. Here BOL stands for the beginning of life. Segmented 4D x-ray CT cathode catalyst layer averaged through its thickness shows the propagation of CL cracks overt 550 AST cycles. (Adapted from [366])

For low-temperature automotive PEFCs, an alteration of the operating parameters such as fixed current density and flow rates, effective water management and a reactant delivery system is suggested as the mitigation strategies to improve the durability of the cell, underlining the importance of the operating parameter and the fuel cell architecture on carbon corrosion [368]. Also, the graphitisation of carbon supports is suggested as one method to improve thermal stability under such conditions maintained [372].

A.4 The composition of reformate

The purity of the reformate reactant coming out of the reformer, in this case, purity of H_2, depends on the type of fuel, type of reformer, and the operating fuel processor efficiency [13]. Steam reforming or autothermal reforming are commonly used methods to produce hydrogen-rich feed, referred as the ‘reformate’ which typically contains 40 – 70% of H_2, 15-25% of carbon compounds including carbon dioxide (CO_2)

and carbon monoxide (CO), and small quantities of inert gases and sulphide impurities[373]. Natural gas reformate could lead to 42 % of H_2, i.e. ~2.4 times lower concentration of the pure H_2, 16% of carbon dioxide (CO_2), and 42% of N_2 [13]. The use of natural gas reformate as fuel results in lowered Nernst cell voltage reducing overall cell performance

Similarly, reformation of methane (CH_4) generates hydrogen-rich fuel feed with ~ 80% of H_2 and ~ 20% of carbon compounds, including CO_2 and carbon monoxide (CO) [374]. CO has a much more severe impact on fuel cell performance than CO_2. However, CO_2 can lead on to the formation of CO through electro-reduction of CO_2 [374], increasing CO concentration in the anode feed. Therefore, operating PEFCs on a hydrocarbon reformate gas could expose the anode CL to CO in the concentration range of 10-100 ppm. At low temperature, Pt has a higher affinity to CO than to H_2; hence, occupying most of the catalyst sites that results in loss of ECSA and leading to carbon corrosion [375]. Therefore, the composition of reformate gas has the following effects on the PEFC performance [13,375],

- Loss of potential due to low H_2 concentration
- Catalyst poisoning due to CO content
- Poisoning of CLs and membrane due to ammonia and hydrogen sulphide.

Appendix B: Mechanical and assembly errors

The large scale market penetration of PEFC technology demands further improvements in the operating and durability performances and the factors defining these performances. The cell assembly process is one of those factors demanding attention and improvement. To meet the required power and voltage demands, multiple fuel cells (PEFCs) composed of MEAs, GDLs, BBPs, gaskets and endplates, are assembled with the help of bolts and tie-bars and subjected to the clamping pressure, as shown in Figure B-1. Practically, it has been seen that several factors such as assembly method, pressure, alignment, manufacturing errors, manufacturing tolerances, all can affect the stack integrity, and hence, the stack performance and durability [376,377]. The various mechanical and assembly errors are shown in Figure . The dimension and the shape error arises from the stamping and forming process (material forming and hydroforming) of the metallic bipolar plate and are unavoidable due to the limitations on the manufacturing process and tooling and forming tolerances [378–380].

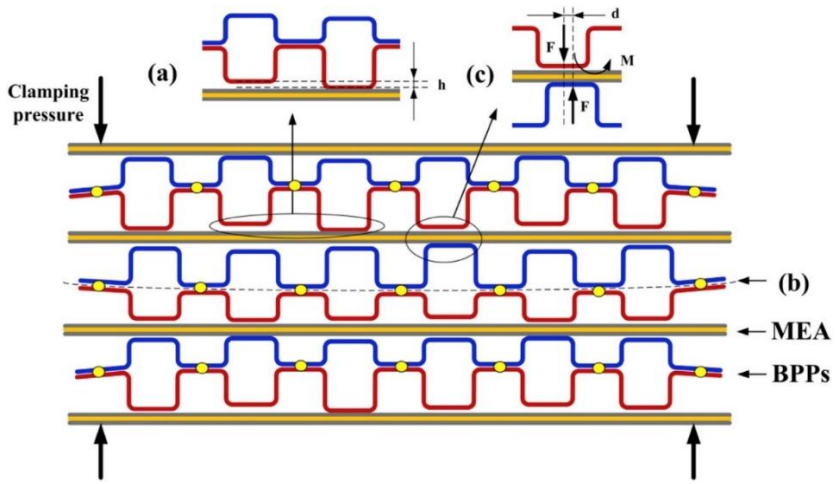

Figure B-1 Schematic of PEM fuel cell stack metallic BPPs' (a) dimensional error; (b) shape error; and (c) assembly error [378]

Practically, hundreds of single cells are assembled in series to meet the required power output and the manual assembly process, which is a commonly used assembly

technique applied to most of the stacks leading to significant assembly errors. An increase in the number of cells in the stack further augments the positioning and cumulative assembly errors. In addition to this, the unavoidable vibration and hygro-thermal cycling present in the operating fuel cell may aggravate the assembly error [381,382]. This is particularly relevant to the automobile application, which is subjected to frequent vibrations. The assembly errors could lead to potentially catastrophic failures of the stack; hence, it is crucial to control and reduce the assembly errors. However; due to the vast variation in the component sizing and tolerances, ranging from few nanometres on the membranes and CLs to few millimetres on the bipolar plates and endplates, it is difficult to control the assembly error without increasing the cost of the assembly process. At present, the positioning and assembly techniques in the stack building are made up of up to 14% of the total fuel cell cost [383]. This emphasises the need to investigate the effect of assembly errors on fuel cell component, in order to achieve a trade-off between non-uniform cell compression, the accuracy of the assembly process and the performance and durability of the cell. Majority of the efforts in the literature are focused on the non-uniform compression of the perfectly aligned fuel cell. The cell compression process results in the in-plane stresses in the membrane and operating cycles results in the non-uniform distribution of hydro-thermal stresses, localised bending stresses and further contribute to the delamination between the GDL and the MEA [225,384].

Liu et al. [385] developed the parameterised FEA model and ‘least squares- support vector machine (LS-SVM)’ simulation to analyse the effect of assembly errors on the pressure distribution and stress failure of the MEA. The simulation results with the aligned flow-field, i.e. without the assembly error and the misaligned flow-fields, i.e. the with the assembly error designs results in the non-uniform contact pressure distribution at the GDL / MEA interface and approximately 25% increase in the von-mises stress at the membrane highlighting the possibility of early failure of the cell(

Figure B-2. The same study also revealed that the probability of the stack failure increases exponentially with the cumulative assembly error and number of cells.

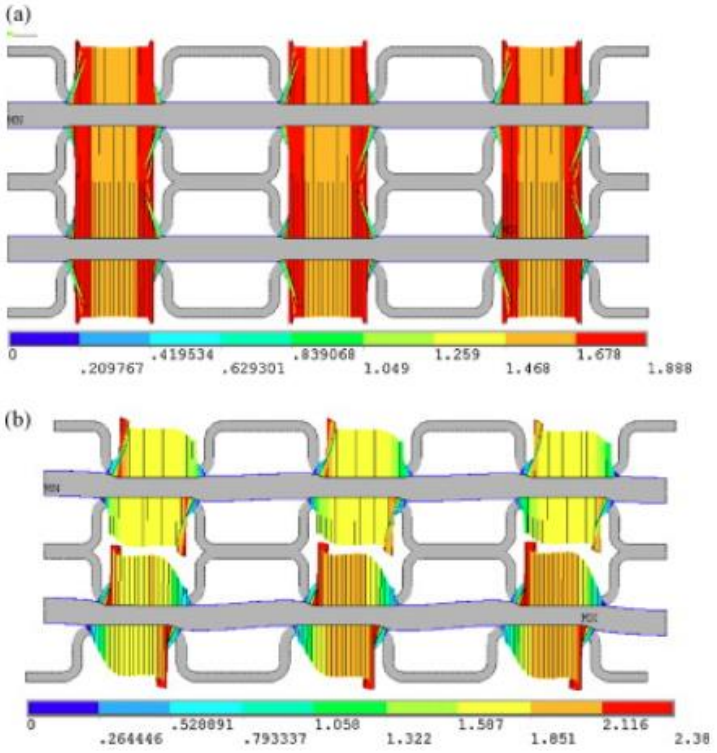

Figure B-2 Contact pressure distribution between BPP and MEA (a) without assembly error (aligned flow-field) and (b) with assembly error (misaligned flow-field) [385]

Banan et al. investigated the effect of 10% and 20% channel misalignment on delamination propagation over the number of operating cycles [381]. The study observed that the GDL/ CL interface experience a higher rate of the delamination propagation in case of misaligned channels compared to the aligned case; i.e. approximately 2-fold increase in the delamination rate when the channels are misaligned by 20%. The higher rate of delamination propagation has occurred from higher von-mises stresses caused by the channel misalignment that lowers the expected life span of the cell.